Discrete Models for Cohesive Frictional Materials

von

Gian Antonio D'Addetta

Discrete Models for
Cohesive Frictional Materials

Von der Fakultät Bau- und Umweltingenieurwissenschaften
der Universität Stuttgart zur Erlangung der Würde eines Doktors der
Ingenieurwissenschaften (Dr.-Ing.) genehmigte Abhandlung

vorgelegt von

Gian Antonio D'Addetta

aus Karlsruhe

Hauptberichter:	Prof. Dr.-Ing. Ekkehard Ramm
1. Mitberichter:	Prof. Dr. rer. nat. Hans Herrmann
2. Mitberichter:	Prof. Dr.-Ing. Stefan Diebels
Tag der mündlichen Prüfung:	28. Mai 2004

Zusammenfassung

Das Auftreten von Geomaterialien ist nicht nur auf die uns umgebenden Natur beschränkt, z. B. in der Form eines natürlich vorgegebenen Bodens. Vielmehr finden diese Materialien schon seit je her im Bauwesen Anwendung, wie z. B. in der Form eines künstlich hergestellten Baumaterials wie Beton. Deren Versagensmechanismen sind durch komplexe Bruchmoden gekennzeichnet und zeigen bedingt durch die inhomogene Mikrostruktur eine anisotrope Ausrichtung. Sobald Lokalisierungsphänomene wie Risse oder Scherbänder auftreten, kann ein solches Material nicht mehr als kontinuierlich betrachtet werden. Die diskontinuierliche Natur des Versagens erfordert angemessene und verlässliche numerische Simulationsmodelle wie die Diskrete Element Methode (DEM). Insofern stellt die Erarbeitung einwandfreier DEM Modelle zur diskontinuierlichen Simulation von Geomaterialien zusammen mit der Entwicklung geeigneter Homogenisierungsverfahren zur Quantifizierung dieser das generelle Ziel dieser Dissertation dar.

Der erste Schwerpunkt dieser Arbeit ist die Weiterentwicklung von DEM Modellen hinsichtlich der Beschreibung kohäsiver Materialien wie Beton, Keramik oder Fels, wie auch nicht kohäsiver Materialien wie Sand. Ausgehend von einem einfachen zweidimensionalen DEM Modell für nicht kohäsive polygonale Partikelensemble wird die Komplexität des Modells schrittweise in Richtung auf die Beschreibung kohäsiver Partikelensemble erhöht. In diesem Zusammenhang werden zwei Ansätze zur Darstellung der Kohäsion, nämlich ein Balken und ein Interface Modell, vorgestellt. Die Einbindung dieser Ansätze in die DEM Methodik über die Einführung anziehender Kräfte zwischen benachbarten Partikeln führt zu erweiterten DEM Modellen. Die Durchführung eines umfangreiches Simulationsprogramms ermöglicht einen qualitativen und quantitativen Vergleich von Simulationen und Experimenten. Dabei steht die zutreffende Wiedergabe der Rissentwicklung unterschiedlicher Belastungsszenarien wie auch die Identifikation des experimentellen Entfestigungsverhalten im Vordergrund. In der Folge ansteigender Komplexität stellt die Umsetzung einer mikrostruktur-basierten Simulationsumgebung, die auf den zuvor erwähnten erweiterten DEM Modellen aufbaut, den letzten Schritt dar. Damit wird eine zwei-Phasen Mikrostruktur berücksichtigt bei der steife Aggregate in einer weichen Matrix eingebettet sind. Schließlich können mit steigender Komplexität die vielfältigen Versagenscharakteristika von Geomaterialien dargestellt werden und ermöglichen eine Quantifizierung dieses DEM Modells.

Der zweite Schwerpunkt dieser Arbeit ist die Entwicklung und Implementierung geeigneter Homogenisierungsansätze zur Beschreibung des Mikro-Makro-Übergangs. Es werden Homogenisierungsprozeduren entwickelt welche es erlauben aus einem einfachen Boltzmann-Kontinuum-basierten Partikelmodell ein komplexeres Kontinuum mit Mikrostruktur nach Mindlin zu definieren. Dabei steht die numerische Umsetzung dieses Übergangs hinsichtlich erweiterter Kontinuumstheorien wie die mikropolare oder Gradiententheorie im Mittelpunkt. Die Größen der Mikro- oder Partikelskala werden mit vergleichbaren kontinuumsmechanischen Größen auf der Makroskala verbunden und erlauben die Ableitung mittlerer dynamischer und kinematischer Größen. Startpunkt dieser Homogenisierungsprozeduren ist die Skalenseparation zwischen den charaketristischen Skalen eines Partikelensembles, nämlich die des makroskopischen Körpers, des repräsentativen Volumens und des einzelnen Partikels. Ausgehend von diesen Argumenten erhält man vereinfachte Gleichgewichtsaussagen für repräsentative Volumenelemente (RVE).

Abstract

Geomaterials are widespread in nature as well as in engineering practice, for example in the form of a naturally given soil or a synthetic manufactured building material. The failure mechanisms of these materials are characterized by complex failure modes and show a highly anisotropic bias due to their inhomogeneous microstructure. Since localization phenomena like cracks or shear bands occur the material cannot be treated as continuous in the usual manner. The discontinuous nature of failure in geomaterials demands an adequate and reliable numerical simulation model like the discrete element method (DEM). The attraction of DEM simulations of continua is attributable to the fact that the appropriate complexity (localization, pattern formation, etc.) appears as an emergent feature, without the need for it to be programmed explicitly. Based on simple contact laws and a limited number of arbitrary parameters a rich behavior is obtained. Therefore, the general goal of the present thesis is to elaborate sound DEM models for the discontinuous simulation of geomaterials which are quantified by adequate homogenization techniques.

The first main focus of this thesis is to advance DEM models in order to account for both the cohesive nature of materials like concrete, ceramics or rock and the cohesionless nature of materials like sand. Starting from a basic two-dimensional DEM model for non-cohesive polygonal particle assemblies, the complexity of the model is successively augmented towards the description of cohesive particle assemblies. In this context two approaches for the representation of cohesion, a beam and an interface model, are elaborated. If included into the DEM methodology by representing an attracting force between neighboring particles these approaches yield enhanced DEM models. An extensive simulation program aims at a qualitative and quantitative comparison of simulations and experiments. The scope of this confrontation is the correct representation of the crack evolution of various loading setups and the full identification of the experimentally measured softening response. The last step in the series of increasing complexity is the realization of a microstructure-based simulation environment which utilizes the foregoing enhanced DEM models. The two-phase microstructure is included, if different properties of the cohesive components (beam or interface) are assigned with respect to their position. In that, the inclusion of a microstructure regards for stiffer aggregates embedded in a less stiffer matrix. With the growing model complexity a wide variety of failure features of geomaterials can be represented and a quantification of the model is enabled.

The second focal point of this thesis concerns the development and numerical implementation of adequate homogenization approaches by means of a micro to macro transition from the particle to the macro level. Homogenization procedures are developed which allow for a transfer from a simple Boltzmann continuum based particle model to a more complex continuum with microstructure according to Mindlin. The numerical realization of the transitions towards enhanced continuum theories like micropolar and gradient models is verified from a micromechanical viewpoint. The quantities of the micro or particle scale are linked to comparable continuum mechanical quantities on the macro scale and, thus, average dynamic and kinematic quantities are derived. Starting point of these homogenization approaches is the argument of scale separation between the characteristic scales of a particle assembly, namely that of a macroscopic body, a representative volume and an individual particle. Use of these arguments yields simplified equilibrium conditions for a representative volume element (RVE) on an intermediate scale.

Vorwort

Die vorliegende Arbeit entstand während meiner Tätigkeit als wissenschaftlicher Mitarbeiter am Institut für Baustatik der Universität Stuttgart im Rahmen der DFG-Forschergruppe FOR 326 in der Zeit vom Mai 1998 bis April 2004. In diesem Kontext sei der Deutschen Forschungsgemeinschaft (DFG) für die finanzielle Unterstützung gedankt.

Mein besonderer Dank gebührt Herrn Prof. Dr.-Ing. Ekkehard Ramm für die Anregung zu dieser Arbeit, seiner fortwährenden Unterstützung während des Zustandekommens der Arbeit und die Übernahme des Hauptberichts. Das optimale wissenschaftliche Umfeld, welches er an seinem Institut geschaffen hat, und die Kombination aus gewährter wissenschaftlicher Freiheit und geforderter zielgerichteter Projektarbeit hat entscheidend zum Gelingen dieses Promotionsprojektes beigetragen. Damit hat er während dieser Zeit einen nicht unwesentlichen Einfluß auf meine persönliche Entwicklung gehabt. Besonders bedanken möchte ich mich auch bei den Herren Prof. Dr. rer. nat. Hans Herrmann und Prof. Dr.-Ing. Stefan Diebels für die bereitwillige Übernahme der Mitberichte und die zügige Durchsicht der vorliegenden Arbeit. Herrn Prof. Dr. rer. nat. Hans Herrmann möchte ich besonders für die Möglichkeit danken zu Beginn meiner Promotionszeit auf einen numerischen Code aus seinem Institut zurückgreifen zu können, der mir den Einstieg in dieses für mich neue Forschungsgebiet entscheidend erleichtert hat. In diesem Zusammenhang gilt Herrn Prof. Dr. rer. nat. Ferenc Kun ein ganz besonderer Dank, denn ohne dessen tatkräftige Unterstützung und zugehörigen Wissenstransfer hätte sich mein Einstieg in die Diskrete Elemente Methode sicher bei weitem schwieriger gestaltet. Herrn Prof. Dr.-Ing. Stefan Diebels danke ich für die stete Unterstützung und Diskussionsbereitschaft während meiner gesamten Promotionszeit. Insbesondere die Diskussionen und Anregungen im Rahmen unserer Zusammenarbeit in der zweiten Phase meiner Tätigkeit haben einen wesentlichen Einfluß auf die Gesamtkomposition dieser Dissertation gehabt.

Mein Dank gilt auch all meinen Kollegen des Instituts für Baustatik für die freundschaftliche kollegiale Atmosphäre und die damit verbundenen idealen Arbeitsbedingungen. Deren stete Hilfsbereitschaft, fachliche Diskussionen und Anregungen sowie die nicht immer ganz so wissenschaftlichen Gespräche haben auch ihren Teil zum Gelingen dieser Arbeit beigetragen. Insbesondere meinem langjährigen Zimmerkollegen und Freund Michael Leukart möchte ich für die äußerst angenehme Zeit in der Außenstelle der Außenstelle danken. Darüber hinaus blicke ich immer wieder gerne auf die gemeinsamen täglichen Zugfahrten mit meinem Kollegen und Freund Roman Kemmler zurück, die mich in den ersten Jahren am Institut begleiteten. Den Kollegen der DFG-Forschergruppe FOR 326 „Modellierung kohäsiver Reibungsmaterialien" sei für die zahlreichen Diskussionen und den Wissensaustausch im Kontext der Forschergruppenseminare und weiterer regelmäßiger Treffen gedankt. Ein besondere Dank gilt Ferenc Kun, Michael Leukart und Stefan Luding für die kritische Durchsicht dieser Arbeit.

Ein ganz herzlicher Dank gebührt meinen lieben Eltern und allen voran meiner liebsten Melanie! Ihre kontinuierliche Unterstützung, ihr liebevolles Verständnis und ihre andauernde Motivation waren nicht nur in den „dunklen" Phasen meiner Promotionszeit von unschätzbaren Wert, sondern boten mir zu jeder Zeit den bedingungslosen Rückhalt der zur Vollendung dieser Arbeit von Nöten war.

Stuttgart, im Juni 2004   Gian Antonio D'Addetta

Preface

The present work was carried out at the Institute of Structural Mechanics of the University of Stuttgart within a project of the DFG research group FOR 326 "Modelling of cohesive frictional materials" from May 1998 to April 2004. In this context i gratefully acknowledge the financial support of the German Research Foundation (DFG).

First of all, i would like to thank my supervisor Prof. Dr.-Ing. Ekkehard Ramm for the motivation to this work and his continual support during the passed six years. The optimal scientific environment which he created at his institute and the combination of granted scientific liberty and required aim-oriented project work contributed in a favorable manner to the success of this dissertation project. Therewith, during the complete time period he had an important impact on my own personal development. Furthermore, i would like to thank Prof. Dr. rer. nat. Hans Herrmann and Prof. Dr.-Ing. Stefan Diebels for their willingness to act as co-referees and their quick and accurate review of the thesis. In particular, i thank Prof. Dr. rer. nat. Hans Herrmann for the possibility to use an open-source numerical code of his institute, which definitely facilitated the start of my research. In this context i am also grateful to Prof. Dr. rer. nat. Ferenc Kun, who introduced me to the Discrete Element Method and with his energetic support and corresponding knowledge transfer paved the way for my research. I would also like to thank Prof. Dr.-Ing. Stefan Diebels for his steady willingness to discuss with me various topics of my work during the last six years. In particular, i am indebted for all his discussion contributions and suggestions during our cooperation in the second phase of my research work. They had a significant effect on the composition of this thesis.

A special thank goes to all my colleagues of the Institute of Structural Mechanics for the cordial cooperative atmosphere and the associated ideal working conditions. Their continual helpfulness, professional discussions, suggestions as well as the sometimes not so scientific discussions have also contributed to the outcome of the present work. In particular, i thank my longstanding roommate and friend Michael Leukart for the very pleasant time in the outpost of the outpost of our institute. Furthermore, i thank my earlier colleague and friend Roman Kemmler for the various discussions on our daily commuter train rides in the first phase of my work. In addition, i acknowledge the numerous discussions and suggestions of the colleagues of the DFG research group "Modelling of cohesive frictional materials" within our group seminars and various regular meetings. A very special thank is dedicated to Ferenc Kun, Michael Leukart and Stefan Luding for proof-reading earlier forms of the manuscript and for their critical review.

Finally, i am deeply indebted for the assistance and support of my dear parents and above all my beloved Melanie! Her continual encouragement, her loving understanding and her tireless motivation were not only an invaluable help in the "dark" phases of my PhD time, but also her unquestioning support was essential for the completion of the present work.

Stuttgart, June 2004   Gian Antonio D'Addetta

Erneut stellte er sich die Frage: Wie weiß man, welcher Gedanke der richtige ist? Es ist, als spiele man mit seinen intuitiven Impulsen Roulette. Schwarz führt in eine Sackgasse, Rot auf den richtigen Weg. Die Zeit ist ein schnell verbrauchtes Kapital.

Randzonen existieren nicht. Unabdingbar ist das, was alle verachten und abstreiten, auf das jedoch alle hoffen: das Glück. Daß der Gedanke den man wählt, sich als der richtige erweist, daß die Spur der man folgt, nicht auf direktem Weg in ein unerwartetes Vakuum führt.

Henning Mankell, Mittsommermord

Contents

Nomenclature

The following abbreviations and symbols will be addressed several times throughout the thesis. Additionally, rarely occurring abbreviations and symbols are noted in the corresponding context.

Abbreviations

CD	Contact Dynamics
DEM	Discrete Element Method
DDA	Discontinuous Deformation Analysis
FE	Finite Element
FEM	Finite Element Method
MD	Molecular Dynamics
MMM	Micro-Meso-Macro principle of homogenization
RVE	Representative Volume Element
SPH	Smooth Particle Hydrodynamics

Symbols in the context of:

General formalism

$\mathbf{I}$	fundamental tensor of second order
$\overset{3}{\mathbf{E}}$	fundamental tensor of third order, Ricci permutation tensor
$\mathcal{I}$	fundamental tensor of fourth order
$\langle \cdot \rangle$	averaging operator of vectorial and tensorial quantity
$\langle\langle \cdot \rangle\rangle$	average of a RVE quantity $\langle \cdot \rangle$ over all RVEs within a sample
$\lvert \cdot \rvert$	L_2 norm of an arbitrary tensorial quantity

Material body

$\mathcal{O}$	origin (fixed point in space)
$\mathcal{B}$	material body
$\mathcal{S} = \partial\mathcal{B}$	boundary of material body
$\mathcal{P}$	material point, macro particle
$\mathcal{P}_{mic}$	micro particle
$\partial\mathcal{P}_{mic}$	boundary of (micro) particle
Γ_N	*Neumann* boundary
Γ_D	*Dirichlet* boundary
$\mathbf{X}$	position vector of material point in reference configuration

$\mathbf{x}$	position vector of material point in actual configuration
$\mathbf{u}$	displacement vector of material point
$\mathbf{v}$	velocity vector of material point
$\mathbf{a}$	acceleration vector of material point

Kinematic measures

$\mathbf{H}$	material displacement gradient
$\mathbf{F}$	material deformation gradient, first deformation gradient
$\mathbf{G}$	second deformation gradient
$\mathbf{K}$	third deformation gradient
$\mathbf{E}$	Green-Lagrangean strain
$\mathbf{E}_{lin} = \boldsymbol{\varepsilon}$	linearized (Green-Lagrangean) strain, macro strain
$\dot{\mathbf{F}}$	material velocity gradient
$\mathbf{L}$	spatial velocity gradient
$\boldsymbol{\Delta}$	non-symmetric deformation rate
$\boldsymbol{\Omega}$	(skew-symmetric) gyration tensor
$\boldsymbol{\varepsilon}_{rot} = \boldsymbol{\varepsilon}_{skw}$	macro rotation, skew-symmetric linearized strain
$\mathbf{H}'$	micro material displacement gradient, micro deformation
$\boldsymbol{\varepsilon}'$	micro strain
$\boldsymbol{\Gamma}$	relative deformation
$\boldsymbol{\mathcal{K}}$	micro deformation gradient, curvature
$\bar{\boldsymbol{\varepsilon}}$	linearized micropolar strain
$\bar{\boldsymbol{\kappa}}$	linearized micropolar curvature
$\bar{\boldsymbol{\Delta}}$	micropolar deformation rate
$\bar{\boldsymbol{\Omega}}$	micropolar gyration tensor

Dynamic measures

$\mathbf{f}$	body force per unit volume
$\mathbf{t}$	contact force, surface traction per unit surface area
$\mathbf{t}_{\mathcal{B}}$	body force per unit volume (e. g. $\mathbf{f}$)
$\mathbf{t}_{\mathcal{S}}$	surface traction per unit surface area (e. g. $\mathbf{t}$)
$\mathbf{b}$	body force (e. g. gravitation force)
$\mathbf{m}$	contact couple density per unit surface area
$\mathbf{m}_{\mathcal{B}}$	double force per unit volume
$\mathbf{m}_{\mathcal{S}}$	double traction per unit surface area (e. g. $\mathbf{m}$)
$\mathbf{T}$	Cauchy stresses
$\mathbf{T}_1$	symmetric stresses, conjugated to linearized strain $\boldsymbol{\varepsilon}$
$\mathbf{T}_2$	relative stresses, conjugated to relative deformation $\boldsymbol{\Gamma}$
$\mathbf{T}_{sym}$	symmetric part of Cauchy stresses
$\mathbf{T}_{skw}$	skew-symmetric part of Cauchy stresses
$\mathbf{T}^c$	contribution of Cauchy stress related to contact forces (boundary terms)
$\mathbf{T}^{vol}$	contribution of Cauchy stress related to volume terms
$\boldsymbol{\mu}$	higher order stresses, conjugated to micro deformation gradient $\boldsymbol{\mathcal{K}}$
$\tilde{\mathbf{M}}$	stress moment, continuum moment (i. e. moment of stress distribution)
$\bar{\mathbf{M}}$	couple stresses
$\mathbf{Q}$	higher order stresses, conjugated to second deformation gradient $\mathbf{G}$

$\mathbf{R}$ higher order stresses, conjugated to third deformation gradient $\mathbf{K}$

Energetic measures

$\Psi, \boldsymbol{\Psi}$	volume specific mechanical quantity
$\boldsymbol{\phi} \cdot \mathbf{n}, \boldsymbol{\Phi} \cdot \mathbf{n}$	flux of mechanical quantity through surface
$\sigma, \boldsymbol{\sigma}$	supply of mechanical quantity
$\hat{\Psi}, \hat{\boldsymbol{\Psi}}$	production of mechanical quantity
$W^{(i)}$	sum of work of internal forces
$W^{(e)}$	sum of work of external forces
$P_{int}, P_{int}{}^*$	mechanical power, rate of mechanical work
$P_{int}{}^1, P_{int}{}^{1*}$	mechanical power of stresses
$P_{int}{}^2, P_{int}{}^{2*}$	mechanical power of higher order stresses

Standard DEM model

$\mathbf{X}_i$	position vector of particle i in reference configuration
$\mathbf{x}_i$	position vector of particle i in actual configuration
$\mathbf{X}_i^g$	spatial position (without rotation) of particle i in reference configuration
$\mathbf{x}_i^g$	spatial position (without rotation) of particle i in actual configuration
φ_i	rotation angle of particle i with respect to reference configuration
$\mathbf{u}_i^g$	displacement vector of particle i
ϕ_i	rotation of particle i
S_i	center of mass of particle i
$\mathbf{v}_i, \dot{\mathbf{x}}_i$	velocity of particle i
$\mathbf{a}_i, \ddot{\mathbf{x}}_i$	acceleration of particle i
$\dot{\varphi}_i$	angular velocity of particle i
$\mathbf{l}_i^c$	contact vector between force point and center of mass of particle i
$\mathbf{r}^c$	branch vector between contacting particles
a	irregularity parameter for mesh generation
E_p	elastic modulus of particle material
γ_n, γ_t	normal and tangential viscous damping coefficient
μ	contact friction coefficient
ρ	density
m_i	mass of particle i
θ_i	mass moment of inertia of particle i
$\mathbf{f}^c$	contact force vector
f_n^c, f_t^c	normal and tangential component of contact force vector
$\mathbf{f}_i$	collection of all interaction forces of particle i
$\mathbf{g}_i$	gravitation forces of particle i
$\mathbf{v}_{rel}$	relative velocity at the contact zone
m_{eff}	effective mass
d^c	characteristic length of contact region
$\mathbf{M}_i$	generalized mass matrix
Δt	time step

Enhanced DEM models

E_b	elastic modulus of beam elements
$\epsilon_{max}^b, \phi_{max}^b$	beam failure parameters for stretching and bending
ϵ^b, ϕ^b	local axial beam strain and beam end rotation (i. e. particle rotation ϕ)
$\mathbf{K}^b$	Timoshenko stiffness matrix
$\mathbf{f}_{ik}^b$	generalized beam force vector for beam between particles i and k
k_n, k_t	normal and tangential stiffnesses of spring
$\mathbf{K}^{bond}$	interface stiffness matrix
$\mathbf{f}_{ik}^{bond}$	generalized bond force vector for bond between particles i and k
$\mathbf{u}$	relative deformation of spring
$\mathbf{u}^e, \mathbf{u}^p$	elastic and plastic part of relative deformation of spring
κ	softening variable of one spring
$\langle \kappa \rangle$	average softening variable of one bond
$\boldsymbol{\sigma}^{tr}, \boldsymbol{\sigma}^0, \boldsymbol{\sigma}$	trial, initial and corrected stress state
$\dot{\lambda}$	plastic multiplier
$\mathbf{g}$	direction of plastic flow
$\mathbf{n}_p, \mathbf{m}_p$	gradients of yield surface f and plastic potential g
σ_n^{max}	maximum tensile stress of spring
σ_t^{max}	maximum shear stress of spring (cohesion)
$G_{f,n}, G_{f,t}$	fracture energy for pure tensile and pure shear softening
φ, γ	shape parameters of yield surface
ψ	shape parameter of plastic potential
f_n^{tr}, f_t^{tr}	normal and tangential spring forces at each integration point/spring
$\sigma_n^{tr}, \sigma_t^{tr}$	local normal and tangential stresses at integration point/spring
$(\cdot)^{(a)}, (\cdot)^{(m)},$ $(\cdot)^{(i)}$	aggregate, matrix and "interface" related quantities

Damage representation

$\mathbf{N}$	fabric tensor of first kind, damage tensor
$\mathbf{F}$	fabric tensor of second kind, crack density tensor
$\mathbf{D}$	fabric tensor of third kind, deviatoric part of damage tensor
$F(\mathbf{n})$	discontinuous crack density distribution
$f(\mathbf{n})$	continuous approximation of crack density distribution
ξ_d	defect correlation length
$d_{i,i+1}$	spatial distance between two successive cracks
$d_{i,i+1}^n, d_{i,i+1}^t$	distance of successive cracks in/perpendicular to direction of shear fault
d_i^s	normal distance between crack position and primary shear zone
$h(d_{i,i+1})$	normalized probability density of successive cracks
A	normalization constant of distribution $h(d_{i,i+1})$

Homogenization procedures

$\mathcal{R}$	representative volume element (RVE)
$\partial\mathcal{R}$	boundary of RVE $\mathcal{R}$
$\mathbf{u}^i, \bar{\boldsymbol{\varphi}}^i$	displacement and rotation of particle i on $\partial\mathcal{R}$
$\mathbf{v}^i, \dot{\bar{\boldsymbol{\varphi}}}^i$	spatial and angular velocity of particle i on $\partial\mathcal{R}$

$\mathbf{n}^i$	unit normal on boundary segment i of $\partial\mathcal{R}$
Δw^i	width of boundary segment i of $\partial\mathcal{R}$
$\mathbf{f}^{(i)}$	resultant force vector per particle i on $\partial\mathcal{R}$
$\mathbf{f}_c^{(i)}, \mathbf{f}_{coh}^{(i)}$	resultant contact and cohesive force vector per particle i on $\partial\mathcal{R}$
$\mathbf{f}^{(i)c}$	contact force vector of outward contact c per particle i on $\partial\mathcal{R}$
$\mathbf{f}^{(i)b}$	cohesive force vector of outward cohesive component b per particle i on $\partial\mathcal{R}$
$\bar{\mathbf{m}}^{(i)}$	resultant moment per particle i on $\partial\mathcal{R}$
$\bar{\mathbf{m}}_c^{(i)}$	resultant contact moment per particle i on $\partial\mathcal{R}$
$\bar{\mathbf{m}}_{coh}^{(i)}$	resultant intrinsic moment of cohesive component per particle i on $\partial\mathcal{R}$
$\bar{\mathbf{m}}^{(i)b}$	intrinsic moment of outward cohesive component b per particle i on $\partial\mathcal{R}$
$V_{\mathcal{R}}$	volume of RVE
V_1, V_2	different volume definitions of RVE
$\partial\mathcal{R}_1, \partial\mathcal{R}_2$	boundary of RVE for alternating volume definition
$r_1, r_2, \Delta r$	equivalent radii and corresponding difference according to RVE definitions
$\mathcal{M}, \mathcal{N}$	base and target particles of RVE
$\boldsymbol{\Delta}\mathbf{x}_0$	distance vector between base $\mathcal{M}$ and target particle $\mathcal{N}$ at initial configuration
$\boldsymbol{\Delta}\mathbf{x}_t$	distance vector between base $\mathcal{M}$ and target particle $\mathcal{N}$ at actual configuration
$\mathbf{x}_0^i$	position vector of particle i within RVE at initial configuration
$\mathbf{x}_t^i$	position vector of particle i within RVE at actual configuration
$\tilde{\mathbf{w}}$	higher order terms of Taylor series, i. e. constant average error per RVE
$\delta\tilde{\mathbf{w}}^j$	fluctuation of constant average error $\tilde{\mathbf{w}} = \langle\tilde{\mathbf{w}}^j\rangle$ per particle pair $(\mathcal{M}, \mathcal{N}^j)$
$\tilde{\mathbf{w}}^j$	microstructural fluctuation field (on particle level) per particle pair $(\mathcal{M}, \mathcal{N}^j)$
$\mathbf{d}^j$	deviation between measured/approximated $\boldsymbol{\Delta}\mathbf{x}_t$ per particle pair $(\mathcal{M}, \mathcal{N}^j)$
$\mathbf{i}, \mathbf{X}, \mathbf{Y}, \mathbf{Z},$ $\mathbf{L}, \mathbf{V}$	auxiliary geometric tensors containing products of $\boldsymbol{\Delta}\mathbf{x}_0$
$\mathbf{j}, \mathbf{W}, \mathbf{H}, \mathbf{J}$	auxiliary geometric tensors containing products of $\boldsymbol{\Delta}\mathbf{x}_0$ and $\boldsymbol{\Delta}\mathbf{x}_t$
s	auxiliary geometric scalar quantity containing product of $\boldsymbol{\Delta}\mathbf{x}_t$
$\mathbf{K}^*, \mathbf{u}^*, \mathbf{P}^*$	auxiliary matrices for systems of equations
$\langle\tilde{\mathbf{W}}\rangle_{\mathcal{R}}, \langle\tilde{T}\rangle_{\mathcal{R}}$	vanishing quantities in the limit of consistent homogenization

Counter variables

N	number of particles within a sample
N_c	number of contacts within a sample
N_b	number of cohesive components within a sample
n_p, n_b, n_{bond}	number of particle contacts, beams and bonds per particle
n_{ip}	number of integration points (i. e. spring) along reference edge of a particle
N^{C^i}	number of contacts per particle i
$n_{\mathcal{R}}$	number of RVEs within a sample
$N_{\mathcal{R}}$	number of particles within RVE $\mathcal{R}$
$N_{\partial\mathcal{R}}$	number of particles on boundary of RVE $\partial\mathcal{R}$
B^i, C^i	number of outward oriented cohesive components and contacts per particle i on boundary of RVE $\partial\mathcal{R}$

Chapter 1

Introduction

1.1 Motivation

Cohesive frictional materials or geomaterials are widespread in nature as well as in engineering practice, for example in the form of a naturally given soil or a synthetic manufactured building material. The application of cohesive frictional materials as basic materials can be traced back to the development of ancient architecture at the time of the Roman Empire. The Roman master builders were among the first ones to "industrially" use concrete-type materials, e. g. opus caementitium, for their buildings, temples and prefabricated parts: Consider one of the most impressive examples of human architecture and one of the first buildings with structurally sensitive members being executed with concrete, the Pantheon in Rome, Italy. A steadily increasing interest in a preferably exact description of geomaterials demonstrates in a formidable manner that the calculation and modeling of these materials still poses a challenge to the research community, as it was since ancient times. The research is driven, on one hand, by the natural endeavor to find an optimal exploitation of the load capacity of engineering structures and, on other hand, to advance the design of new artificial geomaterial-based materials. The last point parallels the developments in neighboring engineering disciplines like aeronautical and space technology or mechanical engineering. These artificial materials combine the advantages of their constituents, while compensating their disadvantages. Two examples are high strength and textile reinforced concrete.

In principal, cohesive frictional materials are a subgroup of the class of geo- or frictional materials. As the name suggests, geomaterials denote materials which have their roots in the natural geology of our environment. This includes original materials that are found in nature like sands or rock, but also secondary materials that are industrially or evolutionary manufactured on the basis of these original materials like concrete or ceramics. Generally, geomaterials can be classified into two categories: cohesive ones like concrete, ceramics, rock or marl and cohesionless ones like sand and other granular type materials. These two classes of materials are not so different as they may look like at first sight. Quite the contrary is the case, as generally their structural composition is very similar. Non-cohesive geomaterials are characterized by the fact that they cannot sustain any tensile load. This is in contrast to the mechanical behavior of cohesive ones. In the case of cohesive geomaterials typically stiff aggregates are embedded in a surrounding soft matrix, as shown for example for concrete in figure 1.1 (a). From a physical point of view geomaterials like concrete, ceramics or marl can be considered as cemented granulates forming a heterogeneous macroscopic solid. In order to predict the remaining load capacity after reaching the ultimate load a substantiated knowledge of the underlying failure mechanisms is essential. For example, this knowledge may be based on micromechanical observations. The failure mechanisms of these materials are characterized by complex
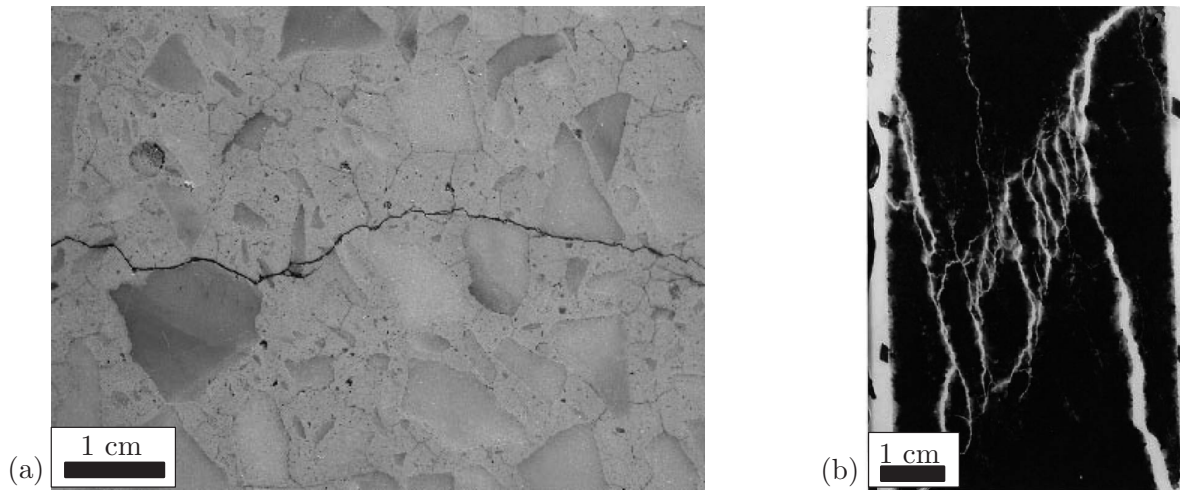
Figure 1.1: (a) Failure mechanism of concrete in tension and (b) rock in compression (courtesy of *Přikryl et al.* [204]).

failure modes in various loading situations and a highly anisotropic bias due to their inhomogeneous microstructure. The growth and coalescence of microcracks in cohesive geomaterials lead to the formation of macroscopic crack patterns. Finally, this results in a fragmentation into separate particle clusters forming a solid-granulates mix. Behaving quasi-brittle under load these materials are characterized by a localization of deformations in narrow zones, as shown for the case of cohesive geomaterials like concrete in tension in figure 1.1 (a), the compressive failure of a rock in figure 1.1 (b) or the biaxial failure of a marl in figure 1.2 (a). The failure in non-cohesive geomaterials is usually dominated by arising rolling modes of the grains. These combine with anticipating force peaks which are the result of a grain interlock. The localization of deformations via an activation of the grain rotation in very narrow bands is typical for materials like sand, compare the experimental observation of a sand footing in figure 1.2 (b).

The increased availability of computational power in the past decades encouraged the development of powerful numerical simulation models. The interaction of researchers from
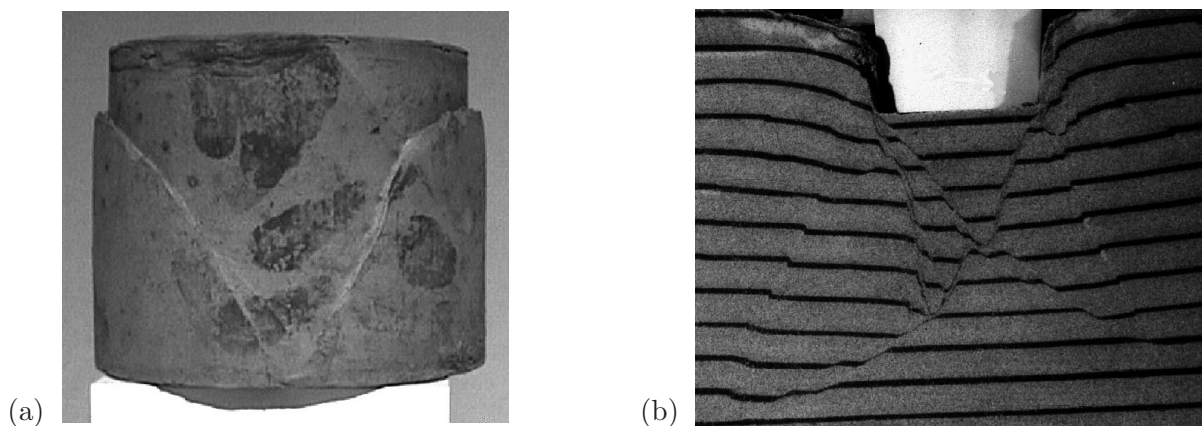
Figure 1.2: (a) Failure mechanism of marl (courtesy of *Marcher* [162]) and (b) sand (courtesy of *Nübel* [188]).

the computational mechanics and material mechanics community was very fruitful in the past. The collaboration of numericians and experimentalists resulted in numerous high level publications. Today, this symbiosis drives the advancement of numerical techniques towards a full multiscale description of engineering structures, from the atomistic to the structural scale.

The application range of a numerical model is directly related to the observation scale, as depicted for selected modeling techniques in figure 1.3. This diagram emphasizes the choice of scale definitions used throughout this thesis. Basically, a class of continuum models can be applied at each size scale, if the local quantities, e. g. like damage, are smeared over a certain region. Emerging heterogeneities, anisotropies and discontinuities are then cast in the form of macroscopic continuum variables, e. g. like a damage variable or a damage tensor in continuum damage mechanics. The verification of this kind of models can be achieved by a comparison with experiments of finite size. In order to allow for a realistic localization an enhancement of the classical continuum models is necessary. This enhancement, which is denoted as regularization, provides an accomplishment of the mathematical difficulties like the loss of ellipticity and well-posedness of the boundary value problem. This was the subject of a predecessor thesis by *Kuhl* [137]. To account for the non-local influence within a material, like crack interaction or stress redistribution effects, a physically motivated internal length scale may be introduced into the model. Along these lines, usual enhancements of continuum formulations are based on the introduction of localization limiters. Typical examples are non-local integral-, gradient- or micropolar-type models or, alternatively, viscous models. The salient characteristic of enhanced continuum models usually implemented in the context of the FEM is mirrored by the following fact: The internal length scale accounts for a microstructure at a given material point through an inclusion of the direct neighborhood either in an implicit or explicit manner. This internal length scales the width of arising localization zones and yields mesh insensitive simulation results. It is an open question, if the internal length is a pure material, a pure model or a combined material-model parameter. In particular, the relation of the internal length scale to the "real" material structure remains yet to be clarified.
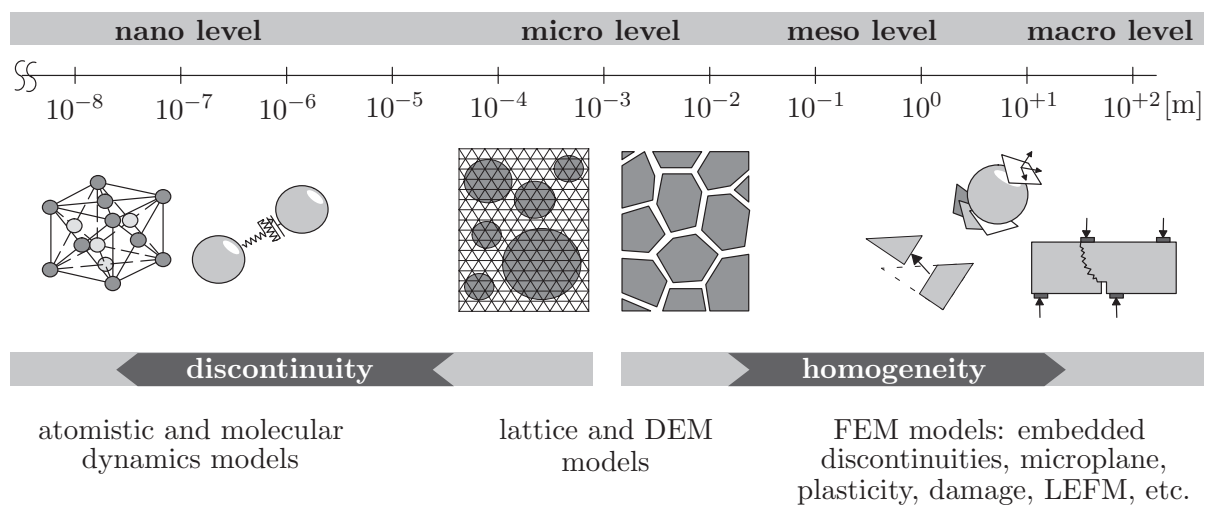
Figure 1.3: Typical observation scales and numerical modeling techniques for cohesive frictional materials.

Admittedly, if one compares the crack and localization zones in figures 1.1 and 1.2, the application of numerical models based on continuum theories seems to be a bold venture. From the point that localization phenomena like cracks or shear bands occur the material cannot be treated as continuous any longer. Due to the creation and continuous motion of the evolving crack surfaces the fracture and fragmentation of the solid is difficult to handle numerically. Therefore, most continuum models, both standard and enhanced ones, cannot account for the discrete nature of material failure in a natural way. Since the pioneering works on interface based models or models that embed discontinuities into continuum formulations, workarounds are available in the broadest sense. Strictly speaking, these models loose the character of being a continuum formulation. Alternatively, discrete models like lattice, granular dynamics or discrete element methods (DEM) have been developed. As the name DEM suggests, a solid is replaced by a discontinuous particle composite which allows for a detachment of bonds between particles (if initially present) and a re-contact of open surfaces. In contrast to continuum models, discrete or discontinuum models are characterized by the fact that displacements and stresses do not vary continuously in space. The DEM describes a class of dynamically driven computational schemes which are based on the motion of contacting particles. Due to computational reasons, mostly two-dimensional models with circular or polygonal particle shapes are employed. The models of this class are able to predict and simulate the fracture behavior of small scale applications of geomaterials very well. Recently, the increasing availability of computer power has made possible large scale computations using these models in the context of industrial applications as well. The attraction of particle simulations of continua is attributable to the fact that the appropriate complexity (localization, pattern formation, etc.) appears as an essential feature, without the need for it to be modeled explicitly. Based on very simple contact laws and a limited number of arbitrary parameters discrete element simulations yield a sophisticated behavior. The involvement of homogenization principles provides for the link between the micro and macro variables and, in analogy to a continuum formulation, provides equivalent continuum measures.

1.2   Scope and objective

The discontinuous nature of failure in geomaterials demands an adequate and reliable numerical simulation model. This model must present the ability to reproduce the characteristic features of cohesive and non-cohesive frictional materials as realistic as possible. This includes the ability to asses the localization in a qualitative manner, e. g. in form of a correct representation of cracks and shear zones. But, such a model requires also a proper quantitative reproduction of typical experimental results, e. g. in terms of a stress-strain diagram.

One of the main objectives of the present thesis is to elaborate a sound numerical model which accounts for both the cohesive nature of materials like concrete and the cohesionless nature of materials like sand. If a correct representation of the localization zones and recontacting crack surfaces comes to the fore, the discrete element method (DEM) seems to be an adequate choice as simulation model. The existence of contacts between discrete particles distinguishes a discontinuous from a continuous medium. Re- or newly contacting surfaces are automatically detected and the virtual overlap area of contacting polygons is related to a contact force. Starting from a basic DEM model for non-cohesive

polygonal particle assemblies, the complexity of the model will be successively augmented towards the description of cohesive particle assemblies. Therefore, two approaches for the representation of cohesion are elaborated: a beam and an interface model. Their advantages and disadvantages are discussed with regard to the interpretability of their parameters.

In the following step, an extensive simulation program aims at a qualitative and quantitative comparison of simulations and experiments. The scope of this confrontation is, on the one hand, the correct representation of the crack evolution of various loading setups and, on the other hand, the full identification of the experimentally measured softening response. The DEM simulations are expected to provide an improved insight in the failure mechanisms of "real" geomaterials from a micromechanical point of view. Experimental evidence of geomaterials points to failure mechanisms like crack face bridging or aggregate interlock to dominate the post-peak response. Therefore, the simulations of typical cohesive geomaterials are carried out on two levels: The examination on an observation scale larger than the resolution of the aggregate-matrix structure expresses the general ability to simulate this kind of material. A successive increasing complexity of the resolution towards a prototype microstructure clarifies the origin of the post-peak softening mode. Thus, a generation algorithm for a virtual microstructure is developed which accounts for a typical two-phase material structure. In order to characterize the evolving damage at different simulation stages and to enable a comparison with general experimental observations a special "tool" box is assembled. The "tools" contained therein represent procedures for the determination of characteristic damage and fracture related quantities.

The final focal point of this thesis concerns the development and numerical implementation of adequate homogenization procedures. They allow linking the quantities of the micro or particle scale to comparable continuum mechanical quantities on the macro scale. In this regard, the general goal is the derivation of average continuum mechanical quantities. On the other hand, the homogenization aims at a motivation of enhanced continuum theories by means of a micropolar and a gradient theory. In particular, the role of the internal length scale and its relation to the width of evolving localization zones is highlighted. On this account it is of special interest to classify the parameter "internal length" as material, model or combined material-model parameter. In order to attain new insights use is made of the explicitly prescribed microstructure and its relation to the internal length scale.

1.3 Organization

The present thesis consists of 10 chapters and each chapter is headed by general introductory remarks which include a summary of relevant literature. The thesis is roughly divided into two parts: In the first part, the details of the DEM models are presented, while the second part is concerned with the derivation of adequate homogenization procedures.

After the introduction, in *chapter 2* the mechanical foundations of a standard Boltzmann continuum and an enriched continuum with microstructure are given. The formulations are embedded in a general framework by universally valid balance laws. In *chapter 3* the formulation of a two-dimensional polygonal DEM model of cohesionless particle assemblies along with representative numerical examples are presented. Afterwards, with regard to a representation of cohesive materials, the DEM model is enhanced by beam

elements in *chapter 4* and, alternatively, by interface elements in *chapter 5.* Simulation results of cohesive particle assemblies clarify the application of the different DEM models. The characterization of damage by means of the texture development and the defect correlation length in *chapter 6* recalls the simulation results presented in the previous chapters from a different viewpoint. In *chapter 7* a procedure for the representation of a virtual microstructure and corresponding simulation results are given.

In the second part of this thesis, the micro to macro transition from the micro or particle level to the macro level is formally carried out by means of different homogenization approaches. *Chapter 8* is dedicated to the numerical verification of the transition from particle models to micropolar continua and *chapter 9* refers to the respective transition to gradient continua. These approaches provide the motivation for the enhanced continuum theories from a micromechanical viewpoint and are supplemented by numerical simulations. A final valuation of the thesis' content and a perspective on future work concludes the thesis in *chapter 10.*

Chapter 2

Fundamentals

The solution of boundary value problems in the context of the discrete element method (DEM) requires the knowledge of basic quantities of continuum mechanics for a description of the kinematics and dynamics of an arbitrary particle assembly. The definition of kinematic measures like strains or dynamic measures like stresses as well as corresponding balance laws provide the general framework for a numerical implementation. In the present chapter only a brief review of the fundamentals is given. Detailed discussion on the theory of elasticity and continuum mechanics can be found elsewhere, see among others the articles in the textbooks by *Ciarlet* [40], *Love* [151], *Malvern* [161], *Marsden & Hughes* [164], *Stein & Barthold* [228], *Truesdell & Noll* [239] or *Truesdell & Toupin* [240].

After presenting the fundamentals of a linear elastic continuum, the formulation of a *continuum with microstructure* according to *Mindlin* [172] is introduced: It represents a linear theory of a three-dimensional elastic continuum and incorporates properties of the microstructure. The standard Boltzmann, a micropolar or a gradient type theory are incorporated as special cases. Therefore, the kinematic and, consequently, dynamic description of the theory is enhanced and yields an adjusted set of balance equations. A motivation for a more detailed description in the context of a particle model is given as follows: The motion of a particle naturally includes a translational part (included in every standard theory) as well as a rotational part. This compares to the formulation of a micropolar theory, where a local rotation of material points as well as a translation is considered. The dynamic quantities of a standard continuum, which include the definition of tractions (forces per unit area), are supplemented by the definition of couple stresses (torques per unit area). A second emphasis is placed on the description of an elastic continuum enhanced by a gradient theory. In that, the surrounding neighborhood of a single particle naturally influences the particle's kinematic behavior. Following these lines the general form of homogenization approaches is discussed. Special reference will be made to the topic of representative elementary volumes and scale separation.

The goal of this chapter is to provide the theoretical frame for the numerical realization of the particle model and, in particular, for the development of corresponding homogenization approaches. More details will be given - if needed - in the respective chapters. In this introduction only mechanical quantities in the context of elastic materials (i. e. reversible deformation) in the small strain regime are noted.

2.1 General

A brief overview of the kinematic and dynamic measures of a standard Boltzmann continuum is given and embedded in a general framework by universally valid balance laws.

2.1.1   Kinematic measures

A material body $\mathcal{B}$ with a body surface $\mathcal{S}$ represents a three-dimensional connected manifold of material points $\mathcal{P}$ embedded in the Euclidean point space E^3 as shown in figure 2.1. The basic measures of the body's kinematic description are the actual position vector $\mathbf{x} = \mathbf{x}(\mathbf{X}, t)$ of a material point $\mathcal{P}$, its velocity vector $\mathbf{v} = \dot{\mathbf{x}} = \dot{\mathbf{x}}(\mathbf{X}, t)$ and acceleration vector $\mathbf{a} = \ddot{\mathbf{x}} = \ddot{\mathbf{x}}(\mathbf{X}, t)$. $\mathbf{x}$ denotes the position vector at the actual configuration at time $t = t_1 > t_0$ and $\mathbf{X}$ refers to the initial configuration $t = t_0$, compare figure 2.1. The parameter line denotes the spatial positions of $\mathcal{P}$ in the course of time t. The displacement vector is obtained as the difference of the initial and actual position vectors $\mathbf{u} = \mathbf{x} - \mathbf{X}$ with $\mathbf{u} = \mathbf{u}(\mathbf{X}, t)$. For brevity, in the following the position and time is neglected in the notion of the variables. The material deformation gradient involving the material displacement gradient $\mathbf{H}$ is constituted by

$$\mathbf{F} = \operatorname{Grad} \mathbf{x} = \frac{\partial \mathbf{x}}{\partial \mathbf{X}} = \frac{\partial (\mathbf{X} + \mathbf{u})}{\partial \mathbf{X}} = \mathbf{I} + \underbrace{\operatorname{Grad} \mathbf{u}}_{\mathbf{H}}, \qquad \text{with} \quad \det \mathbf{F} > 0. \qquad (2.1)$$

The notation $\operatorname{Grad}(\cdot)$ refers to a derivative with respect to the initial configuration, whereby $\operatorname{grad}(\cdot)$ refers to a derivation with respect to the actual configuration. The Green-Lagrangean strain is defined by

$$\mathbf{E} = \frac{1}{2} \left(\mathbf{F}^T \cdot \mathbf{F} - \mathbf{I} \right) = \frac{1}{2} \left(\mathbf{H} + \mathbf{H}^T + \mathbf{H}^T \cdot \mathbf{H} \right). \qquad (2.2)$$

Linearization of the Green-Lagrangean strain $\mathbf{E}$ about the undeformed state by use of the so-called Gâteaux or directional derivative yields the symmetric linearized Green-Lagrangean strain tensor for small displacements

$$\mathbf{E}_{lin} =: \boldsymbol{\varepsilon} = \frac{1}{2} \left(\operatorname{Grad} \mathbf{u} + \operatorname{Grad}^T \mathbf{u} \right) = \frac{1}{2} \left(\mathbf{H} + \mathbf{H}^T \right). \qquad (2.3)$$

The material and spatial velocity gradients are denoted by

$$\dot{\mathbf{F}} = \operatorname{Grad} \dot{\mathbf{x}}, \qquad \mathbf{L} = \dot{\mathbf{F}} \cdot \mathbf{F}^{-1} = \operatorname{grad} \dot{\mathbf{x}}. \qquad (2.4)$$

A splitting of $\mathbf{L}$ via $\mathbf{L} = \boldsymbol{\Delta} + \boldsymbol{\Omega}$ by right decomposition of $\mathbf{F}$ results in the non-symmetric deformation rate $\boldsymbol{\Delta}$ and skew-symmetric gyration tensor $\boldsymbol{\Omega}$ with $\boldsymbol{\Delta} \neq \boldsymbol{\Delta}^T$ and $\boldsymbol{\Omega} = -\boldsymbol{\Omega}^T$.
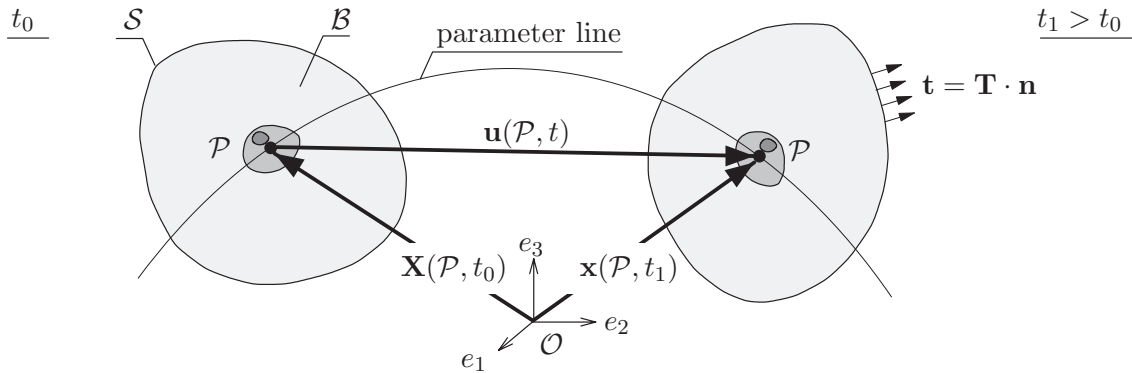
Figure 2.1: The material body $\mathcal{B}$ in initial (t_0) and actual (t_1) configuration.

2.1.2 Dynamic measures

A material body $\mathcal{B}$ is subjected to external body and contact forces by actions from a distance ($\mathbf{f}$: body force per volume element $\mathrm{d}v$) and at the vicinity ($\mathbf{t}$: contact force or surface traction per surface element $\mathrm{d}a$). Usually, the body force represents the gravitational action via $\mathbf{f} = \rho\mathbf{b}$, where $\mathbf{b}$ denotes the gravitation and ρ the density. The surface traction $\mathbf{t}$, like a contact force, depends on the position vector $\mathbf{x}$, the time t and the unit surface normal (outward oriented) $\mathbf{n}$, compare figure 2.1. Hence, the total force $\mathbf{k}$ acting on a body $\mathcal{B}$ is computed by

$$\mathbf{k} = \int_{\mathcal{S}} \mathbf{t}\,\mathrm{d}a + \int_{\mathcal{B}} \rho\mathbf{b}\,\mathrm{d}v\,. \tag{2.5}$$

The first term may be transferred into a volume integral by use of the Cauchy theorem $\mathbf{t}(\mathbf{x},t,\mathbf{n}) = \mathbf{T}(\mathbf{x},t) \cdot \mathbf{n}$ and the divergence theorem. $\mathbf{T}(\mathbf{x},t)$ denotes the Cauchy stress tensor ("true" stress). As a result of the theory enhancement in mind (separate inclusion of rotations and gradients) higher order stresses are constituted. Their formal definition and notation goes beyond the scope of this section and will be postponed to the respective sections.

The link between kinematic and dynamic quantities is expressed by constitutive relations that connect strain measures with stress measures, e. g. $\mathbf{T}(\varepsilon) = \mathbf{C} : \varepsilon$ via a constitutive tensor $\mathbf{C}$. In the context of a DEM implementation the constitutive relation is defined in the form of a local contact law, i. e. the relation between the contact deformation of particles via the penetration depth and the contact force is employed. Its discussion is continued in the context of the description of the particle model, as it represents a specific detail of the model rather than a mechanical principle.

2.1.3 Balance laws

All balance equations in continuum mechanics are structured in the same way, whereby the concept of master balance provides a convenient way for their derivation, compare the illustrative description by *Diebels* [63]. The balance of mass

$$\frac{\mathrm{d}}{\mathrm{d}t} \int_{\mathcal{B}} \rho\,\mathrm{d}v = 0 \tag{2.6}$$

specifies that in a closed system the mass of a body is constant. Note, that the term $\mathrm{d}/\mathrm{d}t$ denotes the material time derivative. The balance of momentum

$$\frac{\mathrm{d}}{\mathrm{d}t} \int_{\mathcal{B}} \rho\dot{\mathbf{x}}\,\mathrm{d}v = \int_{\mathcal{S}} \mathbf{t}\,\mathrm{d}a + \int_{\mathcal{B}} \rho\mathbf{b}\,\mathrm{d}v \tag{2.7}$$

presents the most important balance equation in continuum mechanics. The balance of moment of momentum is defined as

$$\frac{\mathrm{d}}{\mathrm{d}t} \int_{\mathcal{B}} \mathbf{x} \times \rho\dot{\mathbf{x}}\,\mathrm{d}v = \int_{\mathcal{S}} \mathbf{x} \times \mathbf{t}\,\mathrm{d}a + \int_{\mathcal{B}} \mathbf{x} \times \rho\mathbf{b}\,\mathrm{d}v\,. \tag{2.8}$$

If the integrands in equations (2.6) to (2.8) are steady and sufficiently often steadily differentiable (i. e. smooth) a local representation of the balance equation is obtained. The notion "local" denotes that the balance is valid for each material point $\mathcal{P}$ of the material body $\mathcal{B}$. Thus, within the local form of a balance equation no integrals are included. Use of the local moment of momentum balance yields the indicator of a Boltzmann continuum, namely a symmetric stress tensor

$$\mathbf{0} = \mathbf{I} \times \mathbf{T} = \overset{3}{\mathbf{E}} : \mathbf{T}^T \rightarrow \mathbf{T} = \mathbf{T}^T \,. \tag{2.9}$$

In case of a micropolar continuum one obtains a non-symmetric stress tensor, as will be explained later. The balance of kinetic energy for the standard Boltzmann continuum case is denoted as

$$\frac{\mathrm{d}}{\mathrm{d}t} \int_{\mathcal{B}} \frac{1}{2} \rho \dot{\mathbf{x}} \cdot \dot{\mathbf{x}} \, \mathrm{d}v = \int_{\mathcal{S}} \mathbf{t} \cdot \dot{\mathbf{x}} \, \mathrm{d}a + \int_{\mathcal{B}} \rho \mathbf{b} \cdot \mathbf{x} \, \mathrm{d}v \,. \tag{2.10}$$

The left hand side of equation (2.10) refers to the (internal) kinetic energy of the system, while the right hand side describes the external stress power. If one substitutes $\dot{\mathbf{x}}$ by the virtual displacements $\delta\mathbf{x}$ in equation (2.10) and utilizes Gauss divergence theorem, d'Alembert's principle is obtained

$$\int_{\mathcal{B}} \rho \ddot{\mathbf{x}} \cdot \delta\mathbf{x} \, \mathrm{d}v = \int_{\mathcal{B}} (\mathrm{div}\, \mathbf{T} + \rho \mathbf{b}) \cdot \delta\mathbf{x} \, \mathrm{d}v \,. \tag{2.11}$$

In case that additionally $\ddot{\mathbf{x}} \equiv 0$, d'Alembert's principle is known as principle of virtual work.

There is no doubt about the fact that the standard discretization method in the context of continuum mechanics is the finite element method (FEM), see the textbooks by *Bathe* [13], *Hughes* [116] or *Zienkiewicz & Taylor* [266]. In the context of the FEM usually the balance of momentum according to equation (2.7) or (2.11) and corresponding boundary conditions are transferred into a weak formulation which is solved over the volume of the body by discretizing the domain via a FE mesh. Against it, the discrete element method represents a completely different formulation to simulate problems in solid mechanics. The local balance of momentum also denoted Newton's equation of motion $m\ddot{\mathbf{x}} = \mathbf{k}$ is identified as key equation of the DEM. It includes the mass $m = \int_{\mathcal{B}} \rho \, \mathrm{d}v$ and the total external forces $\mathbf{k}$ according to equation (2.5). In the DEM the time t is discretized, i. e. the equation of motion is solved for each individual body (a particle within the DEM) at discrete time steps. Thus, the balance equations are solved in a type of strong form for each individual particle.

The balance equations play a key role when homogenization approaches ought to be specified. In particular, the balances of momentum and moment of momentum in connection with scale separation arguments will be utilized later on for the derivation of average quantities.

2.2   Continuum with microstructure

In order to account for a distinct microstructure like that typically encountered for cohesive and non-cohesive geomaterials, the standard Boltzmann formulation introduced in

the previous section has to be enhanced. A variety of related developments in the context of *generalized continua* like the *continuum with microstructure* by *Mindlin* [172], *multipolar theory* by *Green & Rivlin* [94], *micromorphic continua* by *Eringen* [79] or *nonlocal continuum* by *Kröner* [133] and *Eringen & Edelen* [81] gained increased popularity since the 1960's. Their works represent the point of origin of nowadays enhanced continuum theories. Examples are non-local or gradient enhanced theories implemented within finite element codes as regularization techniques or localization limiters. Therein, the standard continuum is enriched and additional information on the material's microstructure is supplied via a virtual internal length scale. These techniques enforce a realistic and mesh-independent size of the localization zone and are, therefore, called localization limiters. Localization limiters are based on the 1960's concept of a *nonlocal continuum,* or in the differential form on the concept of gradient models resulting from the idea of a *continuum with microstructure.* See chapter 26 of *Jirásek & Bažant's* [124] textbook for an overview.

In this thesis the lines of *Mindlin* [172] are followed and a continuum with microstructure is formulated. It represents a linear theory of a three-dimensional elastic continuum, but incorporates properties of the microstructure. Micropolar and gradient continua are included as special cases. A material body $\mathcal{B}$ consists of a manifold of material points $\mathcal{P}$, that are now represented by a deformable microstructure, denoted as *macro particle* $\mathcal{P}$. This *macro particle* $\mathcal{P}$ is composed by a finite number of *micro particles* $\mathcal{P}_{mic}$, as illustrated in figure 2.2. The general frame of figure 2.2 is given by figure 2.1. There, the macro (middle grey shaded) and micro particles (dark grey shaded) are shown in the global frame of the material body. The inclusion of the microstructure has consequences: The kinematic description of the theory is enhanced, i. e. additional kinematic measures have to be included. Following the lines of *Mindlin* [172] one assumes that each macro particle includes a microstructure. The spatial position vectors of the micro particles $\mathbf{X}'$ and $\mathbf{x}'$ are locally defined in the coordinate system of this microstructure. It is assumed that the position vector of the micro particles is measured with respect to a single Cartesian coordinate system, parallel to the system in $\mathcal{O}$ defined in figure 2.2. The macro particle's origin is fixed at $\mathcal{P}^*$ in the global frame and moves with the macroscopic displacement $\mathbf{u}$. In the remainder all measures that refer to the deformation of the material point or macro particle $\mathcal{P}$ are denoted as *macro* measures. An example is the macro strain in
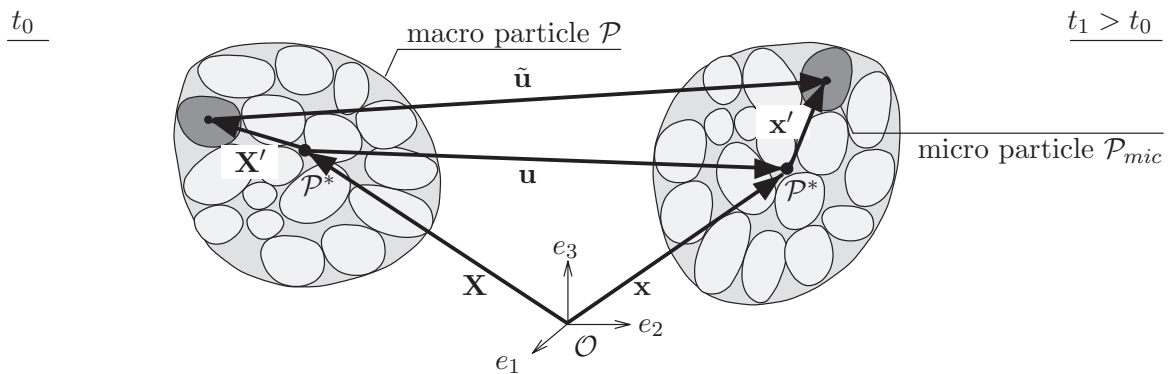
Figure 2.2: Initial (t_0) and actual (t_1) configuration of macro particle according to figure 2.1.

equation (2.3). Those measures that correspond to the deformation of a micro particle $\mathcal{P}_{mic}$ are denoted as *micro* measures and are marked by an inverted comma as superscript $(\cdot)'$.

2.2.1   Kinematic measures

In addition to the linearized strain defined in equation (2.3), the macro rotation is introduced as

$$\boldsymbol{\varepsilon}_{rot} = \frac{1}{2}\left(\operatorname{Grad}\mathbf{u} - \operatorname{Grad}^T\mathbf{u}\right) = \frac{1}{2}\left(\mathbf{H} - \mathbf{H}^T\right). \tag{2.12}$$

The micro displacement $\mathbf{u}' = \mathbf{x}' - \mathbf{X}'$ is defined in the local coordinate system of the macro particle. The key assumption of a *Mindlin continuum* requires that the micro displacement is expressed as a sum of products of specified functions of $\mathbf{x}'$ and arbitrary functions of $\mathbf{x}$ and t. As an approximation, following *Mindlin* [172] $\mathbf{u}'$ is expressed as a first order Taylor expansion of $\mathbf{x}'$ via

$$\mathbf{u}' = \mathbf{x}' \cdot \frac{\partial \mathbf{u}'}{\partial \mathbf{X}} = \mathbf{x}' \cdot \underbrace{\operatorname{Grad}\mathbf{u}'}_{\mathbf{H}'}, \tag{2.13}$$

where the micro material displacement gradient, also denoted as micro deformation, $\mathbf{H}'$ has been introduced. $\mathbf{H}'$ is assumed to be homogeneous within the complete macro particle. In the global frame the total displacement $\tilde{\mathbf{u}}$ is expressed by the Taylor series truncated after the linear term

$$\tilde{\mathbf{u}} = \mathbf{u} + \underbrace{\mathbf{x}' \cdot \mathbf{H}'}_{\mathbf{u}'} + \tilde{\mathbf{w}}, \tag{2.14}$$

with the higher order terms represented by $\tilde{\mathbf{w}}$. This assumption also characterizes the starting point of a micromorphic continuum of grade 1 according to *Eringen* [79]. In his article *Eringen* [79] stated that a micromorphic continuum of grade 1 is identical to *Mindlin's continuum* [172] upon some modifications of terminology. However, *Eringen's* description is more general, in that it allows terms of higher order than linear ones. This is accomplished by further expanding the Taylor series in equations (2.13) and (2.14), respectively, compare the procedure in chapter 9.

In analogy to the macro strain one obtains the micro strain $\boldsymbol{\varepsilon}' = \boldsymbol{\varepsilon}'_{sym} + \boldsymbol{\varepsilon}'_{skw} = \mathbf{H}'$ with the symmetric and skew-symmetric parts

$$\boldsymbol{\varepsilon}'_{sym} = \frac{1}{2}\left(\mathbf{H}' + \mathbf{H}'^T\right), \qquad \boldsymbol{\varepsilon}'_{skw} = \frac{1}{2}\left(\mathbf{H}' - \mathbf{H}'^T\right). \tag{2.15}$$

In between the micro and macro measures combined measures may be introduced, like the relative deformation, i. e. the difference between the macro material displacement gradient and micro material displacement gradient

$$\boldsymbol{\Gamma} = \mathbf{H} - \mathbf{H}'. \tag{2.16}$$

Furthermore, one obtains the micro deformation gradient, that is the macro gradient of the micro strain, in form of a tensor of third order

$$\boldsymbol{\mathcal{K}} = \operatorname{Grad}\boldsymbol{\varepsilon}'. \tag{2.17}$$

The kinematic compatibility is represented by the following conditions

$$\left[\overset{3}{\mathbf{E}} \otimes \overset{3}{\mathbf{E}}\right] \vdots\vdots \frac{\partial \boldsymbol{\varepsilon}^2}{\partial^2 \mathbf{X}} = \mathbf{0}, \qquad \overset{3}{\mathbf{E}} : \frac{\partial \boldsymbol{\mathcal{K}}}{\partial \mathbf{X}} = \mathbf{0}, \qquad \frac{\partial \left(\boldsymbol{\varepsilon} + \boldsymbol{\varepsilon}_{rot} - \boldsymbol{\Gamma}\right)}{\partial \mathbf{X}} = \boldsymbol{\mathcal{K}}. \qquad (2.18)$$

Therein $\overset{3}{\mathbf{E}}$ describes the Ricci permutation tensor of third order.

2.2.2 Dynamic measures

In the next step, energetically conjugated stresses are introduced and fitted into the principle of virtual work comparable to the form shown in equation (2.11). The derivation is carried out along the lines of *Germain* [92]. Alternative ways of derivation are possible, e. g. *Mindlin's* [172] way of deriving the balance equations via Hamilton's principle or by utilizing variational principles as done by *Steinmann & Stein* [229]. The virtual work principle states that the absolute value of work of the internal forces (superscript (i), negative per definition) equals that of the external forces (superscript (e)) according to

$$\delta W^{(i)} + \delta W^{(e)} = \int_{\mathcal{B}} \delta w^{(i)} \, \mathrm{d}v + \int_{\mathcal{B}} \delta w^{(e)} \, \mathrm{d}v = 0. \qquad (2.19)$$

The virtual work of the internal forces at a material point within the body $\mathcal{B}$ is defined as follows

$$\delta w^{(i)} = -\mathbf{T}_1 : \delta \boldsymbol{\varepsilon} - \mathbf{T}_2 : \delta \boldsymbol{\Gamma} - \boldsymbol{\mu} \vdots \delta \boldsymbol{\mathcal{K}}. \qquad (2.20)$$

Therein, the Cauchy stress tensor is decomposed into two parts $\mathbf{T} = \mathbf{T}_1 + \mathbf{T}_2$ and $\boldsymbol{\mu}$ denotes a higher order stress tensor (tensor of third order) that is dual to the micro deformation gradient $\boldsymbol{\mathcal{K}}$. $\mathbf{T}_1$ is a symmetric stress tensor that is energetically dual to the macro strain and $\mathbf{T}_2$ describes the relative stress tensor, conjugated to the relative deformation $\boldsymbol{\Gamma}$. Insertion of equations (2.3), (2.16), (2.17), application of the divergence theorem and reformulation yields

$$\delta w^{(i)} = -\left(\mathbf{T}_1 + \mathbf{T}_2\right) : \frac{\partial \delta \mathbf{u}}{\partial \mathbf{X}} + \mathbf{T}_2 : \delta \boldsymbol{\varepsilon}' - \boldsymbol{\mu} \vdots \frac{\partial \delta \boldsymbol{\varepsilon}'}{\partial \mathbf{X}}. \qquad (2.21)$$

Integration of equation (2.21) over the body volume and subsequent integration by parts yields

$$\delta W^{(i)} = \int_{\mathcal{B}} \delta w^{(i)} \, \mathrm{d}v = \int_{\mathcal{B}} \frac{\partial \left(\mathbf{T}_1 + \mathbf{T}_2\right)}{\partial \mathbf{X}} \cdot \delta \mathbf{u} \, \mathrm{d}v - \int_{\mathcal{S}} \left[\left(\mathbf{T}_1 + \mathbf{T}_2\right) \cdot \mathbf{n}\right] \cdot \delta \mathbf{u} \, \mathrm{d}a +$$
$$\int_{\mathcal{B}} \left[\frac{\partial \boldsymbol{\mu}}{\partial \mathbf{X}} + \mathbf{T}_2\right] : \delta \boldsymbol{\varepsilon}' \, \mathrm{d}v - \int_{\mathcal{S}} \left[\boldsymbol{\mu} \cdot \mathbf{n}\right] : \delta \boldsymbol{\varepsilon}' \, \mathrm{d}a = 0. \qquad (2.22)$$

The work of the external forces is defined by

$$\delta W^{(e)} = \int_{\mathcal{B}} \left(\mathbf{t}_{\mathcal{B}} \cdot \delta \mathbf{u} + \mathbf{m}_{\mathcal{B}} : \delta \boldsymbol{\varepsilon}'\right) \mathrm{d}v + \int_{\mathcal{S}} \left(\mathbf{t}_{\mathcal{S}} \cdot \delta \mathbf{u} + \mathbf{m}_{\mathcal{S}} : \delta \boldsymbol{\varepsilon}'\right) \mathrm{d}a. \qquad (2.23)$$

$\mathbf{t}_{\mathcal{B}}$ is identified as body force per unit volume (e. g. body force $\rho \mathbf{b}$) and $\mathbf{t}_{\mathcal{S}}$ as surface traction per unit surface area (e. g. contact force $\mathbf{t}$), respectively. $\mathbf{m}_{\mathcal{B}}$ represents the

double force per unit volume (e. g. volume couple $\rho\mathbf{c}$) and $\mathbf{m}_\mathcal{S}$ the double traction per unit surface area (e. g. contact couple $\mathbf{m}$). If dynamic terms are included, the body force $\mathbf{t}_\mathcal{B}$ may be replaced by $(\mathbf{t}_\mathcal{B} - \rho\ddot{\mathbf{x}})$ and, analogously, the double force $\mathbf{m}_\mathcal{B}$ is replaced by $(\mathbf{m}_\mathcal{B} - \rho\bar{\boldsymbol{\Theta}}\bar{\boldsymbol{\omega}})$. Thereby, $\rho\bar{\boldsymbol{\Theta}}\bar{\boldsymbol{\omega}}$ represents the dynamic contribution, compare also section 8.2.1 or appendix D.1. It should be emphasized that the variations $\delta\mathbf{u}$ and $\delta\boldsymbol{\varepsilon}'$ are treated independently by definition. Their independence allows for the following derivation. Insertion of equations (2.22) and (2.23) in equation (2.19) and separation by reasons (related to variations $\delta\mathbf{u}$ and $\delta\boldsymbol{\varepsilon}'$) yields two equations: One refers to the macro mechanisms of the medium (associated with $\delta\mathbf{u}$) and another one refers to the micro mechanisms of the medium (associated with $\delta\boldsymbol{\varepsilon}'$)

$$
\begin{aligned}
\int_\mathcal{B} (\operatorname{div}\mathbf{T} + \mathbf{t}_\mathcal{B})\cdot\delta\mathbf{u}\,\mathrm{d}v &= \int_\mathcal{S} (\mathbf{T}\cdot\mathbf{n} - \mathbf{t}_\mathcal{S})\cdot\delta\mathbf{u}\,\mathrm{d}a\,, \\
\int_\mathcal{B} (\mathbf{T}_2 + \operatorname{div}\boldsymbol{\mu} + \mathbf{m}_\mathcal{B})\mathbin{:}\delta\boldsymbol{\varepsilon}'\,\mathrm{d}v &= \int_\mathcal{S} (\boldsymbol{\mu}\cdot\mathbf{n} - \mathbf{m}_\mathcal{S})\mathbin{:}\delta\boldsymbol{\varepsilon}'\,\mathrm{d}a\,.
\end{aligned}
\tag{2.24}
$$

Localization of equations (2.24) under consideration of d'Alembert's principle yields two equation sets for the macro as well as the micro mechanisms. This requires the bracket terms in equation (2.24) to vanish in the limit of infinitesimal variations $\delta\mathbf{u}$ and $\delta\boldsymbol{\varepsilon}'$

$$
\begin{aligned}
\operatorname{div}\mathbf{T} + \mathbf{t}_\mathcal{B} &= \mathbf{0}\,, & \mathbf{T}_2 + \operatorname{div}\boldsymbol{\mu} + \mathbf{m}_\mathcal{B} &= \mathbf{0} & &;\text{ in }\mathcal{B}\,, \\
\mathbf{T}\cdot\mathbf{n} &= \mathbf{t}_\mathcal{S}\,, & \boldsymbol{\mu}\cdot\mathbf{n} &= \mathbf{m}_\mathcal{S} & &;\text{ on }\mathcal{S}\,.
\end{aligned}
\tag{2.25}
$$

The left equation set refers to the macro mechanisms and is identified as the balance equation (balance of momentum) and boundary condition of the standard Boltzmann continuum, compare e. g. equation (2.11). Accordingly, the right equation set refers to the micro mechanisms and represents the local form of the balance of angular momentum of a continuum with microstructure. The balance of angular momentum (and derivatives of it) in equations (2.24) and (2.25) represents the only balance relation where an explicit coupling between the micro and macro scale is present. This coupling is expressed by means of the relation between the macro scale related quantity $\mathbf{T}_2$ and the micro scale related quantity $\boldsymbol{\mu}$.

In the next sections, the special cases *micropolar continuum* and *gradient continuum* are derived from the more general continuum with microstructure by means of *Mindlin's* [172] and *Germain's* [92] realization: Restrictions of the kinematics then lead to adapted balance laws.

2.2.3   Special case I: Micropolar continuum

A micropolar continuum requires the macro particle $\mathcal{P}$, i. e. the collection of micro particles according to figure 2.2, to move as a rigid body. Thus, it represents a continuum model that allows micro particles to displace and rotate. As a result the micro strain, equation (2.15), is purely skew-symmetric and is identified with the independent rotational degree of freedom. Note that in the following bar quantities $(\bar{\cdot})$ represent Cosserat or

micropolar kinematic measures. Following the lines of *Germain* [92] the particle rotation is captured in a tensorial form $\bar{\bar{\Phi}}$ and yields

$$\varepsilon'_{sym} = 0\,, \qquad \varepsilon'_{skw} = \bar{\bar{\Phi}}\,. \tag{2.26}$$

Upon insertion of these assumptions in equation (2.16) one obtains the relative deformation

$$\mathbf{\Gamma} = \underbrace{\varepsilon_{sym}}_{\bar{\varepsilon}_{sym}} + \underbrace{\left(\varepsilon_{skw} - \bar{\bar{\Phi}}\right)}_{\bar{\varepsilon}_{skw}}\,. \tag{2.27}$$

Thus, the symmetric part of $\mathbf{\Gamma}$ coincides with the macro strain ε_{sym}. The difference between macro and micro deformation influences only the skew-symmetric part of the relative deformation. Only if the individual rotation of a micro particle differs from the spin of the domain around the micro particle (denoted as macro particle), a contribution to the skew-symmetric part of the relative deformation is expected. Consequential, the micro deformation gradient in equation (2.17) is identified as the curvature tensor of third order

$$\bar{\mathcal{K}} = \operatorname{Grad} \bar{\bar{\Phi}}\,. \tag{2.28}$$

Following *Germain* [92], using the principle of virtual work one can conclude: The relative stress tensor $\mathbf{T}_2$ in equation (2.20) represents the skew-symmetric part of the total stress tensor $\mathbf{T}$. Furthermore, $\mathbf{m}_\mathcal{B}$ and $\mathbf{m}_\mathcal{S}$ may be assumed skew symmetric and represent the long range volume couple distribution and surface couple stresses. The insertion of adjoint tensors with respect to the first two indices in the balance of moment of momentum in equation $(2.24)_2$ according to

$$\bar{\bar{\Phi}} = - \overset{3}{\mathbf{E}} \cdot \bar{\varphi}\,, \qquad \boldsymbol{\mu} = - \overset{3}{\mathbf{E}} \cdot \mathbf{M}\,, \qquad \mathbf{m}_\mathcal{B} = - \overset{3}{\mathbf{E}} \cdot \rho \mathbf{c}\,, \qquad \mathbf{m}_\mathcal{S} = - \overset{3}{\mathbf{E}} \cdot \mathbf{m} \tag{2.29}$$

provides a more classical description of a micropolar continuum:

$$\begin{aligned} \mathbf{0} &= \underbrace{\mathbf{I} \times \mathbf{T}}_{\overset{3}{\mathbf{E}}\,:\mathbf{T}} + \operatorname{div} \mathbf{M} + \rho \mathbf{c} & &\text{; in } \mathcal{B}\,, \\[2mm] \mathbf{m} &= \mathbf{M} \cdot \mathbf{n} & &\text{; on } \mathcal{S}\,. \end{aligned} \tag{2.30}$$

$\bar{\varphi}$ is interpreted as independent micro particle rotation vector, $\mathbf{M}$ denotes the couple stress and $\mathbf{m}$ as well as $\rho \mathbf{c}$ are couple densities.

In the context of a linear micropolar continuum the linearized macro strain defined in equation (2.3) may be reformulated as follows

$$\bar{\mathbf{E}}_{lin} = \operatorname{Grad} \mathbf{u} + \overset{3}{\mathbf{E}} \bar{\varphi} = \bar{\varepsilon}_{sym} + \bar{\varepsilon}_{skw} =: \bar{\varepsilon}\,, \tag{2.31}$$

with the symmetric and skew-symmetric part

$$\begin{aligned} \bar{\varepsilon}_{sym} &= \frac{1}{2}\left(\operatorname{Grad}\mathbf{u} + \operatorname{Grad}^T\mathbf{u}\right) = \varepsilon\,, \\[2mm] \bar{\varepsilon}_{skw} &= \frac{1}{2}\left(\operatorname{Grad}\mathbf{u} - \operatorname{Grad}^T\mathbf{u}\right) + \overset{3}{\mathbf{E}}\,\bar{\varphi} = \overset{3}{\mathbf{E}}\left(\bar{\varphi} - \varphi\right) =: \overset{3}{\mathbf{E}}\,\varphi^*\,. \end{aligned} \tag{2.32}$$

$\boldsymbol{\varphi}$ represents the continuum rotation via $1/2(\operatorname{Grad}\mathbf{u} - \operatorname{Grad}^T\mathbf{u})$ and $\boldsymbol{\varphi}^*$ the rotation difference of the directors and line elements. A director represents the local orientation of a material point and, in the figurative sense, of a micro particle. Upon consideration of equation (2.29), one obtains the linearized Cosserat curvature tensor

$$\bar{\boldsymbol{\kappa}} = \operatorname{Grad}\bar{\boldsymbol{\varphi}}\,. \tag{2.33}$$

Alternative derivations of the kinematic quantities and, in particular, different curvature formulations are noted along with linearization aspects in *Volk* [251]. The generalized or Cosserat deformation rate is obtained as difference between the spatial velocity gradient and the micropolar gyration tensor

$$\bar{\boldsymbol{\Delta}} = \mathbf{L} - \bar{\boldsymbol{\Omega}}\,. \tag{2.34}$$

The angular velocity $\bar{\boldsymbol{\omega}}$ describes the rotation of the directors and is obtained as axial vector of the micropolar gyration tensor $\bar{\boldsymbol{\Omega}}$.

2.2.4   Special case II: Second gradient continuum

The term *second gradient* refers to the second gradient of displacement. Use of the assumption that the micro particle is subjected to the same deformation as the general continuum via

$$\mathbf{H}' = \operatorname{Grad}\mathbf{u}' = \operatorname{Grad}\mathbf{u} = \mathbf{H}\,, \tag{2.35}$$

provides a second gradient theory from a continuum with microstructure. Thus, it depends on the displacement field $\mathbf{u}$. Consequently, the relative deformation $\boldsymbol{\Gamma}$ in equation (2.16) vanishes. The micro deformation gradient $\boldsymbol{\mathcal{K}}$ is expressed as the second gradient of displacement according to

$$\boldsymbol{\mathcal{K}} = \frac{\partial\delta\mathbf{H}'}{\partial\mathbf{X}} = \frac{\partial\delta\mathbf{u}^2}{\partial^2\mathbf{X}}\,, \tag{2.36}$$

and is symmetric with respect to the first two indices. Since $\mathbf{u}$ and $\mathbf{H}'$ are not independent fields, the virtual work of the internal forces in equation (2.20) is modified

$$\delta w^{(i)} = \mathbf{T}_1 : \frac{\partial\delta\mathbf{u}}{\partial\mathbf{X}} + \boldsymbol{\mu} : \frac{\partial\delta\mathbf{u}^2}{\partial^2\mathbf{X}}\,. \tag{2.37}$$

The further reformulation of the principle of virtual work implies the introduction of normal and surface gradients of the field $\delta\mathbf{u}$. The balance of moment of momentum and in particular the boundary condition then resemble a more complicated form as presented for the micropolar case. These equations are skipped for brevity, but can be found elsewhere, compare *Mindlin* [172] or *Germain* [92]. It should be noticed that second gradient continuum models as developed above represent the starting point of several microstructure oriented gradient theories implemented in continuum models within the framework of the FEM, see e. g. *Chambon et al.* [33], *Fleck & Hutchinson* [87], *Kouznetsova et al.* [129], *Sulem et al.* [232] or *Zervos et al.* [264].

Note that this form of a gradient continuum represents only one specific choice. Since the 1960's a wide variety of alternative forms has been proposed which for didactical reasons are discussed in the general context of a non-local continuum in the following.

In a classical sense one could build up an enhanced continuum theory based on strains and

strain gradients by strictly following the presented *Mindlin formalism* [172, 173]: Then the free energy contains the strain and additional strain gradients which in turn yield energetically conjugated higher stresses as additional dynamic quantities. Alternatively, the free energy could be kept in a strain dependent form (without strain gradients) and the constitutive law is adapted, i. e. the stress response at a given material point is not only dependent on the strain, but also on higher gradients of the strain at this point. Then, no additional higher stress measures need to be introduced. An alternative way, is to follow *Aifantis'* [2] ideas by enhance those components of a theory that are responsible for the mesh dependent post-peak behavior, i. e. the gradient "improvement" of the theory enters at start of localization. For example, in the context of plastic deformations this is the activation of the flow rule. Correspondingly, the yield condition may contain gradients of the hardening variable, as suggested by *Mühlhaus & Aifantis* [179] or *Vardoulakis & Aifantis* [246, 247].

Gradient models as those mentioned above are closely related to non-local models of the integral-type which also represent enriched continuum models. Starting from the early ideas of *Duhem,* a broad range of model classes were developed. *Duhem* remarked that a stress at a material point should, in principle, not only depend on the state of that material point (e. g. strain), but also on the state of the whole body. Bear in mind that in a strict sense to follow this idea means to abandon the well known mechanical principle of local action. *Duhem's* thought was further elaborated and embedded into continuum mechanical considerations, see *Eringen & Edelen* [81], *Eringen* [80], *Kröner* [133] or *Pijaudier-Cabot & Bažant* [197]. In general, integral-type non-local models denote models where the constitutive law at a material point involves weighted averages of a state variable over a certain neighborhood of that material point. A gradient-type model, while adhering physically to the principle of local action, takes the field in the immediate vicinity of the material point into account, i. e. the local constitutive relations are enriched by the higher order gradients of some state variables via a Taylor expansion. In the figurative sense, this kind of models accounts for the microstructure through the inclusion of the neighborhood in an implicit manner. As generally both type of models implicitly and explicitly account for the underlying microstructure, integral-, gradient- and even micropolar-type models are denoted as non-local models in the literature. Integral- and gradient-type theories may be easily converted one into another, cf. *Mühlhaus & Aifantis* [179].

Please bear in mind that whether *Duhem's* principle contradicts non-local theories or not is a matter of opinion, since the enhancements included in general non-local models represent rather artificial measures (approximation of surrounding neighborhood) than strict physical facts.

2.3 Homogenization approaches

The heterogeneous composition of various materials on the micro scale is generally unavailable in terms of its mechanical interaction on the macro scale, compare fiber reinforced materials, general composite materials or granular materials. In most cases an exact knowledge of the material on the micro scale is neither possible nor necessary. If problems are addressed which involve two distinct scales, namely a *micro* and a *macro scale,* it is advantageous to consider statistically homogeneous materials. For these materials it

is possible to define a *representative volume element (RVE)* and, thus, to introduce an *equivalent homogeneous medium.* This means that an inhomogeneous body is replaced by a substitute fictitious homogeneous material which behaves globally in the same way and, therefore, is equivalent from a mechanical point of view. This mapping procedure is called *homogenization.* Its development traces back to the works of *Voigt* and *Reuss* starting in the late 19th century. The increasing research and development of composite materials progressively motivated a new interest in this field and led to continuum micromechanics. Todays continuum micromechanics formulations go back to the works of *Hill* [108, 109, 110] and have been steadily extended and enhanced, see the textbooks by *Bear & Bachmat* [19], *Krajcinovic* [130], *Mura* [183] or *Nemat-Nasser & Hori* [185].

The key idea of continuum micromechanics is the characterization of mechanical interrelationships by the simultaneous use of different observation levels (micro, macro). These observation levels represent different length scales, compare e. g. the book of *van Mier* [243] for a detailed picture on concrete. The absolute order of magnitude of a certain observation level is unimportant, but rather the relative ratio between two levels is crucial. This fact is closely related to the term *scale separation:* If the macro scale is determined by the length D and the micro scale by the length δ, the relation $D \gg \delta$ must hold for an application of scale separation arguments.

2.3.1   Representative volume element

The effective material properties determined via the introduction of a representative volume element (RVE) are unique only in the case of a statistically representative (statistically homogeneous) material. It should be mentioned that an equivalent terminology for a RVE, namely representative elementary volume (REV), goes back to *Bear & Bachmat* [19]. Several more or less blurred definitions of the RVE size have been suggested in the literature, compare among others *Drugan & Willis* [75], *Hashin* [102] or *Ostoja-Starzewski* [194]. A comprehensive description of a RVE capturing the full flavor of this topic in one sentence was formulated by *Hill* [108] back in the 1960's:

> *A representative volume element refers to a sample that (a) is structurally entirely typical of the whole mixture on average, and (b) contains a sufficient number of inclusions for the apparent overall moduli to be effectively independent of the surface values of traction and displacement, so long as these values are 'macroscopically uniform'.*

In general, a RVE may be characterized as a lower bound on the size of the microstructural cell. Some definitions, e. g. those following the class of *Ostoja-Starzewski* [194], imply a mathematically infinite size of the RVE in order to be statistically homogeneous. For practical applications a finite size is present and the user himself has to define the tolerable statistical error. Typically, this statistical error is directly related to the fluctuations, i. e. the monitored average quantities within a sample fluctuate around an average value. The size of these fluctuations is a matter of the corresponding averaging radius, but also of the material composition within this radius. For example, in the context of granular materials the evolution of anisotropies by rearranging force chains as a result of the grain skeleton may have significant influence on the fluctuations. Thus, the fluctuations play an important role when deriving homogenization procedures. On account of these statements it must be remarked that the determination of the RVE size is by no

means straightforward. In fact, it depends on what the user has in mind with the chosen homogenization approach.

The procedures derived in the context of this thesis will leave behind the original idea of a statistically homogeneous RVE that yields the same effective properties regardless of its position within the material body. Therefore, the RVE definition is adapted to the problems in mind. In fact, the main interest in the context of homogenization and representative volume elements focuses in two directions in this thesis:

- On the one hand, an averaging procedure should yield average quantities, while the RVE size must be appropriate to resolve local inhomogeneities, like shear bands. Thus, a filtering of the relevant quantities is obtained: The fluctuations related to microscopic inhomogeneities (e. g. local particle rotations) are smeared out, but the RVE size still allows to reflect macroscopic inhomogeneities and instabilities (e. g. evolution of a shear band). Hence, the RVE is seen more as an *averaging volume* than as a *representative volume*.

- On the other hand, the formulation of corresponding homogenization approaches should motivate enhanced continuum theories like the micropolar or gradient enhanced ones. This is accomplished by an evaluation of the balance laws of a continuum with microstructure and a realization of the enhanced continuum description in the context of a particle model.

Following the usual terminology the spatial average of tensorial quantities is denoted as

$$\langle \mathbf{A} \rangle = \frac{1}{V} \int_{\mathcal{B}} \mathbf{A}(\mathbf{x}) \, \mathrm{d}v \,, \tag{2.38}$$

where $\langle \cdot \rangle$ represents a spatial average. In the following, in contrast to section 2.2 the formal terminology "macro particle" is replaced by "representative volume element" and "micro particle" is replaced by "particle", which defines the usual notation. Bear in mind that a macro particle $\mathcal{P}$ represents an ensemble composed of a finite number of micro particles $\mathcal{P}_{mic}$ and the whole body $\mathcal{B}$ is composed of macro particles $\mathcal{P}$. If the scale difference between single particles $\mathcal{P}_{mic}$ on the one hand and the whole body $\mathcal{B}$ on the other hand is sufficiently large, a meso scale in the sense of a RVE can be introduced. This RVE is considered as an ensemble of particles. Following the realization of a continuum with microstructure in section 2.2 and the preceding remark the following conclusion can be drawn: A standard continuum which is generally understood to consist of a manifold of abstract material points $\mathcal{P}$ is now understood to consist of a manifold of RVEs. Hence, the arguments of scale separation are applied twice: First, when the RVE is constructed as a manifold of grains by linking the micro to the meso scale. Second, when the body is constructed as a manifold of RVEs by linking the meso scale to the macro scale. This situation, where three scales are touched, is well known as *Hashin's MMM (micro-meso-macro) principle of homogenization* [102]. It is intensively discussed with respect to the definition of the RVE by *Bear & Bachmat* [19] or *Nemat-Nasser & Hori* [185]. Upon introduction of a meso scale defined by the length d, the formal context of the MMM principle is represented by $D \gg d \gg \delta$.

2.3.2   Energetical considerations

A consistent homogenization requires the fulfillment of the *Hill condition* [107], i. e. the micro energy equals the macro energy. In a general framework the internal stress power is balanced by the external stress power and the kinetic energy. The notion stress power can be substituted by the rate of stress work without any restriction on the validity of the condition. Depending on the form of the continuum (standard Boltzmann, micropolar or gradient) corresponding products of dynamic and kinematic quantities are implied. Under consideration of section 2.2 and the remarks by *Diebels* [63], for a standard Boltzmann and a micropolar continuum the Hill condition on the RVE or meso level is represented as follows

$$
\underbrace{\langle \mathbf{T}{:}\mathbf{L} \rangle}_{P_{int}} = \underbrace{\langle \mathbf{T} \rangle{:}\langle \mathbf{L} \rangle}_{P_{int}{}^*},
$$
$$
\underbrace{\langle \mathbf{T} \rangle{:}\langle \bar{\boldsymbol{\Delta}} \rangle}_{P_{int}{}^1} + \underbrace{\langle \mathbf{M} \rangle{:}\langle \mathrm{grad}\,\bar{\boldsymbol{\omega}} \rangle}_{P_{int}{}^2} = \underbrace{\langle \mathbf{T}{:}\bar{\boldsymbol{\Delta}} \rangle}_{P_{int}{}^{1*}} + \underbrace{\langle \mathbf{M}{:}\mathrm{grad}\,\bar{\boldsymbol{\omega}} \rangle}_{P_{int}{}^{2*}}.
\tag{2.39}
$$

P_{int} or $P_{int}{}^1$, respectively, describe the energetical contribution of the stresses, while in the case of a continuum with microstructure $P_{int}{}^2$ refers to the contribution of the higher order stresses. In the micropolar case $P_{int}{}^1$ and $P_{int}{}^{1*}$ denote the work of the non-symmetric stresses on the non-symmetric spatial velocity gradients. In the DEM context for simplicity the term $\mathrm{grad}\,\bar{\boldsymbol{\omega}}$ may be identified as $\dot{\bar{\boldsymbol{\kappa}}} = \mathrm{grad}\,\dot{\bar{\boldsymbol{\varphi}}}$, which is used in the following. In general (i. e. for a bounded space domain $D \not\to \infty$), the Hill condition is fulfilled if particular boundary conditions are met, compare with *Nemat-Nasser & Hori* [185]. Three types of boundary conditions on the meso scale are distinguished: uniform kinematic, uniform traction or uniform kinematic-traction (also called orthogonal-mixed) conditions. In the present case one assumes linear displacements, uniform tractions or mixed realizations for the terms involving translational motion, or one assumes a linear distribution of rotations or higher order gradients, uniform higher order stresses or mixed forms for the terms involving the higher order motion (rotation or gradient). For the micropolar case generally a separation of the Hill condition into two terms like

$$
\langle \mathbf{T} \rangle{:}\langle \bar{\boldsymbol{\Delta}} \rangle = \langle \mathbf{T}{:}\bar{\boldsymbol{\Delta}} \rangle, \qquad \text{or} \qquad \langle \mathbf{M} \rangle{:}\langle \dot{\bar{\boldsymbol{\kappa}}} \rangle = \langle \mathbf{M}{:}\dot{\bar{\boldsymbol{\kappa}}} \rangle,
\tag{2.40}
$$

is not necessarily valid, as a coupling of $\langle \mathbf{T} \rangle$ and $\langle \mathbf{M} \rangle$ exists, i. e. the appearance of couple stresses $\langle \mathbf{M} \rangle$ implies the asymmetry of the Cauchy stress tensor $\langle \mathbf{T} \rangle$, compare also equation (2.25).

Chapter 3

Discrete element modeling

3.1 General

There is no doubt, that the finite element method (FEM) is the most important numerical method in todays computational mechanics applications. However, in conjunction with the developments in computer science and software technology an emerging number of new ideas led to alternative methodologies since the 1970's. These new models now compete with the traditional FEM, boundary element methods (BEM) and finite difference methods (FDM). One main direction resulted in the class of meshless methods that differ from the mesh dependent methods like the FEM in several key points, see the review articles by *Belytschko et al.* [20] and *Li & Liu* [148] for an overview. Among various innovative ideas, the most prominent ones are smooth particle hydrodynamics (SPH), moving least square (MLS) or element free Galerkin (EFG) methods. The general objective of the meshless methods is to eliminate at least part of the traditional FEM structure by constructing the approximation ansatz entirely in terms of nodes instead of elements aligned with a mesh. A second, apparently different direction resulted in the class of particle or discrete element methods (DEM). The crucial difference between this kind of models and the FEM is that the material is represented by a discontinuous particle structure without any need of a mesh in the strict sense. The infinite number of material points of the continuum is replaced by a finite number of particles of finite extent that interact through collisions with each other. The DEM shows several apparent similarities compared to the "classical" meshfree methods introduced above. From a mathematical point of view discrete element methods may be interpreted in the spirit of smooth particle hydrodynamics (SPH) with discontinuous kernel functions, as already stated by *Mühlhaus et al.* [180]. In the broader sense, they could be viewed as a sub-category of the meshless methods. However, the key difference between the DEM on the one side and traditional mesh-aligned methods (FEM, BEM, FDM) and meshless methods (SPH, MLS, PIC, etc.) on the other side is that the first one describes a discontinuum, while the last groups describe a continuum. This means that the methods which describe a continuum are all based on a formal discretization, while methods like the DEM are based on a physical discretization, i. e. elements of the DEM represent physical objects.

Most physical materials and systems are discontinuous at some level. Admittedly, materials such as concrete or soil are often treated as continuous even though they consist of discrete grains at a microscopic level. Usual continuum approaches used in a FEM description are successful because the microstructure has a length scale much smaller than that of the objects that are normally of interest (e. g. building structures, dams etc.). Following the previous discussion it is often rewarding to model such materials as discontinua because new knowledge can be gained about their macroscopic behavior when their microscopic mechanisms are understood. Materials like concrete, masonry or jointed

rocks are ideal candidates for modeling as discrete systems after material disintegration has started. Then, the length scale of interest for the mechanical behavior is similar to that of the discontinuity spacing. In that, the inability of classical continuum models to reproduce correctly the phenomena associated with discontinuous material behavior like strain localization at crack initiation directly led to the development of discrete models. Discontinuities were first introduced into numerical models in the late 1960's by more or less parallel developments in soil and concrete mechanics by *Goodman et al.* [93] and *Ngo & Scordelis* [186] via modifications of existing continuum methods.

Soon, an alternative approach termed *distinct element method* was introduced by *Cundall* [45]. He designed this method specifically to model a-priori discontinua and treating continua, if any, as a special case. Collectively, this type of method is also called *discrete element methods.* The basic ingredients of these models are the representation of the solid material, the representation of the contacts and the scheme used to detect and revise the set of contacts. Following the lines of *Cundall & Hart* [48] the name discrete element method should apply to a method only if: First, the model allows for finite displacements and rotations of discrete bodies including a complete detachment, and second, the model recognizes new contacts automatically as the calculation progresses. It should be noticed that at that time *Cundall* introduced the DEM without referring to a very similar and also established method, namely *molecular dynamics* (MD). This methodology was introduced in the field of atomic physics in the 1950's by *Alder & Wainwright* [4] or *Metropolis et al.* [168] for simulating the motion of particles which behaved like hard spheres. Increasing computational power in the 1960's paved the way to its further development in computer codes and numerical simulations. Interestingly, at that time *Alder & Wainwright's* technique [4] allowed them to perform simulations of a system containing 500 particles which interacted like billiard balls and performed 250 collisions in thirty minutes of computer time.

Briefly speaking, the DEM is essentially a numerical technique to model the motion of an assembly of particles interacting with each other through collisions. Hence, it is very similar to the molecular dynamics (MD), from which it adopts most of its techniques. In both cases, DEM and MD, the forces acting on particles are summed up and Newton's equation of motion is integrated to obtain acceleration, velocity and position of the particles at the next time step. In principle the DEM can be characterized as (soft particle) MD with alternative definition of the force law. In the DEM the particles are not point masses as in MD, but necessarily have a finite extent in 2 or 3 dimensions. The DEM was applied mainly in the context of rock mechanics or geotechnics, e. g. for the failure prediction of small samples of sand and related geomaterials. Since the end of the 1980's its application includes the constitutive modeling on different scales within several fields of material science. Since the pioneering work of *Cundall* [45] in the framework of rock mechanics the model maintains still its attractiveness for the simulation of rock: For example, *Mühlhaus et al.* [180] applied the method for destruction simulations of rock due to blasting and *Huang* [114] applied it for the simulation of tool-rock interaction, just to give two examples. DEM in the context of dynamic loading scenarios along with a validation via experimental results became a topic of increasing interest in the last years, e. g. as shown by the works of *Klepaczko et al.* [24], *Donze et al.* [73] or *Krajcinovic & Mastilovic* [132]. Application to the fragmentation of ice was reported by *Hocking* [112] or *Selvadurai & Sepehr* [221] and showed that this method is not restricted to the application to classical geomaterials like concrete or soils. The past years showed a strong implica-

tion of the DEM into industrial applications in the context of granular flows, e. g. see the work by *Cleary* [41, 42] on the simulation of centrifugal mill, excavation by dragline, ball milling, hopper flow, segregation by vibration, commodity sampling, conveyor belt segregation etc.

An important side development of the DEM is the *discontinuous deformation analysis* (DDA). This method was introduced in the 1980's by *Shi* [222, 223] and was used for the simulation of blocky samples mainly in the context of rock mechanics, see the recent conference proceedings [22]. The primary numerical difference with regard to usual DEM models is the realization of the time discretization: Instead of utilizing an explicit finite difference time discretization approach (force-based due to evaluation of equation of motion) as in conventional DEM, the DDA employs a finite element style stiffness matrix approach (displacement-based) which is embedded in the framework of an implicit time discretization scheme. In contrast to usual DEM models, the condition of non-interpenetration is achieved by an iteration within the DDA scheme, whereby in the DEM typically an overlap displacement-force law including a penetration of contacting particles applies. The *contact dynamics method* (CD) proposed by *Jean* [123] and *Moreau* [176] in the 1990's represents a further implicit computation scheme: In contrast to the DEM, the grains are assumed to be rigid bodies without any stiffness at the contact. Similar to the DDA, the rigidity of the contact implies that no (virtual) interpenetration between contacting particles occurs. Summarizing, according to *Unger et al.* [241] the fundamental difference between DEM and CD is the retrieval of the contact forces: In the DEM they are calculated according to their cause, i. e. deformation ($\rightarrow$ overlap) at contact region, while in the CD they are a result of their effect, i. e. fulfillment of deformation constraints. There are several published schemes that appear to fit into the DEM logic, but are different in character or are lacking one or more essential ingredients. One of these side developments in the context of limit analysis and limit equilibrium methods concerns the *kinematic element method* employed by *Gussmann* [97]. A more detailed discussion on available models can be found in the review article by *Cundall & Hart* [48].

In summary, the discrete element method can be classified as a family of related numerical techniques specifically designed to solve problems in applied mechanics that exhibit gross discontinuous material and geometrical behavior. In many of these discontinuous situations, continuity constraints are either inappropriate or relaxed because of the physics of the problem. Hence, they are either intractable or very difficult to analyze with procedures based upon continuum principles, such as conventional methods like FEM, BEM or FDM.

Although several commercial DEM codes are on the market, the use of an open source research code was preferred since it provides by far more possibilities for code advancements and implementations. Only the open-source character of such a code guarantees the working environment needed for an implementation of the tasks outlined in the introduction. In the framework of the research group *Modelling of cohesive frictional materials as continuum and discontinuum* the author had the opportunity for a strong collaboration with the group of *Prof. H. J. Herrmann* and in particular with his co-worker *Prof. F. Kun* at the Institute for Computational Physics at the University of Stuttgart. With start of this cooperation, *Prof. H. J. Herrmann* kindly agreed to put one of his institutes' non-commercial research codes (a two-dimensional polygonal DEM code) to the author's disposal. The author is very grateful for this and wishes to express his sincere thanks to *Prof. H. J. Herrmann* and *Prof. F. Kun*. The research code which is based on the articles

by *Kun & Herrmann* [140, 141] and *Tillemans & Herrmann* [237] denoted the starting point of the present work. The accompanying theory of the starting model is presented within chapters 3 and 4 and is supplemented by new simulation results of quasi-static loading scenarios.

3.2   Particle distribution & mesh generation

The crucial point within a DEM simulation is the creation of a more or less representative particle sample with respect to the problem in mind. In this context the particle shape as well as the particle distribution play an important role. Different particle shapes are typically applied, starting from regular ones like circles, ellipses, squares or rectangles to irregular ones like polygons or superquadrics as firstly introduced by *Barr* [12]. In this listing only 2D shapes are noted since the focus of this thesis is on 2D problems. Currently, the only tractable particle shapes in 3D are spheres. 3D simulations with irregular shaped particles like polyhedra are not yet so common due to their computational costs. Therefore, the 1996 remark by *Potapov & Campbell* [200], that the most valuable result of 3D simulations using irregular shaped particles is to lend more credence to detailed 2D studies, still holds. Each particle shape combines advantages and disadvantages with respect to the considered application. Circular and elliptical shapes are mostly used for the simulation of laboratory tests or silo filling problems of non-cohesive granular materials like sands. For spherical particles different classes of packings with respect to their dispersity can be distinguished: mono disperse (one unique particle size for the whole sample), bi-disperse (two particle sizes for the whole sample) and poly-disperse (various different particle sizes for the whole sample). A typical application field of rectangular particle geometries in connection with the DEM is the simulation of masonry structures, see e. g. the theses by *Brzoska* [26] and *Plieninger* [198]. Recently, more complex shapes like superquadrics have been introduced to the DEM field e. g. to cover simulations of industrial parts in process engineering, compare *Williams & Pentland* [260]. In this thesis polygonal particle shapes are used, as the task is to model geomaterials like ceramics, concrete, marl or sand. Typically, the meso structure of cohesive frictional materials contains aggregates embedded into matrix material. Thus, polygonal particles seem most appropriate for this class of problems, as they can approximate the aggregates far better than circular or ellipsoidal ones. If the particle shape is fixed, different techniques for the creation of a particle sample are available depending on the target density of the sample. The polygonal shaped particles utilized in the present DEM model are represented by Voronoi polygons. In this thesis completely dense samples without any pores as well as porous samples are used. Therefore, first, the technique for generating dense particle samples according to *Moukarzel & Herrmann* [177] is presented, and afterwards, a technique for the generation of porous samples is developed.

For the generation of dense samples a special form of the Voronoi tessellation called vectorizable random lattice developed by *Moukarzel & Herrmann* [177] is applied in order to obtain an initial configuration of the mesh. It is performed by first putting a regular grid with $1 \, \text{cm} \times 1 \, \text{cm}$ spacing onto the plane and throwing points randomly and independently in a square of side length a centered on the plaquettes of the regular grid, see figure 3.1 (a). Using these points for the Voronoi construction, the randomness of the tessellation can be controlled by tuning the value of the parameter a between 0 and the lattice spacing of the
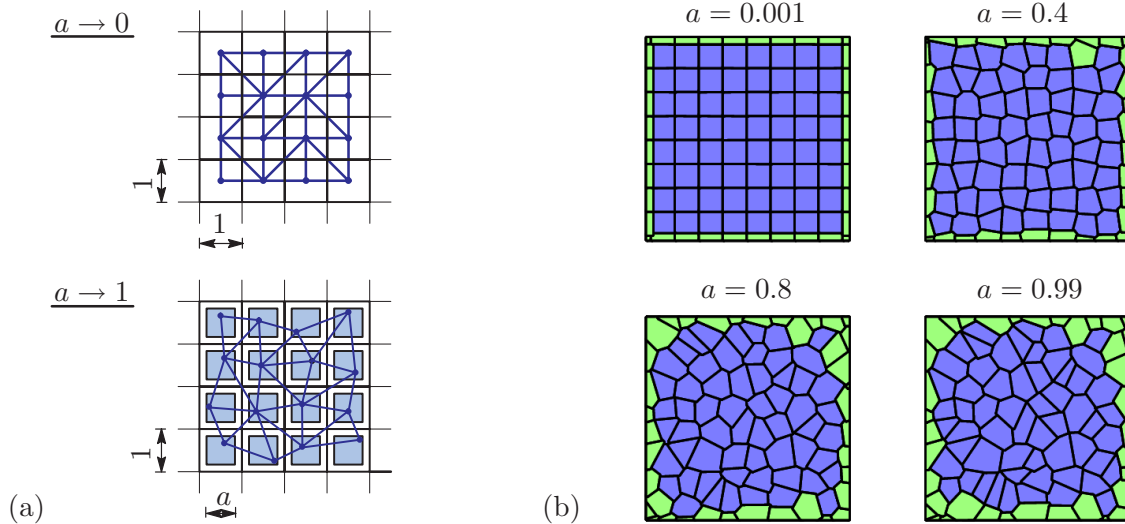
Figure 3.1: (a) Construction of the vectorizable random lattice and (b) random lattices generated at different values of a.

grid (here: 1 cm) as shown in figure 3.1 (b). After finding the generating points, shown in figure 3.1 (a) the Voronoi construction proceeds as in the standard version, see *Preparata & Shamos* [203] for an overview of different techniques. The average particle area then results in 1 cm^2, i. e. the area of a square of the regular grid. The vectorizable random lattice has several advantages compared to the standard Voronoi tessellation, also referred to as Poissonian Voronoi tessellation: First, the number of neighbors of each polygon is limited and, thus, the probability to have polygons with very small angles is limited. Second, this makes the computer code faster and allows to simulate larger systems. It is important to note that the generating points in figure 3.1 (a) are not identical to the polygon's centers of mass.

An alternative method for the generation of a dense particle assembly is the meshing of a sample via a digital image processing. Based on the color or greyscale density of a section of a specific specimen the geometry of particles is fixed and eventually, e. g. for the case of a concrete-like material, embedded into a matrix material. The meshing could approximately look like the schematic sketch in figure 3.2. An alternative way of creating a prototype microstructure is developed in chapter 7.

Next, after a brief introduction on available generation techniques for porous packings,
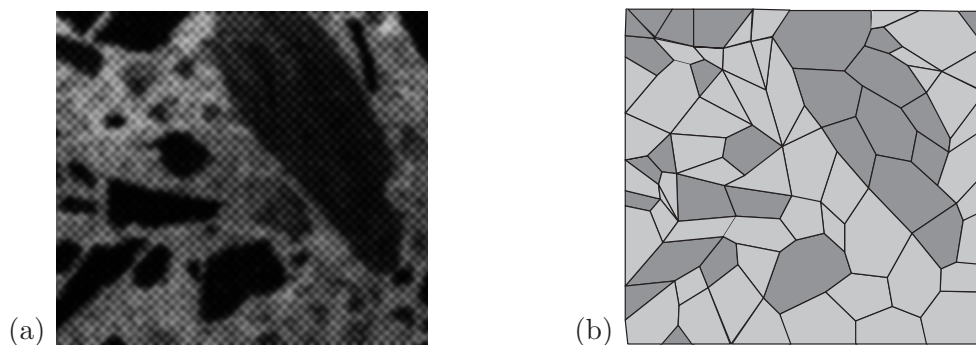

Figure 3.2: Mesh creation utilizing digital image processing.

an alternative method for the generation of porous particle samples is illustrated. If
a porous sample ought to be modeled, e. g. for the simulation of non-cohesive particle
samples, alternative procedures compared to that for dense samples are needed. For
example for an optimal geometric packing of monodisperse circular particles analytical
solutions are available which, however, aren't valid anymore for polydisperse packings.
Generally, two kind of procedure classes can be distinguished: A *static* one where the
particles are positioned *without* any use of the general DEM methodology. In contrast
to this, a *dynamic* one *with* use of the DEM methodology itself to find the final particle
packing may be employed. Recently, based on the advancing front technology *Feng et
al.* [83, 85] have shown for the *static* case that a stable and fast solution for circular,
ellipsoidal and polygonal particles can be obtained. Alternative *static* particle packing
schemes have been presented for example by *Dobry & Ng* [71], *Sakaguchi & Murakami*
[212] or in the *PFC manual* [120] (Particle Flow Code, commercial DEM software). As
an alternative, the *dynamic* case is utilized throughout this thesis for the generation of a
porous packing. The developed procedure is illustrated in figure 3.3 for a 10×20 particle
sample with $a = 0.99$. First, a completely dense packing (without any pores) following
the algorithm presented on the previous pages is created, ①. Second, all particles are
scaled down and possibly rotated controlled by a statistical measure, ②. Afterwards,
all particles are positioned into a box and are released using gravitational action via the
DEM methodology. When all particles come to rest, ③, the top of the sample is cut
and the configuration is saved, ④. Although this procedure is more time consuming it
is preferred to the *static* one outlined above for the generation of porous samples. The
clear advantage of this procedure is that the physics behind the packing formation is
represented by far more realistically than in the static case. Of course, for a completely
dense sample without any pores the approach of *Moukarzel & Herrmann* [177], which
was presented before, is followed. Different grading curves are obtained depending on
the scaling ratio used within the above procedure. Normally distributed ratios between
10-90 % of the original size of an initially 50×50 particle packing lead to the curves given
in figure 3.4. Thereby, the diameter of the particles is computed via an approximation of
the polygonal particles as circles utilizing $d = \sqrt{A_{pol}/\pi}$ with A_{pol} being the polygon area.
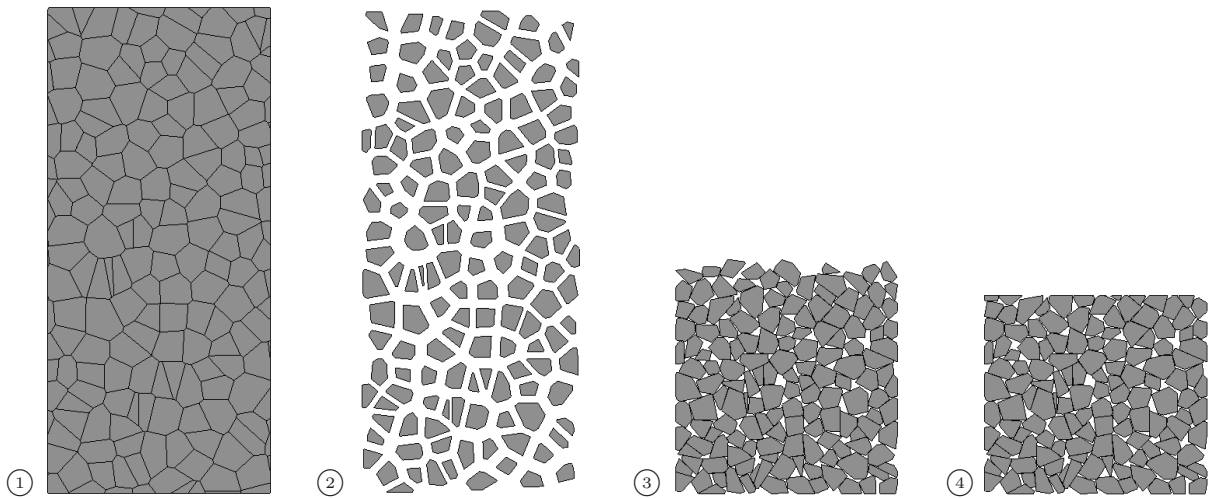

Figure 3.3: Construction of a porous packing using a *dynamic* mesh creation by scaling
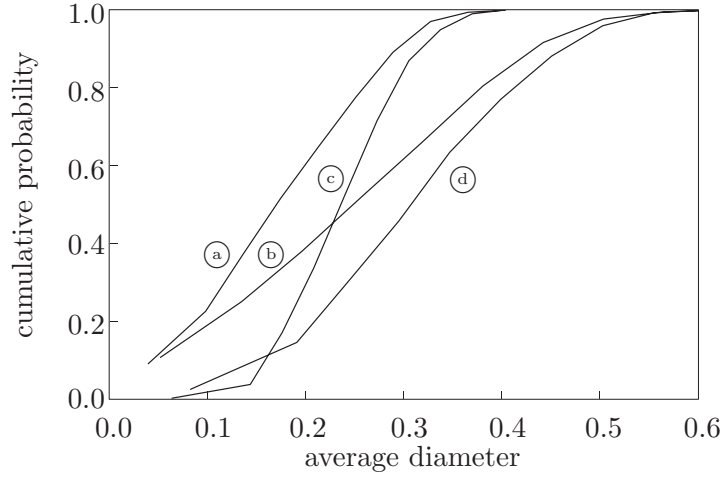the particles to 30 - 60 % of their original size.

Figure 3.4: Influence of particle scaling on grading curve: (a) $= 10 - 60\%$, (b) $= 10 - 90\%$, (c) $= 30 - 60\%$, (d) $= 30 - 90\%$.

Curve (c) refers to the construction of the porous packing shown in figure 3.3.

3.3 Kinematics

In the two dimensional model the particles have three continuous degrees of freedom, i. e. two referring to the translational and one to the rotational motion. The position of particle i is given by the vector $\mathbf{x}_i = \begin{pmatrix} x_i & y_i & \varphi_i \end{pmatrix}^T = \begin{pmatrix} \mathbf{x}_i^g & \varphi_i \end{pmatrix}^T$, where the first two components denote the spatial coordinates of the center of mass that can be cast into the vector $\mathbf{x}_i^g$. The third component is the rotation angle φ_i. It describes the total rotation about the particle's center of mass with respect to its initial position. The particles are assumed to be unbreakable and formally undeformable and can, therefore, solely undergo translational and rotational displacements, which are fully described by $\mathbf{x}_i$. The terminology "formally undeformable" is used above, since the local deformational behavior of the particles is captured by an elastic repulsive force which is related to the overlap area of contacting particles and approximates the deformability of the particles. Introducing the total displacements and rotations of the particles, the actual state of deformation within the sample with respect to the initial configuration can be obtained in vectorial form as $\mathbf{u}_i = \begin{pmatrix} u_{x,i} & u_{y,i} & \phi_i \end{pmatrix}^T = \begin{pmatrix} \mathbf{u}_i^g & \phi_i \end{pmatrix}^T = \begin{pmatrix} \mathbf{X}_i^g - \mathbf{x}_i^g & \varphi_i^{t=0} - \varphi_i^{t=t_1} \end{pmatrix}^T$, cf. figure 3.5. Due to the rigidity of the particles, the term deformation is used here only in the context of the complete, global particle assembly. φ_i and ϕ_i are identical according to their definition and indicated in separate terminology solely for completeness. As introduced in chapter 2, capital letters correspond to the initial configuration of a particle. The translational and angular velocity of particle i are defined by $\mathbf{v}_i$ and $\dot{\varphi}$ and are depicted in figure 3.6. In the case of a three dimensional extension of the model the number of degrees of freedom increases from three to six.
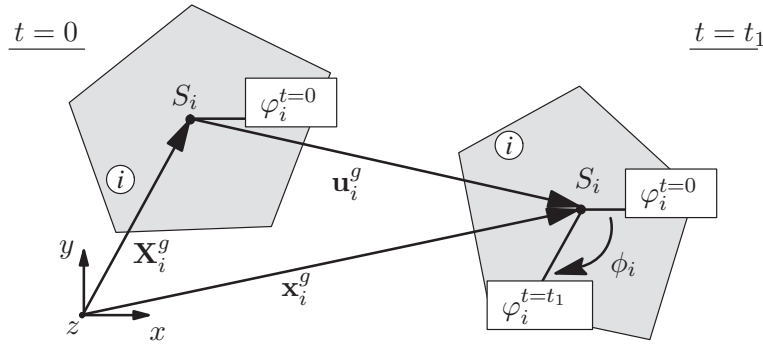
Figure 3.5: Definition of kinematics of one particle.

3.4   Interaction forces

3.4.1   Contact representation

The existence of contacts between discrete particles distinguishes a discontinuous from a continuous medium. As mentioned in the introduction to this chapter the *representation of the contacts* is one of the three basic features a DEM program must be able to handle. In this context two different possibilities, namely the *hard* and *soft contact* approach, have to be distinguished: In the case of the *hard contact* approach no interpenetration of two contacting particles is allowed and equilibrium is guaranteed. Insofar, the displacement compatibility between the two bodies is assured, which in turn demands a high computational cost when realized as numerical scheme. This type of contact formulation is typically encountered in DDA approaches as discussed by *Shi* [222] or in corresponding MD approaches, e. g. see *Allen & Tildesley* [5]. The terminology *hard contact* stems from the fact that particles are viewed as rigid and inelastic. This is in contrast to the definition of a *soft contact,* where the particles are regarded as virtual deformable. Thereby, the terminology "virtual deformable" does not refer to a particle deformation, but to the existence of contact forces as direct implication of being deformable. In the *soft contact* approach the measurable normal stiffness existing at a contact is represented by a finite stiffness that comes into play by a rheological contact model. In this approach two contacting bodies must overlap each other in order to produce a contact force since the contact forces are related to contact displacements. Actually, overlapping and interpenetration of colliding bodies do not occur in nature, but surface deformation instead allow these relative movements. This idea goes back to the pioneering work of *Hertz* [106] at the end of the 19th century. By use of the assumption of elastic contacts and, thus, that the radius of the contact area is small with respect to the radius of the particle, *Hertz* analytically derived a force-displacement relation of contacting spheres. A further elaboration of *Hertz's* ideas in the direction of frictional contacts by use of tangential and normal displacements was done by *Mindlin & Deresiewicz* [174]. Apparently, an interpenetration seems non-physical and could be classified as a crude approximation. However, the existence of a physically measurable stiffness gives rise to the concept that the interpenetration represents the virtual elasto-plastic surface deformation that is expected to occur when two bodies get into contact. Moreover, this procedure shows up to be an elegant and fast way to represent contacting particles as long as the interpenetration remains small compared to the particle size. This implies a finite contact duration and,

therefore, that a contact situation with more than one particle is possible at a point in time. This is in contrast to the *hard contact* approach realized in the context of MD. There the contact duration is zero, i. e. the collisions of particles occur instantaneously due to the rigidity of the interaction, compare *Allen & Tildesley* [5] or a recent review article by *Luding* [155].

Certainly, the choice of the contact law is a crucial point in DEM simulations, especially if no direct analytical evidence is present for such a law, as in the case of a polygonal contact. Since an analytical derivation of the real deformational behavior of contacting polygons with arbitrary shape is impossible, an approximative model based on the *soft contact* approach is used, which was introduced in the following form by *Kohring et al.* [126], *Potapov et al.* [201] or *Tillemans & Herrmann* [237]. This means that the polygonal overlap area of contacting polygons is related to an elastic repulsive contact force. Alternative polygonal contact schemes have been proposed earlier, e. g. by *Walton* [257] using a traditional Hertz contact logic or *Issa & Nelson* [119] by relating the relative displacements to a Hertz-Mindlin type force law via an idealization of the polygons as spheres. The unit contact vectors in tangential and normal direction **t** and **n**, respectively, are defined by the shear line vector $\overline{\mathbf{P_1P_2}}$ connecting the intersection points P_1 and P_2 and its perpendicular bisector as shown in figure 3.6. The local coordinate system of the contact is then defined at the midpoint of this effective shear line $\overline{\mathbf{P_1P_2}}$. Although this choice seems rather crude at first glance, there is a clear mathematical evidence for this option. *Feng & Owen* [84, 86] showed that this choice can be explicitly derived based on energy considerations. The contact force is decomposed with respect to the local coordinate system of the contact zone

$$\mathbf{f}^c = f_n^c \, \mathbf{n} + f_t^c \, \mathbf{t} \, . \tag{3.1}$$

The normal and tangential components of the contact force vector $\mathbf{f}^c$ are defined by

$$f_n^c = -\frac{E_p A_p}{d^c} - m_{eff}\gamma_n v_{rel,n} \, , \qquad\qquad f_t^c = -\min\left(m_{eff}\gamma_t \left|v_{rel,t}\right|, \mu \left|f_n^c\right|\right) \, . \tag{3.2}$$

The coefficients γ_n and γ_t refer to the viscous dissipative damping and μ is chosen according to Coulomb's friction law. E_p denotes the elastic modulus of the particle material
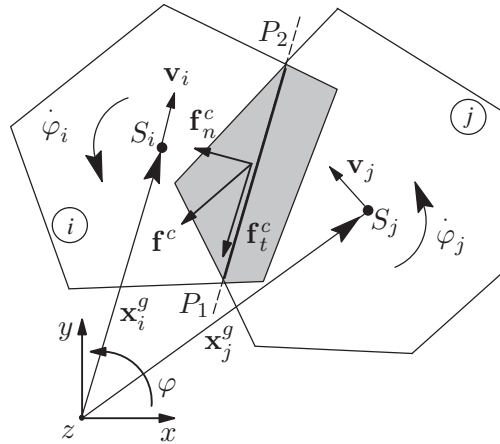

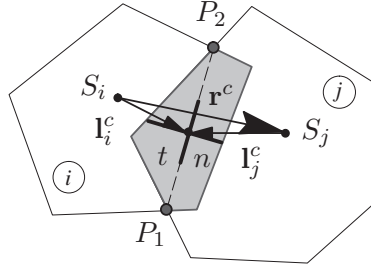Figure 3.6: Geometry of the polygonal contact.

Figure 3.7: Local coordinate system of contact.

and A_p the overlap area of two contacting polygons indicated by the shaded region in figures 3.6 and 3.7. Note, that in the present formulation identical stiffnesses E_p for all particles of a sample are considered. Due to the reduced dimensionality (2D instead of 3D) the particles are related to a certain length. One could imagine the particles to be rods with a unit length of 1 cm in three dimensions. Therefore, the dimension of E_p is of order kN/cm instead of kN/cm^2 in 3D and that of the overlap area A_p is of order cm^2 instead of cm^3 in 3D. The relative velocity at the contact zone, the effective mass and the characteristic length of the contact region of two contacting particles i and j are given by

$$\mathbf{v}_{rel} = \mathbf{v}_j - \mathbf{v}_i \,, \qquad m_{eff} = \frac{m_i m_j}{m_i + m_j} \,, \qquad \frac{1}{d^c} = \frac{1}{d_i} + \frac{1}{d_j} \,. \qquad (3.3)$$

d_i and d_j define the diameters of circles of equivalent areas as the polygons i and j. The choice of the characteristic length of the contact region is arbitrary. Here, the choice is based on the assumption that a stack of solid rectangles should behave similar to a large rectangle of the same height, see the discussion in *Matuttis* [165] and *Matuttis et al.* [166] in the context of an interpretation of the contact logic of *Tillemans & Herrmann* [237]. The contact vector $\mathbf{l}_i^c$, defining the connection of the contact point (midpoint of line $\overline{\mathbf{P}_1\mathbf{P}_2}$) and the center of mass of the particle i, is illustrated together with the branch vector $\mathbf{r}^c$ in figure 3.7. $\mathbf{r}^c$ connects the centers of mass of the two contacting polygons.

The use of the Coulomb-type frictional law in equation (3.2) is interpreted as follows: For $\mu > 0$ the present scheme allows for a non-associated plasticity law, as schematically shown in figure 3.8 for three characteristic situations. If the grey shaded flow surface is left as for point ③, the force state is reflected back in vertical direction onto the surface confined by the Coulomb criterion μf_n^c. Alternatively, the tangential force could be handled via a *Cundall-Strack spring* [49]. This version has been widely used in the literature, especially in the context of circular particles, because it allows to carry load even if a particle sample, e. g. a heap is in rest, compare *Matuttis et al.* [166]. As the focus lies on polygonal shaped particles in this thesis, there is no need for such an extension. A more extensive discussion on the choice of the tangential forces in the context of DEM simulation is found in *Brendel & Dippel* [25], *Dippel* [70], *Lätzel* [144] or *Luding* [153]. The approximative calculation of the normal part of the contact force within equation (3.2) results in a nonlinear relation between the contact force and the relative displacements of two particles. A detailed description of the procedure for calculating these polygonal contact areas and the corresponding two or in rare cases four intersection points is given in *Tillemans & Herrmann* [237]. Moments with respect to the center of mass of a particle exist only due to the eccentricity of the contact forces $\mathbf{f}^c$. The corresponding moment in
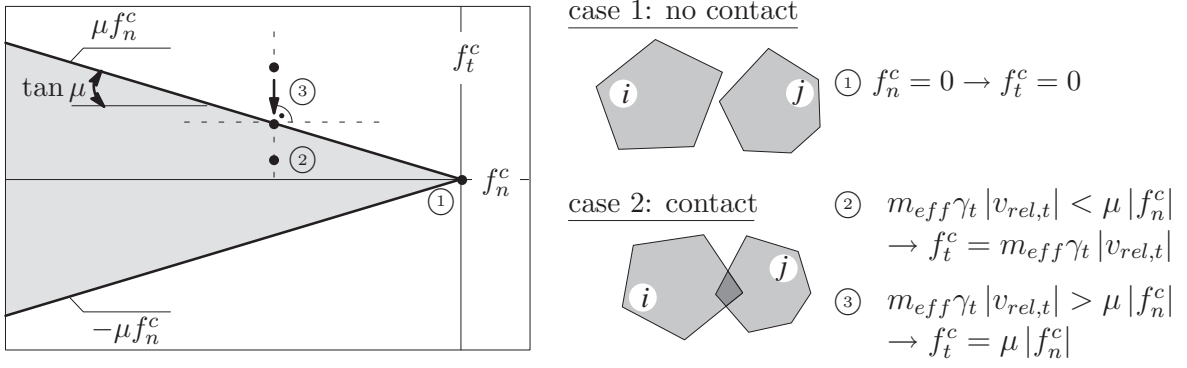
Figure 3.8: Interpretation of contact force logic in terms of plasticity.

2D is given by the scalar $m^c = \mathbf{f}^c \times \mathbf{l}^c$ and leads to the generalized particle force vector $\mathbf{f}^p = [\mathbf{f}^c \quad m^c]^T$. As already mentioned above, the overlap area shown in grey in figure 3.6 represents up to some extent the local deformation of the polygons. This compares with that in the Hertzian contact law for spherical particles. Again, it should be noted that a small overlap of particles compared to the particle size is possible and necessary in order to obtain contact forces.

3.4.2 Contact search & neighborhood lists

Efficiency arguments come into play when focusing on the contact search. Contact detection is in general a hierarchical process and its algorithms usually consist of at least two phases: In the first phase, the spatial sorting optimizes the number of particles which must be considered as potential contactors of a certain particle. In the second phase, the contact resolution identifies the details of the contact between two possibly contacting particles. In this last phase, the geometric intersection is resolved and the overlap area is computed. Various algorithms are on the market, see the review papers in the context of DEM and MD applications by *Williams & O'Connor* [258, 259], and the book by *Allen & Tildesley* [5]. Generally, available algorithms can be organized into body- or spatial-based categories. As an efficient book-keeping is crucial for the solution of diverse problem classes, the question of neighborhood lists is not restricted to DEM or MD models only. It touches several branches of computational mechanics, e. g. the so-called meshfree methods, where in contrast to mesh-aligned methods the topology information is not included a-priori.

In this thesis a multilevel approach on the basis of a spatial-based linked cell algorithm is adopted for the preparation of neighborhood lists, compare *Allen & Tildesley* [5]. The particles are linked to the grid points of the quadratic starting mesh according to the position of their centers of mass, as shown in figure 3.9 (a). Only a region of three boxes around the grid point associated with particle i is considered for the contact search. For example, if one considers that particle i is positioned inside of the box in dark grey in figure 3.9 (b), only the particles within the boxes in light grey are considered for a finer contact search. The numbers in each box represent an exemplary assumed amount of particles per box. It can be proven that in the framework of a vectorizable random lattice, as used herein, a polygon can have neighbors within three lattice spacings of the square lattice, compare *Moukarzel & Herrmann* [177]. Afterwards, a refined edge by edge
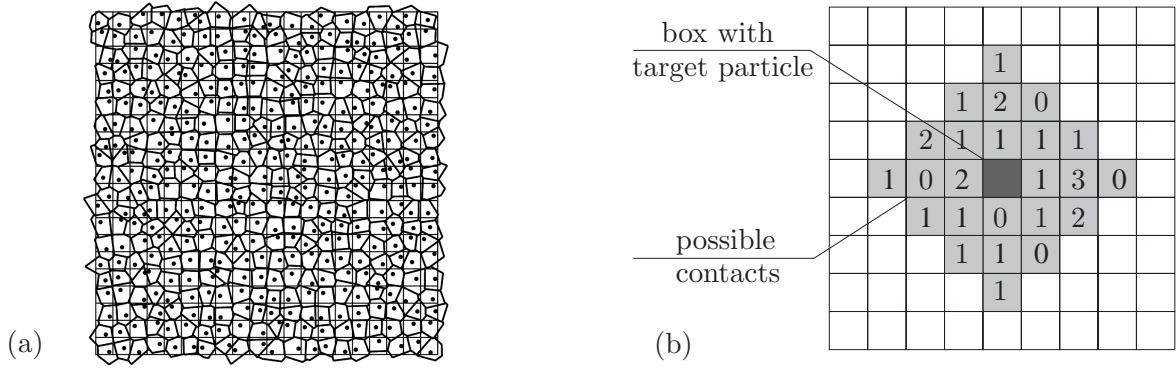
Figure 3.9: Representation of neighborhoodlists: (a) Voronoi tessellation with background linked cell mesh, (b) check area with virtual number of particles saved to background grid.

check of those particles in the light grey boxes and the target particle in the dark shaded box is done. This check is based on a comparison of the maximum radii of the target particle (edge point to particle center) and the possible contacting edge (mid point of edge to target particle center) minus half the edge length. Thus, starting from an array containing all particles in the grey shaded boxes, one ends up with an array containing a considerably smaller amount of particles. These particles are then checked along the lines of the contact logic presented in section 3.4.1 and extensively described in *Tillemans & Herrmann* [237]. An update of the neighborhood lists may be done after each iteration step, however, in quasi-static problems as used here a smaller update frequency is accurate enough.

3.5   Equation of motion

The dynamical basis of the DEM implies the solution of the equation of motion at discrete time steps $t + \Delta t$ for each particle i of all particles N within the sample. The equation of motion has already been introduced in the context of the balance of momentum in equation (2.7) and can be cast in matrix form for each individual particle i

$$\mathbf{M}_i\,\ddot{\mathbf{x}}_i = \mathbf{f}_i + \mathbf{g}_i\,, \qquad \text{with} \qquad \mathbf{M}_i = \begin{bmatrix} m_i & 0 & 0 \\ 0 & m_i & 0 \\ 0 & 0 & \theta_i \end{bmatrix}. \qquad (3.4)$$

$\mathbf{M}_i$ represents the diagonal generalized mass matrix and $\ddot{\mathbf{x}}_i$ the generalized acceleration of particle i. m_i describes the mass of polygon i related to the translational degrees of freedom and θ_i describes the mass moment of inertia of polygon i related to the rotational degree of freedom. $\mathbf{f}_i$ in equation (3.4) stands for all interaction forces of a particle i and its neighborhood and $\mathbf{g}_i$ specifies the gravitational forces of the same particle. In the case of a simple (non-cohesive) particle contact one obtains

$$\mathbf{f}_i = \sum_{j=1}^{n_p} \mathbf{f}_{ij}^{p}\,, \qquad (3.5)$$

where n_p denotes the number of contacts of particle i. Cohesive forces, as introduced in chapter 4 and 5, will be simply added on the right hand side of equation (3.4). This equation resembles a system of second order differential equations of the form $\ddot{\mathbf{x}}_i = f(\mathbf{x}_i, \dot{\mathbf{x}}_i)$. In general, the acceleration $\ddot{\mathbf{x}}_i$ of a particle depends on all other particles in the assembly and results in a coupled system of differential equations. Starting from classical methods like Euler, Runge-Kutta or general finite difference algorithms to adopted MD methods like Verlet, leapfrog, velocity Verlet or predictor-corrector algorithms, a broad spectrum of possibilities to encompass the numerical time integration of equation (3.4) is available. See the books by *Hairer et al.* [98] and *Hairer & Wanner* [99] for a general overview and the book by *Allen & Tildesley* [5] for methods in the context of MD. In the present thesis a Gear predictor-corrector scheme is used which takes into account the time derivatives of $\mathbf{x}_i$ up to the fifth order. This scheme is a finite-difference-based multistep method and, in short, is composed of three basic steps: (a) Predictor step: All kinematic variables are predicted based on the available information and the time step. (b) Calculation step: The individual equation of motion of each particle is solved, i. e. the acceleration of the particles is calculated based on the overlap forces. Thereby, the forces are calculated using the predicted coordinates and velocities. (c) Corrector step: All kinematic variables are corrected based on an error criterion applied onto the accelerations. Afterwards one could add another loop over the procedure (a) to (c) or step further by increasing the time. Therewith, the new positions, velocities and accelerations of the particle sample are computed. In the form implemented here the method is explicit, as the procedure (a) to (c) is repeated only once per particle at each time step. If the loop is repeated as often as the acceleration error decreases to zero, equilibrium would be obtained and the algorithm could be termed implicit. Unfortunately, most of the time within a DEM simulation is used for the location of contacts and the calculation of the overlap area. Therefore, an implicit version of the Gear predictor-corrector scheme is prohibitive from the standpoint of computational cost. A simplified representation of the program structure of the DEM model highlighting the predictor-corrector algorithm is shown in appendix B in figure B.1. Additional aspects in the framework of a numerical realization of the DEM, especially the definition of boundary conditions as well as problems that arise if an inappropriate time step is used, are also reviewed in appendix B.

Coming back to the sample creation technique shown in figure 3.3 of section 3.2, the performance of the predictor-corrector algorithm is examined. The particles are released using gravitational action and at the end come to rest in the form of an almost rectangular heap. In figure 3.10 the ratio between the actual overlap area of all contacts $\sum_{i=1}^{N} \sum_{j=1}^{n_p} A_p$ to the total area of all particles $\sum_{i=1}^{N} A_i$ of a starting sample composed by 40×260 particles is plotted over the number of calculation steps. Up to calculation or iteration step 150000, ①, a standard (explicit) version of the predictor-corrector algorithm is applied ($\rightarrow$ procedure (a) to (c) is repeated only once per particle per step). At calculation step 62000 all particles have dropped down leading to a maximum in the ratio of the cumulative overlap area. Afterwards, the sample levels off onto a ratio of 0.5 %. This means that by the explicit version of the predictor-corrector algorithm applied within ① a small but tolerable error (0.5 %) is made at each time step. In the last time step (150000) the loop (a) to (c) is repeated until the maximum error of the particle accelerations has decreased to a negligible amount of 10^{-8}, ②. Within some thousands of predictor-corrector steps the ratio of the cumulative overlap area decreases to nearly zero, as shown on the detail diagram on the right hand side of figure 3.10.
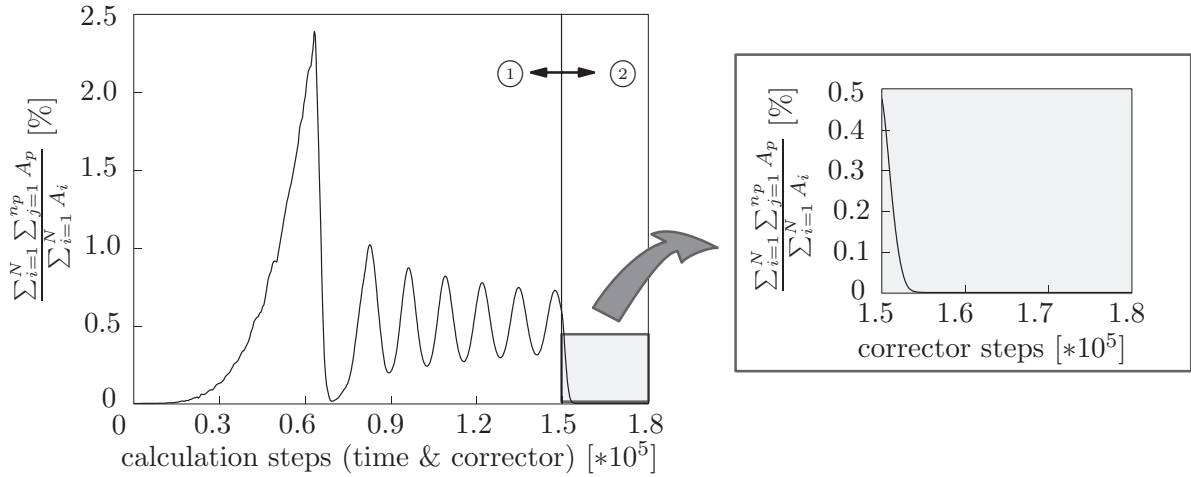
Figure 3.10: Predictor-corrector algorithm in practice.

3.6 Numerical results

In the following, the presented DEM model is validated by two-dimensional simulations of different boundary-value problems. These simulation results are thought as academic examples highlighting the basic features of the DEM model in the framework of quasi-static applications. A quasi-static loading is obtained if the process is slowly enough so that all the variables have a definite value through the entire path taken by the process, i. e. at each time step the system is effectively at equilibrium. In practice, a quasi-static loading must be carried out on a time-scale which is much longer than the relaxation time of the system. Highly dynamic load setups like impact, explosion or collision simulations are not treated here. More information on those examples can be found in the articles by *Kun* & *Herrmann* [140, 141, 142], *Kun et al.* [139] or *D'Addetta et al.* [51]. In fact, here, the emphasis lies on the qualitative application of the model to realistic experimental setups in order to reproduce typical phenomena observed in non-cohesive geomaterials. The detailed characterization of the observable damage and failure within the simulations is postponed to the separate chapter 6.

In order to represent the load-displacement behavior of characteristic rectangular samples within the next paragraphs and in chapters 4 and 5, a normalized load-displacement diagram is introduced. A nominal vertical stress at the boundaries of a specimen is calculated after each time step in the form of a normalized load. Therefore, all reaction forces of the particles on the boundary are summed up and divided by the initial width of the specimen. If the load is applied through loading platens, only the reaction force of the particle representing the loading platen is used and divided by the initial width of the specimen (not of the complete platen). A nominal longitudinal strain is computed in a similar fashion: The length change of the distance between the upper and lower boundary particles is averaged over the width w and divided by the initial height h of the specimen. Thus, one obtains a stress-strain diagram in the sense of a normalized load-displacement diagram. This easy and comprehensive procedure that follows the style of experimental measure techniques represents the form of a globally homogenized consideration of the stresses and strains of the complete sample. It provides a related output comparable to that of computer controlled load carrying capacities as described e. g. by *van Mier* [243].
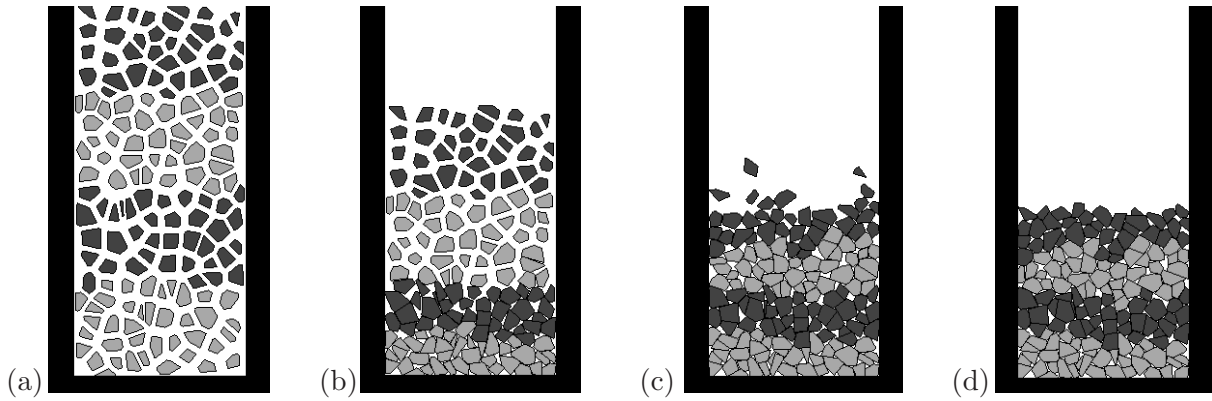
Figure 3.11: Filling of a box.

The definition of average quantities like stresses, strains etc. is treated separately in the context of homogenization procedures in a later chapter. As will be shown there, the above definition agrees with theoretical derivations based on homogenization principles.

The first numerical example was already presented in section 3.2 in the context of the mesh generation of porous particle samples, see figure 3.3. The DEM was utilized to obtain the final stage of a porous packing. Certainly, the example presented in figure 3.3 is rather academic in that a quite small amount of particles has been used. However, a larger amount would have made the visualization of the procedure impossible. In between situations ② and ③ in figure 3.3 the particles are loaded by gravitational forces and start immediately to move towards the bottom plate. Consequently, starting from their initial positions in figure 3.11 (a), the particles get into contact and repel each other until they form one layer after another on the ground of the box, see figure 3.11 (b). Particles in the region of the upper layer bounce up and down as visible in figure 3.11 (c). Finally, all particles settle down due to the energy they dissipate through the collisions as shown in figure 3.11 (d). Different grey shadings in figure 3.11 are used for visualization reasons only. In the next subsection, first, dense and porous biaxial box simulations with different height to width ratios are investigated. Afterwards, the simulation of the extension of a dense and porous granular layer is studied.

3.6.1 Biaxial tests

A typical benchmark problem in the context of non-cohesive geomaterials is the biaxial test. The two-dimensional case studied here involves the simulation of a plane strain biaxial apparatus according to Hambly, as described by *Kuntsche* [143] and *Topolnicki* [238]. In short, this experimental setup represents a strain driven loading of a rectangular sample with rigid side walls and variable height to width ratios. The granular sample is constrained in the lateral x direction and vertical y direction by four loading platens, usually made of steel, compare with *Kuntsche* [143] or *Topolnicki* [238]. The key fact that characterizes this load setup is an independent movement of the opposite plate pairs by the bearing of the apparatus. This setup is on contrast to those ones applying flexible side walls, compare the experiments by *Viggiani et al.* [250] or corresponding DEM simulations by *Åström et al.* [7].

The rectangular test sample with a height to width ratio of 1.6 consists of approximately
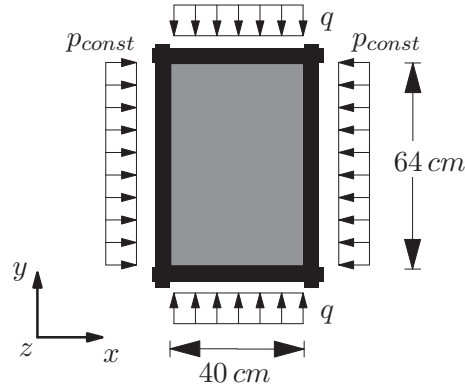
Figure 3.12: Simulation setup of Hambly-type biaxial test.

2500 particles. The specimen is loaded by four non-deformable walls at the top, bottom
and on both sides, represented by large rectangular particles, see figure 3.12. A con-
stant pressure $p_{const} = 1$ kN/cm^2 is applied on the side walls. The vertical loading q is
applied in a strain driven format by a constant increase of the velocity of the top and
bottom plate following the procedure described in appendix B. A background friction
term according to *Luding & Herrmann* [156], compare also *Luding* [154], is included in
the stress-controlled motion of the two side walls. Thereby, the background friction is
controlled by the product of a damping coefficient and the velocity of the side walls and
represents a strong frictional force which damps the motion of the wall so that oscillations
are reduced, i. e. a stabilization of the movement of these walls in terms of their inertia
is obtained. In order to constitute a Hambly-type configuration the surrounding platens
may overlap each other during the simulation progress without creating any contact force.
The following parameters have been used: $E_p = 100$ kN/cm^2, $\gamma_N = 10^5, \gamma_T = 0$, $\mu = 0$,
$\rho = 5$ g/cm^3. The time step is fixed to $\Delta t = 10^{-6}$ s. The biaxial test is a well known
experimental setup in geotechnics. Based on this experience a failure evolution dominated
by shear localization in zones of finite width is expected for not too large side pressures.
No quantitative comparison with a real granular structure is performed at the present
stage. In figure 3.13 (a) the initial particle structure of the test is presented. The ap-
proximately 2500 particles are colored in light, medium and dark grey for visualization
reasons only. The deformed sample at a later stage of the simulation in figure 3.13 (b)
reveals the formation of parallel shear zones, whereby the upper shear zone ① appears
at first. The particles located above shear zone ① and below shear zone ② form wedges
that undergo a rigid body translation with little visible internal deformation. The middle
region between both shear zones behaves like a rectangular block sheared along its top
and bottom boundary. In between, a region of finite width represents the shear bands,
governed by dilation and particle rotation. A separate discussion dedicated to shear zones
and their width is pursued in the context of the defect correlation length in section 6.4
and homogenization procedures in chapters 8 and 9. The purely local deformation of the
vertical line of dark grey shaded particles in figure 3.13 reveals a highly localized action
and a reorganization of the particle structure. In principle, this line remains vertical,
except the "discontinuity" in the region of the shear zones. The simulation results are in
good qualitative agreement with experimental results of dry granular materials like sand.
See for instance the Hambly-type biaxial experiments of hard corundum grains by *Nübel*
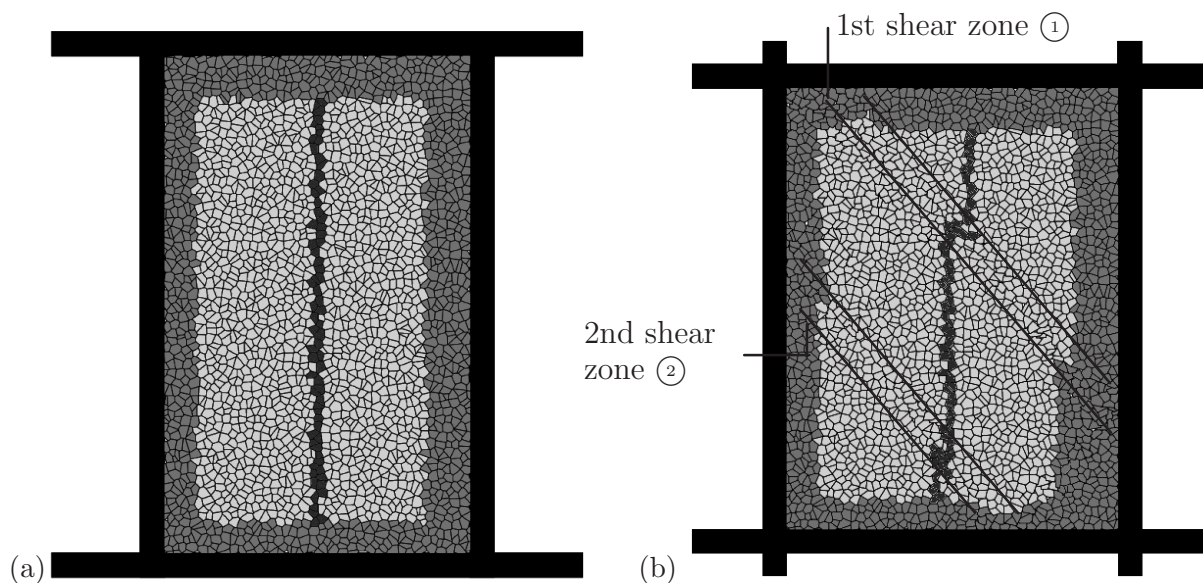
Figure 3.13: (a) Initial and (b) deformed state of dense biaxial test.

[188] or the biaxial experiments with flexible side membrane on Hostun sand by *Viggiani et al.* [250]. Simulations with the same height to width ratio and up to 900000 particles (sample size: 225 cm × 360 cm) showed nearly the same failure pattern aligned with practically the same shear band inclination. Since a visualization of such a high particle amount is by far more complicated compared to that in figure 3.13 due to the necessary scale effect, these results are left out of consideration in the context of this thesis.

Porous biaxial simulations in principle yield related results depending on the initial porosity. A porous rectangular test sample with a height to width ratio of 1.6 and approximately 2900 particles was used. The specimen was loaded in the same way as the dense sample introduced before, while the values of the constant side pressure $p_{const} = 1$ kN/cm^2 and the other variables were kept constant. The situation at the start of the simulation is il-
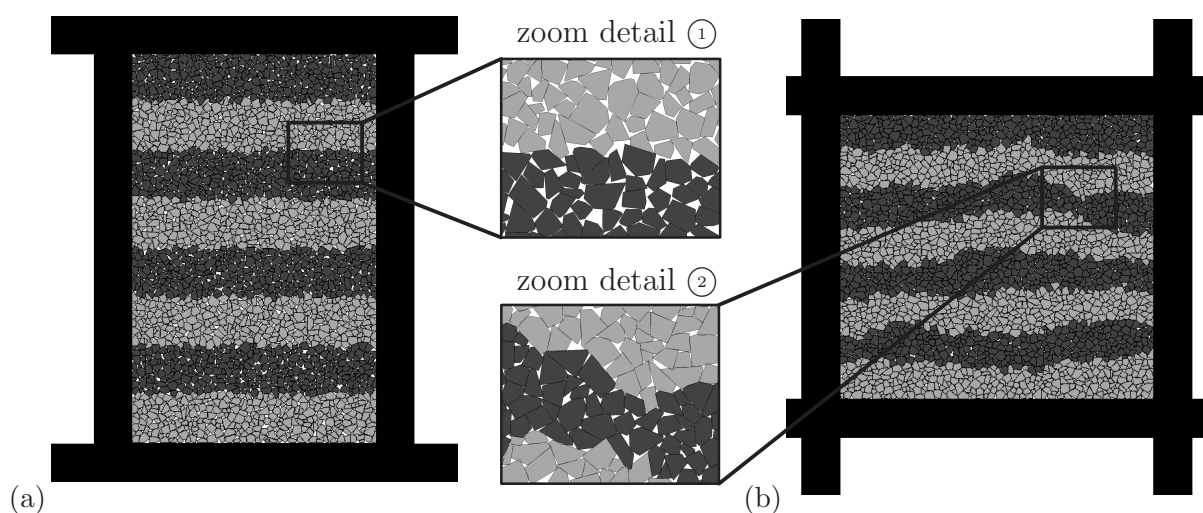
Figure 3.14: (a) Initial and (b) deformed state of porous biaxial test.
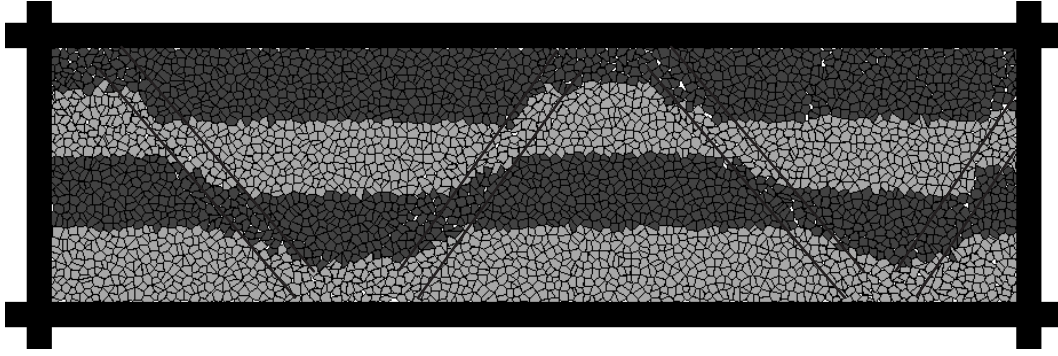
Figure 3.15:   Deformed state of compact dense biaxial test.

lustrated in figure 3.14 (a). The zoom detail ① emphasizes the porous structure. During the course of simulation a variety of competing shear bands appear. Indeed, in contrast to the dense sample in figure 3.13, no clear band formation is observed. The formation of shear bands becomes obvious in figure 3.14 (b) or the detailed view ② by observing the local thickness change of the grey shaded particle layers in the horizontal direction. Moreover, zoom detail ② clarifies that in the course of the simulation the porosity, i. e. the ratio of pores to the complete volume, decreases.

In the next step, the height to width ratio of the dense specimen was changed from 1:1.6 to 1:0.37, but using the same loading setup presented in figure 3.12. Therewith, a compact dense sample is represented. The rectangular block is made of 3800 densely packed particles and a dimension of 38 cm × 102 cm. A similar failure behavior as for the slender biaxial test is encountered. However, a higher amount of dominant shear zones appears, leading to a good qualitative agreement with experimental observations, e. g. compare with those of *Nübel & Gudehus* [189]. The shear band pattern in an advanced simulation stage forms a zig-zag line, as shown within the output of the simulation in figure 3.15. The inclination of the shear zones does not change significantly compared to the biaxial simulation shown in figure 3.13.

3.6.2   Extension of granular layer

The extension of a granular layer was firstly presented by *Nübel & Gudehus* [189] in order to investigate the shear band pattern of sand. An elastic strip is placed at the bottom of
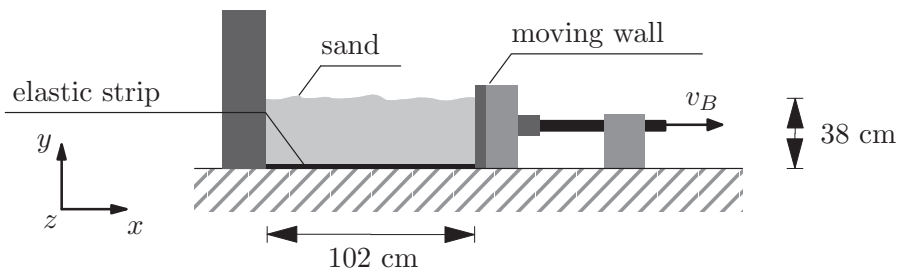
Figure 3.16:   Extension of granular layer - experimental setup.
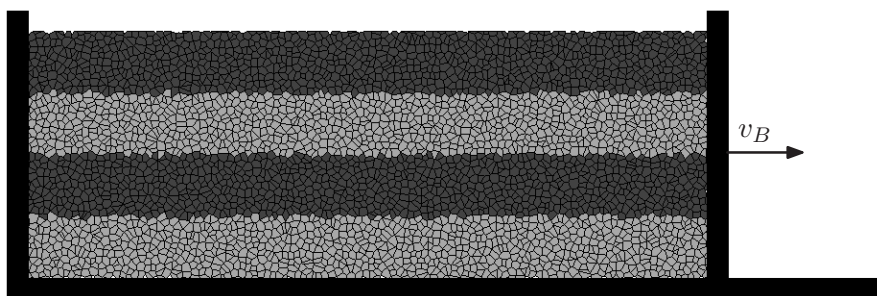
Figure 3.17: Extension of dense granular layer - initial stage.
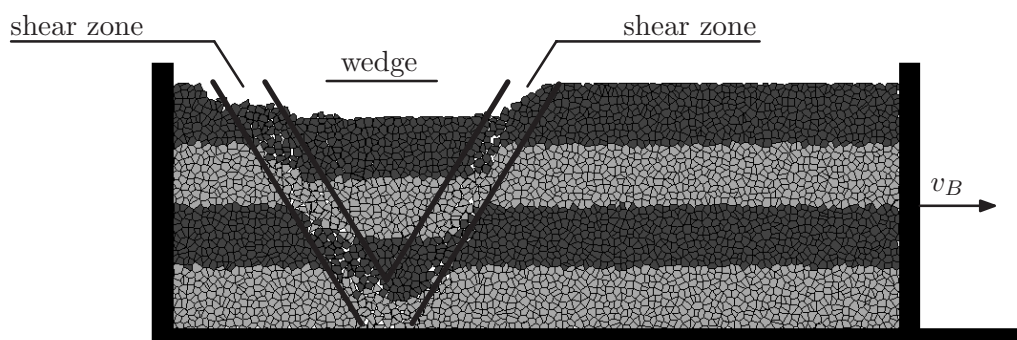
Figure 3.18: Extension of dense granular layer with small v_B - failure stage.

a sand filled box and attached between a fixed and a movable vertical side wall, compare the simulation setup in figure 3.16. By constantly shifting the right side wall rightwards a linear stretch at the bottom is attained and failure within the sample is induced. This example was simulated with a specimen consisting of 3800 particles with a height to width ratio of 1:0.37. The load was applied in the following way: The right side wall is moved rightwards in a deformation controlled manner with a constant velocity $v = v_B$. The velocity distribution of the bottom particles adjacent to the elastic strip is presumed to be linear. Therefore, these particles are moved with a constant velocity ranging from $v = 0$ to $v = v_B$ depending on their position with respect to the moving wall. In contrast to the
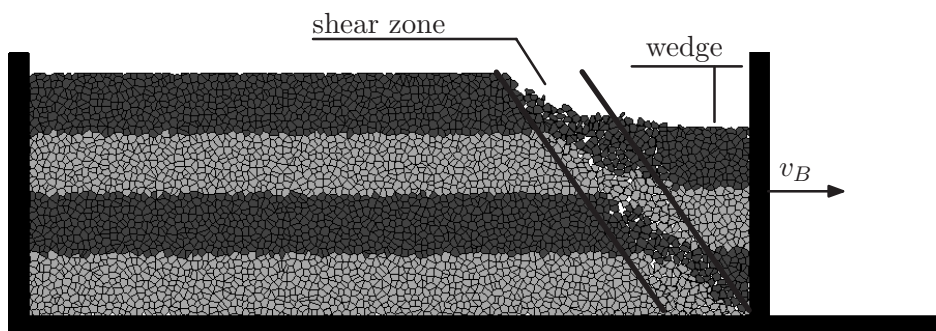
Figure 3.19: Extension of dense granular layer with high v_B - failure stage.

(a)   (b)
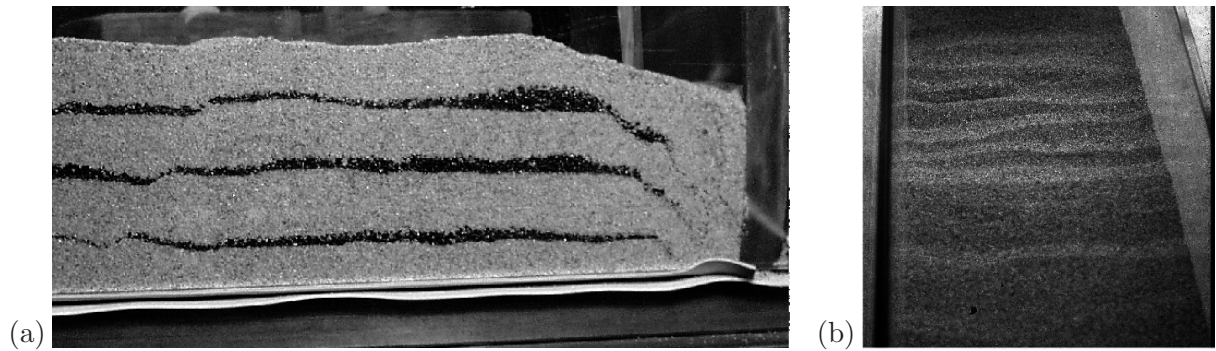
Figure 3.20: Extension of a granular layer - experimental results (courtesy of *Nübel* [188]): (a) shear bands (side view) and (b) surface waves (top view).

previous examples, additionally a vertical loading in the form of gravitation is applied to each particle. The initial stage of simulation is depicted in figure 3.17. The basic failure mechanism is developed by the formation of a wedge, bounded by two inclined fault zones, as shown in figure 3.18. The failure behavior is very sensitive to the applied boundary velocity $v = v_B$. Therefore, the simulation has been carried out with a ten times higher velocity v_B of the side plate. Now, the failure pattern changes: Only one shear zone appears and a single wedge between this zone and the boundary plate forms, compare figure 3.19. However, the inclination of the shear fault is the same as for the low velocity case. Basically, the behavior found in the simulations compares to the experimental results in *Nübel* [188] or *Nübel* & *Gudehus* [189], see figure 3.20. There, a wavy top surface of the sample appears due to the formation of a series of inclined fault zones. Therewith, a series of wedges is formed. Besides of one of these wedge mechanisms, this behavior could not be reproduced in the same way by the various dense simulations. One reason could be the small amount of particles in comparison to the number of grains in the experiment. This fact may influence the sample behavior more significantly as in the case of the biaxial simulations, where a good agreement of the general failure behavior was found. Another, more probable reason could be the compact composition of the initial dense particle sample, i. e. no pores are contained in the initial configuration. This may restrict the deformations of the system in an unfavorable manner.

Additionally, an initially porous sample was investigated, compare the initial stage of the simulation in figure 3.21. The specimen is composed of a comparable amount of particles, namely 4550, and a comparable height to width ratio as the dense specimen above. Now,
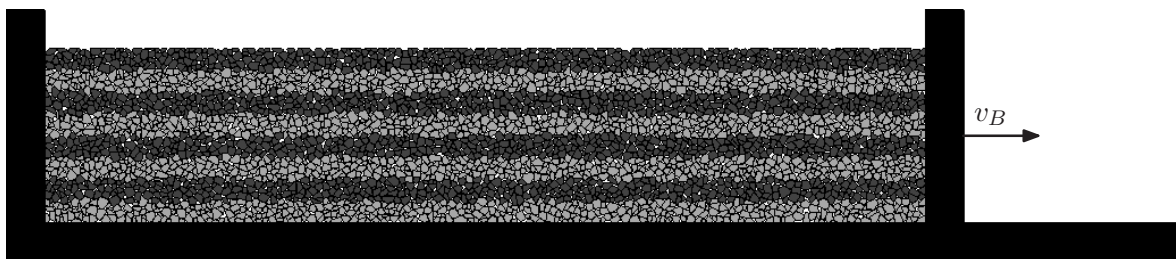
Figure 3.21: Extension of a porous granular layer - initial stage.
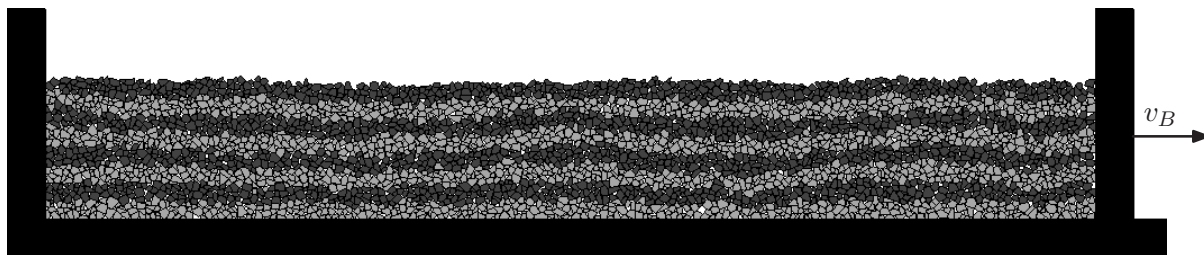
Figure 3.22: Extension of a porous granular layer - failure stage.

the simulation results agree quite well with those of *Nübel & Gudehus* [189] in terms of the wavy surface and the accompanying failure mechanisms, compare figures 3.20 and 3.22.

Chapter 4

Modeling of cohesion via beams

4.1 General

The model presented so far allows for the application to non-cohesive granular materials like sand, stone or rock heaps, but also vegetables. Admittedly, most geomaterials are more or less cohesive. Therefore, a model is demanded which is capable to describe this kind of materials and represent cohesion. In other words, attractive forces between particles are necessary to bond the particles together to some extent. Thereby, usually the physical effect of cohesion is limited for tension. Several ways of incorporating cohesion into particle models are feasible. The implementation strongly depends on the chosen particle shape and problem class. The easiest way in the case of circular particles is the introduction of attractive potentials like in MD. In this regard, the most prominent law that accounts for attractive action between particles is the Lennard-Jones potential adopted from physical chemistry, see the description in *Allen & Tildesley* [5]. Another way, only reasonable for circular particles, is based on an extension of the Hertz contact law for "negative" overlaps. An implementation is rather straightforward as the primary geometric variable defining the contact of circles is the distance between the particle centroids, compare *Donzé & Magnier* [72], *Mühlhaus et al.* [180] or *Zhong & Chang* [265]. Following this line *Magnier & Donzé* [159] proposed an alternative model where an initial overlap of circular particles accounted for the attracting force law. In contrast to circles, the geometric definition of polygonal particles in contact is by far more complex. This is the case as more than one geometric variable describing the contact and the position of the individual bonded edges is involved. The distinction between a point contact (circles) and line contact (polygons) must be drawn. Therefore, alternative options have to be considered. In the following, two different approaches that account for cohesive bonds between two polygon edges will be presented: In the first approach, in the present chapter, beam elements between the centers of mass of neighboring particles are introduced. As an alternative, in chapter 5, continuous interfaces along common particle edges represent the bonding component.

If the particle assemblies generated in the previous chapter are meshed via beam elements through the particle centers, an overlaying network results. These networks are generally termed lattice networks and are applied in various areas of science. General lattice models, in principle, are based on the fundamental idea of an atomic lattice approximation of materials. The development of these ideas traces back to the beginning of the 19th century. *Cauchy* and *Poisson* tried to derive elastic properties of crystalline solids like Hooke's law or strain energy functions by idealizing isotropic structures via attracting and repelling particles ordered on regular lattices. Todays beam lattice models have their roots in the theoretical developments of *Hrennikoff* [113] in the context of the discretization of structural members like plates via spatial truss networks. *Hrennikoff's* ideas on the so-

called *framework method* where a continuous surface structure is replaced by an idealized discrete system also represents one of the various roots of the FEM, cf. *Szillard* [233].

Theoretical physicists in the field of statistical mechanics extensively studied and applied beam lattices to model fracture and related mechanisms since the 1980's, see *Hansen et al.* [101], *Herrmann et al.* [104] or *Roux & Guyon* [211]. A variety of similar lattice models (so-called central-force, bond-bending or Born models) were used since these years for various purposes, cf. the textbook by *Herrmann & Roux* [105]. On the other hand, engineers in the field of materials research like *Bažant et al.* [18], *Burt & Dougill* [27], *Diekkämper* [68], *Schlangen & van Mier* [217], *Schorn* [219, 220] or *Zubelewicz & Bažant* [267], applied pure bar or beam lattice models since the 1970's with varying success for the simulation of fracture in heterogeneous materials. Pioneers in the systematic application of lattice models as tool for interpretation and design of laboratory experiments are certainly *van Mier* and his co-workers, see the book [243] for an overview on lattice ideas in the context of concrete research. This kind of models have proven to be very valuable tools for a better understanding of *micro* induced effects on the *macro* fracture. But, pure beam lattice models still show some significant deficiencies when the goal in mind is the modeling of cohesive and non-cohesive geomaterials. Drawbacks are, for example, the limitations in compressive simulations of cohesive granular materials, the brittleness of the stress-strain response or the simulation of less or non-cohesive granular materials. Therefore, it is assumed that an improvement of a pure particle method by a beam lattice helps to overcome these deficiencies.

Starting from the familiar knowledge on lattice models, the incorporation into DEM based particle models for the representation of cohesion is a straightforward task. The beam enhanced DEM model in the form used here was introduced by *Kun & Herrmann* [141] by an enhancement of the pure particle model of *Tillemans & Herrmann* [237]. First encouraging applications in the context of the dynamic fragmentation of solids by *Kun et al.* [139] and *Kun & Herrmann* [140, 141, 142] paved the way to a quasi-static use of this methodology by *D'Addetta et al.* [50, 51, 52, 55] and *Kun et al.* [139]. In consequence of the positive results, this methodology was adopted by other authors, too, compare the contributions by *Delaplace & Ibrahimbegovic* [117], *Ibrahimbegovic & Delaplace* [118] or *Tavarez et al.* [234]. Admittedly, it is important to note that the beams contained in this beam enhanced DEM model have no structural mechanical relevance. Paralleling the use of beams in pure beam lattice models, the beam elements are understood as a simple tool for the representation of cohesion and fracture development.

4.2   Beam mesh & statistical properties

Starting with a particle sample, as shown in figures 3.3 or 3.9 (a), the key issue for an introduction of beams is to mesh the system via an interconnection of the particle centroids. Usually, a Delaunay triangulation is applied to achieve this task for dense systems, e. g. like that shown in figure 3.9 (a). If one draws a line between any two particle centers where Voronoi polygons touch each other, a set of triangles is obtained known as the Delaunay triangulation. Generally, this triangulation is unique and dual to the Voronoi tessellation according to *Moukarzel & Herrmann* [177] introduced in section 3.2. The key point of this Voronoi tessellation aligned with the corresponding triangulation is the fact that a random lattice is obtained that does not introduce any anisotropy into the mesh.

A basic property of the Delaunay triangulation is that the outcircle of every triangle does not contain any other point, see *Preparata & Shamos* [203]. If a porous packing as shown in 3.3, ④ is meshed, an alternative algorithm following *Renka* [207] is applied. The results of the different meshing techniques are illustrated in figure 4.1. It is not the plan in this study to simulate cohesive porous samples in the fashion exemplified in figure 4.1 (b). In fact, the beam mesh is not only applied for the representation of cohesion, but also as a basic ingredient for the numerical realization of the homogenization techniques to be introduced in chapters 8 and 9.

The irregularity parameter a, introduced in section 3.2 for the mesh generation, allows a smooth transition from an anisotropic mesh ($a \to 0$) with two pronounced main directions to a more isotropic mesh ($a \to 1$) without any pronounced direction, compare with *Moukarzel & Herrmann* [177]. Isotropy, in this sense, is characterized by a homogeneous distribution of a large enough amount of beam elements with respect to the angle orientation. Compared to usual random lattices this mesh could be called a regularized random lattice where a certain regulative effect on the neighborhood of a given point exists. This limits the number of neighboring particles in a range from 3 to 12 and, thus, leads to a homogeneous distribution of the lattice properties. The probability of any beam connection with respect to the orientation angle can be expressed in form of a polar plot. In figure 4.2 the corresponding graphs of an analysis of a quadratic 40×40 particle sample are given. The transition from a rather irregular distribution with peaks in the main directions for small values of a to a more or less regular distribution for $a \to 1$ clearly shows the effect of a on the isotropy of a sample. A mild anisotropy is still persistent due to the initial underlying quadratic grid. However, this has no apparent effect on the simulation results, as will be shown later. Indeed, the picture changes, if a sample is loaded. Then, in the course of simulation an anisotropic texture, also denoted as sample fabric, is obtained. A detailed investigation of the anisotropy of the sample fabric along with an introduction of anisotropy measures will be done in section 6.3. The relevant parameters of the beam geometry are the length l_b, cross-section A_b and moment of inertia I_b of the beams. These parameters are statistically determined by the mesh generation technique. More information concerning the statistics of the beam mesh is reported in *D'Addetta et al.* [52] or *Moukarzel & Herrmann* [177]. The length of the beams l_b is determined by the distance of the centers of mass of the particles, cf. figure 4.3. The cross section A_b and moment of inertia I_b of a beam are directly related to the initial length of the common side of two neighboring polygons h_b which represents the height of the considered beam for

(a)   (b)
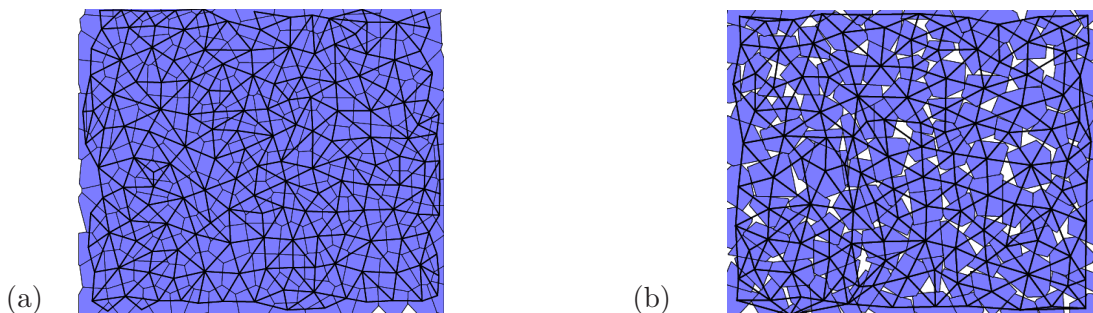
Figure 4.1: Delaunay triangulation of (a) a dense sample according to *Moukarzel & Herrmann* [177] and (b) a porous sample according to *Renka* [207].
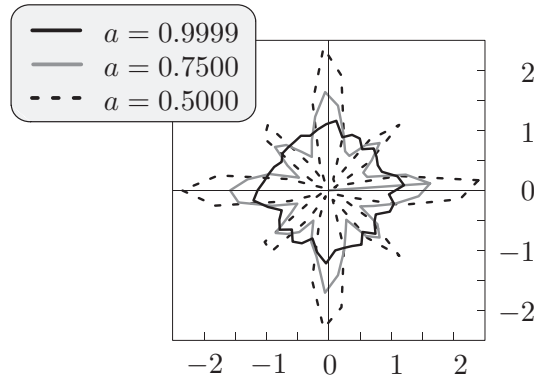
Figure 4.2: Orientation distribution of beams normalized to average value.

the case of a dense sample. Note, that for visualization reasons the beams are displayed thinner than the real thickness h_b in figure 4.3. The only form of disorder in the model is represented by quenched structural disorder. If porous cohesive samples are to be used in combination with beam lattices, which is not the case in this thesis, A_b and I_b must be defined alternatively. Keep in mind that in this two-dimensional model A_b and I_b refer to a unit thickness for dimensionality reasons.

4.3   Forces & stiffnesses

The definition of the beam elements implies the same number of degrees of freedom as the underlying particles, namely 3 as depicted schematically in figure 4.3 (a). *Schlangen & Garboczi* [216] have shown that this form of the beam model is most appropriate for fracture problems, as a reduction of the amount of degrees of freedom of the cohesive connections (e. g. leading to one or two springs) may lead to unrealistic crack pattern. This form of a beam model is a discretization of the simplified Cosserat equations of continuum elasticity which can be used to describe the elastic behavior of granular solids instead of the Lamé equations, see for instance *Bažant & Christensen* [14]. In anticipation of a detailed discussion of the breaking conditions of the beams it is remarked that the physical effect of the cohesion is limited for tension by a predefined breaking law. Hence, overstressed beams break and are removed from the calculation. Due to the displacements and rotations of the particles in figure 4.3 (a) a deformation of the overlaying beams follows, as shown in figure 4.3 (b). The stored potential energy within the beams due to this deformation is reflected back onto the particles in form of elastic repulsive reaction
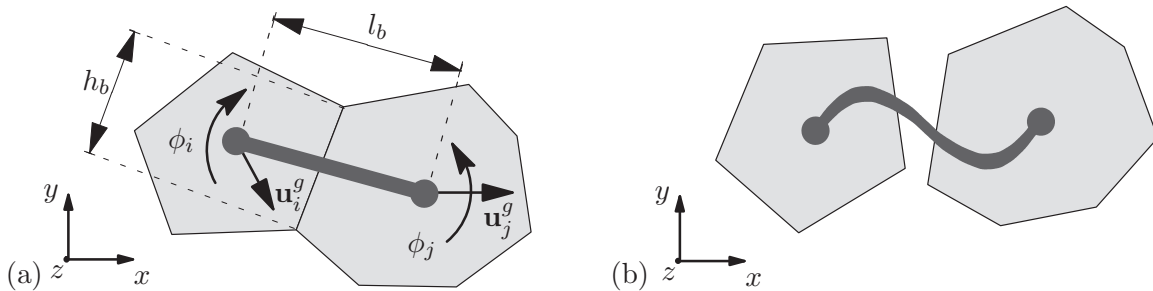
Figure 4.3: Beam deformation by particle movement.

forces and moments. The repelling action at both particles is driven by the generalized beam force vector $\mathbf{f}_i^b = \begin{bmatrix} f_{i,x}^b & f_{i,y}^b & m_i^b \end{bmatrix}$ at particle i and an analogous definition for particle j. $\mathbf{f}_i^b$ is defined in analogy to the definition of the deformation measure introduced in section 3.3 and is computed with the aid of the Timoshenko beam theory

$$\begin{bmatrix} \mathbf{f}_i^b \\ \mathbf{f}_j^b \end{bmatrix} = \mathbf{K}^b \begin{bmatrix} \mathbf{u}_i \\ \mathbf{u}_j \end{bmatrix}. \tag{4.1}$$

$\mathbf{K}^b$ resembles the stiffness matrix which is calculated based on the normal, shear and bending flexibilities of the beams. The beam force vector enters the equation of motion in equation (3.4) via the interaction force vector

$$\mathbf{f}_i = \sum_{j=1}^{n_p} \mathbf{f}_{ij}^p + \sum_{k=1}^{n_b} \mathbf{f}_{ik}^b. \tag{4.2}$$

Additionally to n_p, noting the number of particle contacts of particle i, n_b denotes the number of existing beams of particle i. In general, there are different basic ways to introduce disorder in a model that ought to represent geomaterials like concrete or ceramics, see the discussion in *D'Addetta et al.* [52]. In this beam model the disorder is introduced through the mesh generation. Different flexibility values are assigned to each beam at the beginning of the simulation on the basis of the initially defined geometric parameters l^b, A^b and I^b. The beam length l^b represents a relational parameter that controls the effective beam stiffness and, thus, influences the strength distribution of the particle connections. Keep in mind that the usual assumption of the beam theory, small height to length ratio, is violated due to typically large ratios ($\rightarrow 1$) of the beam height to length. Since the beam model represents only a tool for the modeling of cohesion within this enhanced DEM model the violation of this assumption is accepted. As a result, the initial distribution controlled by the statistically determined Voronoi generation process influences the transition from the "microscopic" parameters to the "macroscopic" measurable values, e. g. the elasticity modulus as reported by *D'Addetta et al.* [52].

4.4   Failure representation

The primary microscopic fracture process within cohesive frictional materials is caused by a tensile failure of the cohesive bonds between the grain boundaries. The beams in this DEM model are thought to represent this effect between the initially bonded particles. Therefore, a breaking situation is attained solely in the case of elongation of the beams. Different breaking criteria, either deformation- or force-based, are conceivable, see the overview given in *Herrmann & Roux* [105]. Among others the following force-based breaking rules have been introduced: A normal force-bending moment interaction by *Herrmann et al.* [104] and in similar fashion by *Schlangen & van Mier* [217], a normal force-shear force interaction by *Beranek & Hobbelmann* [21] and a decoupled normal force-shear force criterion by *Zubelewicz & Bažant* [267]. Since the movement of the particles is the primary measure, a displacement-based breaking criterion in the style of that reported by *Herrmann et al.* [104] is used here. This criterion accounts for the fact that the breaking of a beam is only caused by stretching and bending. Therefore, long or thin beams are easier to break than short or thick ones. Two predefined parameters ϵ_{max}^b

(for stretching) and ϕ_{max} (for bending), each defining a different physical fracture mode, are introduced. The beam breakage is controlled by the following condition

$$p^b = \left(\frac{\epsilon^b}{\epsilon^b_{max}}\right)^2 + \frac{\max\left(|\phi_i|\,,\,|\phi_j|\right)}{\phi^b_{max}} \leq 1 \qquad ;\; \epsilon^b \geq 0\,. \qquad (4.3)$$

If $p^b > 1$ and $\epsilon^b \geq 0$ the corresponding beam is eliminated, i. e. "broken". For $p^b \leq 1$ the corresponding beam is kept in the model. In this failure surface formulation ϵ^b denotes the local axial beam strain due to the new positions of particles i and j. This value is related to the threshold value for the elongation mode ϵ^b_{max}, while the maximum of the rotations ϕ of one of the particles i or j is related to the threshold value for the bending rotation ϕ^b_{max}. This criterion can alternatively be derived in a force-based fashion starting from limit analysis ideas, as stated by *D'Addetta et al.* [50] and represents a brittle beam failure.

An update of the beam connections is carried out after each time step when the equation of motion is solved for all particles. Hence, the updated coordinates of the centers of mass of the particles are taken into account. Those beams that do not fulfill the condition in equation (4.3) are removed from the calculation and can never be restored during the simulation. Therefore, it is possible to remove more than one beam within one time step. The numerical realization of the beam enhanced DEM model in form of a simplified program structure is shown in figure B.2 in appendix B.

4.5   Numerical results

Instead of sand-type materials like in section 3.6 now cohesive geomaterials like cement, marble, marl or concrete are addressed. First, standard tests for the determination of the compressive, tensile and shear resistance of rectangular samples are presented. This is followed by more practice relevant setups, like biaxial, notched tension, Brazilian or L-shape tests.

In order to visualize a sample's failure in terms of the microscopic component *beam*, an alternative display procedure compared to that used in the previous chapter for the non-cohesive particles is introduced. Midpoints of eliminated beam elements are plotted in a box which determines the initial sample geometry. This methodology was firstly introduced in *D'Addetta et al.* [51] and gives further evidence on the loss of contacts and the cracking in a sample.

4.5.1   Standard tests

The parameters used for the simulations of the standard test are as follows: $E^p = 100$ kN/cm^2, $E^b = 1000$ kN/cm^2, $\gamma_N = 10^5, \gamma_T = 0$, $\mu = 0$, $\rho = 5$ g/cm^3, $\Delta t = 10^{-6}$ s, $\epsilon^b_{max} = 3\,\%$, $\phi^b_{max} = 3^0$. Since at the present stage the reproduction of typical failure mechanisms of cohesive geomaterials is to the fore and not a quantification of the model, the above parameters are not fitted to any material.

Compression simulations

Rectangular specimens with a height to width ratio of 1.6 consisting of 1000 particles (25 cm $\times$ 40 cm) and 2870 beam elements have been chosen for the simulation of com-

pressive load scenarios, see the simulation setup in figure 4.4 (a). The specimens are loaded under constant strain rate conditions applying the same loading procedure as introduced in section 3.6.1 and explained in appendix B. The loading is applied by moving the two stiffer boundary layers inwards. Thereby, the loading platens are conducted vertically without any possibility of lateral or rotational movement. The choice of the boundary conditions usually plays an important role in the context of experimental techniques. For a general discussion on the importance of the boundary conditions in experiments the reader is referred to section 4.1.3 of *van Mier's* [243] book. Here, two different boundary conditions have been studied: with and without friction between the boundary particles and the load platens at the upper and lower boundary. In the frictional case (case (a)) all particles in contact with the plates are confined, i. e. they are fixed against horizontal and rotational movement (load setup in figure 4.4 (a) including dark grey shaded quads). Thus, this case could also be considered as a sticky case, as the boundary particles are practically stuck to the boundary layers. In the non-frictional case (case (b)) no lateral constraint is present and these particles are free to move either in horizontal or rotational direction at all boundaries (load setup in figure 4.4 (a) excluding dark grey shaded quads). Thus, if a confinement is present, the particles are restricted in the x- and ϕ-direction. In both cases the lateral boundary particles are not fixed and, therefore, allow for a completely free boundary. Altogether, the loading, boundary and geometry settings resemble the setup of a strain driven uniaxial compression test.

The nominal stress and strain in y-direction is calculated according to the procedure pointed out in section 3.6 and plotted in figure 4.4 (b) for both cases. The behavior reveals a linear elastic regime with a constant "macroscopic" elasticity modulus up to the peak, followed by a rather sharp drop indicating the "macroscopic" disintegration of the specimen. In this framework the beam breaking is considered as "microscopic" failure of the sample material. When more energy is lost during a certain time period due to the beam breaking than it is induced by the loading procedure, an average negative tangent modulus results which yields a brittle failure of the material. The confinement at the boundaries leads to a slightly higher peak stress for case (a), while the macroscopic elasticity modulus is identical for both cases. The situation almost at the end of the simulations is depicted in figure 4.5 and reveals two different failure mechanisms: For
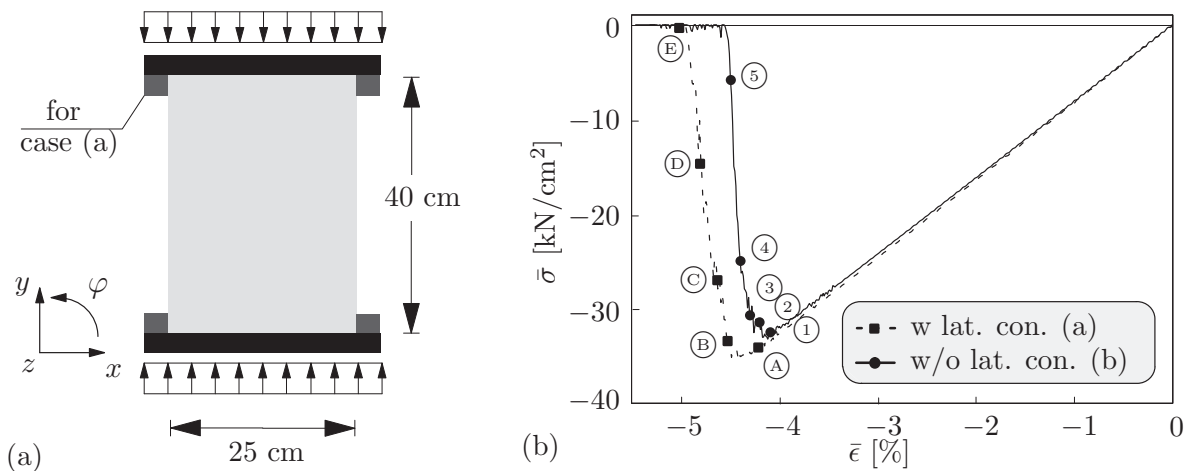
Figure 4.4: Compression test: (a) Simulation setup and (b) nominal stress-strain diagram.
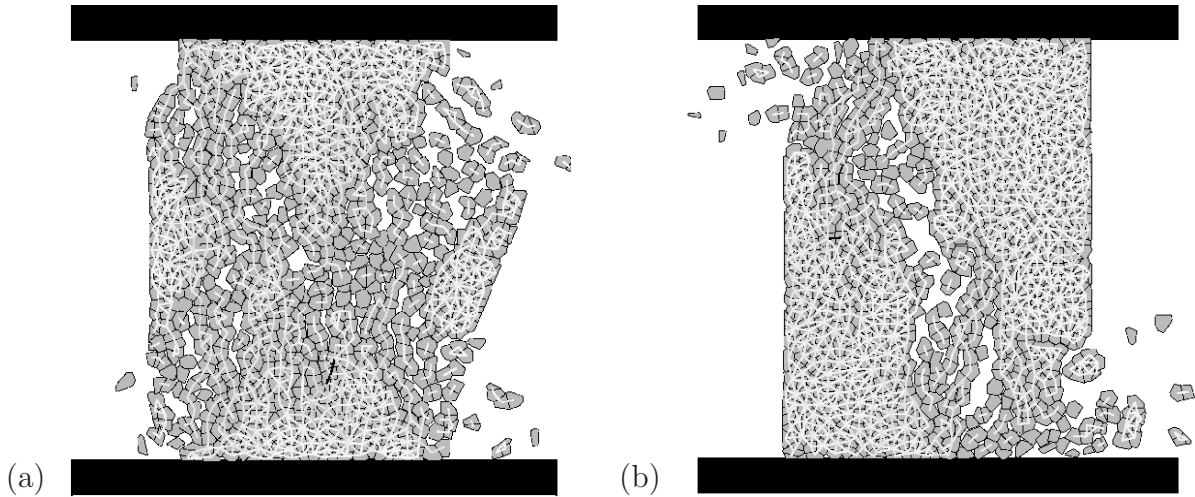
Figure 4.5: Failure evolution of compression simulation.

case (a), following a localization of deformations on diagonal bands, the failure planes start to orient on the two main diagonals connecting the edges of the specimen. The loss of lateral stiffness due to progressive beam breaking in the horizontal direction leads to a bulging of the specimen accompanied by the development of column-type structures on the two diagonals of the specimen. In the literature this behavior is usually termed hourglass failure. In contrast to the failure mode for the confined specimen, in case (b) the macroscopic failure behavior is determined by two non-crossing shear lines emerging from the right side, moving to the bottom and then growing upwards to the opposite edge.

These results agree qualitatively well with observations in (real) cohesive granular materials, e. g. the failure formation of uniaxially compressed concrete cylinders, compare with the results in *van Mier* [243]. The development of a biaxial (triaxial in 3D) compressive state for case (a) hinders cracks to appear within a triangular region neighboring the boundary confinements. The existence of a triaxial compressed cone is often observed when concrete is compressed uniaxially by a much stiffer steel plate with a persistent effect of friction between the two different materials. Especially for confined specimens a splitting type failure with prevalent tensile cracks mainly in direction of the applied loading can be observed according to figure 4.5 (a). Similar to experiments with concrete prisms loaded between brushes, internally inclined fracture planes develop in case (b) and determine the global fracture behavior. Simulations of specimens with slenderness ratios between 1.0 and 2.0 also led to a good qualitative agreement with experimental fracture observations as described by *van Mier* [243]. Midpoints of the broken beams are used to visualize the cracking within the specimen. The failure evolution for both cases is drawn according to its appearance in the stress-strain diagram, in figure 4.6. Compression simulations resembling case (a) without use of boundary platens, but by loading the specimens through an application of the loading procedure to the upper and lower boundary particles approve the above findings, cf. *D'Addetta et al.* [50, 52].
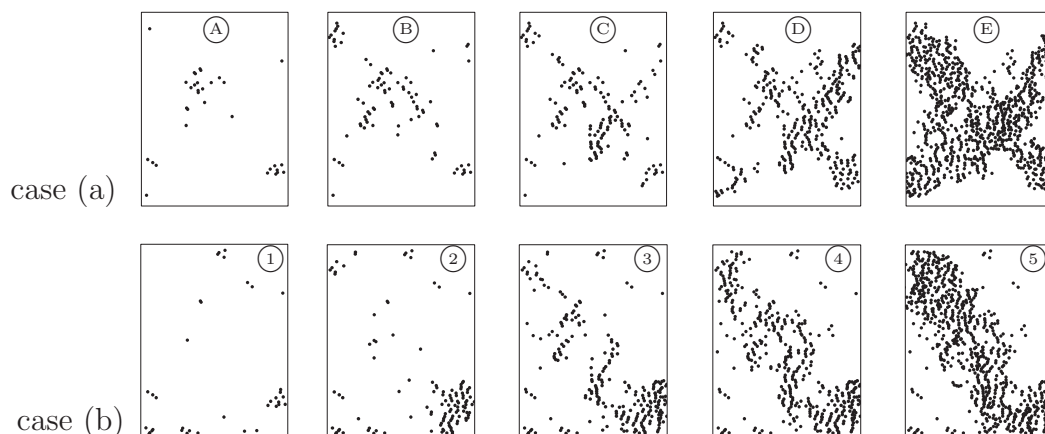
Figure 4.6: Failure evolution for cases (a) and (b).

Tension simulation

A similar particle sample (1000 particles & 2870 beams) as used before for the compression simulations was subjected to uniaxial tension. In contrast to the previous setup, now the constant strain rate loading is applied by tearing the first row of upper and lower boundary particles outwards. In this case the failure behavior is completely determined by the beam lattice and its corresponding stiffness and statistical values, as generally no noteworthy particle contact is induced by this load setup. Thus, the effective macroscopic stiffnesses in tension and compression are different. Again, the stress-strain relation results in a linear response up to the peak level, figure 4.7 (a). In contrast to the compression simulation, nearly no cracking appears before the peak value is reached. Only 9 of 2870 initial beams break up to point ① and almost no fluctuations within the stress-strain diagram are observed before the peak value is reached as a result of an energy release due to beam cracking. The failure evolution is depicted in figure 4.8 according to the points taken from the diagram in figure 4.7 (a). The fragmented state where the specimen breaks into two main pieces separated by one main horizontal crack orthogonal to the loading direction is shown in figure 4.7 (b). Additionally, some short arrested cracks appear which spread out

(a)   (b)
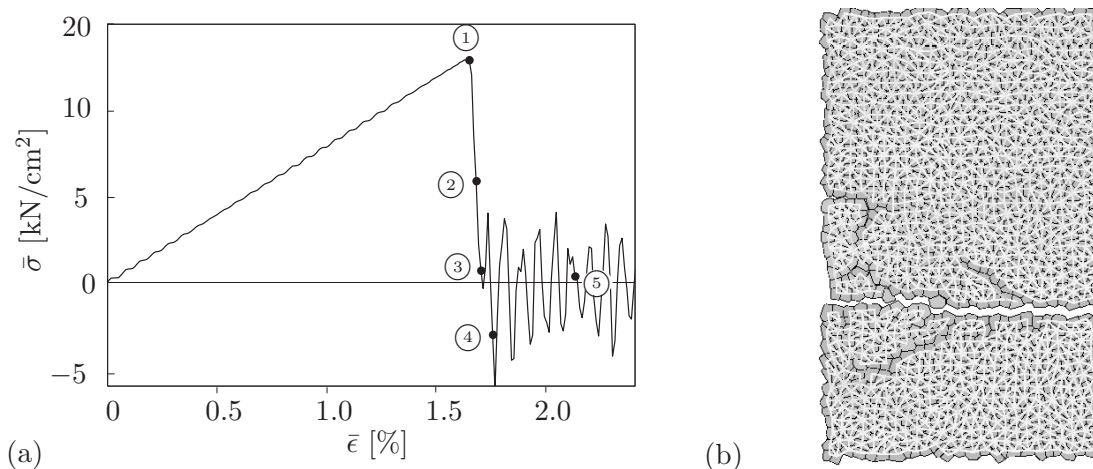
Figure 4.7: Tension test: (a) Stress-strain diagram and (b) graphical output at stage ④.
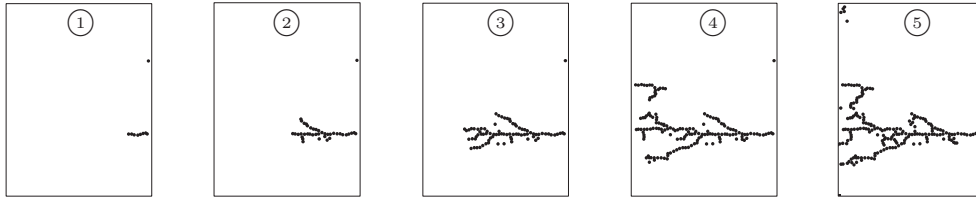
Figure 4.8: Failure evolution of tension simulation.

from the main crack. These cracks indicate the effect of a bending moment resulting from an increasing load eccentricity due to crack formation. In contrast to the compression simulations, the failure zone is highly localized. Again, the observed failure pattern agrees with realistic experiments found in the literature, compare the summary by *van Mier* [243]. It should be noticed that the macroscopic failure starts by the cracking of one weak beam with a low effective stiffness at the boundary. According to the stress-strain graph in figure 4.7 (a) point ③ represents the stage where the system has completely unloaded. This is the case although still 40 % of the cross section is intact as can be followed from the corresponding picture in figure 4.8. This circumstance can be attributed to the crack induced waves: These waves provide compressive reaction forces at the right side of the specimen below and above of the propagating crack, while on the left side still tensile reaction forces, due to the applied deformation controlled loading procedure are obtained. This results in a cancellation of the vertical stress component in the normalized load-displacement graph.

Shear simulation

A quadratic block consisting of 900 (30 cm × 30 cm) particles was sheared by a constant shear velocity v_s at the top, while the bottom was completely fixed. The height was kept constant in order to resemble the setup of a simple shear test as drawn in figure 4.9 (a). The principal stress directions develop on two crossing diagonals, compressive from the lower left corner to the upper right corner and tensile on the perpendicular direction. Since beam rupture is possible only in tension cracks appear mostly in the second direction. The graphical output of the simulation program at the final stage is plotted in figure 4.9 (b). More details on this simulation like normalized load-displacement diagrams, failure evolution etc. can be found in *D'Addetta et al.* [51, 52].
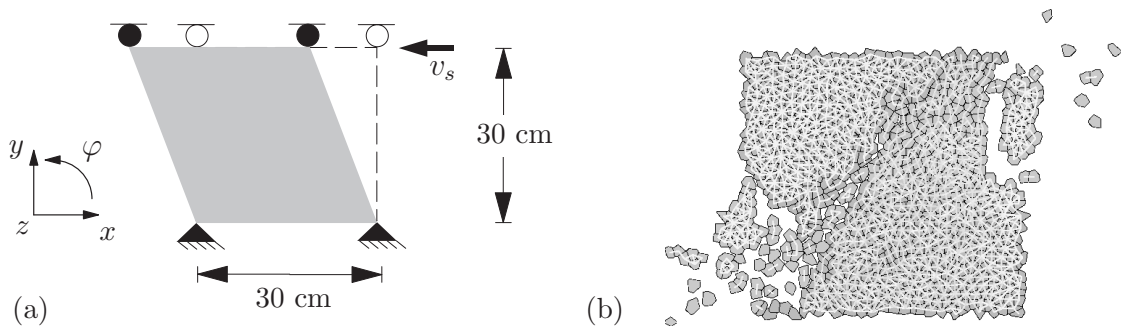
Figure 4.9: Simple shear test: (a) Simulation setup and (b) graphical output at final stage.
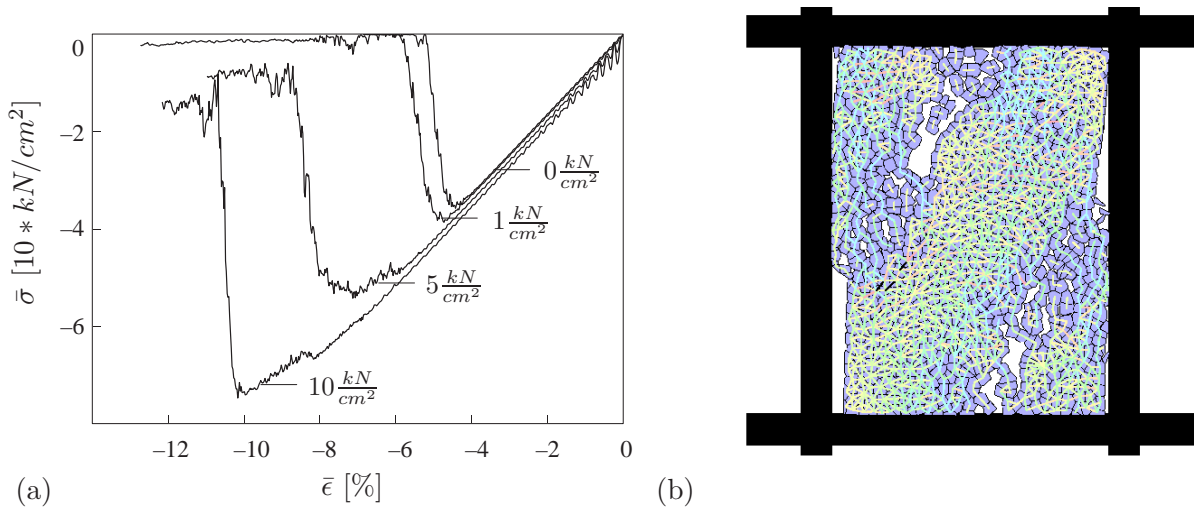
Figure 4.10: Biaxial test: (a) Stress-strain diagram with different lateral pressures p and (b) simulation output in the post-peak regime for $p = 1\,kN/cm^2$.

4.5.2 Practice relevant tests

Biaxial simulation

The specimen shown in figure 4.5 consisting of approximately 1000 particles was used for a Hambly-type biaxial simulation already introduced in section 3.6.1. The loading was applied in a strain controlled manner in the vertical direction, while a uniform pressure on the side walls provided for the lateral loading. Again, a background friction term according to *Luding & Herrmann* [156], see also section 3.6.1, is included in the stress-controlled motion of the two side walls. Four different lateral pressures $p_{const} = 0, 1, 5$ and $10\,kN/cm^2$ have been investigated leading to the stress-strain relations shown in figure 4.10 (a). The vertical stress is drawn over the vertical deformation of the sample. With increasing pressure p_{const} a higher peak stress and corresponding larger deformations are obtained. After a linear increase of the stress a sharp drop determines the macroscopic failure of the material which is similar to the behavior of the compression simulations indicated earlier. For higher lateral pressures $p_{const} = 5$ and $10\,kN/cm^2$ a plateau for the stresses is reached. This observation agrees qualitatively well with geotechnical experiments with cohesive soils. For the case $p_{const} = 1\,kN/cm^2$ the output of the simulation program in the post-peak regime is indicated in figure 4.10 (b). Similar as in the case of the dense non-cohesive sample simulated in section 3.6.1, two parallel shear zones evolve which represent the macroscopic failure mechanism of the specimen. This basic failure feature does not change with increasing lateral pressure p, if an identical particle sample is used. The only observable change is a faster horizontal compaction of the specimen within the post-peak regime.

Brazilian test simulation

In a Brazilian test setup a cylindrical specimen is loaded along a diametral plane, see figure 4.11 (a). This test setup is typically used for the indirect calculation of the tensile strength of a material. Indeed, direct calculations of the tensile strength of e. g. cohesive geomaterials like concrete are difficult to handle experimentally. This is due to the fact
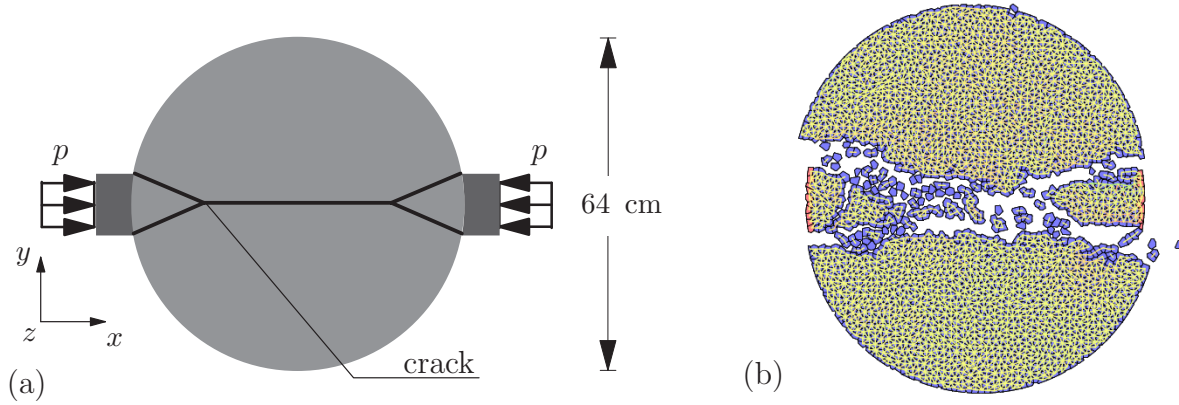
Figure 4.11: Brazilian test: (a) Simulation setup and (b) final stage of simulation.

that samples tend to fail at the bearing of the load apparatus, when loaded as described in the previous section. The test sample consists of approximately 3200 particles with a diameter of 64 cm, i. e. 64 particles in the diametral plane. The circular sample is loaded in a strain driven format by pushing 10 boundary particles (ca. 3.5 % of the circle perimeter) horizontally inwards on the left and right side. Depending on the width of the bearing strip, the load application (radially inward or horizontal), the constraint effect of the bearing strip in vertical direction (effect of friction) and the ratio E^b/E^p, different kinds of failure evolutions are obtained, both, in simulations and in experiments, compare the observations by *Castro et al.* [32] or *Rocco et al.* [208]. Based on their experimental knowledge, a failure evolution dominated by tensile splitting in a zone of finite width in the horizontal section of the sample is expected. Thus, the output of the simulation in figure 4.11 (b) agrees qualitatively well with the experimental observations. Alternative simulations with a varying bearing width and using only a half circle also confirm the experimental results, see e. g. *Nante* [184]. The same parameters as used in section 4.5.1 have been applied, except $E^b = 50$ kN/cm^2.

Notched tension simulation

Typically, in laboratories no tension simulation as discussed in section 4.5.1 are encountered. In order to confine crack growth to a known location and to control the placement of strain gauges, e. g. linear variable displacement transducer (LVDTs), test specimens are notched. Notches restrict the number of possibilities where a crack may nucleate and influence the global fracture behavior, but this is exactly what the experimentalist wants. Simulations with a 40 cm × 64 cm specimen composed of 2560 particles and a notch width of 3 cm are carried out. The notch is positioned in the middle of the right border of the specimen, as shown in the initial stage of the simulation in figure 4.12 (a). The same loading procedure as for the case of the unnotched specimen in the previous section is used. The horizontal crack seen in the final stage of the simulation in figure 4.12 (b) starts from the notch and spreads through the specimen from the right to the left. Again, due to the load eccentricity in the partially cracked intermediate situations a larger fragment develops at the left boundary and breaks apart.
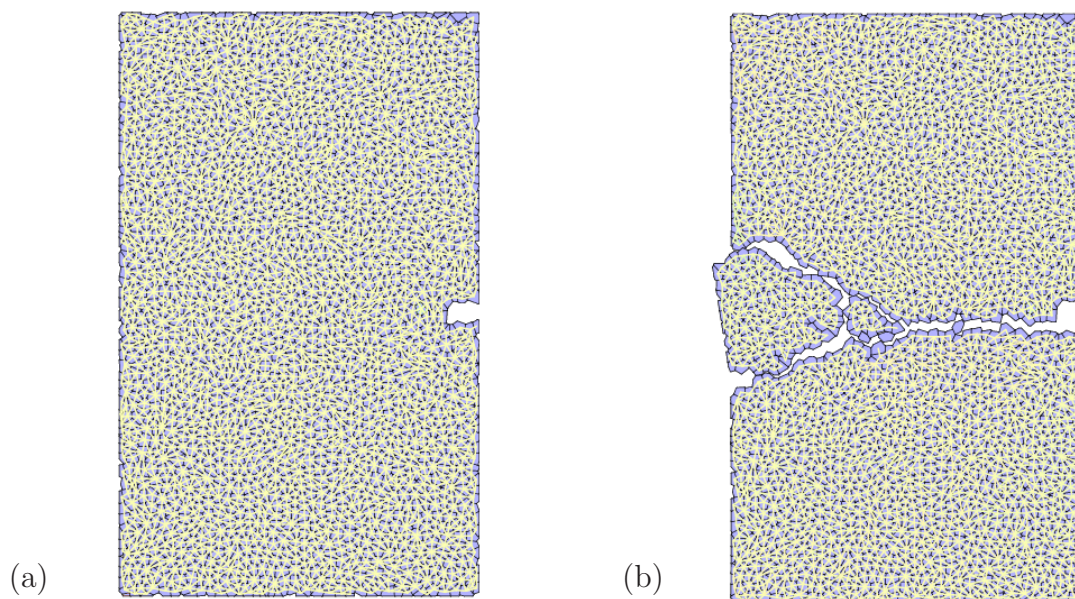
Figure 4.12: Failure evolution of notched tension simulation.

L-shape simulation

Finally, a L-shaped specimen is simulated. This setup was experimentally investigated in its original form at the University of Innsbruck, Austria in the context of a benchmark series in the late 1990's. A description of the experimental results as well as a detailed documentation of the load setup can be found in the thesis of *Winkler* [261]. The specimen is completely fixed at the bottom and vertically loaded at the right boundary. In the original experimental setup the vertical load is applied through an elevator mechanism inducing a displacement at point Ⓐ. The load setup is slightly adopted here in order to accommodate to the specific model characteristics. Hence, a loading procedure as typically applied in the context of FEM modeling is implemented, see e. g. *Kuhl* [137] or *Menrath* [167]: All boundary particles positioned at the right edge of the specimen are vertically loaded in a deformation controlled manner. These particles are free to move in
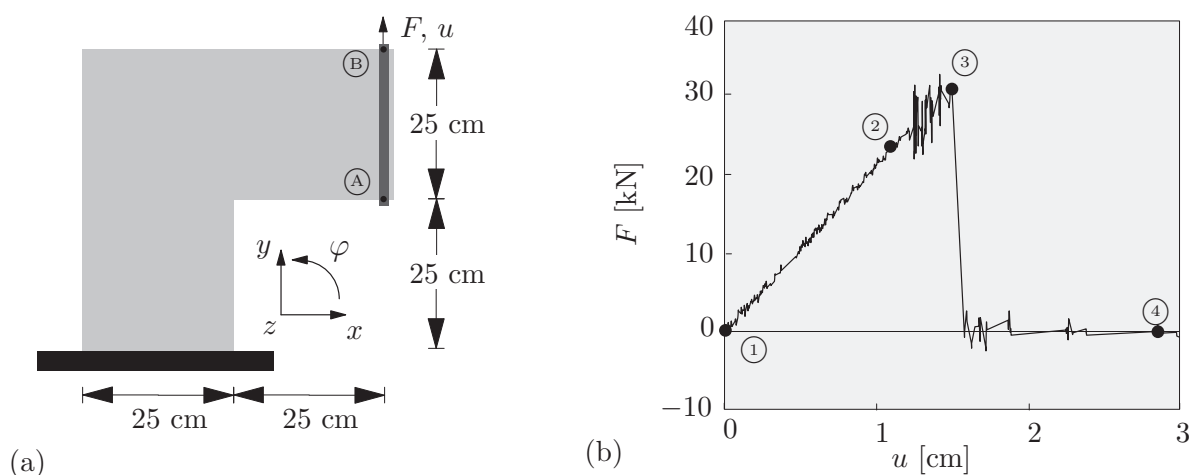
Figure 4.13: L-shape test: (a) Simulation setup and (b) load-displacement diagram.

the horizontal direction. The displacement is uniformly applied along the line between points Ⓐ and Ⓑ. The complete setup is shown in figure 4.13 (a). Starting from an initially 50 cm × 50 cm quadratic specimen, via an exclusion of the lower right quadrant one ends up with the sample shown in figure 4.14, composed of approximately 1900 particles. The vertical displacement u of a particle in the upper right corner of the specimen is controlled and drawn together with the cumulative reaction forces F of the boundary particles at the right edge. The load-displacement diagram is shown in figure 4.13 (b). The output of the simulation program in figure 4.14 displays the failure of the sample. The crack initiates at the inlying edge (stage ②), progresses with a small inclination (stage ③) and then propagates horizontally through the specimen (stage ④). The corresponding stages are also specified in the diagram in figure 4.13 (b). Between stages ③ and ④ the reaction force F drops down and the visible crack is arrested, as all beams on the left side of the specimen are compressed and, thus, cannot break. In consequence, up to stage ④ the deformation increases without carrying any load. At stage ④ the complete separation of the specimen into two pieces is achieved by a further increase of the vertical deformation of the upper part of the specimen. The simulation results fit the experiments by *Winkler* [261] qualitatively very well. After crack initiation in diagonal direction the crack propagates nearly horizontally through the sample. This behavior is also observed in most experiment sets tested by *Winkler* [261].
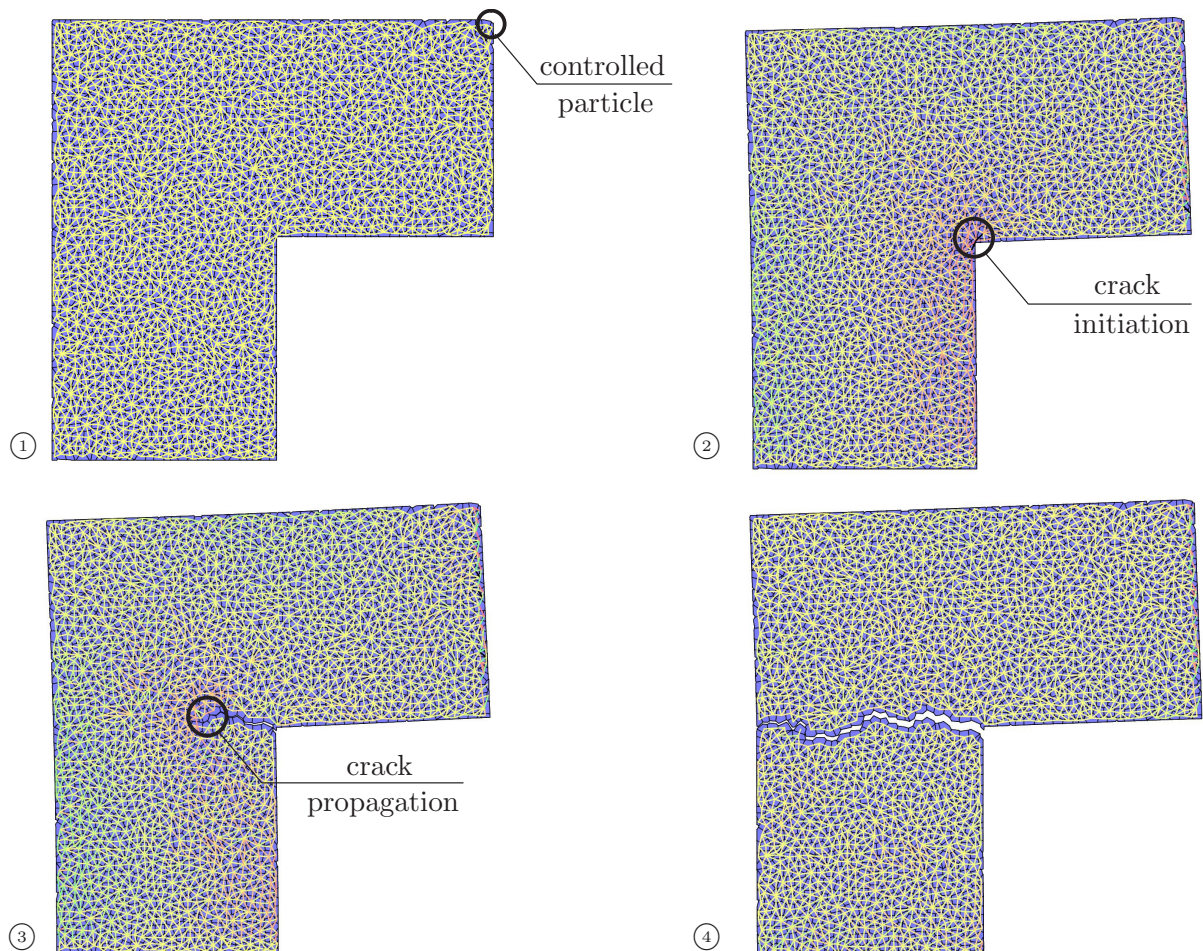
Figure 4.14: Failure evolution of L-shape simulation.

Chapter 5

Modeling of cohesion via interfaces

5.1 General

Since the expectable simulation response in terms of a stress-strain diagram is too brittle by use of the beam enhanced DEM model, no parameter identification has been carried out in the previous chapter. The focus has been laid on the reproduction of typical failure mechanisms of cohesive geomaterials rather than on a quantification of the model. Note that a physical motivation of the corresponding beam parameters is debatable, since the beam forces are created at the mass centers of the particles instead of the particle edges. Therefore, an alternative approach, borrowed from FE-technology, is adopted to represent the cohesion between particles in a DEM model. It makes use of so-called interface elements that are directly defined at the particle edges. Apparently, this approach pictures the real physics involved in the debonding process of bonded granulates far better than the previous one.

Generally, macroscopic constitutive models are assumed to be deducible from simpler models and mechanisms on a smaller scale, i. e. starting from a very simplistic initial point, a more complex behavior on a higher scale may be obtained. As stated in the previous chapter, following the lines of *Cauchy* and *Poisson* various scientists were able to motivate macroscopic models by atomistic ideas, e. g. crystal reorganization led to corresponding plasticity models. For the particle model presented so far this was not the case, since the softening mechanisms on the macro scale cannot be reproduced by a simulation with this beam enhanced DEM model using the breaking criterion according to equation (4.3). Therefore, the model is made more complex: Instead of simple elastic beams with an oversimplified brittle failure law, more elaborate interface elements with a rheological law on the basis of the plasticity theory are used. The motivation to use this constitutive law in the context of the DEM follows the principle that a proven and established macroscopic material law may be at least so successful in modeling the failure on a smaller scale as in a continuum model.

A variety of models for the representation of the interaction between the constituents of two- and more-phase particle composites via interface elements have been proposed since the late 1960's. The works by *Goodman et al.* [93] and *Ngo & Scordelis* [186] have been pioneering as they were among the first ones to introduce discontinuities into numerical models in the context of the FEM: continuous interface elements and lumped or point interface elements. On the one hand, lumped interface elements evaluate a force-relative displacement constitutive relation at a nodal point. Insofar, to a certain extent they exert a similar behavior as simple springs. No further assumptions with regard to tractions and relative displacement distributions across the interfaces are made. On the other hand, the formulation of continuous interface elements (line, plane or shell type) implies a continuous relative displacement field and a traction-relative displacement constitutive

relation. A detailed comparison of lumped and continuous interface elements can be found in *Rots* [210]. Following these lines interface elements have been the focus of intensive studies in the context of FEM. For example, they have been used for the modeling of discrete fracture in form of a standard FE mesh by *Camacho & Ortiz* [28], *Rots* [210], *Xu & Needleman* [263] or in form of a two-phase composite mesh by *Stankowski* [227] or more recently by *Carol et al.* [30]. Furthermore, this family of elements has been applied for the simulation of the bond-slip behavior in composite constructions, see e. g. *Menrath* [167], as well as for the delamination of layered materials as proposed e. g. by *Schellekens* [214].

5.2 Basic idea

Similar to the procedure for the beam elements, an interface layer that represents the bond between adjacent particles is introduced. This interface layer can be regarded as infinitely thin in the initial stage, as schematically depicted in figure 5.1 (a). Since the particles are undeformable by definition, use is made of the key assumption that the deformation of the interface is constrained to be linear. In analogy to the previously introduced beam model this fact represents the Bernoulli-hypothesis of a planar cross-section to some extent. The interface can be discretized and is represented in a lumped sense by a fixed number of normal and tangential spring sets with stiffnesses k_n and k_t. These springs are attached along the common edge of two initially bonded particles i and j, as shown in figure 5.2 (a). The current location of start and end points of the springs relative to the bond are initially fixed and evaluated after each time step. It is important to note that the interface shown in figure 5.2 (a) has a visible initial thickness for visualization reasons only. Ongoing relative motion of the particles leads to a finite value of relative deformation for each spring, i. e. overlapping of particles and, thus, contraction of springs (negative relative deformation) is also allowed. The relative deformation of the bonds is represented by the extension and contraction of the springs, as indicated in figure 5.2 (b). As further assumption the numerical integration of the constitutive law over the integration points of the bond (spring sets) yields an approximated stepwise constant stress distribution over the edge, see the schematic figure 5.1 (b). This procedure compares to the computation of stress resultants in beams. The constitutive law used throughout this chapter is a non-associated Mohr-Coulomb type softening plasticity model defined by two yield surfaces according to *Vonk* [255] and is discussed in more detail in section 5.3. A failure, or more precisely detachment, of the bonds is achieved, if all integration points
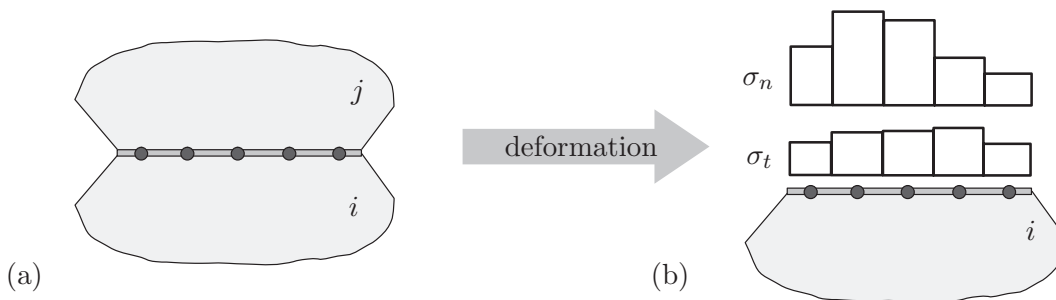
Figure 5.1: (a) Schematic picture of interface and (b) resulting stress distribution.
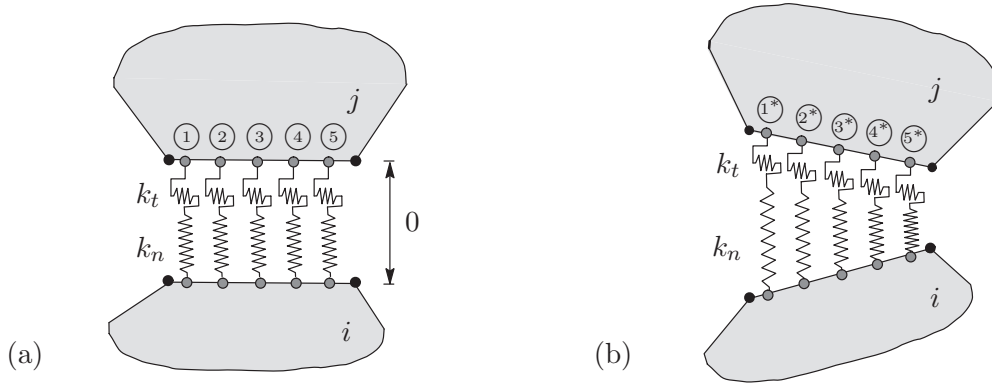
Figure 5.2: Idealization of interface in (a) undeformed stage and in (b) deformed stage.

of the interface layer are completely softened. It should be kept in mind that comparable to the beam enhanced DEM model no extra contact force according to equation (3.1) is created, as long as a bond between two particles exists. This means that once the bond is completely detached, a "standard contact" according to section 3.4.1 is assumed to control the interaction between two particles. The forces evaluated in the integration points can be combined to a bond force vector and transferred to the mass centers of the involved particles, thus, giving rise to a moment. The bond force vector then takes the form $\mathbf{f}^{bond} = [f_x^{bond} \quad f_y^{bond} \quad m^{bond}]^T$ and enters the equation of motion. Therefore, the interaction force vector in equation (3.4) is reformulated

$$\mathbf{f}_i = \sum_{j=1}^{n_p} \mathbf{f}_{ij}^p + \sum_{k=1}^{n_{bond}} \mathbf{f}_{ik}^{bond} \,. \tag{5.1}$$

Additionally to n_p, noting the number of particle contacts of a particle i, n_{bond} denotes the overall number of existing bonds of a particle i. Most of the program infrastructure of the beam enhanced DEM model introduced in chapter 4 remains unchanged, unless routines concerning the bond determination, bond deformation and plasticity evaluation.

5.3 Mohr-Coulomb plasticity model

The principal ingredients of a plasticity formulation are the yield condition, the flow rule and the hardening law (if needed), compare *Jirásek & Bažant* [124], *Lemaitre & Chaboche* [147] or *Simo & Hughes* [224]. In the present context the basic idea of a strain-driven formulation from classical plasticity is straightforwardly transferred to a "relative displacement-driven" formulation. The actual state of the spring set is determined by the total relative displacement $\mathbf{u}$, the plastic relative displacement $\mathbf{u}^p$ and the softening variable κ. Here, the range of validity is restricted to small strains and, following the above logic, small relative displacements. Hence, an additive elastic-plastic split of the relative deformation $\mathbf{u}$ of one spring set is admissible

$$\mathbf{u} = \mathbf{u}^e + \mathbf{u}^p \qquad \text{with} \qquad \mathbf{u} = \begin{bmatrix} u_n \\ u_t \end{bmatrix}. \tag{5.2}$$

The stress-relative deformation law for the elastic part yields

$$\boldsymbol{\sigma}^{tr} = \boldsymbol{\sigma}^0 + \mathbf{K}^{bond} \cdot \mathbf{u} \qquad \text{with} \qquad \mathbf{K}^{bond} = \begin{bmatrix} k_n & 0 \\ 0 & k_t \end{bmatrix}, \tag{5.3}$$

where $\boldsymbol{\sigma}^{tr}$ is the trial stress state, that may lie outside the flow surface $f(\boldsymbol{\sigma}) = 0$. k_n and k_t represent the normal and tangential spring stiffnesses. The flow rule is denoted by

$$\dot{\mathbf{u}}^p = \dot{\lambda}\,\mathbf{g}(\boldsymbol{\sigma}, \kappa) \tag{5.4}$$

with the plastic multiplier $\dot{\lambda}$. $\mathbf{g}(\boldsymbol{\sigma}, \kappa)$ represents the direction of the plastic flow and depends upon the fact whether an associated or non-associated flow rule is included. Since associated flow rules for pressure-sensitive materials like geomaterials are often unrealistic a non-associated one is used, i. e. the direction of plastic flow is prescribed by the gradient of the plastic potential g in the form $\mathbf{g}(\boldsymbol{\sigma}, \kappa) = \partial g/\partial \boldsymbol{\sigma}$. Differentiation with respect to time is denoted by a dot over a symbol. However, the time does not play any role in the rate-independent form of plasticity introduced here, but is used as formal parameter controlling the loading process. In general, plastic flow occurs if the yield function $f(\boldsymbol{\sigma}, \kappa)$ and its derivative both vanish: $f = 0$ and $\dot{f} = 0$. The consistency condition $\dot{f} = 0$ then yields

$$\left[\frac{\partial f}{\partial \boldsymbol{\sigma}}\right] \dot{\boldsymbol{\sigma}} - h\dot{\lambda} = 0 \qquad \text{with} \qquad h = -\left[\frac{\partial f}{\partial \kappa}\right]\left[\frac{\partial \kappa}{\partial \mathbf{u}^p}\right] \cdot \left[\frac{\partial g}{\partial \boldsymbol{\sigma}}\right], \tag{5.5}$$

where h expresses the hardening parameter. Further elaboration, including a combination of equations (5.2) to (5.5) results in a relation between stress and relative displacement rates and, finally, in the corrected stress state $\boldsymbol{\sigma}$ along with the plastic multiplier $\dot{\lambda}$

$$\boldsymbol{\sigma} = \boldsymbol{\sigma}^{tr} - \underbrace{\frac{f(\boldsymbol{\sigma}^{tr}, \kappa)}{-\left[\dfrac{\partial f}{\partial \kappa}\right]\left[\dfrac{\partial \kappa}{\partial \mathbf{u}^p}\right] \cdot \left[\dfrac{\partial g}{\partial \boldsymbol{\sigma}}\right] + \left[\dfrac{\partial f}{\partial \boldsymbol{\sigma}}\right] \cdot \mathbf{K}^{bond} \cdot \left[\dfrac{\partial g}{\partial \boldsymbol{\sigma}}\right]}}_{\dot{\lambda}} \mathbf{K}^{bond} \cdot \left[\frac{\partial g}{\partial \boldsymbol{\sigma}}\right]. \tag{5.6}$$

The procedure in equation (5.6) operates as a one-step return mapping algorithm, so that no iteration is needed. However, a simple one-step algorithm that yields an explicit solution for the corrected stress state is only possible if linear yield surfaces, linear plastic potentials and linear softening evolution laws are chosen. The bracket terms in equation (5.6) are either of scalar or vectorial order and are listed in appendix C.

The initial behavior of the spring sets is assumed to be linear elastic and to depend on the spring constants k_n and k_t. Therefore, no coupling of the springs in the elastic regime is assumed. The softening of a spring set starts when the stress state $\boldsymbol{\sigma} = [\sigma_n \ \sigma_t]^T$ reaches the yield surface that in the present context could be viewed as a failure surface. The initial failure surface in the biaxial stress plane is given in figure 5.3 (a) by graph ① and is symmetric with respect to the normal stress. Since the failure mechanisms dominated by shear and tension differ substantially in geomaterials, it is advisable to model them separately. This implies the bounding of the elastic domain by two distinct failure surfaces, usually termed two- or in the general case multi-surface plasticity. Indeed, this does not substantially change the treatment presented above for one single surface, except the singularities in the failure surface at the segue of different failure surface segments, i. e. a
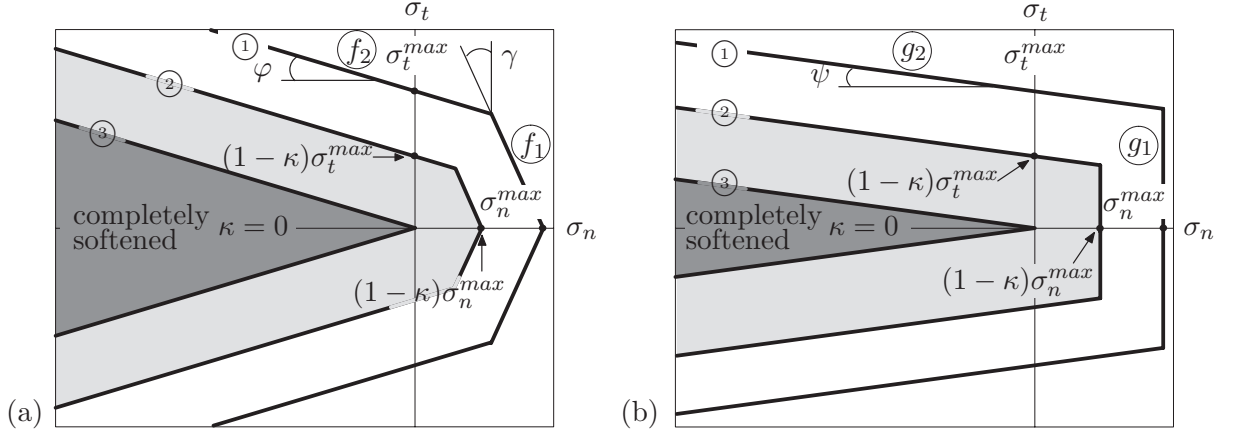
Figure 5.3: (a) Failure surface and (b) plastic potential of interface constitutive law in biaxial stress plane.

unique flow direction cannot be specified. The solution of this problem has been treated by *Koiter* [127] or *de Borst* [57, 58], cf. the detailed derivation in appendix C. In short, in analogy to equation (5.4) the flow rule

$$\dot{\mathbf{u}}^p = \dot{\lambda}_1 \frac{\partial g_1}{\partial \boldsymbol{\sigma}} + \dot{\lambda}_2 \frac{\partial g_2}{\partial \boldsymbol{\sigma}} \tag{5.7}$$

is adapted to capture the flow directions defined by the two plastic potentials along with the essential constraints $\dot{\lambda}_1 \geq 0$ and $\dot{\lambda}_2 \geq 0$.

In the present case the failure surface resembles a two-surface Mohr-Coulomb type plasticity criterion. The tensile failure is governed by a normal stress $\sigma_n^{max} > 0$ and an angle γ which define the yield surface f_1. Whereas the shear failure is controlled by a classical Mohr-Coulomb failure envelope with tangential stress $\sigma_t^{max} > 0$ and friction angle $\varphi > 0$ which define the yield surface f_2. In the compressive regime (for negative σ_n) the trapezoidal or triangle (in the final state) formed by the flow surfaces is open, as no failure is possible in pure compression. With ongoing softening the failure surface shrinks to an intermediate stage (②️ in figure 5.3 (a)) and ends up on the classical Mohr-Coulomb failure surface without any cohesion $\sigma_t = 0$ and tension limit $\sigma_n = 0$, expressed by ③️ in figure 5.3 (a). The functional representation of the failure surfaces is given by

$$f_1 = \sigma_n + \sigma_t \tan \gamma - (1-\kappa)\sigma_n^{max} \leq 0, \qquad f_2 = \sigma_n \tan \varphi + \sigma_t - (1-\kappa)\sigma_t^{max} \leq 0. \tag{5.8}$$

In order to describe a non-associated plasticity along the lines of the two-surface formulation, two plastic potential surfaces are introduced:

$$g_1 = \sigma_n - (1-\kappa)\sigma_n^{max} = 0, \qquad g_2 = \sigma_n \tan \psi + \sigma_t - (1-\kappa)\sigma_t^{max} = 0. \tag{5.9}$$

The plastic potential surfaces are also symmetric with respect to the normal stress, as visualized in figure 5.3 (b). Figure 5.4 represents the one-step return mapping algorithm based on equation (5.6) in more detail for the following three different cases: Yield surface f_1 active (case ⓐ), yield surface f_2 active (case ⓑ) and combined activation of yield surfaces f_1 & f_2 (case ⓒ). Starting from an elastic stress state $\boldsymbol{\sigma}^0$, an elastic predictor step yields a non valid trial stress state outside of the yield surface $\boldsymbol{\sigma}^{tr}$. The following
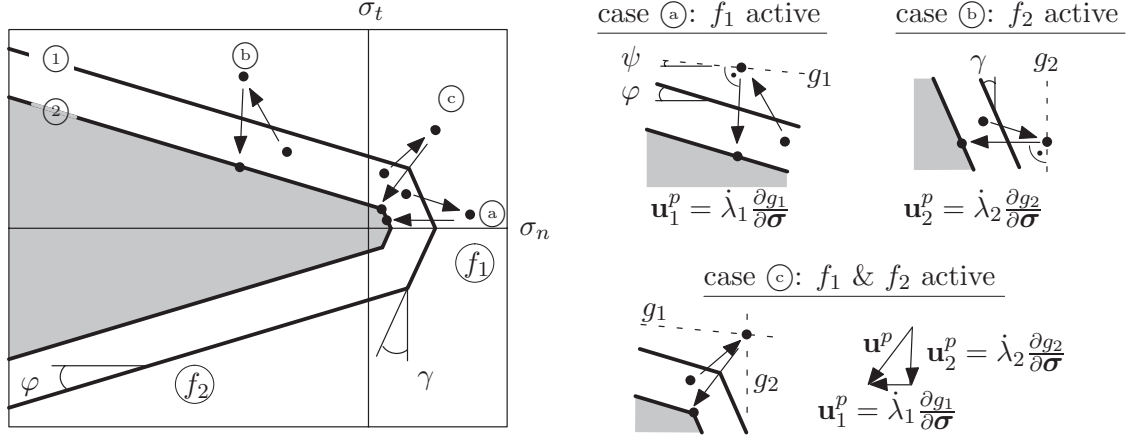
Figure 5.4: Representation of return mapping algorithm.

plastic corrector step towards the yield surface in direction perpendicular to the plastic potential results in a valid stress state on the yield surface $\boldsymbol{\sigma}$. As explained above, the special case of a projection in the influence area of the corner (case ©) is treated by a linear combination of both directions and is outlined in more detail in appendix C. Graph ① in figure 5.4 denotes the yield surface at the start of the step and graph ② that one at the end of the step. The representation includes a shrinking of the yield surface from ① to ② due to softening.

The softening of the spring set is described by the parameter κ which represents the actual state of damage: κ ranges from 0 in the undamaged state to 1 in the fully damaged state. The softening behavior is driven by the plastic deformation u_n^p and u_t^p of the spring sets in form of predefined fracture energies $G_{f,n}$ and $G_{f,t}$. In the case of a two-surface plasticity this involves two different softening evolutions for tension and shear either, see figure 5.5 (a) and (b). Pure tensile softening ends after a fracture energy $G_{f,n}$ has been released and pure shear softening ends after a fracture energy $G_{f,t}$ has been released. In the decoupled case, if only one mechanism is active, the softening variable for the tensile and shear loading is defined by

$$\kappa = \frac{1}{u_n^{max} - u_n^*}u_n^p\,, \qquad\qquad \kappa = \frac{1}{u_t^{max} - u_t^*}u_t^p\,, \qquad (5.10)$$

with $u_n^* = \sigma_n^{max}/k_n$ and $u_t^* = \sigma_t^{max}/k_t$, see figure 5.5. The plastic part of the deformation starts at u_n^* and u_t^*. These evolutions are coupled in that, both tensile strength σ_n^{max} and cohesion σ_t^{max} decrease at the same time and at the same rate. This yields an isotropic shrinkage of the failure surfaces, as shown in figure 5.3 (a). A simultaneous tensile and shear softening is treated as linear combination of both, as depicted in figure 5.5 (c). Therefore, the definitions in equation (5.10) are formally coupled

$$\kappa = \frac{1}{u_n^{max} - u_n^*}u_n^p + \frac{1}{u_t^{max} - u_t^*}u_t^p \le 1\,. \qquad (5.11)$$

By definition, in combined softening u_n^p is solely determined by the plastic deformation due to tensile loading (surface 1 - f_1 & g_1) and not by the normal part of the plastic shear deformation. For this reason, the dilatant behavior with shear loading does not
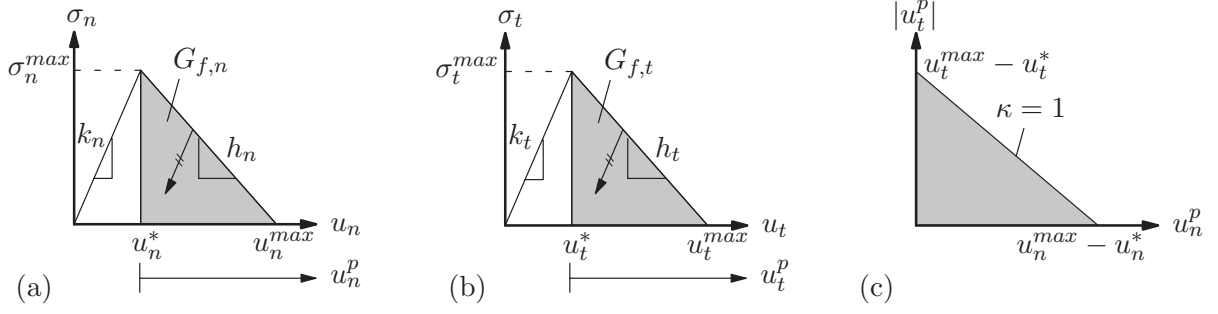
Figure 5.5: (a) Evolution law for tensile, (b) shear and (c) combined softening.

influence the softening since it is physically not justified in combined softening. The predefined fracture energies for mode I and II softening enter the above equations through the integral expression of the graphs in figure 5.5 (a) and (b). This formalism may be interpreted in the sense of the cohesive crack concept of *Hillerborg et al.* [111], see also the book by *Bažant & Planas* [17]. However, here the crack opening of the *Hillerborg* model is replaced by the components of the plastic relative displacement. The evolution laws of the normal and tangential stresses

$$\sigma_n(u_n^p) = \sigma_n^{max} \left(1 - \frac{u_n^p}{u_n^{max} - u_n^*} \right) , \qquad \sigma_t(u_t^p) = \sigma_t^{max} \left(1 - \frac{u_t^p}{u_t^{max} - u_t^*} \right) , \qquad (5.12)$$

are inserted into the conditional equations of the fracture energies

$$
\begin{aligned}
G_{f,n} &= \int_0^{u_n^{max}-u_n^*} \sigma_n(u_n^p) \, \mathrm{d}u_n^p = \frac{1}{2} \left(u_n^{max} - u_n^* \right) \sigma_n^{max} , \\
G_{f,t} &= \int_0^{u_t^{max}-u_t^*} \sigma_t(u_t^p) \, \mathrm{d}u_t^p = \frac{1}{2} \left(u_t^{max} - u_t^* \right) \sigma_t^{max} .
\end{aligned}
\qquad (5.13)
$$

5.4 Numerical realization

The numerical realization of the interface model combined with the plasticity theory in the context of the DEM model is a straightforward task. However, in the case of the interface enhanced DEM model the numerical expense is by far higher compared to the beam enhanced version of the DEM model. Each spring set is described by the material law and along each common edge a fixed number of spring sets, termed integration points, are chosen. From there, it is important to define a reference edge where the corresponding relative displacement-force law is evaluated. Different possibilities are feasible: One way is the definition of the reference line in between the bonded edges by connecting the midpoints of the deformation vectors of the bond, as shown in figure 5.6 (a), compare also a similar definition of the interface by *Grujicic et al.* [95]. Admittedly, the length of the reference line is generally smaller than the bond width h and induces a more demanding numerical treatment as the alternative approach which is followed here and shown in figure 5.6 (b): One bond is chosen as reference edge and the local coordinate system with the normal vector $\mathbf{n}$ is fixed along this bond. Particle i can be considered as the *master* and the other one
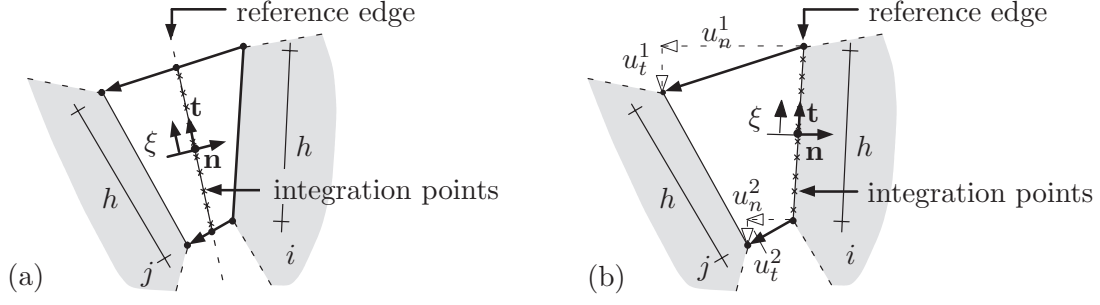
Figure 5.6: Numerical integration - Two different possibilities of definition of reference edge.

as the *slave* particle. By definition the particle with the smaller internal number is chosen as *master* particle. For this case, the relative deformation of the start and end point of the reference edge are split up into a normal and tangential part. The normal and tangential relative deformation distribution between the start and end point of the reference edge are linearly approximated. The actual complete relative deformation **u** is evaluated at each integration point and processed in an incremental format $\Delta\mathbf{u}$ by subtracting the complete relative deformations of two successive time steps. The straightforward implementation of the elastic predictor step for the calculation of the trial stress state in equation (5.3) implies the determination of the spring forces at each integration point k of the bond

$$
\begin{aligned}
p_n^{tr}(\xi) &= \frac{1}{n_{ip}} \left[p_n^{old}(\xi) + k_n \Delta u_n(\xi) \right] , \\
p_t^{tr}(\xi) &= \frac{1}{n_{ip}} \left[p_t^{old}(\xi) + k_t \Delta u_t(\xi) \right] .
\end{aligned}
\tag{5.14}
$$

n_{ip} denotes the number of integration points along the reference edge and is fixed for all polygon's bonds. The position of the integration point k is determined in the local coordinate system by the normalized coordinate ξ ranging from $[-1, 1]$. In order to evaluate the yield conditions $f_{1/2}(\boldsymbol{\sigma}^{tr}(\xi), \kappa^{old}(\xi)) \leq 0$ in equation (5.8) the local stresses at each integration point are computed

$$
\sigma_n^{tr}(\xi) = \frac{p_n^{tr}(\xi)}{h/n_{ip}} , \qquad\qquad \sigma_t^{tr}(\xi) = \frac{p_t^{tr}(\xi)}{h/n_{ip}} .
\tag{5.15}
$$

If the yield surfaces $f_{1/2}$ are left, a plastic corrector step is necessary. Therefore, the type of back projection mode (determination which yield surface/s is/are active) according to figure 5.4 has to be evaluated. Equation (5.6) yields the corrected stress state at the integration point. Afterwards, an a-posteriori check is performed, because it cannot completely be excluded that erroneously a corner regime is predicted, although this is actually not the case. This behavior may appear, as the final position of the yield surface, e. g. curve ② in figure 5.4, is not known a-priori, see *de Borst* [57, 58]. In particular, for stress states in the influence region of the corner a transition from case ⓐ or ⓑ to case ⓒ of figure 5.4 may be encountered during the return mapping algorithm. Thereafter, the corresponding forces at the integration points are calculated via an inversion of equation (5.15). The new forces, the actual relative deformation and the state of softening are saved as history variables for the next time step. All forces along a bond are summed
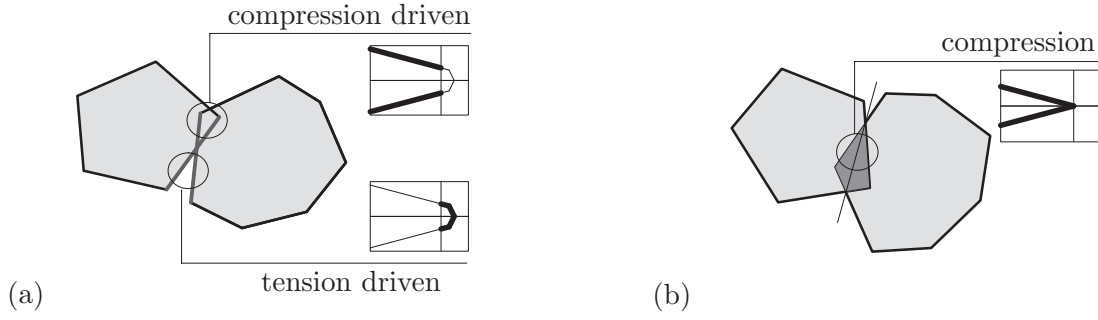
Figure 5.7: Difference between interface and particle contact: (a) Deformed situation (interface activated) and (b) after complete interface failure and re-activation of contact.

up and transferred to the center of the *master* particle giving rise to a moment. A force and moment with the same absolute values are applied to the *slave* particle. An interface is detached or eliminated, if at all integration points of this interface the softening is completed, i. e. $\langle \kappa \rangle = 1$ according to

$$\langle \kappa \rangle = \frac{1}{h} \int_{-1}^{1} \kappa(\xi) \, \mathrm{d}\xi = \frac{1}{n_{ip}} \sum_{k=1}^{n_{ip}} \kappa(\xi_k) \,. \tag{5.16}$$

Since a "healing" of bonds, i. e. a re-introduction of new interfaces, is not modeled, these new contacts are treated using the standard methodology presented in section 3.4.1, compare also the schematic figure 5.7. Then the plasticity law is evaluated in an approximative format on the basis of the overlap area. A detailed chart of the interface plasticity law algorithm for one interface with k integration points is described in figure C.1 in appendix C.

5.5 Numerical results

The DEM model enhanced by interface elements for the representation of cohesion is involved in the simulation of the standard loading setups already presented in the context of the beam enhanced DEM model in chapter 4. The validation of this model was done in a structured fashion: First, the model is validated on the integration point level by very simple tensile, shear and coupled tensile-shear loadings. This has been done independently of the DEM part in order to test only the performance of the interface model. Afterwards, simple loading setups of quadratic particle rows with a thickness of one particle have been simulated in order to examine on a simple basis the performance of the combination of DEM and interface model. Both the integration point and quadratic particle row examples are only briefly discussed here. As these preliminary test programs have been successful, larger samples with variable particle shapes are simulated in uniaxial tension and compression. Finally, the DEM interface model is involved in the simulation of a discrete microstructure, which is presented in the separate chapter 7.

5.5.1 Tensile particle row

The interface model was validated first on the integration point level by a comparison with corresponding results of *Vonk* [254, 255] based on a very similar model as that

used herein and results of *Carol et al.* [30, 31] with a more complex hyperbolic-surface-based plasticity law. The comparison with *Vonk's* [254] very basic results of deformation controlled tension and shear loading using his parameter set provided exactly the same results for all examples presented in his report. The comparison with *Carol* [31] yields also a good agreement in the context of the simple pure tension and shear simulations.

As introductory example the extension of a simple particle row composed of 2, 6, 11 and 21 quadratic particles bonded together by 1, 5, 10 and 20 interfaces is considered. The samples are denoted by ①, ②, ③ and ④, respectively, and are illustrated schematically in figure 5.8 (c). The side length of one particle is 1 cm and the parameters of the plasticity model are as follows: Elastic stiffnesses $k_n = 1000$ kN/cm^2 and $k_t = 250$ kN/cm^2, yield stresses $\sigma_n^{max} = \sigma_t^{max} = 1$ kN/cm^2, shape parameters $\varphi = 26.6°$, $\gamma = 10°$ and $\psi = 0°$ and, finally, the softening parameters $G_{f,n} = G_{f,t} = 0.0495$ kN/cm^2. Thereby, the yield stresses of the interfaces are statistically distributed (based on a uniform distribution) around ± 10 % the average value defined above. The general parameters of the particle model are chosen in analogy to the previous chapters $\rho = 5$ g/cm^3, $\Delta t = 10^{-6}$ s, $\gamma_N = 10^5$, $\gamma_T = 0$, $\mu = 0$ and $E_p = 100$ kN/cm^2. The stresses are measured in the form of a normalized load as the ratio of the reaction force of the boundary particle and the width of one particle. The strain is measured by determination of the ratio of the actual length and the initial length of the row. The corresponding crack width is approximated as the elongation of the row: This is justified in the post-peak regime, as the deformation controlled loading yields the localization in one single interface, namely the weakest one. However, it is an approximation in the elastic regime, as all interfaces are loaded elastically. The weakest interface will start to soften, while the other interfaces will undergo elastic unloading. Thus, the more interfaces are included, the steeper the descent of the corresponding stress-strain curve gets, compare figure 5.8 (a). If only the absolute elongation Δw of the bar is measured, the accompanying stress-deformation curves differ in the pre-peak region, but coincide in the post-peak region, compare figure 5.8 (b). The above mentioned mesh/length dependence of the strain is one of the main reasons why data of tension tests (of experimental as well as simulation nature) is typically displayed by a stress or load vs. crack width diagram in the literature. This is shown in figure 5.8 (b) and further discussed by *Hillerborg et al.* [111] or *van Mier* [243]. Therefore, the results in form
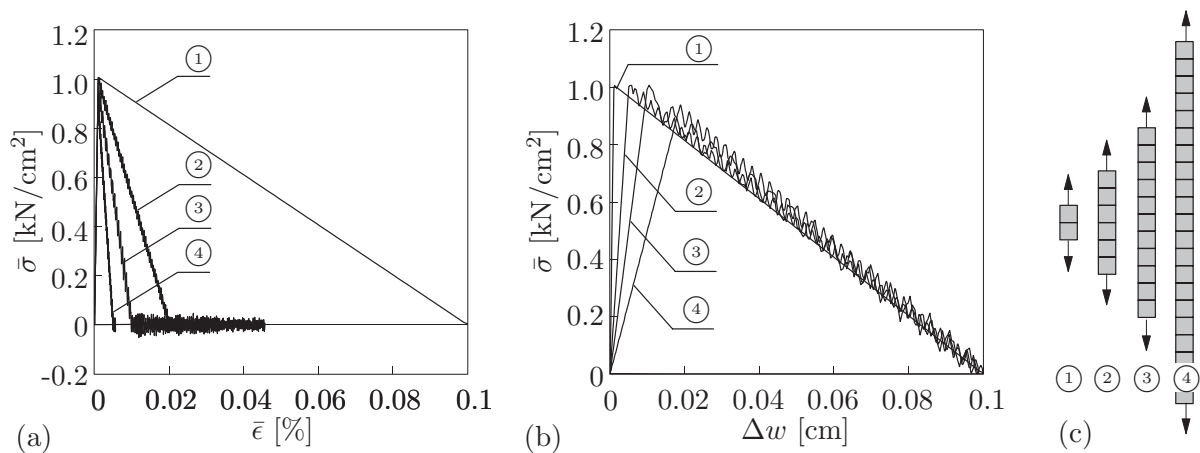
Figure 5.8: Diagrams for simple tension test of particle rows.

of a stress-strain diagram or normalized load-displacement diagram are not objective for tensile tests. However, as will be shown in the next section, the objectivity is preserved for compressive tests. The same problem may be encountered also in continuum models in the context of the FEM and results in mesh-dependent results. This problem is typically solved by introduction of localization limiters, i. e. continuum models that include an internal length scale and yield mesh-independent results, cf. section 2.2.

5.5.2 Standard tests

As mentioned earlier, the parameter identification of the beam failure parameters with respect to a quantification of the load-displacement behavior of geomaterials is not convincing at all. In order to approach the debonding and softening in geomaterials in a physical more coherent way, the interface model for a representation of cohesion was introduced here. The following examples will highlight that the bond description via interfaces is capable to represent the softening not only in very simple tests, as shown before, but also in the context of standard experiments. The softening behavior is investigated by means of a comparative study of rectangular plates with the width 40 cm and a variable height of 10 cm ①, 20 cm ②, 30 cm ③, 40 cm ④, 64 cm ⑤ and 72 cm ⑥. Thus, the amount of included particles ranges from 400 to 2880. The uniaxial tension setup procedure according to section 4.5.1 was followed, compare also the inset in figure 5.9 (b). The parameters and material properties of the model have been chosen in order to obtain results that are as close as possible to experimental results obtained from the literature. However, only limited information on the "real" values of the bond strength and the corresponding softening behavior is available in the literature. Therefore, no attempt was undertaken to fit the material parameters more closely than needed.

Uniaxial tension experiments by *Evans & Marathe* [82] as well as *van Mier* [243] are considered for a quantitative comparison. The normal and tangential stiffness of the interfaces are chosen as $k_n = 1200$ kN/cm^2 and $k_t = 360$ kN/cm^2. Moreover, the density was chosen as $\rho = 2.5$ g/cm^3 and the time step as $\Delta t = 5 \cdot 10^{-7}$ s. The additional parameters in the context of the plasticity model are as noted above, except the maximum
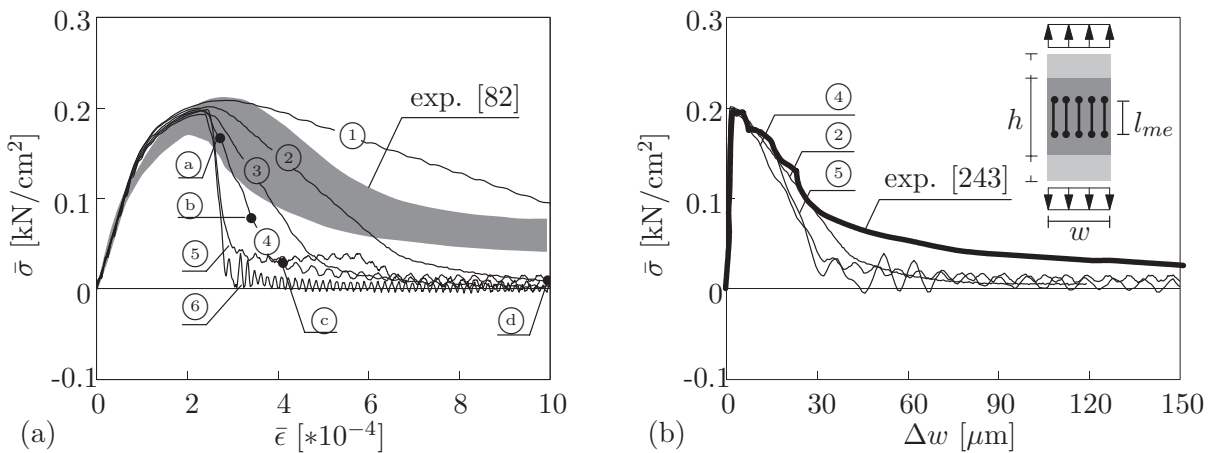
Figure 5.9: (a) Stress-strain and (b) stress-displacement diagram of tension tests.

yield stress $\sigma_n^{max} = \sigma_t^{max} = 0.12$ kN/cm^2 and the softening parameters $G_{f,n} = 5.94 \cdot 10^{-4}$ kN/cm^2 and $G_{f,t} = 2.98 \cdot 10^{-3}$ kN/cm^2. Again, the yield stresses for each interface are statistically distributed around ± 10 % the average value defined above. Parameters of the contact model like those concerning the viscous damping and friction are set to zero ($\gamma_N = 0$, $\gamma_T = 0$, $\mu = 0$) and the contact stiffness to $E_p = 100$ kN/cm^2. The stress-strain relation for the six simulations from ① to ⑥ are plotted in figure 5.9 (a) along with the experimental results by *Evans & Marathe* [82], which are included as a grey shaded band. It becomes clear that the stress-strain relation is a non-objective measure of the softening for tensile tests, compare also the discussion in the context of figure 5.8. But nevertheless, the normalized load-displacement relations in figure 5.9 (a) generally elucidate the transition from a linear relation to a horizontal tangent up to a complete overall softening of the sample.

Next, the axial deformation is evaluated in a comparable format as in experiments by a measuring device of fixed length $l_{me} = 5$ cm for all simulations. This means that not the elongation of the complete specimen, but the extension of a fixed area of the specimen containing the macroscopic crack is evaluated. The extension of this fixed area compares to the crack width Δw, see the inset of figure 5.9 (b). Thus, if a stress-Δw diagram is plotted, all curves coincide and the softening effect is the same regardless of the height of the sample, compare figure 5.9 (b). Moreover, these results have been compared with experimental results in the form of the stress-average-crack opening diagram of a concrete with a maximum aggregate size $d_{max} = 1.6$ cm according to figure 3.49 of *van Mier's* [243] book. The numerical results fit qualitatively as well as quantitatively the experimental ones. However, the height of the tail in the softening region could not completely be recast, as the stress drops below the experimental value in the later simulation stages. Compare the experimental results where still a considerable stress transfer is obtained in the later softening regime. The reason for this is quite conceivable and can be traced back to the maximum size of aggregates contained within a sample. Moreover, following the discussion in *van Mier* [243] and *van Mier et al.* [244] this behavior is an indirect effect of crack face bridging which provides a crack toughening mechanism. In order to enclose the feature of crack face bridging and a corresponding stress transfer even in a later softening stage, one may include a distinct microstructure which for example regards for stiffer aggregates embedded in a less stiffer matrix. This path will be followed in chapter 7. An alternative concept accounts for a higher dispersion (i. e. a higher amount of disorder) of bond stiffness and/or yield stresses.

A cutout of the deformed sample ④ at four different time steps ⓐ, ⓑ, ⓒ and ⓓ in figure 5.10 emphasizes the distinct macroscopic crack opening as well as the evolution of softening. The bonds are represented by a line between the respective particles. The color scale defines the transition from a non-softening stage (light blue) to a fully softened stage just before elimination of the bond (black). The state of softening of the bonds $\langle \kappa \rangle$ in figure 5.10 (b) is computed based on equation (5.16) as the average of the softening of all springs (i. e. integration points) representing this bond. One can see that at stage ⓐ the macroscopic crack has completely formed. However, three interfaces positioned perpendicular to the primary load transfer direction (marked by circles in figure 5.10) sustain the load and yield a non-vanishing stress of curve ④.

Next, uniaxial compression tests of plates with different geometries using the same parameter set as for the tension simulation are carried out. Therefore, the same load setup as discussed in figure 4.4 (a) is applied. Different boundary conditions have been studied:
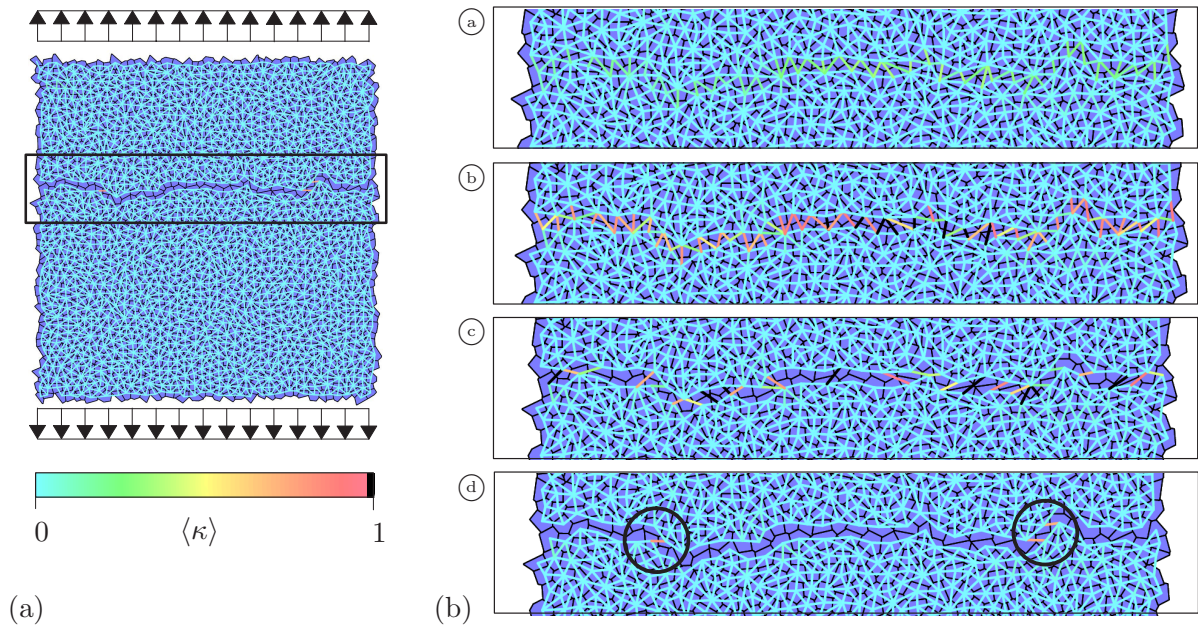
Figure 5.10: Simulation output in the post-peak regime: (a) Final stage ⓓ and (b) detail of macroscopic crack of stages ⓐ to ⓓ.

On the one hand, a restricted boundary representing a situation with very high friction, as if a specimen is loaded by dry platens. On the other hand, a specimen is tested where the particles forming the upper and lower boundary are completely free to move and non restricted, e. g. as if the friction effect is very small like a loading by teflon platens or platens with brushes. In figure 5.11 (a) the stress-strain diagrams of a 40 cm × 40 cm sample with both types of boundary conditions are plotted. The simulation results are roughly confronted with results obtained from uniaxial compression experiments shown in figure 5.11 (b). Note, that in contrast to the tension test shown before, for compression tests the objectivity of the results is preserved. Since the localization is expected not to be restricted to a small band perpendicular to the loading (and measuring) direction
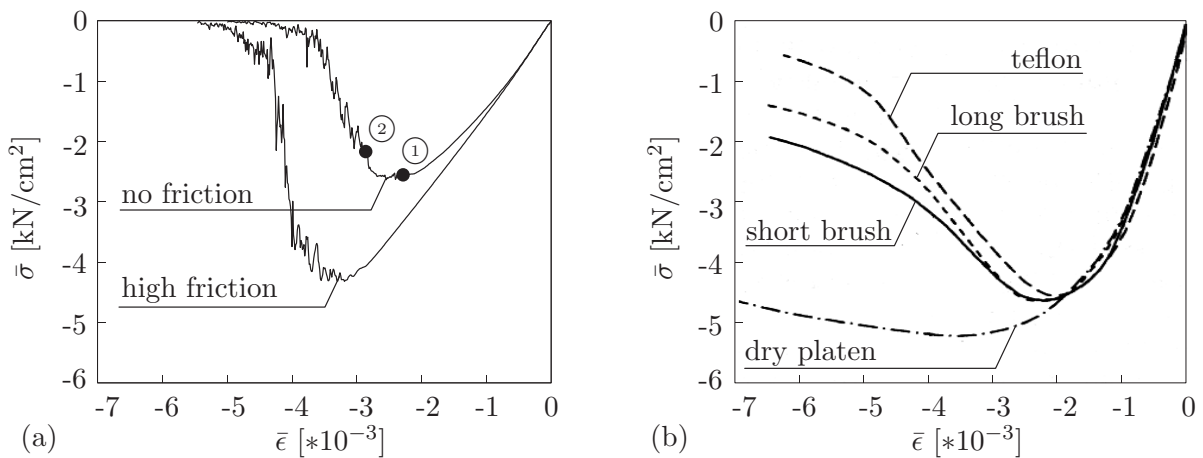
Figure 5.11: (a) Stress-strain diagrams of simulations and (b) experiments by *Vonk* [253].

as in the tension test, no mesh-dependent results in terms of the stress-strain relation
are expected. The different curves in figure 5.11 (b) represent the stress-strain relations
under consideration of different boundary conditions (teflon, long and short brushes and
dry platens) of cubic concrete specimens with a side length of 10 cm. The experiments
have been carried out by *Vonk* [253], compare also *Vonk* [255] or *van Mier* [243]. As
the parameters of the interface enhanced DEM model, in particular the stiffnesses, have
been fitted to a calibration of the tension experiments by *Evans & Marathe* [82], the
simulation results in compression are not fully comparable to the experimental ones. A
comparison of the corresponding curves in figures 5.11 (a) and (b) clearly shows that the
macroscopic elastic stiffnesses of the simulation are smaller by a factor of two compared
to the experimental one. This is due to the fact that the concrete used in the experi-
ments by *Vonk* [253] is stiffer than that used by *Evans & Marathe* [82]. Certainly, the
simulation parameters can be fit to *Vonk's* experiment, too. The measured peak loads fit
quantitatively well. The most apparent difference concerns the post-peak behavior: The
post-peak behavior is not so pronounced as in the case of the tension simulations. The
main reason for this lies in the fact that mostly the interfaces perpendicular to the load
direction soften, while those interfaces oriented in direction of the load do not soften, as
they are in a high compression regime. The stress state of these interfaces lies at the left
(open) end of the Mohr-Coulomb failure surface in figure 5.3 (a). Finally, an increasing
shear load on the corresponding interfaces results in a sudden failure after time stage ②.
Again, the inclusion of a microstructure is conceivable as a possible way out and may
provide for the required complexity to display a more distinct post-peak behavior in the
context of the stress-strain relation. The failure evolution of the unrestricted compression
simulation is visualized by means of the output at time stages ① and ② in figure 5.12.
Once again, the bonds between the particles are represented by a line between them.
Time stage ① refers to a situation just before the peak and stage ② to a situation after
formation of a failure pattern. The gradual development of the inclined localization zones,
as shown in figure 5.12 (b) has started long before the peak value is reached and yields

(a)   stage ①   (b)   stage ②
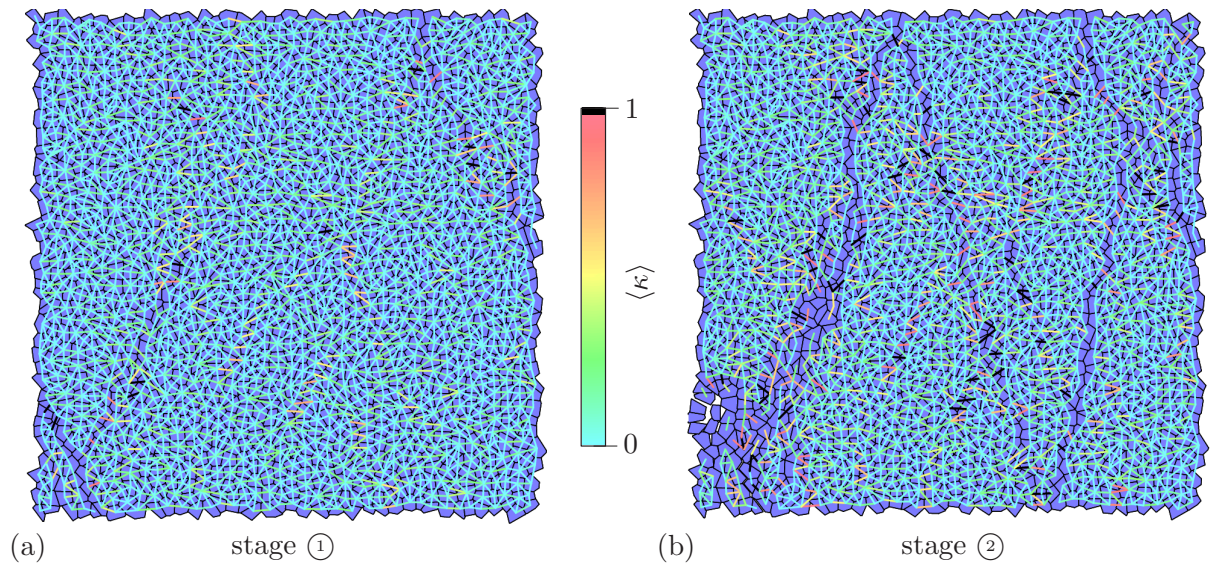
Figure 5.12: Failure evolution of compression simulation.

a sudden breakdown of the particle composite. This result agrees quite well with the experimental results on the cubical specimens by *Vonk* [253, 255]. The simulation output of the restricted sample resembles the same hourglass failure mode as presented for the case of the beam enhanced DEM model in chapter 4, compare figure 4.5 (a).

Note that the additional complexity of the bond description compared to the beam one is accompanied by a higher sensitivity of the parameter choice with respect to the post-peak failure. This implies that the more or less "controlled" failure in compression as obtained with the beam enhanced DEM model, e. g. compare figure 4.5, is not reproducible with the interface enhanced DEM model in the present form. For example, a continuation of the loading after formation of a failure pattern like that presented in figure 5.12 yields a complete disintegration of the initially bonded particle assembly. Thus, no conical rest pieces as in the experiments, e. g. in the form of fragments composed by bonded particles, remain after complete cracking. In the context of this destabilizing effect the following two points are worth to be further investigated: First, the formulation of the interface model has to be enhanced. For example an inclusion of a physical coherent damping or comparable stabilizing contribution to the interface forces may provide for a stable simulation path in the later post-peak regime. Furthermore, a second, probable reason for the found behavior is the missing rotational resistance of two bonded granulates in the interface enhanced model compared to a consideration of it in the beam enhanced model. There, the rotational resistance is considered via the corresponding stiffness entry in the Timoshenko stiffness matrix in equation (4.1) and the corresponding breaking parameter ϕ_{max}^b in equation (4.3). In an enhanced version of the interface model the concept of rotational resistance may be included by additionally incorporating rotational springs between the centers of gravity of bonded granulates. Experimental and numerical evidence on the persistent effect of rotational resistance has been reported in *Iwashita & Oda* [121, 122] and *Oda & Kazama* [192]. The inherent effect of the rotational resistance in the beam enhanced model plays a key role for the simulation of geomaterials in the form of a necessary basic microdeformational mechanism, see also the discussion by *Oda & Kazama* [192].

5.6 Discussion of cohesion modeling

Two approaches that account for cohesion between two polygon edges have been presented and validated in chapters 4 and 5 by means of a variety of representative examples: In the first, rather simplistic approach beam elements between the centers of mass of neighboring particles have been introduced. As an alternative, a model based on continuous interfaces along common particle edges was proposed. Both models show advantages and disadvantages that ought to be discussed within the next paragraphs.

The first approach based on the introduction of beam elements has shown to be capable to represent most inherent fracture mechanisms of cohesive frictional materials. Thus, it fits qualitatively very well experimental observations. However, the quantification of the corresponding parameters with respect to the output of experiments like stress-strain curves is unsatisfactory. This is primary due to the choice of the two beam breaking parameters axial beam strain and beam end rotation. Although physically plausible from the micromechanical point of view, these parameters cannot be identified with any known (micro) material parameters of geomaterials. Hence, a pure parameter search would end

up in a curve fitting without winning any new knowledge on the physics behind it. Anyhow, it should be kept in mind that this model is very well suited for a visualization of typical failure mechanisms appearing in the testing of cohesive geomaterials, compare also the upcoming section 6.2.2.

As the parameter identification of the corresponding beam failure parameters is a demanding task an interface enhanced DEM model was introduced. This approach shows the advantage to picture the real physics involved in the debonding process of bonded granulates far better than the previous one. However, this is only possible at the expense of a higher computational cost which is required due to the increased complexity of the model and a higher sensitivity of the simulation results with respect to the chosen parameters. The inclusion of the more complex bond representation favors the quantification of the model to experimental results, i. e. the post-peak softening is better reproducible and quantifiable than in the case of the beam enhanced model. Though, still some features like the softening behavior at a later simulation stage in tension (e. g. in consequence of crack face bridging) as well as a less pronounced softening in compression are to be clarified.

The inclusion of a more physical representation of the considered microstructure of geomaterials in chapter 7 is thought to remedy these missing features. Thereby, the microstructure is represented by means of a separate inclusion of aggregates, matrix and the bond between them.

Chapter 6

Characterization of damage

6.1 General

It is quite reasonable to devote further discussion on the characterization of damage found in the simulations with the enhanced DEM models. Generally, on the macroscopic or, more appropriately, observable scale the changes in the microstructure lead to a degradation of the material stiffness. The DEM model at hand provides the opportunity to follow the observable damage step by step via the loss of contacts and elimination of cohesive components (beam or interface). In this chapter different failure related characteristic quantities are utilized to understand the general failure mechanism from a micromechanical point of view. In this context the term micromechanical refers to the beams and interfaces as representatives of the observable damage.

The most obvious failure related quantity is the amount of eliminated beams or interfaces within a sample. In particular, the relation between the time scale and the density of eliminated beams or interfaces, denoted as crack density, give a valuable insight in the failure process. The crack density is an integral quantity since it does not depend on the position of the corresponding cohesive components within the sample. Simulations with different particle numbers under consideration of a constant height to width ratio confirm a strong size dependent effect, i. e. with increasing particle and subsequent beam or interface amount a lower crack density at peak load and at the end of the softening path is found. For a detailed and exemplary discussion of the crack density in terms of a broken beams vs. normalized displacement diagram the reader is referred to *D'Addetta et al.* [51]. The size dependent behavior is in agreement with the theoretical calculations for pure lattices, as shown by *Hansen et al.* [101] and *Herrmann et al.* [104] and discussed in the context of continuum damage mechanics by *Delaplace et al.* [61] and *Krajcinovic & Basista* [131]. These results clarify that the damage or crack density is not an objective measure of the state of damage within the specimen.

A further way to characterize and visualize the state of damage is the procedure utilized before in chapters 4 and 5, namely to plot the midpoints of eliminated beams or interfaces. The incremental display style as followed in *D'Addetta et al.* [52] by plotting all cracking events between successive stages ⓘ reveals interesting similarities with acoustic emission tests, see *van Mier* [243] for more information on this technique. Acoustic emission (AE) is the technical term for the noise emitted by materials and structures when they are subjected to stresses. The emission is caused by the rapid release of energy within a material due to crack formation and subsequent extension occurring under applied stresses. Thus, AE analysis represents a useful method for the investigation of local damage in materials. In analogy to the AE results on rocks by *Lockner et al.* [150], compare also *Vujosevic & Krajcinovic* [256], in figure 6.1 all successive crack events of the non-restricted compression simulation (case (b)), see figure 4.5 (b), are illustrated. This
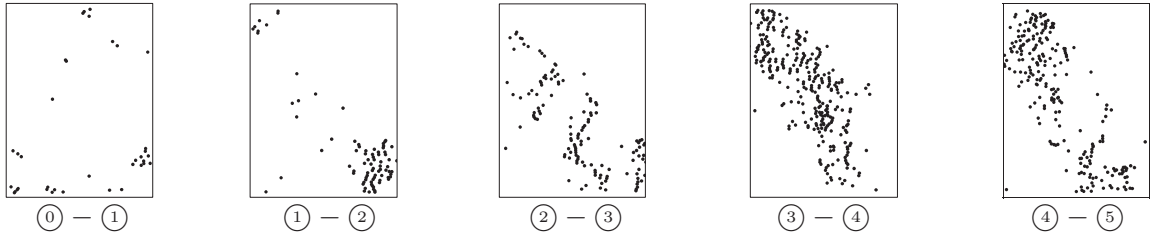
Figure 6.1: Failure evolution of compression simulation (case (b)) according to figure 4.5 (b) - Ruptured beams between successive stages ⓘ.

simulation was discussed in section 4.5.1, see figure 4.6 for the crack events. The plots of all events between successive stages ⓘ give further evidence about the temporal progress of localization and the corresponding crack events.

The goal of this chapter is to recall the salient aspects of the obtained localization phenomena and softening responses from a different point of view. Therefore, the non-deterministic role of the microstructural disorder will be explored in more detail. First, the different failure modes observed in the afore outlined simulations will be discussed. Polar plots of the damage distribution by means of the directions of the cohesive components provide information on the anisotropy and the predominant failure directions of the sample. This information is closely related to the question of texture development and the definition of fabric tensors. Finally, the defect correlation length is employed to characterize the spatial distribution of the cracks. Its occurrence determines the transition point from a crack nucleation to a crack propagation regime. Note that if cohesive samples have been regarded for the evaluation, the simulation results of the beam enhanced DEM model are used. A transfer of the forthcoming methodologies to the evaluation of simulation data resulting from interface enhanced DEM simulation is also conceivable.

6.2   Failure modes

In the following paragraphs, the basic failure mechanisms observed in the presented DEM simulations are discussed.

6.2.1   Non-cohesive particle samples

In this context one has to distinguish dense from porous particle samples, as the failure mechanism may differ substantially. For non-cohesive samples the coordination number of a granular specimen plays an important role. The number of contacts per particle is cast into the average coordination number. This quantity can be traced back to the 1920's and the work of *Smith et al.* [226]. It is usually defined as $\bar{N} = 2N_c/N$ with the number of contacts N_c and the number of particles N of a sample, see the textbook by *Oda & Iwashita* [190]. For example, for the dense and the porous biaxial simulations introduced in section 3.6.1 the initial average number of contacts and, thus, the coordination number is around 3 for the porous sample and approximately 6 for the dense case. For dense samples containing polygonal particles the particles block each other starting with the initial stage of deformation, see the zoom of the biaxial simulation of figure 3.13 in figure 6.2 (a). The failure appears suddenly when the resistance of the particle interlock has overcome by local
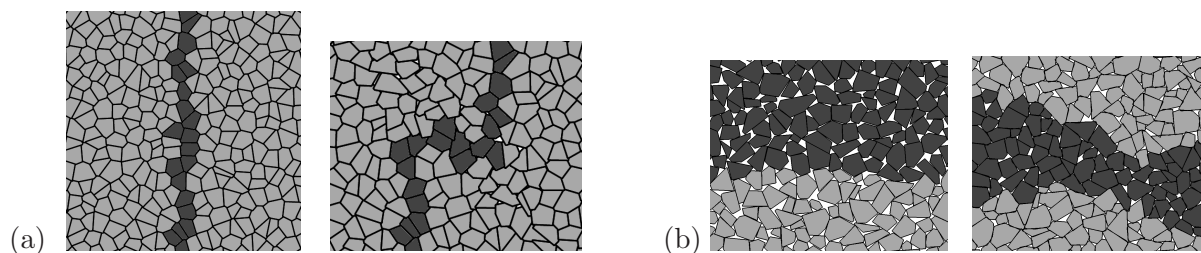
Figure 6.2: Detailed view of (a) dense and (b) porous biaxial simulation - initial and failure stage of simulation.

force peaks. Note that the different grey shading of the particles in figure 6.2 is due to visualization reasons only. The picture changes for porous samples: No initial interlock of the particles is present, as the average number of contacts is small compared to that in the dense case. Thus, the coordination number substantially influences the failure behavior. No clear localization zone is visible in this case, compare figure 3.14. Instead, a pattern of competing failure zones appears, e. g. see the zone visualized in figure 6.2 (b). In the course of simulation the coordination number increases slightly, but does not reach the level of the dense simulation. The failure behavior becomes obvious when the normalized load-displacement curves are compared: The abrupt evolution of failure zones, as for the case of dense packings, leads to an immediate drop of the normalized load-displacement diagram, compare *D'Addetta et al.* [54] or *Ehlers et al.* [77]. Contrary to this, the evolution of the various deformation zones within the porous sample do not influence the normalized load-displacement behavior. The driving force of the failure within the non-cohesive simulations are the rotations of the particles. Although their effect is not so pronounced as for round shaped particles, see e. g. *Åström et al.* [7], *Ehlers et al.* [76], *Lätzel & Luding* [145] or *Lätzel et al.* [146], in particular for not too dense samples (→ smaller coordination numbers), the rolling modes determine the observable behavior. The same failure characteristics is encountered in the simulation of the extension of a granular layer including gravitational influence as presented in section 3.6.2. In contrast to the previous case, here, a loosening (decrease of the coordination number) of the particle sample appears in the dense and porous case. Thereby, the angle of repose differs: For the dense sample the inclination angle is higher than for the porous one.

6.2.2 Cohesive particle samples

In the case of cohesive particle samples the failure behavior is characterized by the elimination of the cohesive components instead of particle interlock or rotational freedom.

Compression

The failure behavior of the compression simulation in section 4.5.1 is dominated by the evolution and rupture of force chains which develop along of particle columns. This effect is independent of the choice of boundary conditions and can be classified as crucial for compressive failure. In the first loading phase all beams in direction of the loading are compressed and those ones perpendicular to the loading direction are elongated. A breaking of the beams in the loading direction is not possible, as they are compressed. Therefore, only those beams perpendicular to the loading direction are eliminated in further course
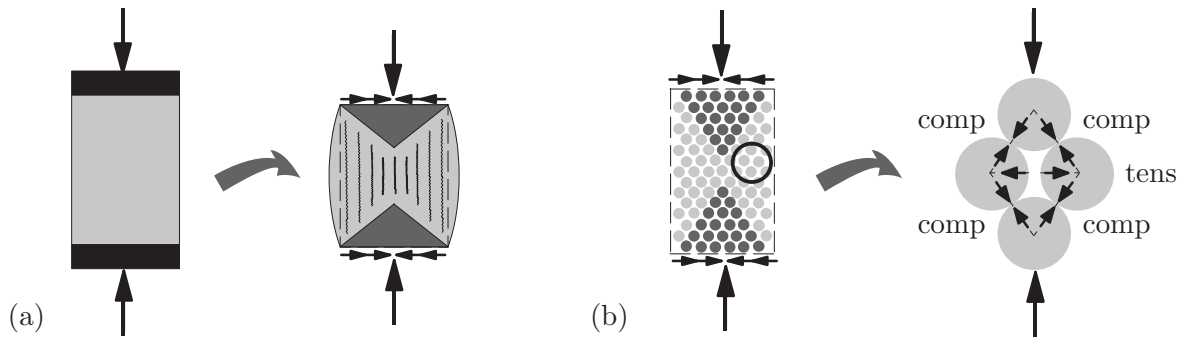
Figure 6.3: (a) Macroscopic and (b) microscopic behavior in compression.

of simulation. The loss of lateral stiffness due to the progressive beam elimination in the direction perpendicular to the loading then yields a bulging of the specimen. This is accompanied by the development of column-type structures in the region of the diagonals which connect the corners of the specimen. This hourglass failure mode agrees qualitatively well with the failure formation of uniaxial compressed concrete cylinders with a persistent effect of friction.

The failure behavior of the compression simulation on the macroscopic (observable) level is schematically depicted in figure 6.3 (a). On the microscopic level (usually invisible in experiments) the behavior shown in figure 6.3 (b) is typically resolved. The microstructure can be considered as a stack of spherical particles where under external compressive forces splitting-type tensile forces develop in the perpendicular direction. Simple photoelastic experiments, see e. g. *Gallagher et al.* [88] or *Lusche* [158], with disk shaped "model" material can explain these splitting forces on a microstructural level. The observation of a column-type structure of a sample is very similar to the experimental results on concrete reported in *Vonk* [255] or rock as documented by *Přikryl et al.* [204], compare also figure 1.1 (b): There, it was found that a buckling of the arising load transferring "particle bridges" leads to the final failure of the specimens and defines the dominant microstructural effect for cracking in compression situations, see figure 6.4 (a). In the compression simulations the array of parallel splitting cracks, enclosing the vertical particle bridges, becomes unstable at a certain load level, buckles and leads to a diagonal failure zone, as reported in *D'Addetta et al.* [51, 52]. This fact is valid regardless of frictional or frictionless boundaries. The formation of parallel cracks and load transferring "particle bridges" is clearly visible in figure 6.4 (b) and indicates the agreement between experiment and simulation. Following the lines of *van Mier* [243] it can be concluded that most likely
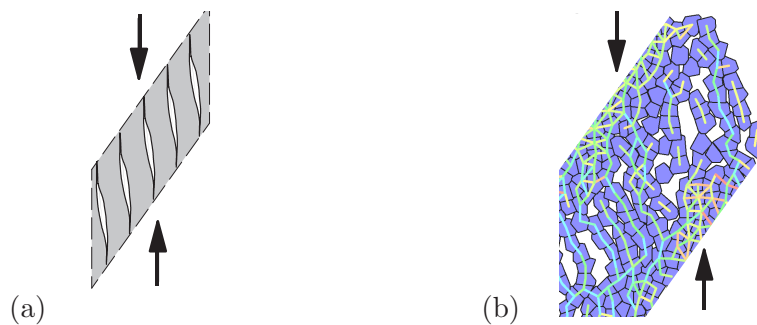
Figure 6.4: (a) Array of splitting cracks and (b) enlarged view of simulation output.
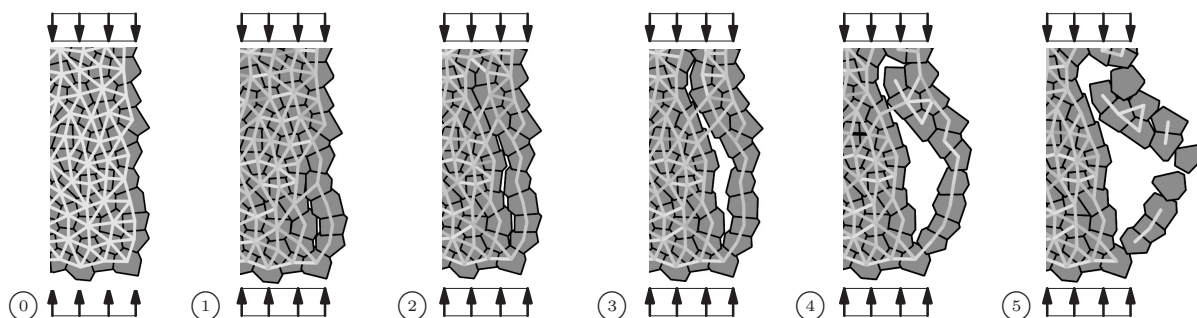
Figure 6.5: Buckling of a boundary particle column within a compression simulation.

crack initiation may be caused by the splitting forces according to the mechanism shown in figure 6.3 (b). Whereas, the global failure may eventually occur when the so-called "en-echelon" shear zones according to the mechanism described in figure 6.4 start to develop. Typically, in concrete or rock experiments en-echelon cracks represent the failure which occurs between a triaxially stressed region above and below of a stiff aggregate particle and the surrounding neighborhood, see *Stroeven* [231] and *van Mier* [243]. Based on the DEM investigations it can be concluded that in compression simulations tensile splitting on the micro level leads to a shear-crack failure on the macro level. Therewith, these investigations correctly resemble the reported crack mechanisms which are quite difficult to observe in experiments.

Experiments with different sands and rod-like particles by *Oda & Kazama* [192] confirm the described failure mechanism and, thus, the results of the presented simulations and the experiments on concrete by *Vonk* [255]. Thus, the same basic failure mechanism may appear in cohesive and non-cohesive geomaterials. Furthermore, the effect of the rotational resistance, intrinsically included within the beam enhanced DEM model, is emphasized as a basic microdeformation mechanism in *Iwashita & Oda* [121] and *Oda & Kazama* [192]. An example for the effect of the rotational resistance at contacts is shown in Fig. 6.5 for the lateral boundary zone of a compressed sample. The evolution of tensile cracks parallel to the loading direction (①, ②) leads to a rotation of the particles within a particle column (③, ④) and, thus, to a bending of the column. The failure results in a buckling of this particle chain due to the bending mechanism (⑤).

Tension

In the tension case the failure behavior is completely determined by the beam or interface component, i. e. their corresponding stiffnesses and statistical values. As consequence of the statistical distribution of the effective stiffness parameters, mostly a single (macroscopically observable), more or less straight crack appears, i. e. a localization in a small band of adjacent particles is obtained. Compare the detail of the simulation results obtained with the enhanced DEM models in figure 6.6. As reported earlier, a distributed cracking that provides one final crack along with the effect of crack face bridging, see e. g. *van Mier* [243] or *van Mier et al.* [244], could not be represented in a satisfactory manner. The same applies for the pre-peak uniformly distributed microcracking, often observed in tension experiments on concrete. In this regard, also inspect the failure evolution in figure 4.8 along with the normalized load-displacement diagram in figure 4.7 (a) or the corresponding diagram for the interface enhanced DEM model in figure 5.9 along
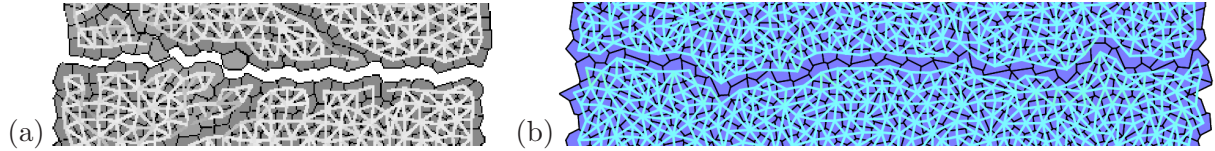
Figure 6.6: Enlarged view of simulation output for tension: (a) beam enhanced and (b) interface enhanced DEM model.

with the failure evolution in figure 5.10. Different reasons can be attributed to this fact: One possibility is the rapid effect of material degradation due to the dynamically driven progressive beam or interface elimination. Another point is the unknown influence of the third dimensional direction due to the two-dimensional basis of the model. For further informations on this topic see the detailed discussion in *D'Addetta et al.* [51, 52]. The most probable reason for this lack is the missing link to a real microstructure, i. e. a regard of stiff aggregates embedded in a soft matrix. It is known from simulations with pure beam or lattice models which account for a more or less realistic microstructure that this deficiency can be overcome, compare with *Schlangen & van Mier* [217], *Schlangen & Garboczi* [215, 216] or *Schorn* [220]. These authors represent a type of artificial microstructure by assigning different parameters according to the position of the microstructural component (beam or rod). This idea is not new: *Wittmann et al.* [262] introduced it in the context of a FEM model denoting the whole procedure "numerical concrete". Therefore, in analogy to the given literature a simulation environment for a prototype artificial microstructure is presented in chapter 7.

Shear

In contrast to the compression and tension simulations, in simple shear no sudden failure is obtained. As expected from experimental knowledge, the Reynolds effect becomes visible by an increase of the normalized load measured at the top. After beam breaking occurs within a diagonal band, compare figure 4.9, the frictional particle contact instead of the beam deformation plays the dominant role with regard to the global failure behavior. The principal stress directions develop on two crossing diagonals, compressive from the lower left corner to the upper right corner and tensile in the perpendicular direction. Since beam rupture is possible only in tension, cracks appear mostly in the latter direction. With ongoing deformation the reaction forces at the top boundary are no longer uniformly distributed. Then, an increasing pressure is needed at the right corner to keep the initial height of the specimen compared to a low value at the left corner. Therefore, the beams within the right area of the top boundary are completely compressed. The complete failure of the specimen is accomplished by a fracturing of these vertical beam chains through the same mechanism as described for the compression simulation in figure 6.4.

6.3   Texture development - fabric tensors

The discussion of the failure modes in the previous section revealed the highly anisotropic failure behavior observed in the standard simulations in a qualitative manner. In order to quantify and visualize the anisotropy and the level of damage the texture development of the microstructural ingredients (here: cohesive components) is utilized. Similar to the

procedure in continuum damage mechanics (CDM), the amount and the anisotropy of damage can be cast into tensorial formulations. In doing so, *Kanatani's* [125] pioneering work on directional data and fabric tensors is followed. First, the theoretical background of the methodology for the continuous representation of the directionality information of eliminated cohesive components is introduced. Afterwards, the discontinuous distribution of the directional data of the compression simulation with lateral constraint according to section 4.5.1 is evaluated for characteristic simulation stages. Finally, the procedure is discussed for these representative stages.

6.3.1 Theoretical background

Following *Kanatani's* [125] statistical approach even order damage tensors of zeroth (scalar), second and fourth order, also called fabric tensors, are derived. The so-called fabric tensor is known since the end of the 1970's to characterize the geometry of the local solid structure of a porous material, compare the work of *Cowin* [44] or *Oda et al.* [193]. Usually, the fabric tensor has the form of a symmetric second order tensor. Since its first appearance it has been suggested that the fabric tensor is defined as an additional measure of the microstructure and supplements the usual porosity measures. *Kanatani's* approach on the definition of fabric tensors was originally intended for the analysis of the interparticle contact distribution of granular materials. However, the application of this theory is not limited to the mechanics of granular materials, since it can be applied to a wide variety of physical problems. For example, *Lubarda & Krajcinovic* [152] introduced it with success in continuum damage mechanics some years later. In the present case all cohesive components within a sample are characterized by an initially defined unit normal $\mathbf{n} = [\cos\phi \ \sin\phi]^T$. This normal is parallel to the vector which connects the midpoints of initially bonded particles, see figure 6.7 (a). The key variable for the directionality is the angle ϕ with respect to the horizontal axis, see figure 6.7 (b). If one considers all cohesive components within a sample, all directions of the unit circle are available, as schematically depicted in figure 6.7 (c). $f(\mathbf{n})$ defines the corresponding distribution density and in a graphical format is usually given in the form of a polar plot, see the example in figure 6.8. The general aim of the forthcoming procedure is to transform the discontinuous distribution to a continuous representation. The procedure is shortly outlined here, for details see the article by *Kanatani* [125]. Following *Kanatani* the estimation of the distribution density $f(\mathbf{n})$ is achieved by assuming a "parametric form", i. e. a family of distributions involving several parameters. This approximated distribution is denoted as $F(\mathbf{n})$. Afterwards, an "approximation measure" is introduced which represents the difference between a measured distribution density $f(\mathbf{n})$ of the type as shown in figure 6.8 and the approximated distribution density $F(\mathbf{n})$. The task is now to determine the parameters of $F(\mathbf{n})$ so
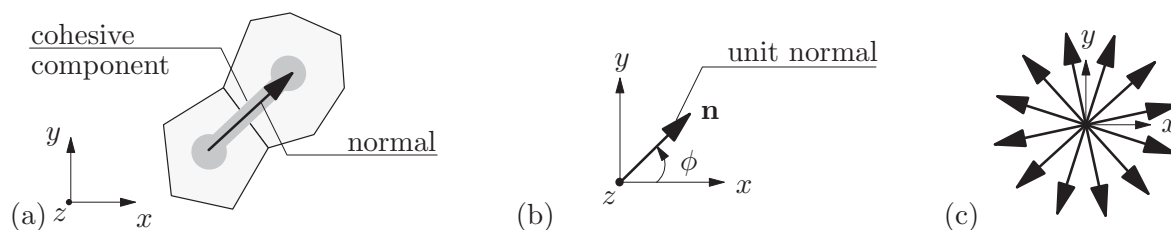
Figure 6.7: Definition of unit normal vector through connectivity.

that the difference between $f(\mathbf{n})$ and $F(\mathbf{n})$ is minimized. Among various possibilities one can choose a least-square error approximation. For the two-dimensional case discussed here this approximation turns out to be the Fourier series expansion.

Different directionality tensors termed fabric tensors of first up to third kind are introduced. For clarity, the index notation will be used in the following, i. e. the summation convention over tensor indices is applied. *Kanatani* introduced the following measure denoted as *fabric tensor of the first kind* $\mathbf{N}$ with order n. In the context of damage related quantities also the notion *damage tensor* may be found

$$N_{i_1 i_2 \ldots i_n} = \langle n_{i_1} n_{i_2} \ldots n_{i_n} \rangle. \tag{6.1}$$

$n_{i_1} \ldots n_{i_n}$ represent the unit normal vector $\mathbf{n}$ in index notation, whereby the indexes $i_1 \ldots i_n$ are placeholders for the usual indexes $i, j, k, l \ldots$. Depending on the order n of the fabric tensor the dyadic products of the normal vectors contained in equation (6.1) are averaged, i. e. $\langle \; \rangle$ denotes the sample mean. For example for the typical case $n = 2$ ($i_1 = i$, $i_n = j \rightarrow n_{i_1} = n_i$, $n_{i_n} = n_j$) one obtains $\sum_{q=1}^{N_b} n_i^q n_j^q / N_b$ and for $n = 4$ ($i_1 = i$, $i_2 = j$, $i_3 = k$, $i_n = l \rightarrow n_{i_1} = n_i$, $n_{i_2} = n_j$, $n_{i_3} = n_k$, $n_{i_n} = n_l$) one obtains $\sum_{q=1}^{N_b} n_i^q n_j^q n_k^q n_l^q / N_b$. The upper index q runs over all cohesive components within a sample N_b, i. e. the dyadic products of the unit normal vector of each cohesive component are summed and divided by the total number of them. The *fabric tensor of second kind* or *crack density tensor*

$$
\begin{aligned}
F_{i_1 i_2 \ldots i_n} \;=\; & 2^n \left[N_{i_1 i_2 \ldots i_n} + a_{n-2}^n \delta_{(i_1 i_2} N_{i_3 \ldots i_n)} + a_{n-4}^n \delta_{(i_1 i_2} \delta_{i_3 i_4} N_{i_5 \ldots i_n)} + \cdots \right. \\
& \left. + \; a_0^n \delta_{(i_1 i_2} \delta_{i_3 i_4} \ldots \delta_{i_{n-1} i_n)} \right]
\end{aligned} \tag{6.2}
$$

is determined directly from the least square error calculation mentioned above. The brackets in the index line denote a pairwise symmetry with respect to all indices. Thus, the following symmetrizations are obtained:

$$
\begin{aligned}
\delta_{(ij} \delta_{kl)} \;&=\; \frac{1}{3} \left[\delta_{ij} \delta_{kl} + \delta_{ik} \delta_{jl} + \delta_{il} \delta_{jk} \right], \\
\delta_{(ij} N_{kl)} \;&=\; \frac{1}{6} \left[\delta_{ij} N_{kl} + \delta_{kl} N_{ij} + \delta_{ik} N_{jl} + \delta_{jl} N_{ik} + \delta_{il} N_{jk} + \delta_{jk} N_{il} \right].
\end{aligned} \tag{6.3}
$$

In equation (6.2) use was made of the variable a_m^n which with regard to the order of the fabric tensors n is defined as follows

$$a_m^n = \frac{1}{2^n} \sum_{\substack{k=m \\ k:=even}}^{n} 2^k c_{k-m}^k, \qquad c_m^n = \frac{(-1)^{m/2}}{2^m} \frac{n}{n - m/2} \binom{n - m/2}{m/2}. \tag{6.4}$$

Finally, the *fabric tensor of third kind* or the *deviatoric part of the damage tensor* is obtained

$$D_{i_1 i_2 \ldots i_n} = 2^n N_{i_1 i_2 \ldots i_n}. \tag{6.5}$$

The fabric tensors of second and third kind in equations (6.2) and (6.5) can easily be correlated to each other. With the aid of the fabric tensor of second kind in equation (6.2) the discontinuous crack density distribution $f(\mathbf{n})$ is approximated by a continuous field $F(\mathbf{n})$

$$f(\mathbf{n}) \sim F(\mathbf{n}) = \frac{1}{2\pi} F_{i_1 i_2 \ldots i_n} n_{i_1 i_2 \ldots i_n}. \tag{6.6}$$

An alternative representation is obtained, if the fabric tensor of third kind noted in equation (6.5) is utilized. Then, the approximation of $f(\mathbf{n})$ takes the form

$$f(\mathbf{n}) \sim F(\mathbf{n}) = \frac{1}{2\pi} \left[D + D_{ij} n_i n_j + D_{ijkl} n_i n_j n_k n_l + \cdots \right] . \tag{6.7}$$

Since for the order $n = 0 \rightarrow N = 1$ (i. e. representation of an isotropic distribution $\rightarrow$ circular distribution density in polar diagram, see e. g. figure 6.9), it follows from equation (6.5) that for $n = 0 \rightarrow D = 1$. Equation (6.7) can be rewritten as a Fourier series

$$\frac{1}{2\pi} \left[1 + a_2 \cos 2\phi + b_2 \sin 2\phi + a_4 \cos 4\phi + b_4 \sin 4\phi + \cdots \right] \tag{6.8}$$

with the Fourier coefficients a_n and b_n. As the tensor $D_{i_1 i_2 \ldots i_n}$ has only two independent components, a_n and b_n are introduced as $a_n = D_{1 \ldots 1} \rightarrow$ e. g. D_{11}, D_{1111} and $b_n = D_{1 \ldots 12} \rightarrow$ e. g. D_{12}, D_{1112}. Depending on the approximation order n and the amount p of indices between the first '2' index and the last '2' index in the index line of $D_{1 \ldots 12 \ldots 2}$, all Fourier coefficients can be defined

$$D_{1 \ldots \underbrace{12 \ldots 2}_{p}} = \begin{cases} (-1)^{p/2} \, a_n & ; p = \text{even} \\ (-1)^{(p-1)/2} \, b_n & ; p = \text{odd} . \end{cases} \tag{6.9}$$

For example, for the approximation up to order 4 utilized in the next section the following coefficients a_n and b_n are provided for equation (6.8): $a_2 = D_{11} = -D_{22}$, $b_2 = D_{12}$, $a_4 = D_{1111} = D_{2222} = -D_{1122}$ and $b_4 = D_{1112} = -D_{1222}$. As an example, the fabric tensors of second and third kind (crack density tensor and deviatoric part of damage tensor) for approximation orders 0, 2 and 4 are given in the following. These have been implemented for an evaluation of the directional data and are utilized in the next section:

$$
\begin{aligned}
F &= 1 , & D &= 1 , \\[2mm]
F_{ij} &= 4 \left[N_{ij} - \frac{1}{4} \delta_{ij} \right] , & D_{ij} &= 4 \left[N_{ij} - \frac{1}{2} \delta_{ij} \right] , \\[2mm]
F_{ijkl} &= 16 \left[N_{ijkl} - \frac{3}{4} \delta_{(ij} N_{kl)} + \frac{1}{16} \delta_{(ij} \delta_{kl)} \right] , & D_{ijkl} &= 16 \left[N_{ijkl} - \delta_{(ij} N_{kl)} + \frac{1}{8} \delta_{(ij} \delta_{kl)} \right] .
\end{aligned}
\tag{6.10}
$$

The fabric tensor of first kind represents the discontinuous distribution of the available directional data and is used for the determination of the tensorial approximation in form of the fabric tensors of second and third kind. For example, in the case of a beam enhanced DEM model it may include the information of the eliminated beams with respect to their orientation according to figure 6.7. The fabric tensors of second and third kind, which are included in the shape of a Fourier series here, represent a continuous approximation of the directional data, i. e. in the form of a continuous function. The final aim is to characterize a given discontinuous distribution by tensors which may be related to macroscopic physical quantities. Note that the different denominations for the same tensorial quantities (fabric tensor of first kind is identical to damage tensor, fabric tensor of second kind is identical to crack density tensor, fabric tensor of third kind is identical to deviatoric part of damage tensor) are attributed to the fact that damage related quantities along the lines of *Lubarda & Krajcinovic* [152] will be described in the following. This is in contrast to contact related quantities which *Kanatani* [125] had in mind. However, this difference is only a

fact of terminology and does not affect the content of the derivations and definitions. An application of the given theory to non-cohesive samples as introduced in chapter 3, e. g. by evaluation and approximation of the contact density, is also conceivable, but not done here for brevity.

6.3.2   Numerical results

The theory presented above is now applied for the description of the damage distribution of the compression simulation with lateral constraint (case (a)), see figure 4.5 (a) in section 4.5.1. The damage and crack density tensor as well as the approximation of the crack density are evaluated. Comparable evaluations in the context of the interface enhanced DEM model are also possible, but skipped here for briefness. Polar graphs of the damage fabric are employed to visualize the crack density. These graphs are discontinuous and represent a radial histogram of crack density usually termed rose or rosette diagram in the literature, see e. g. *Hallbauer et al.* [100], *Kanatani* [125] or *Lubarda & Krajcinovic* [152]. In order to allow the comparison of crack densities at different time stages the information of radial histograms is condensed according to figure 6.8. The outmost angular midpoints of each histogram segment (light and dark grey) are connected and form a polygon shaped graph, as shown for example for the examined sample (ca. 3000 beams). This simplified representation of the rosette diagram is used in the following.

The outer graph in figure 6.9 shows the initial beam distribution of the examined sample, i. e. all beams within the sample. Keep in mind that no beams are eliminated at the initial stage. This distribution is considered as the limiting fracture distribution of all beams, i. e. if all beams contained within the sample would failure, this fracture distribution would be obtained. However, only a part of the beams, namely approximately 30 % of all initial existing beams are eliminated in the course of this compression simulation. The inner graphs represent intermediate fracture distributions, i. e. the distribution of eliminated beams at stages Ⓐ to Ⓔ according to the normalized load-displacement diagram in figure 4.4 (b). Therein, the innermost distribution represents simulation stage Ⓐ and the outmost inner distribution represents simulation stage Ⓔ. All distributions are normalized by the factor $1/2\pi$. Note that the polar plot of this data is symmetric with
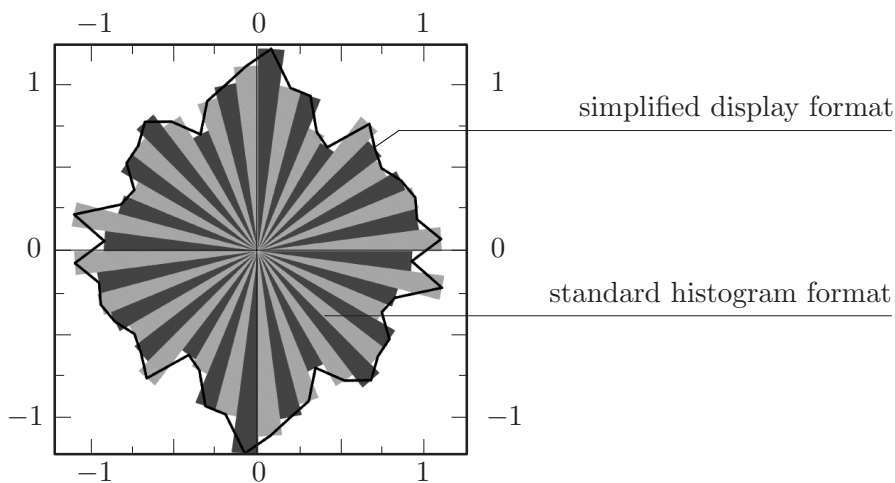
Figure 6.8: Simplification of rosette histogram.
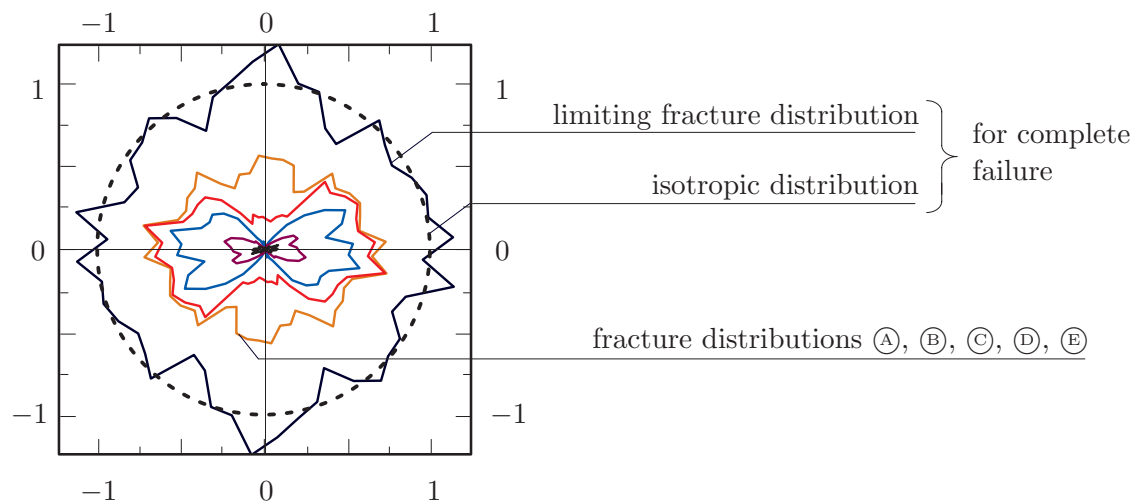
Figure 6.9: Damage distributions of evolving failure for compression simulation case (a) according to figure 4.5 (a).

respect to the origin of the diagram in figure 6.9, i. e. it is point symmetric. This means that for every point in the figure, there is another point found directly opposite it on the other side of the origin of the diagram. This is a result of a double counting of each beam due to the numerical update algorithm, i. e. a beam connecting particle i and j is counted when all beams of particle i are checked and once again when all beams of particle j are checked. Thus, when counted first the normal is prescribed by an angle ϕ^* and when counted for the second time the corresponding normal is prescribed by the angle $\phi^* + \pi/2$. A comparison of the initial distribution with the dotted circular curve shows a good agreement with the completely isotropic distribution. As noted earlier, the complete starting beam mesh (i. e. limiting fracture distribution) can be considered as almost isotropic. The tendency to an anisotropic failure of the sample within the descending branch of the stress-strain diagram in figure 4.4 (b) is apparent. Up to point Ⓓ almost half of the initially existing horizontal beams ($-45° \leq \phi \leq 45°$, with ϕ defined with respect to the horizontal x-axis, see figure 6.7) have been broken. In contrast, nearly no breaking is observed in the vertical direction. This is not surprising at all. As has been explained in the context of the failure modes of the compression simulations in section 6.2.2, first the horizontal beams are elongated, while the vertical ones are compressed. Due to the breaking criterion implemented, compare equation (4.3), only the more or less horizontal beams break. Afterwards, the remaining vertical beam chains are still able to sustain and transfer load. The complete failure results by a loss of this transfer mechanism up to Ⓔ.

In order to visualize the choice of the approximation order, the crack density tensor was evaluated for all initial existing beams, i. e. the limiting fracture distribution. The results are given in figure 6.10 where the approximations of zeroth, second and fourth order are compared to the measured distribution, which is also shown in figures 6.8 and 6.9. The zeroth order approximation represents a circular graph (dotted black), the second order one an elliptical one (dotted light grey) and the fourth order one a deviated elliptical one (dotted dark grey), compare the functional representation in equations (6.7) and (6.8). As the initial distribution is almost isotropic, even the lowest order approximation (zeroth order) compares quite well with the measured data. However, in order to account for the slight initial anisotropy of the distribution the fourth order approximation is needed. The
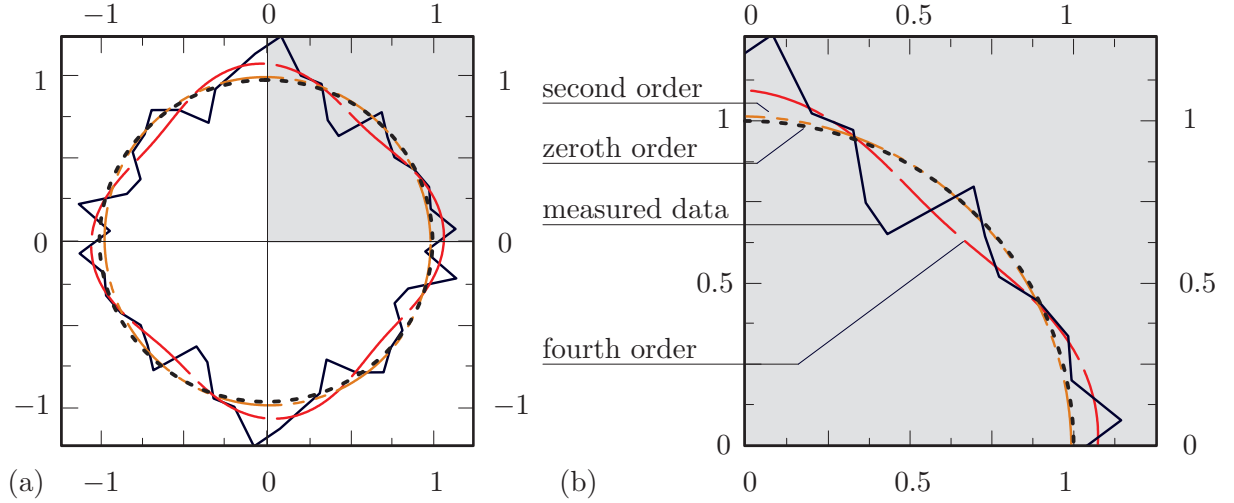
Figure 6.10: (a) Approximation of limit fracture distribution including (b) detailed view.

computation of the crack density approximation of fourth order is done in the following way: The damage tensor $\mathbf{N}$ in equation (6.1) and either the crack density tensor $\mathbf{F}$ in equation (6.2) or the deviatoric part of the damage tensor $\mathbf{D}$ in equation (6.5) are inserted into equations (6.6) or (6.7). $\mathbf{F} = f(\mathbf{N})$ and $\mathbf{D} = f(\mathbf{N})$ are calculated via equations $(6.10)_3$. The crack densities in figure 6.11 (a) correspond to the measured densities in figure 6.9. Curves representing the three different approximation orders are shown together with the measured situation for simulation stage $\circledD$ in figure 6.11 (b). As an example for the functional representation of this simulation stage, coefficients of the damage tensor $\mathbf{N}$

$$
\begin{array}{llllll}
N_{11} & = & 0.6485 & N_{12} & = & 0.0180 & N_{22} & = & 0.3515 \\
N_{1111} & = & 0.5210 & N_{1112} & = & 0.0104 & N_{1122} & = & 0.1274 \\
N_{1222} & = & 0.0076 & N_{2222} & = & 0.2241,
\end{array}
$$

the crack density tensor $\mathbf{F}$

$$
\begin{array}{llllll}
F_{11} & = & 1.5938 & F_{12} & = & 0.0720 & F_{22} & = & 0.4062 \\
F_{1111} & = & 1.5552 & F_{1112} & = & 0.0589 & F_{1122} & = & 0.3720 \\
F_{1222} & = & 0.0131 & F_{2222} & = & 0.3675,
\end{array}
$$

and the deviatoric part of the damage tensor $\mathbf{D}$

$$
\begin{array}{llllll}
D_{11} & = & 0.5938 & D_{12} & = & 0.0720 & D_{22} & = & -0.5938 \\
D_{1111} & = & -0.0386 & D_{1112} & = & 0.0229 & D_{1122} & = & 0.0386 \\
D_{1222} & = & -0.0229 & D_{2222} & = & -0.0386,
\end{array}
$$

are noted. The distribution density according to equation (6.6) is skipped here for brevity. With the deviatoric part of the damage tensor $\mathbf{D}$ one obtains the crack density distribution in the form of a Fourier series

$$
\begin{aligned}
f(\mathbf{n}) & = \frac{1}{2\pi} \left[1 + D_{11} \cos 2\phi + D_{12} \sin 2\phi + D_{1111} \cos 4\phi + D_{1112} \sin 4\phi + \cdots \right] \quad (6.11) \\
& = \frac{1}{2\pi} \left[1 + 0.5938 \cos 2\phi + 0.0720 \sin 2\phi - 0.0386 \cos 4\phi + 0.0229 \sin 4\phi + \cdots \right].
\end{aligned}
$$
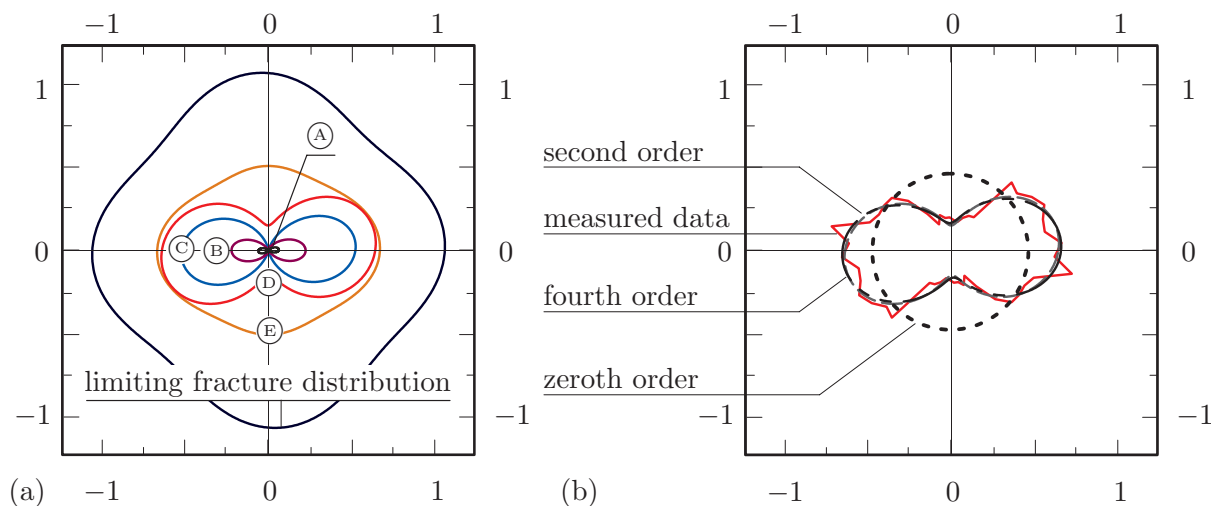
Figure 6.11: (a) Fourth order approximation of fracture distributions of figure 6.9 and (b) different approximation orders at simulation stage Ⓓ.

 It can be concluded that experimental or, as in the present case, simulated data can be cast in a rosette diagram and, subsequently, approximated by distribution functions which may be defined on a unit sphere in the general 3D case. The discontinuous distributions can be cast into a series of spherical functions. Thereby, the ensuing series is typically truncated at a desired tensorial order of the corresponding dyadic products forming the damage tensor. In this sense, this methodology not only may serve for a better interpretation of the previous simulation data. It describes a simple way to include simulated or measured data into continuum formulations, e. g. damage formulations incorporated in the FEM, see *Lubarda & Krajcinovic* [152]. Such an approximative representation of damage densities may be relevant for the derivation and corroboration of phenomenologically motivated damage tensors. On this account compare the classical formulations based on the effective stress principle like those in *Krajcinovic* [130] or *Lemaitre & Chaboche* [147]. Furthermore, this procedure may help to motivate the anisotropic damage evolution of the Microplane model in the context of the FEM, compare with *Bažant & Oh* [16] or *Kuhl* [137]. Then, the directional representation may be understood as a homogenized response around the unit sphere and centered in a material point, compare the approach by *Kuhl et al.* [136]. A coupling of Microplane-based FEM models with DEM models may be promising. Different realizations are conceivable: First, by means of an inclusion of the anisotropic damage or the contact density distribution of particle assemblies. Second, by using the directional data to substantiate the available Microplane evolution laws or to define new evolution laws for a Microplane model for granular-type materials.

6.4   Defect correlation length

In the previous sections the observable damage was characterized by means of different failure modes as well as the anisotropy of the damage fabric. However, a salient feature in the context of a failure description of cohesive and non-cohesive geomaterials, namely the width of a failure zone, was not considered up to now. Failure zones are represented for example by shear bands like those observable in figures 4.5 or 4.10 or typical mode I (pure tensile) failure in figure 4.7. The discussion of the width of shear zones is not

new, compare the theoretical, experimental or numerical results of Åström et al. [7], Herrmann [103], Mühlhaus & Vardoulakis [181], Oda & Iwashita [191], Oda & Kazama [192] or Vardoulakis & Graf [248]. The main focus of this section lies on the investigation of consecutive defects and the introduction of a defect correlation length which easily gives access to an estimate of the failure zone width. The term "defect" refers to the observable cracking within the simulations by means of eliminated beams or interfaces. In short words, the defect correlation length is defined by the fact that if the distance of two consecutive defects is smaller than this length, these defects are correlated, while they are not correlated, if the distance is larger than this length. The defect correlation length is considered as a further failure related characteristic quantity. It is studied for the compression simulation without lateral restriction (case (b)) shown in figure 4.5 of section 4.5.1. Thus, the beam enhanced DEM model has been utilized. Due to its coupling to the particle size this quantity represents an inherent internal length scale, cf. D'Addetta et al. [51].

6.4.1   Theoretical background

The defect correlation length was originally proposed in different forms: on the one hand, in the context of experimental measurements of geomaterials via acoustic emission tests by Lockner et al. [150]. On the other hand, Delaplace et al. [61] studied it in the context of statistical measures of pure lattice models, compare also the book of Krajcinovic [130]. The existence of a correlation length ξ_d expresses the limit between the statistically local and homogeneous regime (i. e. without correlation) and the statistically non-local regime (i. e. with correlation). Thus, this length gives an estimate of the process zone width. The correlation length is evaluated by means of the distance between two successive cracks $d_{i,i+1}$ and a histogramatic representation of this data. In the pre-localization regime the distance of two consecutive cracks is uncorrelated, i. e. the probability to find a distant crack from a given crack on average is the same one as to find a near crack. This means that the cracks within a tested specimen are more or less randomly distributed over the entire specimen volume. With onset of localization by distinct elimination of beams in one "macroscopic" crack zone, e. g. as seen for the compression simulation in figure 4.6 or tension simulations in figure 4.8, the picture changes: The probability that the next crack is near to a previous one is much higher than that the consecutive crack is distant from it. This behavior is schematically depicted in figure 6.12 (a) where the probability distribution density $h(d_{i,i+1})$ is drawn over the distance of successive cracks $d_{i,i+1}$. The transition point between the two described modes can be determined depending on the existence of ξ_d for a certain data representation. The existence of ξ_d reflects the beginning of localization by fixing a point in time when the change from diffuse damage to progressive localization occurs: For dimensions larger than the correlation length the material can be characterized as statistically local and homogeneous as the defects are uncorrelated. In order to determine the correlation length a theoretical approach along the lines of Delaplace et al. [61] is followed. There, a continuous approximation of distributions comparable to that in figure 6.12 (a), right is utilized. On a length scale smaller than the defect correlation length ξ_d one assumes that the normalized probability density distribution $h(d_{i,i+1})$ of two consecutive cracks $d_{i,i+1}$ is a homogeneous function of $d_{i,i+1}$ itself (here: power law). Hence, the distribution density is approximated in the
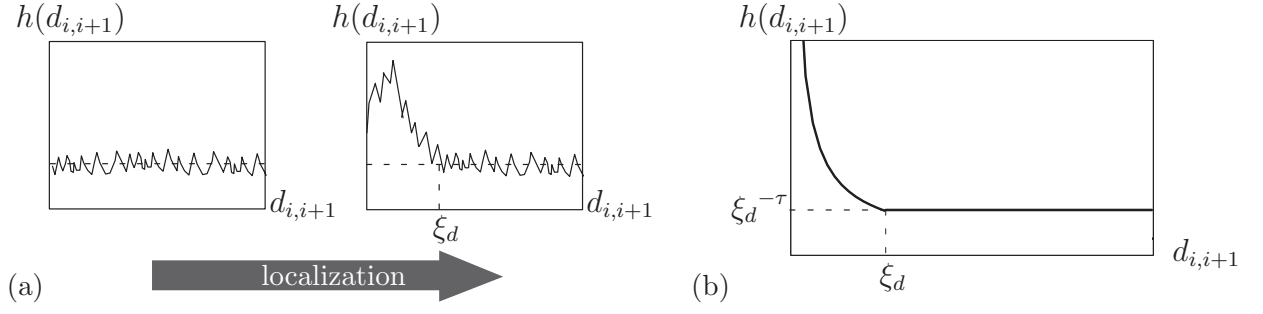
Figure 6.12: (a) Schematic view of histograms in pre- and post-localization regime and (b) approximation of histograms.

form of a case differentiation

$$
h(d_{i,i+1}) = \begin{cases} A\, d_{i,i+1}^{-\tau} & ;\, d_{i,i+1} \leq \xi_d \\ A\, \xi_d^{-\tau} & ;\, \xi_d \leq d_{i,i+1} \leq L/2\,, \end{cases} \tag{6.12}
$$

see also the graphical representation in figure 6.12 (b). The system length L represents the macro scale and, therewith, the size of the specimen, i. e. the side length of the system. The parameter τ is estimated by an evaluation of the measured histogramatic distributions. The constant part denoted by $\xi_d^{-\tau}$ provides a measure of the initial distributed damage in absence of correlation. The value ξ_d according to figure 6.12 (b) is estimated by plotting $h(d_{i,i+1})$ as a function of $d_{i,i+1}$. The constant A describes the normalization of the histogramatic distribution $h(d_{i,i+1})$ of a certain simulation stage. Evaluation of $A = \int h(d_{i,i+1})d_{i,i+1}\, \mathrm{d}d_{i,i+1} = 1$ yields

$$
A = \frac{(1-\tau)\xi_d^{\tau}}{\xi_d^{\tau} + 2L(1-\tau)}\,. \tag{6.13}
$$

It must be pointed out that this approach is formally correct only for pure elastic lattice models loaded in tension (i. e. the crack propagates by the removal of beams ahead of the crack tip). However, it will be demonstrated that the above approximation is also correct for localization phenomena in compression simulations (e. g. shear bands) along with a beam enhanced DEM model.

6.4.2 Numerical results

The defect correlation length for the compression simulation without lateral restriction (case (b)) shown in figure 4.5 (b) is examined. As shown in figure 4.6 through the evolution of cracks within the specimen, the failure is characterized by two non-crossing shear zones. The focus lies on the main zone from the upper left to the lower boundary which is denoted as primary shear zone in the following. The distribution of distances of two consecutively broken beams $d_{i,i+1}$ is depicted in the histogram in figure 6.13 (a). The simulation stages ① - ⑤ correspond to those introduced in section 4.5.1 for the compression simulation (case(b)). Curve ① shows a distributed behavior of the distances of successive defects in the range of half the system height (20 cm). At this stage the next broken beam can be found anywhere within the sample with equal probability. From stage ③ up to stage ⑤ a clear preference of the small distances can be observed and,

thus, a correlation of the defects is obtained. According to *Vujosevic & Krajcinovic* [256] this behavior could be interpreted as a switch-over from a crack nucleation to a crack propagation mode. A determination of the defect correlation length for stages ③ - ⑤ according to equations (6.12) and (6.13) approximately yields the same defect correlation length $\xi_d \approx 5$ cm. Thereby, a value $\tau = 1.297$ is measured and the normalization constant is $A = 43.246$ for stage ③ and $A = 134.217$ for stage ⑤. The distribution of the normal distances between the crack positions and the primary shear zone d_i^s is shown in figure 6.13 (b). d_i^s is measured perpendicular to the primary shear zone. These graphs indicate the finite width of the evolving shear zone. Bear in mind that only the absolute value is counted as d_i^s. In figure 6.13 (b) a plateau for distances between 0 cm and 5 cm can be recognized. Thereby, the average beam length is 1.1 cm and the average particle size is 1 cm. With increasing vertical loading the specimen separates into three parts that are pushed apart as simplistically depicted within the diagram in figure 6.13 (b). This fracture behavior not only leads to a nearly constant increase of distances between 0 cm and 5 cm (plateau), but also results in an increase of distances in the area between 5 cm and 8 cm, which represents the border zone of the localization zone. This underlines the fact that the shear zone width remains constant from localization onset at stage ② up to the end of the shear band formation at stage ⑤. With the help of the histogram in figure 6.13 (b) the thickness of the shear band can be determined. Neglecting the effect of the described block separation mode a thickness of 10 times the average particle size is found. The histograms in figure 6.14 show the distances of sequential failure event pairs in direction of the localization zone $d_{i,i+1}^t$ and perpendicular to it $d_{i,i+1}^n$. This is done by a simple vectorial decomposition of $d_{i,i+1}$. The results are in contrast to *Krajcinovic's* [130] speculation that the distance between two consecutively removed links is likely to be random in the direction of the shear band and distributed in a manner favoring small distances in the direction of its thickness. As the probability to get very small distances is pronounced both in direction normal and tangential to the evolving shear zone *Krajcinovic's* speculation is not supported by the presented evaluations.

In summary, the defect correlation length as well as the histogramatic representation of successive cracks have proven to be a useful tool: On the one hand, it served for a first estimation of the shear band zone width. On the other hand, the instant when the damage skips from a diffuse cracking to a progressive localization could be determined. Furthermore, these results give a first hint on the estimation of the size of a representative elementary volume and, in particular, on how many microstructural components like
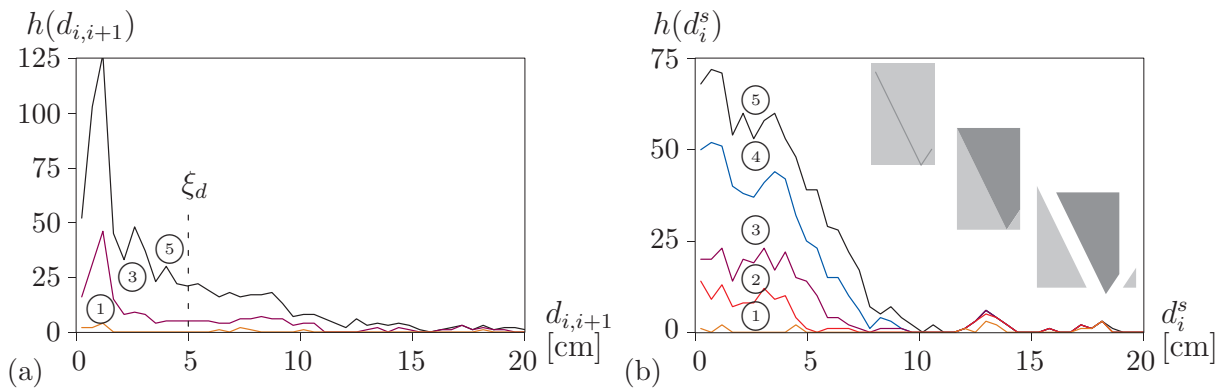
Figure 6.13: (a) Distance from next crack and (b) from primary shear zone.
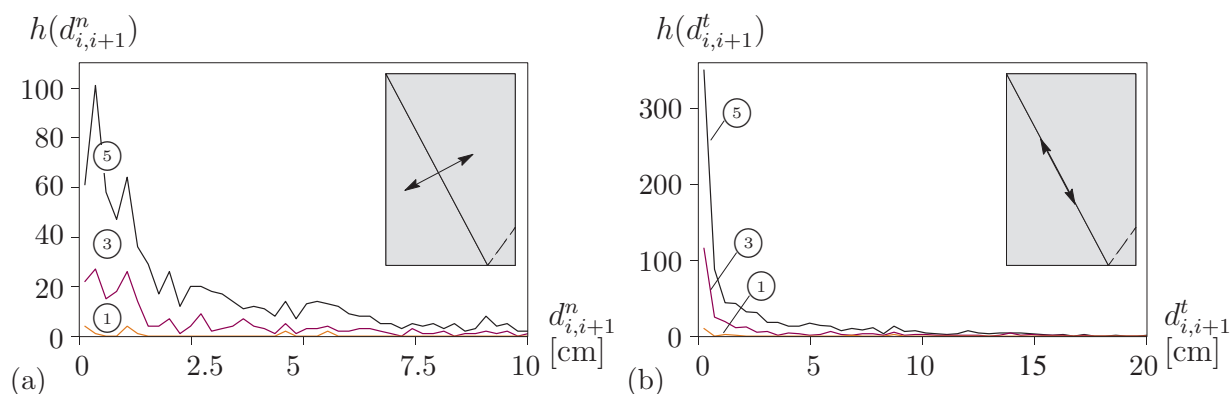
Figure 6.14: (a) Distance from next crack normal and (b) tangential to primary shear zone.

beams or interfaces have to be included in this volume. Finally, since a defect correlation length exists and the defects within the localization zone are correlated, the conclusion is drawn that the material within this zone is an example of a non-local material from a continuum point of view. As indicated by experimental and simulation results, a disordered microstructure leads to localization zones of irregular shape. These zones are neither thin nor smooth, as typically considered in continuum damage theories in the context of the FEM or as simplistically depicted in figure 6.13 (b). The interface between the interior (damaged) and exterior (undamaged) of the localization zone is blurry. Thus, it is deduced that the geometry of this zone and, in particular, its width cannot be uniquely determined. According to the discussion in *Vujosevic & Krajcinovic* [256] it seems more reasonable to determine the shear band width by measuring its effect on the effective transport properties. Therefore, later in this thesis the "effective" stress and strain fields of representative elementary volumes are evaluated. These intrinsically include the effect of damage. The procedures presented in the context of homogenization theories in chapters 8 and 9 may contribute to improve the description of a shear band zone, as it exceeds the purely geometric description introduced above.

Chapter 7

Discretization of a microstructure

The beam as well as the interface enhanced DEM model presented in chapters 4 and 5 have shown to be capable to simulate some of the qualitative as well as quantitative aspects of failure in cohesive geomaterials. While the beam enhanced DEM model is in general not capable to represent the softening, the interface enhanced model represents it far better. Nevertheless, for the latter model the general description of softening in compression is still unsatisfactory. As pointed out earlier, the inclusion of a microstructure is thought to remedy these points. This chapter comprises simulations with the interface enhanced DEM model where the particle mesh represents an artificial microstructure. Therefore, stiff macro particles that are composed by an agglomeration of a finite number of particles are embedded in a soft matrix, which is also represented by a composition of particles. In order to include a "real" microstructure corresponding digital image processing software has to be connected to the mesh generation module of the DEM program. Since at the present stage an easily realizable implementation is sought, this way is not followed here. Instead, an alternative, approximative implementation is carried out by creating an "artificial" microstructure. In that, the procedures proposed in in the framework of the FEM by *Carol et al.* [31], *Stankowski* [227] and *Vonk* [255] are principally paralleled, as these publications concern the creation of artificial two-phase materials using polygonal aggregate shapes. Furthermore, the present approach is related to that of *Schlangen & van Mier* [217], see also *van Mier* [243], where circular aggregate particles are generated based on a statistical distribution which is related to grading curves of concrete. Thus, the composition of a real microstructure of concrete-type materials as shown in figures 1.1 (a) and 3.2 is treated in an approximate and artificial way here. It is not thought that the simulation results based on a "real" and an "artificial" two-phase microstructure differ that much though.

7.1   Generation of a microstructure

The generation of an artificial microstructure is based on the formulation of macro particles, i. e. one macro particle is composed by an accumulation of a finite number of polygonal particles which are denoted as micro particles. An initially created polygon mesh is overlaid by a mesh composed of larger particles. Certainly, as mentioned before, the geometry of a known microstructure, e. g. by means of electron microscopy images, could be included as an overlaying mesh. This option is not considered here, however, is in the realm of possibility in future implementations. Two possibilities to create an overlaying mesh that ought to represent this artificial microstructure are conceivable: The first one implies the creation technique for dense particle assemblies according to section 3.2. Alternatively, the application of the procedure for the generation of a porous sample may be utilized, compare the procedure via figure 3.3. In both cases, after gen-
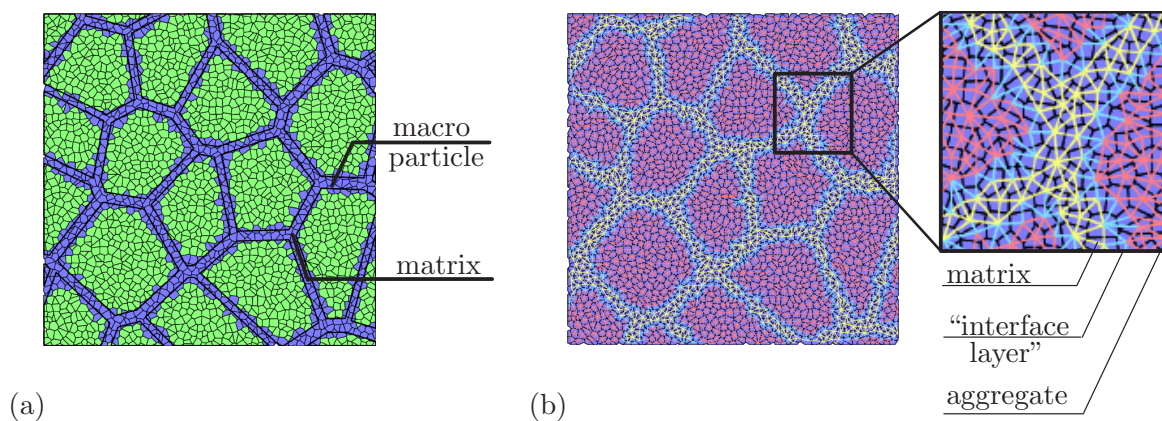
Figure 7.1: (a) Definition of particle properties and (b) definition of properties of cohesive component.

erating the corresponding particle assembly, the particles are scaled down and rotated in a statistical fashion. The scaling down of these (macro) particles by a variable factor is controlled by the desired proportion of aggregate to matrix volume. In order to obtain the overlaying mesh of larger particles the afore mentioned mesh is scaled up. This scaling up depends on the favored size of aggregates. Finally, this mesh is laid over the (underlying) dense particle mesh and represents the pattern for the definition of the macro particles. Based on this information the (micro) particles of the underlying mesh are flagged as being inside or outside the macro particles. The macro particles represent the stiff aggregates and the remaining particles define the matrix. As example the contiguous green particles in figure 7.1 (a) are identified as the macro particles and the blue ones as the matrix material. Thereby, the matrix material represents a softer material than the embedded aggregate material (like a cement surrounding the stiff aggregates), i. e. the material properties of the corresponding interface elements are adopted appropriately. The corresponding cohesive components are classified as follows, compare also the sketch in figure 7.1 (b): Inside the aggregate (a), inside the matrix (m) and defining the "interface layer" between aggregate and matrix (i). Note that the color scale in figure 7.1 (a) and (b) differs: Figure 7.1 (a) concerns solely the particle mesh and highlights the two-phase composition, while in figure 7.1 (b) the particle mesh is unicolored and lies in the background of the interface element mesh which highlights the cohesive component classification. The "interface layers" should not be confused with the interface elements used within the interface enhanced DEM model. The first one describes a real material interface layer (between aggregate and matrix), while the latter one represents a model interface in form of a component of the enhanced DEM model. Finally, the values of either the stiffnesses of the cohesive component (E^b or k_n, k_t), the corresponding fracture law (ϵ_{max}^b or $\sigma_n^{max}, \sigma_t^{max}$) or both stiffness and fracture law parameters, are chosen accordingly. In order to consider the microstructural properties of concrete-type materials as best as possible, benefit was made from the extensive knowledge of the group of *van Mier*. This knowledge comprises the simulation of microstructures via pure beam lattice models starting from the first publication by *Schlangen & van Mier* [217], see also *van Mier* [243]. The respective parameter ratios between (a), (m) and (i) are estimated based on the corresponding ratios introduced in the context of lattice models. In that, an analogous approach of scaling the stiffnesses and fracture law parameters noted in *van Mier et al.*

[245] is partially followed. In order to prevent aggregate cracking (i. e. macro particle) at the present stage the original ratios noted in *van Mier et al.* [245] are partly adopted. For the parameters of the interface enhanced model the following choices are made:

$$\frac{k_n^{(i)}}{k_n^{(m)}} = 0.1\,, \qquad \frac{k_t^{(i)}}{k_t^{(m)}} = 0.4\,, \qquad \frac{\sigma_{n,t}^{max,(i)}}{\sigma_{n,t}^{max,(m)}} = 0.25\,,$$

$$\frac{k_n^{(a)}}{k_n^{(m)}} = 2.8\,, \qquad \frac{k_t^{(a)}}{k_t^{(m)}} = 2.8\,, \qquad \frac{\sigma_{n,t}^{max,(a)}}{\sigma_{n,t}^{max,(m)}} = 100\,. \tag{7.1}$$

The matrix values $(\cdot)^m$ are used as input values and the other values, $(\cdot)^a$ and $(\cdot)^i$, result from equation (7.1). A similar calibration of the parameters is also possible for the parameters of the beam enhanced model. Keep in mind that the choice of parameters is only influenced by the fitting of the softening behavior and without consideration of a detailed, because unknown, knowledge of the "real" micromechanical parameters. Despite the advanced measuring devices and setups available in laboratories, the "real" parameters of the phases (a), (m) and (i) actually remain in the dark, i. e. no precise and experimentally verified values of the phases' stiffness, yield strength and softening law are available. In order to fit experimental results of concrete-type materials these parameters may be estimated on the basis of a macroscopic view of the problem: One supposes that the known macroscopic parameters of concrete-type materials are identical to the microscopic ones. For example, the fracture energy of the interface elements is identified as the experimentally measured, macroscopic one and so forth. An alternative and, in the author's opinion, more promising way is the estimation of these parameters on the basis of the insights of chapter 5 and utilizing the experience of the group of *van Mier* in the context of the micromechanical simulations of concrete-type materials.

7.2 Numerical results

It is a moot point whether the inclusion of a material description based on an artificial microstructure as introduced in the previous section instead of the "model" material may help to overcome the deficiencies of the beam and interface enhanced DEM models. Recall that the "model" material in chapters 4 and 5 included nearly identical stiffnesses and failure laws of the cohesive components. Compression and tension simulations of an artificial microstructure using the interface enhanced DEM model are presented. This microstructure has been created by using a porous sample as overlaying mesh for the definition of the macro particles. The model parameters have been fit to the compression experiments by *Vonk* [253], also presented in figure 5.11 (b). Corresponding simulations with the beam enhanced model yield similar results with respect to the final failure picture and are not given here for brevity.

7.2.1 Compression simulations

The load setup of the compression simulations was already discussed in sections 4.5.1 and 5.5.2. The measuring of the nominal strain is accommodated by controlling the distance between the upper and lower boundary particles adjacent to the loading platens. The nominal stress is computed by division of the reaction force on the boundary platen by
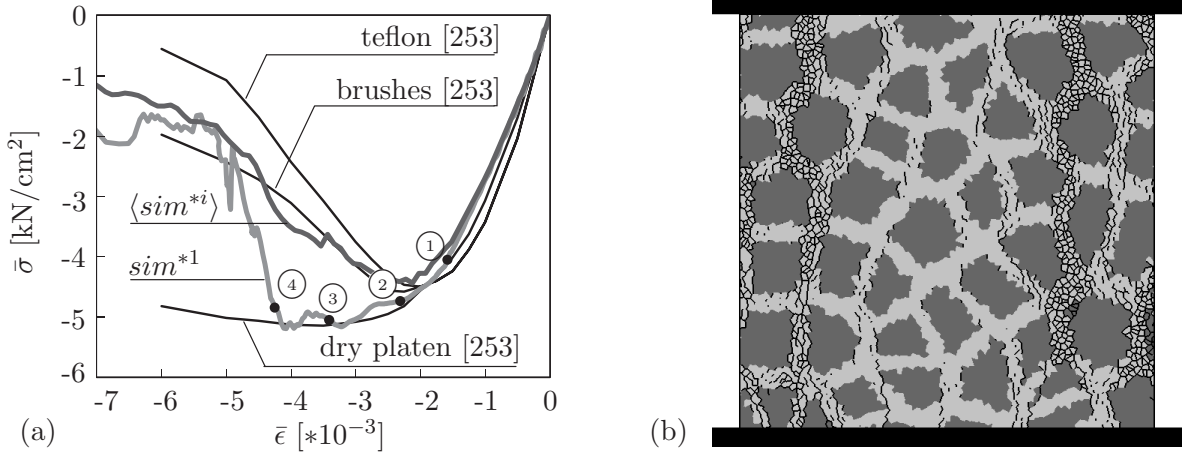
Figure 7.2: (a) Stress-strain diagram of simulations and experiments by *Vonk* [253] and (b) eliminated bonds at stage ④.

the initial width of the specimen. Various parameter sets have been tested. For the sake of simplicity, only the results of one parameter set are given without going into the details of the parameter study. Note that the parameter choice is the result of a parameter fitting to experimental results on concrete in absence of more detailed information on the micromechanical parameters. The following matrix parameters have been used: The normal and tangential stiffnesses are chosen as $k_n^{(m)} = 2000$ kN/cm^2, $k_t^{(m)} = 600$ kN/cm^2 and the fracture energies as $G_{f,n}^{(m)} = 4.996 \cdot 10^{-4}$ kN/cm^2, $G_{f,t}^{(m)} = 5.988 \cdot 10^{-3}$ kN/cm^2. The yield stresses are statistically distributed for each interface about ± 10 % the average value. On average one gets $\sigma_n^{max,(m)} = 0.04$ kN/cm^2, $\sigma_t^{max,(m)} = 0.12$ kN/cm^2. Corresponding values for the aggregate and the interface layer between aggregate and matrix are obtained via equation (7.1). The shape parameters are unaltered with respect to the choice in chapter 5 and are noted $\varphi = 26.6°$, $\gamma = 10°$ and $\psi = 0°$. The general parameters of the DEM model are also unchanged: The density was chosen as $\rho = 2.5$ g/cm^3, the time step as $\Delta t = 5 \cdot 10^{-7}$ s, the viscous damping and friction are set to zero ($\gamma_N = 0$, $\gamma_T = 0$, $\mu = 0$) and the contact stiffness amounts to $E_p = 100$ kN/cm^2.

Seven compression simulations with the same amount of aggregates and almost identical aggregate/matrix ratios have been carried out. The only difference between these simulation sets is the starting number of the random number generator for the generation of the underlying particle mesh. The quadratic 75 cm × 75 cm sample used in simulation series sim^{*1} is composed by 5501 particles and a total of 16489 interface elements between all particles within the sample. The microstructure is created by use of 46 macro particles. The composition of the sample includes a total of 2896 particles representing the aggregates and a total of 2605 particles representing the matrix. Thus, the fraction of aggregate volume to complete volume is 0.525.

The simulations are confronted with the experiments of *Vonk* [253, 255] by means of the nominal stress vs. nominal strain diagram and, in particular, the associated softening branch. The stress-strain curves of all simulation series sim^{*i} with $i = 1...7$ are averaged via a superposition of the corresponding data files. This average curve is symbolically denoted by $\langle sim^{*i} \rangle$. In figure 7.2 (a) the comparison of $\langle sim^{*i} \rangle$, simulation series sim^{*1} and *Vonk's* [253] tests on concrete with different boundary conditions is presented. After linearly increasing in the first part of the loading program the average stress-strain

curve $\langle sim^{*i}\rangle$ turns into a nonlinear regime up to the peak. Afterwards, in contrast to the simulation results presented in the previous chapters the softening regime is less pronounced, i. e. it follows the predicted experimental results quite well. The continuous failure of interface elements yields a decrease of the stresses with increasing strains. The average simulation result $\langle sim^{*i}\rangle$ lies near the limit curves of the low friction boundary cases (teflon/brushes) in the post-peak regime. In summary, the inclusion of the artificial microstructure has proven to be an important feature for a realistic representation of the post-peak softening behavior in terms of the stress-strain relation.

The interface enhanced DEM model provides the opportunity for a detailed view on the microstructural softening process by monitoring the softening of the interface elements. In order to give a detailed view of the failure within the specimen snapshots of simulation series sim^{*1} are considered. The softening stadium of the interface elements is monitored at four time steps ① to ④ in figure 7.3. These simulation stages document the course of the nonlinear and softening branch of curve sim^{*1} in figure 7.2 (a). The simplified picture of the composite structure of the sample in figure 7.2 (b) highlights the crack propagation through the specimen shortly after peak load. The dark grey color denotes the aggregate particles and light grey the surrounding matrix. Bear in mind that the aggregates are represented by a finite amount of (macro) particles. For this reason, the shape of the aggregates is irregular. The black lines define those interface elements that have been eliminated in the course of the simulation, i. e. $\langle\kappa\rangle = 1$. In contrast to the line representation in figure 7.3 where lines between the centers of bonded particles represent the softening stadium of the interface elements, these lines represent the real geometry of the interface. They connect the start and end point of an eliminated interface and represent the corresponding particle edges. The tensile splitting type failure, mostly along the boundaries of the aggregates, is obvious. Two cracks in the left and right part of the specimen initiate the macroscopic failure of the particle sample. In figure 7.3 the brighter (green gleaming) background area represents the aggregates, while the darker (blue gleaming) background displays the matrix. Note that for visualization and didactical reasons a different color definition for the interface elements compared to that in figure 7.1 has been used. The color scale included in this figure refers only to the softening of the interface elements marked by the line connections between bonded particles. As mentioned earlier, it has nothing to do with the particle coloring. Please note that if an interface reaches a stage $\langle\kappa\rangle > 1$, the corresponding line connection in figure 7.3 is eliminated. Thus, the purple color of the underlying (background) matrix particles becomes visible in regions where the failure localizes. At simulation stage ① very few interfaces have been eliminated and an increased cumulative softening $\langle\kappa\rangle$ is apparent in vertical zones by the yellow, red and black colored connections. In the course of simulation within stages ② and ③ two macroscopic failure zones form. The continuous debonding results in the final failure mechanism in form of a complete disintegration of the matrix material in these zones, compare stage ④. At this stage even a breaking of aggregates at the lateral boundaries of the sample is possible, as seen in the lower right region of the specimen. In summary, the final failure at stage ④ pictures the reality quite well, compare the fractured samples by *Vonk* [255].
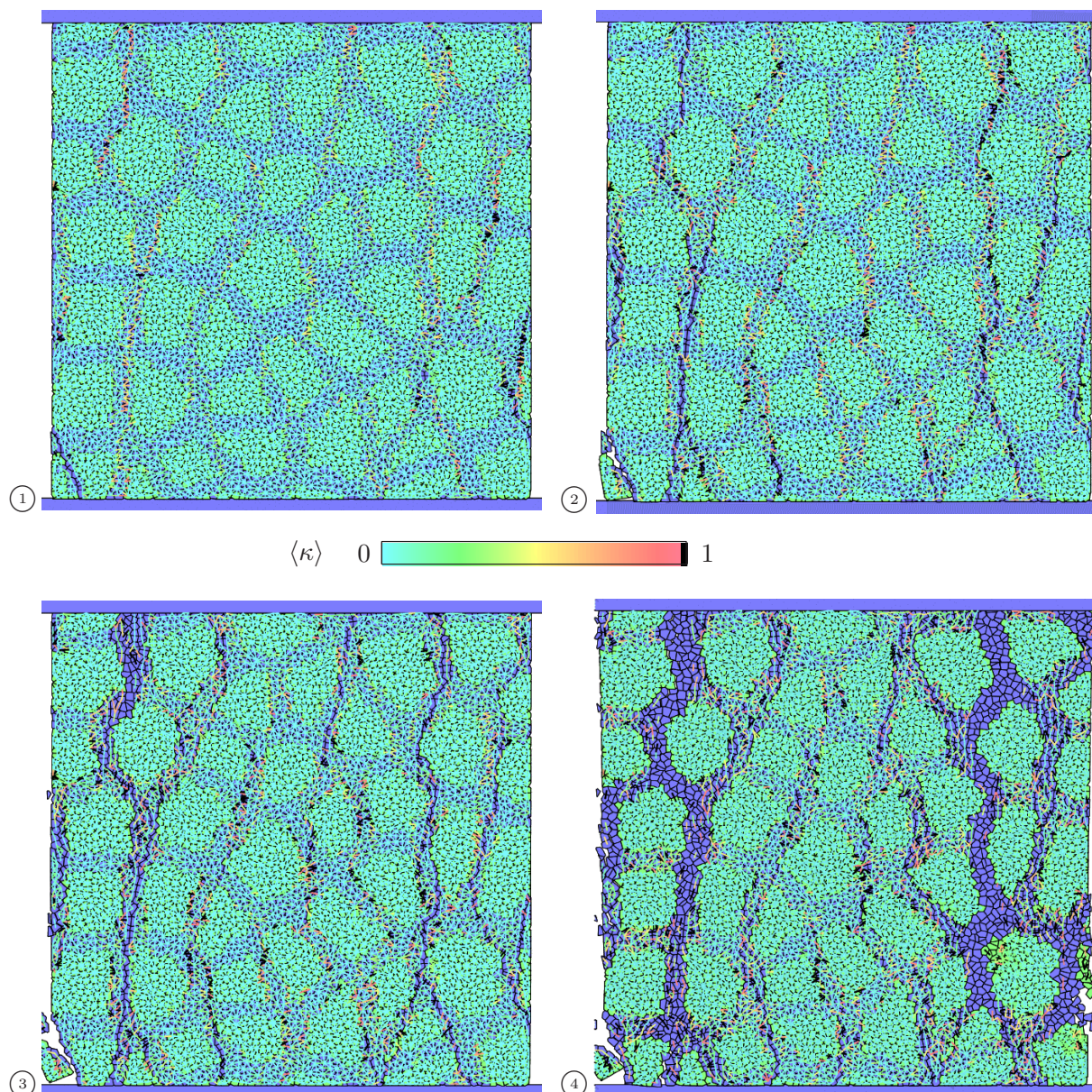
Figure 7.3: Graphical output of compression simulation.

7.2.2   Tension simulations

The load setup of the tension simulations was already discussed in sections 4.5.1 and 5.5.2. The strain measurement is accommodated as detailed in the previous section. Irrespective of the different material parameters of the target concretes to be compared with, the same DEM parameters as used in the compression simulations are considered in the tension simulations. In tension the experiments by *van Mier* [243] with a concrete with a maximum aggregate size $d_{max} = 1.6$ cm are considered, compare also figure 5.9 (b). Simulations with different aggregate sizes and varying dispersions of the yield stresses have been performed. The yield stresses have been statistically distributed for each interface about ± 10 %, ± 50 % and ± 90 % the average values. The exemplary results detailed below are concerned with a simulation series with a dispersion of the yield stresses of ± 50 % and inclusion of 220 aggregates. Thus, the aggregate size is smaller compared to
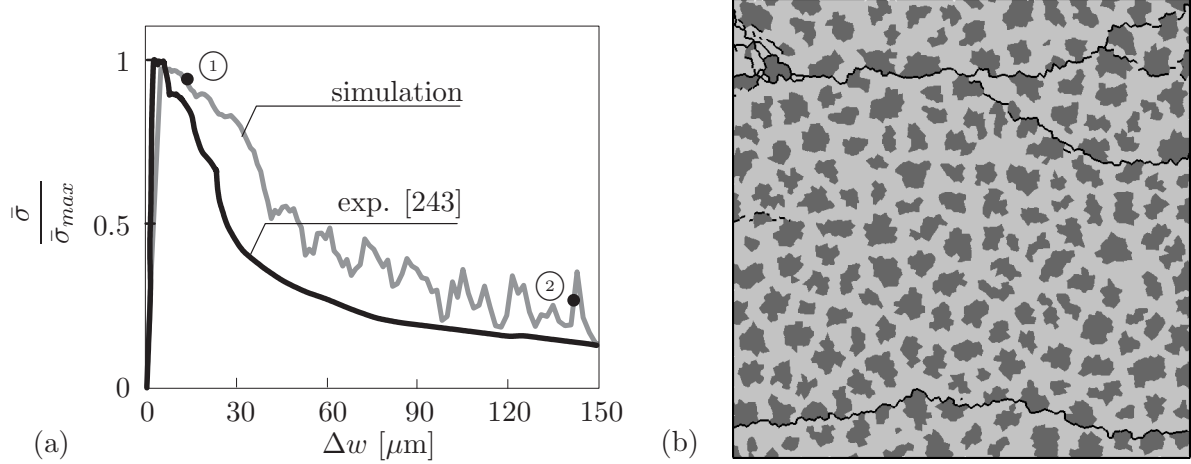
Figure 7.4: (a) Stress-displacement diagram of simulations and experiments by *van Mier* [243] and (b) eliminated bonds at stage ②.

the compression simulations. Smaller aggregate sizes have been considered to accommodate the smaller maximum aggregate size of the target material in mind. In the context of the realized implementation, the higher the amount of aggregates is chosen, the smaller is the corresponding aggregate size. This yields a higher volume fraction of matrix particles and, finally, a smaller effective stiffness of the composite sample. The 75 cm × 75 cm test sample was composed by 2145 particles representing the aggregates and 3354 particles representing the matrix. The fraction of aggregate volume to the complete volume amounts to 38.4 % and the ratio of aggregate to matrix volume to 0.623.

Figure 7.4 (a) compares the described simulation series and experimental results of a concrete with a maximum aggregate size $d_{max} = 1.6$ cm according to *van Mier* [243]. The crack width Δw is measured as difference between the top and bottom particles, as two macroscopically observable cracks appear, see figure 7.4 (b). The sample height is assumed as a representary crack zone with a finite width. The simulated peak stress is less than the experimental one by a factor of 2, if the parameter set of the compression simulation is used, i. e. no further adjustment of the parameter choice was undertaken. One reason for this difference is the uncertainty of the parameter choice, since the extraction of "real" parameters from laboratory tests for a definition of the model parameters is not straightforward. Another reason concerns the different target concretes used for the comparisons in the compression and tension simulations. Therefore, the corresponding curves are given in a normalized format by scaling the stresses by the respective maximum stress. Besides this point, the course of the simulated and experimental curves agree qualitatively well. The post-peak behavior is more ductile than predicted by the experiments. In contrast to the tension simulations of the simple composite sample in chapter 5 and the experimental results, the tail of the corresponding graph in figure 7.4 is higher. Probably, this means that the fracture energy choice used in the previous section is slightly to high. This is not astonishing at all, as the parameters have been pre-optimized for the compression simulations and the corresponding material parameters. As the concrete tested by *Vonk* differs from that used by *van Mier* with regard to the different key material parameters, this behavior is quite comprehensible.
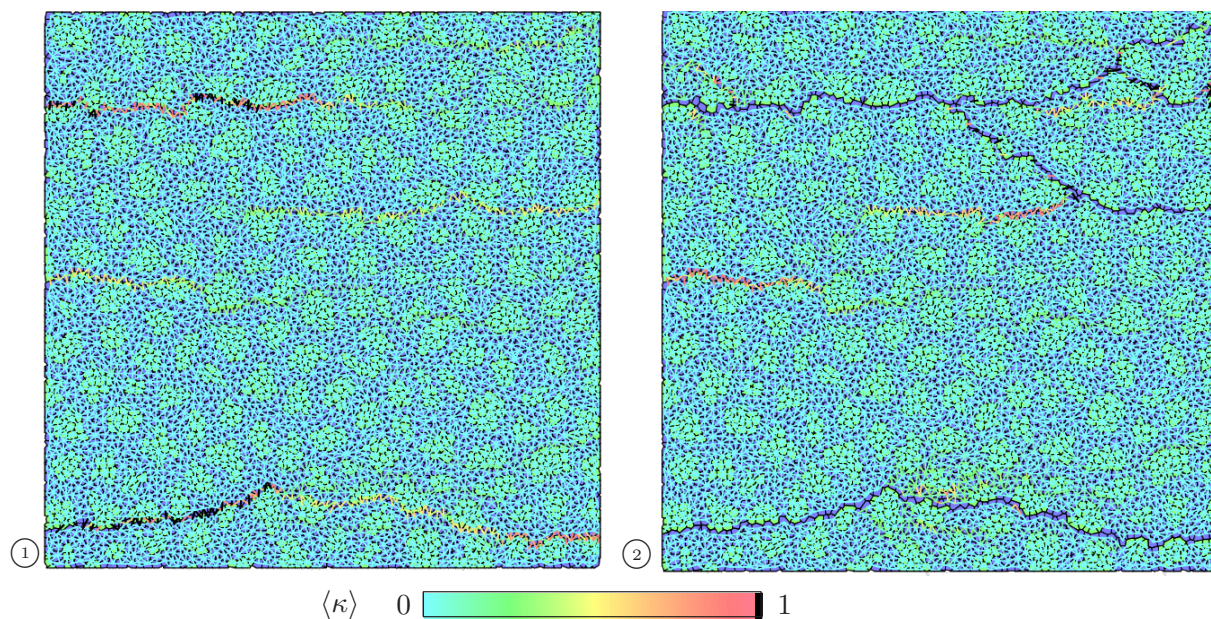
Figure 7.5: Graphical output of tension simulation.

The snapshot in form of the simplified picture of eliminated interface elements in figure 7.4 (b) highlights the crack propagation through the specimen. As expected, only cracks in the horizontal direction and, thus, perpendicular to the loading direction are obtained. The cracks appear mostly at the "interface" between aggregate and matrix and fit quite well to the cracking in concrete, compare figure 1.1 (a). In figure 7.5 the softening stadium of the interface elements is displayed at two time stages, one at the beginning of the post-peak regime, ①, and one at a later stage of the post-peak regime, ②. At stage ① practically no interface element has been eliminated and only few interface elements are near to the fully softened state $\langle\kappa\rangle = 1$ marked by the black color. The localization zones appear parallel to each other and are initiated by independently arising softening elements at the "interface" between aggregates and matrix. The yellow, red and black colored line connections at stage ① emphasize this behavior. In the later stage ② some of these zones evolve into macroscopically observable cracks and join together in the upper part of the specimen. However, at this time stage still a considerable load transfer is obtained, i. e. although the specimen seems completely torn into two parts, various horizontal interface elements (normal vector on the interface element points in the horizontal direction) withstand the cracking mechanism. These interface elements are still able to transfer load in the vertical direction via shear forces, compare also the discussion in the context of figure 5.10. A possible reason for the appearance of more than one main crack can be attributed to the fact that a higher sensitivity with regard to induced waves is present for certain interface elements. In particular, those interface elements which represent the interface layers between aggregates and matrix are concerned. This seems conceivable, as the stiffness difference between the interface layers' and aggregates' interface elements amounts to a factor of approximately 30.

7.3 Discussion

Microstructure-based interface enhanced DEM simulations are an effective approach to remedy the deficiencies of non-microstructure simulations. The inclusion of a microstructure via the definition of corresponding stiffnesses and yield stresses has shown up to be an important feature for a realistic representation of the post-peak softening behavior in terms of the stress-strain relation. With increasing complexity and, therewith, degree of freedom of the model all characteristics of a cohesive frictional material can be represented, compare the schematic figure 7.6. Admittedly, the increasing complexity is at the expense of the choice and definition of material and model parameters. Starting from the standard DEM model with a total number of 6 parameters and the beam enhanced DEM model with 9 parameters over the interface enhanced DEM model with 13 parameters, the microstructure-based interface enhanced DEM model includes the definition of 18 independent parameters. This fact may be seen as a disadvantage of the procedure, as typically material parameters should be physically coherent and directly determined by experiments. Indeed, alternative models which account for a simplified form of the microstructure and enable a reduction of the number of parameters, but still allow for a quantification of the softening regime are also conceivable: for example, by a physically coherent distribution of yield strengths and stiffnesses of the interface elements. As future perspective, the procedures for a quantification of the parameters should be advanced. A first step is a direct identification of model parameters by simple tests on "model" composite materials. For example, a "model" material can be created which is composed by regular polygonal particles embedded in a soft matrix with glue between matrix and particles. Then, all micromechanical material parameters of the model can be directly identified. If this point is satisfactorily solved, a real microstructure-based DEM environment should be considered. This represents the last point in the process of increasing complexity, see figure 7.6. Then, an interface module between a digital image processing tool that is capable to handle electron microscopy images and the mesh generation module of the DEM program may be incorporated.
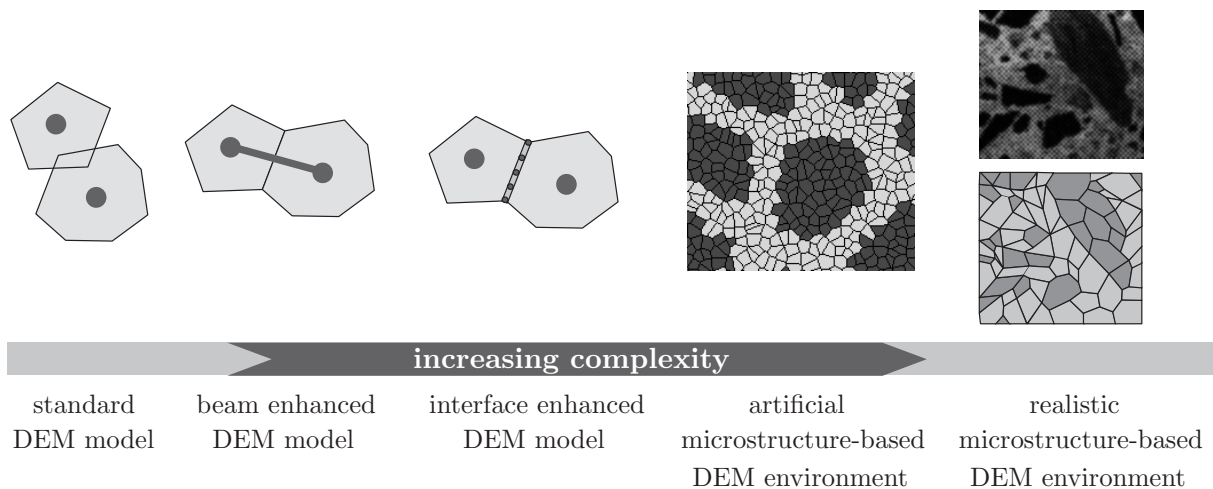
Figure 7.6: Grading of investigated DEM models with respect to complexity.

Chapter 8

From particle models to micropolar continua

In the second part of this thesis, the formal realization of the micro to macro transition from the particle to the macro level by means of different homogenization approaches is addressed. The present chapter is dedicated to the numerical verification of the transition from particle models to micropolar continua and chapter 9 refers to the respective transition to gradient continua. In more detail, the focal point of the next two chapters concerns the development and numerical implementation of adequate homogenization procedures in order to link particle quantities on the micro scale to comparable continuum mechanical quantities on the macro scale. For this, one starts from a standard continuum on the micro scale and obtains an enhanced continuum on the macro scale. On the one hand, based on the information on the particle scale average continuum mechanical quantities are derived. On the other hand, a formalism that motivates enhanced continuum theories by means of types of micropolar and gradient theories is presented. In this context one of the key interests to be investigated, is the role of the internal length scale and its relation to the width of evolving localization zones. In doing so, the results on the evolution of failure zones obtained in the context of the presented simulations are examined from a different point of view. Use is made of the explicitly prescribed microstructures by means of given particle meshes and their relation to the internal length scale.

Typically, the connection of effects or quantities on different levels of observation is realized by so-called micro to macro transitions, which in our context may simply be interpreted as homogenization processes. However, micro to macro transitions and the associated problems are not restricted to physics or engineering in the narrow sense. There is no doubt that this terminology stands for more than that: In various areas of science like mathematics, economics, sociology or politics, just to name some examples, micro to macro transitions play central roles when one must bridge the scales between different levels of "size" in the general sense. The term "size" is a general placeholder. In engineering it may stand for a geometrical measure, but e. g. in economics for the amount of cash flow or for the group size in sociology. Certainly, the realizations are different than those in mind here, but the global frame and the basis are the same.

In the context of engineering and, in particular, within the description of cohesive and non-cohesive granular media basic work on the formal realization of these transitions can be traced back to articles by *Christoffersen et al.* [39], *Cundall et al.* [47], *Drescher & De Josseling De Jong* [74] or *Rothenburg & Selvadurai* [209]. Increasing computational power aligned with a growing interest in the incorporation of microstructural effects into simulation models resulted in a variety of contributions in the last years, see *Bagi* [8], *Cambou et al.* [29], *Kruyt & Rothenburg* [135] or *Liao et al.* [149]. Moreover, the development of micro to macro procedures was one of the central points of the research

group *Modelling of Cohesive-Frictional Materials as Continuum and Discontinuum* at the University of Stuttgart. The research progress is documented by the proceedings of *Vermeer et al.* [249] or selected publications on this topic by the group members *D'Addetta et al.* [54], *Ehlers et al.* [77], *Kuhl et al.* [138], *Lätzel et al.* [145] or *Luding et al.* [157].

8.1 General

Starting from the formulation of a *continuum with microstructure* according to *Mindlin* [172], the special case of a micropolar theory was obtained in chapter 2: If *Mindlin's continuum* is represented as microscopic rigid body rather than as sub-continuum at the material point level, it ends up with a micropolar theory. Early theoretical work on micropolar theories can be traced back to the brothers *Cosserat* [43] in the early 20th century. Their ideas were later reappraised by *Eringen* [79], *Günther* [96], *Nowacki* [187] or *Schaefer* [213]. Experimental evidence of Cosserat-type continua by detection of rotations in deforming solids have been found by model materials like the well known *Schneebeli* materials according to the work of *Bogdanova-Bontcheva & Lippmann* [23] or *Schneebeli* [218]. Experimental realizations of real geomaterials like deformed sand samples emphasize the occurrence of rotating grains as a basic micromechanical failure mechanism. DEM simulations like those presented in section 3.6 and further discussed in section 6.2.1 support this fact. In this thesis a linear micropolar theory according to section 2.2 is deployed and, thus, only small displacements and strains are treated. Since the regularizing influence of micropolar theories on the numerical solution of localization simulations by means of the FEM has been recognized in the 1990's, an increasing interest in the numerical involvement of micropolar theories is noticed, cf. *de Borst* [60], *Dietsche* [69], *Mühlhaus & Vardoulakis* [181], *Steinmann & Willam* [230] or *Volk* [251]. However, a general, physically coherent motivation of the internal length, that in the simplest case is simply represented by an additional parameter in the constitutive law, is lacking, compare *Mühlhaus* [178], *Ramm et al.* [205, 206] and *Vermeer et al.* [249]. For the case of a micropolar continuum the internal length relates the couple stress tensor $\bar{\mathbf{M}}$ to the curvature tensor $\bar{\boldsymbol{\kappa}}$ via $\bar{\mathbf{M}} = 2\mu_c l_c^2 \bar{\boldsymbol{\kappa}}$. This parameter cannot be identified with material specific quantities like the grain size in a granular material so far. Generally, the internal length can be estimated by a fit of numerically simulated boundary value problems to experimental results via an inverse modeling technique, compare *Kuhl* [137] and *Mahnken & Kuhl* [160]. One motivation of this internal length scale from a theoretical point of view is given in *Volk* [251] and *Volk et al.* [252]. An alternative justification along the lines of *D'Addetta et al.* [53], *D'Addetta et al.* [54], *Diebels & Ehlers* [65] and *Ehlers et al.* [77] will be presented in this thesis.

The key question that arises in this context is:

> *How large has a RVE to be in order to provide continuum mechanical quantities that are comparable to macroscopic quantities, but still mirror the locality of a discrete system?*

In this regard, the general goal of this chapter is, on the one hand, to derive average standard and micropolar quantities and, on the other hand, to give a motivation of a micropolar theory as example of a regularization theory. Starting from the balance laws of

single particles and embedded particles across to the balance laws of embedded ensembles of particles, a methodology for the computation of couple stresses is derived. Kinematic and energetic quantities according to section 2.2.3 are deduced in a similar fashion. Finally, a numerical validation by means of representative examples proves the efficiency of the proposed method.

8.2 Balance laws

8.2.1 Balance laws for individual particles

Basic results of rigid body dynamics as well as of mechanics of deformable bodies are recalled in this section according to *Ehlers et al.* [77]. These results represent the onset of the homogenization process applied to single particles and to ensembles of particles in order to compute macroscopic stresses and couple stresses from the distribution of contact forces.

The motion of a single rigid or deformable particle $\mathcal{P}_{mic}$ of arbitrary shape is described by the translation of its center of mass and by the rotation around it. In accordance with chapter 2 single particles are denoted by $\mathcal{P}_{mic}$ and the macroscopic body as $\mathcal{B}$. The mass m and position vector of the center of mass $\mathbf{x}_M$ of $\mathcal{P}_{mic}$ are given by

$$m = \int_{\mathcal{P}_{mic}} \mathrm{d}m = \int_{\mathcal{P}_{mic}} \rho \, \mathrm{d}v \,, \qquad\qquad \mathbf{x}_M = \frac{1}{m} \int_{\mathcal{P}_{mic}} \mathbf{x} \, \mathrm{d}m \,, \qquad (8.1)$$

where $\mathrm{d}m$ is the mass element, ρ the mass density and $\mathrm{d}v$ the volume element of $\mathcal{P}_{mic}$. The introduction of the local position vector $\bar{\mathbf{x}}$ relative to the center of mass M via $\mathbf{x} = \mathbf{x}_M + \bar{\mathbf{x}}$, compare figure 8.1, and the combination with the definition $(8.1)_2$ yields $\int_{\mathcal{P}_{mic}} \bar{\mathbf{x}} \, \mathrm{d}m = \mathbf{0}$. In the following, based on the basic principles in section 2.1.3 balances of momentum and angular momentum for a rigid and deformable particle as well as for a micropolar continuum are summarized. In case of particle mechanics one is interested in the balance of momentum of rigid particles in a global form rather than in a local form

$$m\ddot{\mathbf{x}}_M = \mathbf{k} \,, \qquad (8.2)$$

with the external forces $\mathbf{k}$ according to equation (2.5) with $\mathcal{S} = \partial \mathcal{P}_{mic}$ and $\mathcal{B} = \mathcal{P}_{mic}$. The term global refers to the validity of a balance law for a complete particle, while the term local refers to a validity for one single material point. Thus, a global relation is accomplished in an integral sense. This means that at each point within a particle $\mathcal{P}_{mic}$ a stress tensor can be defined, which, however, in the present context is not of interest, since the stresses on the particle, RVE and macro level are needed. If a deformable particle is considered, upon consideration of the Cauchy theorem one obtains the balance of momentum either in the global or local form, recall also equations (2.7) or (2.11),

$$\int_{\mathcal{P}_{mic}} \rho \ddot{\mathbf{x}} \, \mathrm{d}v = \int_{\mathcal{P}_{mic}} (\mathrm{div} \, \mathbf{T} + \rho \mathbf{b}) \, \mathrm{d}v \,, \qquad\qquad \rho \ddot{\mathbf{x}} = \mathrm{div} \, \mathbf{T} + \rho \mathbf{b} \,. \qquad (8.3)$$

The balance of angular momentum of rigid particles is defined with respect to an arbitrary, but fixed point in space, namely the origin $\mathcal{O}$. The insertion of the mass tensor of
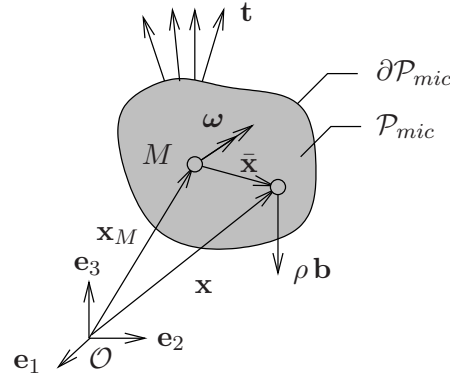
Figure 8.1: Forces acting on a single particle $\mathcal{P}_{mic}$.

inertia $\boldsymbol{\Theta}_M$, the angular velocity of the rigid body motion $\boldsymbol{\omega}$ and the corresponding skew-symmetric gyration tensor $\boldsymbol{\Omega}$ leads to two separate statements

$$\mathbf{x}_M \times m\ddot{\mathbf{x}}_m = \mathbf{x}_M \times \mathbf{k}\,,$$
$$\boldsymbol{\Theta}_M \cdot \dot{\boldsymbol{\omega}} + 2\mathrm{sym}(\boldsymbol{\Omega} \cdot \boldsymbol{\Theta}_M) \cdot \boldsymbol{\omega} = \mathbf{m}_M\,. \tag{8.4}$$

The second relation is generally known as Euler's gyration equation and has the property of an axiom, while the first one is a result of the momentum balance. The interested reader is referred to appendix D.1 for a more detailed derivation and discussion of the angular momentum balance in the context of rigid body mechanics and the role of Euler's gyration equation therein. In the limit of a particle $\mathcal{P}_{mic}$ reducing to a mathematical point the values of $|\bar{\mathbf{x}}|$ vanish, cf. figure 8.1. Then, both the moments $\mathbf{m}_M$ of $\mathcal{P}_{mic}$ with respect to M and the tensor of inertia $\boldsymbol{\Theta}_M$ vanish, too, and only equation $(8.4)_1$ remains. In the case of deformable particles one obtains the global and local form of the balance of angular momentum

$$\int_{\mathcal{P}_{mic}} \mathbf{x} \times \rho\ddot{\mathbf{x}}\,\mathrm{d}v = \int_{\mathcal{P}_{mic}} (\mathrm{div}\,\mathbf{M} + \mathbf{x} \times \rho\mathbf{b})\mathrm{d}v\,, \qquad \mathbf{x} \times \rho\ddot{\mathbf{x}} = \mathrm{div}\,\mathbf{M} + \mathbf{x} \times \rho\mathbf{b}\,. \tag{8.5}$$

According to section 2.2.3 $\mathbf{M}$ denotes the couple stresses density. Application of $\mathrm{div}\,\mathbf{M} = \mathbf{I} \times \mathbf{T} + \mathbf{x} \times \mathrm{div}\,\mathbf{T}$ provides two different statements of the local form

$$\mathbf{x} \times \rho\ddot{\mathbf{x}} = \mathbf{x} \times (\mathrm{div}\,\mathbf{T} + \rho\mathbf{b})\,,$$
$$\mathbf{0} = \mathbf{I} \times \mathbf{T}\,. \tag{8.6}$$

Again, as in equation (8.4) only the second relation includes the axiom of the angular momentum balance, while the first one results from the momentum balance. It is well known that equation $(8.6)_2$ yields a symmetric Cauchy stress, see section 2.1.3. If, by definition, a continuous body is considered as a Cosserat continuum, the following balance of angular momentum in the global form is obtained

$$\int_{\mathcal{P}_{mic}} \left[\mathbf{x} \times \rho\ddot{\mathbf{x}} + \rho(\bar{\boldsymbol{\Theta}} \cdot \bar{\boldsymbol{\omega}})^{\cdot}\right] \mathrm{d}v = \int_{\mathcal{P}_{mic}} \left[\mathrm{div}\,(\tilde{\mathbf{M}} + \bar{\mathbf{M}}) + \mathbf{x} \times \rho\mathbf{b} + \rho\mathbf{c}\right] \mathrm{d}v\,. \tag{8.7}$$

$\bar{\boldsymbol{\Theta}}$ is defined as symmetric tensor of microinertia, $\bar{\boldsymbol{\omega}}$ represents the total rotational velocity composed by both the continuum rotation and the independent Cosserat rotation and, recalling the definitions in section 2.2.3, $\rho\mathbf{c}$ are the couple densities. Furthermore, $\mathbf{M}$ can be split up into the stress or continuum moment tensor $\tilde{\mathbf{M}}$ and the couple stress tensor $\bar{\mathbf{M}}$. Note that the couple stress tensor $\bar{\mathbf{M}}$ is related to the contact moments $\bar{\mathbf{m}}$ through the Cauchy theorem $\bar{\mathbf{m}} = \bar{\mathbf{M}} \cdot \mathbf{n}$. Again, the application of the rule for $\operatorname{div}\mathbf{M}$ (see above) results into two statements

$$\mathbf{x} \times \rho\ddot{\mathbf{x}} = \mathbf{x} \times (\operatorname{div}\mathbf{T} + \rho\mathbf{b})\,,$$
$$\rho(\bar{\boldsymbol{\Theta}} \cdot \bar{\boldsymbol{\omega}})^{\boldsymbol{\cdot}} = \mathbf{I} \times \mathbf{T} + \operatorname{div}\bar{\mathbf{M}} + \rho\mathbf{c}\,. \tag{8.8}$$

The second relation includes the axiom of the angular momentum balance in the frame of micropolar continua. In contrast to equation $(8.6)_2$ leading to a symmetric stress $\mathbf{T}$, equation (8.8) yields a non-symmetric stress $\mathbf{T}$, whenever the continuum is micropolar. Furthermore, equation $(8.8)_2$ compares to equation $(8.4)_2$, if: the right hand side of equation $(8.8)_2$ is identified with the total local moment by contact and volume terms and the time differentiation on the left hand side of equation $(8.8)_2$ is realized utilizing a vanishing Green-Naghdi rate, cf. appendix D.1.

8.2.2 Balance laws for embedded particles

Generally, one is interested in the description of the macroscopic behavior of a granular medium by means of a body $\mathcal{B}$ consisting of a large amount of particles $\mathcal{P}_{mic}$ rather than in the behavior of a single particle $\mathcal{P}_{mic}$. Obviously, the macroscopic scale D of $\mathcal{B}$ is much larger than the characteristic dimension δ of a single particle $\mathcal{P}_{mic}$. Since the motion of the particles takes place on a scale $\varepsilon = \delta/D \ll 1$, the use of scale separation arguments yields simplified forms of the balances of momentum and angular momentum of single particles. As the volume of the particles decreases with order $\mathcal{O}(\varepsilon^3)$, while the corresponding surface decreases only with order $\mathcal{O}(\varepsilon^2)$, the volume terms in the corresponding balance equations can be neglected, compare also the remarks in appendix D.2. This assumption is valid for the limiting case of small particles embedded in a large particle ensemble, where a scale separation $\varepsilon \to 0$ according to section 2.3.1 is obtained. In addition to the presented formal derivation, the validity of the scale separation assumption will be numerically checked in the context of section 8.5.1. Starting from the balances of momentum and angular momentum for a rigid body in equations (8.2) and $(8.4)_1$, equilibrium conditions of forces are obtained. An insertion of the external forces according to equation (2.5) and application of the scale separation arguments yields

$$\mathbf{0} = \int\limits_{\partial\mathcal{P}_{mic}^{(i)}} \mathbf{t}\,\mathrm{d}a = \int\limits_{\mathcal{P}_{mic}^{(i)}} \operatorname{div}\mathbf{T}\,\mathrm{d}v\,, \qquad \mathbf{0} = \int\limits_{\partial\mathcal{P}_{mic}^{(i)}} \mathbf{x} \times \mathbf{t}\,\mathrm{d}a = \int\limits_{\mathcal{P}_{mic}^{(i)}} \operatorname{div}\mathbf{M}\,\mathrm{d}v\,. \tag{8.9}$$

Again, a symmetric stress at the particle level $\mathbf{T} = \mathbf{T}^T$ is recovered. Index i denotes an arbitrary particle of all particles N contained within a sample. In the context of rigid particles point contacts are preferred over area contacts due to their simplicity. This assumption is admissible as the contact zones are small compared to the particle surface. Then, the contact forces are given by discrete single forces $\mathbf{f}^{(i)c}$ that act at the contact point c. In analogy to the definitions in section 3.4.1, the contact vector $\mathbf{l}^{(i)c}$ points from

the mass center $\mathcal{M}^{(i)}$ of the particle $\mathcal{P}^{(i)}_{mic}$ to the contact point. Hence, the continuous equilibrium conditions in equation (8.9) reduce to discrete formulations over the number of contacts N^{Ci} of a particle i

$$\mathbf{0} = \int_{\partial \mathcal{P}^{(i)}_{mic}} \mathbf{t}\,\mathrm{d}a = \sum_{c=1}^{N^{Ci}} \mathbf{f}^{(i)c}, \qquad \mathbf{0} = \int_{\partial \mathcal{P}^{(i)}_{mic}} \bar{\mathbf{x}} \times \mathbf{t}\,\mathrm{d}a = \sum_{c=1}^{N^{Ci}} \mathbf{l}^{(i)c} \times \mathbf{f}^{(i)c}. \qquad (8.10)$$

Therein, $\mathbf{x} = \mathbf{x}_M + \bar{\mathbf{x}}$ and equation $(8.10)_1$ have been used to obtain equation $(8.10)_2$ from equation $(8.9)_2$.

8.2.3   Balance laws for embedded particle ensembles

If the scale difference between single particles $\mathcal{P}_{mic}$ on the micro scale and the whole body $\mathcal{B}$ on the macro scale is sufficiently large, a meso scale d can be introduced. This meso scale consists of an ensemble of particles in the sense of a RVE according to the remarks in section 2.3.1. Consider figure 8.2 for a graphical interpretation with regard to *Hashin's* [102] MMM principle $D \gg d \gg \delta$. Note that the partially detailed picture of the macroscopic body $\mathcal{B}$ in figure 8.2, left, is for visualization reasons only. The previously noted balance equations for a single and embedded particle are now formulated to capture the situation of embedded ensembles of particles. Under consideration of scale separation arguments the discrete position vectors of the mass centers $\mathbf{x}_M$ of individual particles $\mathcal{P}_{mic}$ can be understood as field quantities in the RVE with boundary $\partial \mathcal{R}$. This represents one of the key points in the context of the procedure in *Ehlers et al.* [77]. Then, the boundary of the RVE is represented by the mass centers of the bounding particles, cf. figures 8.2 and 8.3. This implies a statically equivalent transfer ("reduction") of the outward oriented contact forces acting on the outer boundary of the RVE to resultant forces and corresponding moments acting in the center of mass of the particles, see figure 8.3. This elegant way, whose general idea was firstly introduced by *Diebels & Ehlers* [65], here
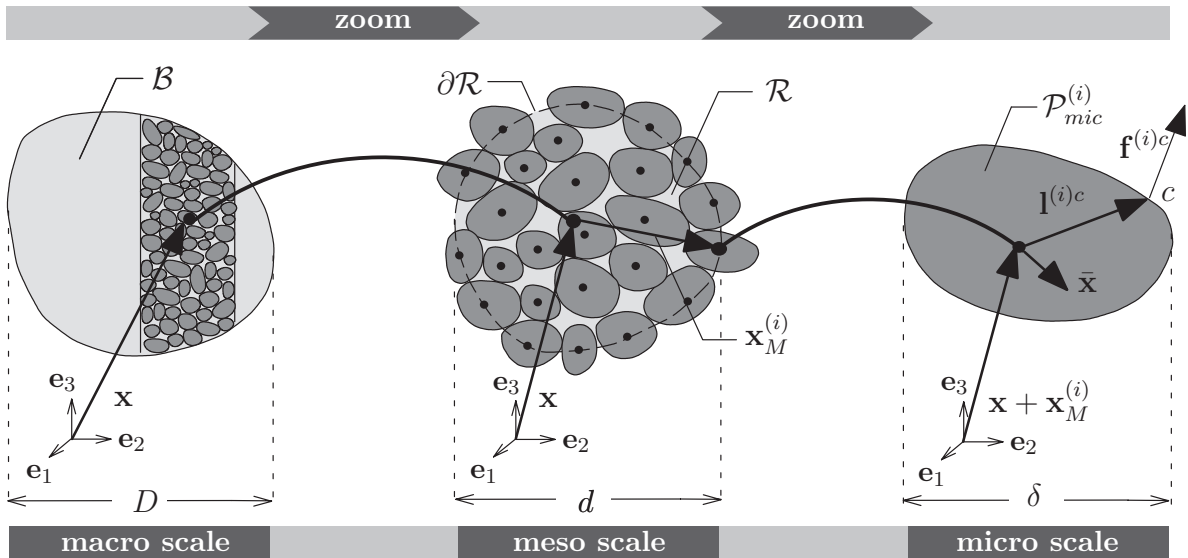
Figure 8.2: Body $\mathcal{B}$ consisting of ensembles of particles.
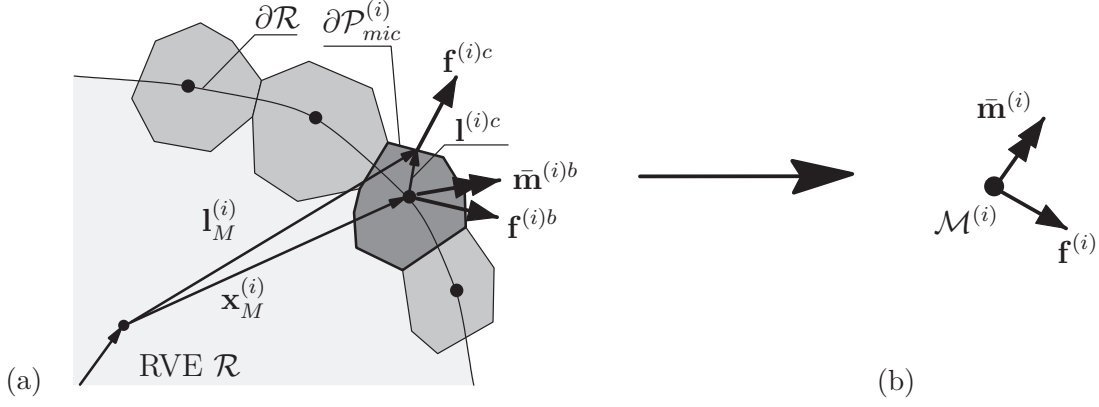
Figure 8.3: Boundary of the RVE: (a) Boundary particles with contact forces $\mathbf{f}^{(i)c}$ of one outward contact c and cohesive forces $\mathbf{f}^{(i)b}$ of one outward cohesive connection b and (b) resultant forces $\mathbf{f}^{(i)}$ and moments $\bar{\mathbf{m}}^{(i)}$ at center of boundary particle.

naturally yields boundary moments on the idealized RVE boundary. This applies even if cohesive components are not included. Note that the moment in figure 8.3 (a) is only obtained for the case of beams as cohesive components, since the beams act in the particle centers. For the case of interface elements no extra moment is included. The RVE boundary is identified by the polygon through the position vectors of the mass centers. The scale separation arguments implicate the motion of the particles in the RVE to take place on the scale $\varepsilon_\delta = \delta/d$, while the RVE deforms on the scale of the macroscopic body via $\varepsilon_d = d/D$. If $\varepsilon_\delta \ll 1$ and $\varepsilon_d \ll 1$, the simplified balance equations (8.9) of the particles hold in the RVE $\mathcal{R}$ and equivalent relations of the RVE hold in $\mathcal{B}$. On the RVE level this yields

$$\mathbf{0} = \int_{\partial\mathcal{R}} \mathbf{t}\, \mathrm{d}a\,, \qquad \mathbf{0} = \int_{\partial\mathcal{R}} (\mathbf{x}_M \times \mathbf{t} + \bar{\mathbf{x}} \times \mathbf{t})\, \mathrm{d}a\,. \qquad (8.11)$$

It is evident from the character of the RVE that the magnitude of the norms of $\mathbf{x}_M$ and of $\bar{\mathbf{x}}$ are of different size. Hence, one may interpret $\bar{\mathbf{x}} \times \mathbf{t}$ as the fluctuations of $\mathbf{x}_M \times \mathbf{t}$, comparable to the turbulence contributions to the fluid stresses in fluid mechanics. It should be pointed out that in addition to the restrictions of *Hashin's* [102] MMM principle, where one obtains $\varepsilon = \delta/D \ll 1$, $\varepsilon_\delta \ll 1$ and $\varepsilon_d \ll 1$, the existence of non-vanishing fluctuations also implies that $\varepsilon_d \ll \varepsilon_\delta$. Upon substitution of $\bar{\mathbf{m}} = \bar{\mathbf{x}} \times \mathbf{t}$ and application of the Cauchy together with the Gaussian integral theorem in equation (8.11) one obtains the global and local form of the RVE balances, respectively:

$$\mathbf{0} \;=\; \int_{\partial\mathcal{R}} \mathbf{t}\, \mathrm{d}a = \int_{\mathcal{R}} \mathrm{div}_M \mathbf{T}\, \mathrm{d}v\,, \qquad \mathbf{0} \;=\; \int_{\partial\mathcal{R}} (\mathbf{x}_M \times \mathbf{t} + \bar{\mathbf{x}} \times \mathbf{t})\, \mathrm{d}a = \int_{\mathcal{R}} \mathrm{div}_M (\tilde{\mathbf{M}} + \bar{\mathbf{M}})\, \mathrm{d}v\,,$$

$$\mathbf{0} \;=\; \mathrm{div}_M \mathbf{T}\,, \qquad\qquad \mathbf{0} \;=\; \mathrm{div}_M (\tilde{\mathbf{M}} + \bar{\mathbf{M}})\,. \qquad (8.12)$$

In analogy to $\mathrm{grad}_M(\cdot)$ denoting the gradient operator with respect to the field quantity $\mathbf{x}_M$, $\mathrm{div}_M(\cdot)$ denotes the divergence operator with respect to $\mathbf{x}_M$. The contact moment $\bar{\mathbf{m}}$ is defined via Cauchy's theorem as

$$\bar{\mathbf{m}} = \bar{\mathbf{M}} \cdot \mathbf{n} = (\bar{\mathbf{x}} \times \mathbf{T}) \cdot \mathbf{n} = \bar{\mathbf{x}} \times \mathbf{t}\,. \qquad (8.13)$$

Insertion of $\mathrm{div}_M \tilde{\mathbf{M}} = \mathbf{I} \times \mathbf{T} + \mathbf{x}_M \times \mathrm{div}_M \mathbf{T}$ into the local form of the RVE's angular momentum balance in equation $(8.12)_2$ yields

$$\mathbf{0} = \mathbf{I} \times \mathbf{T} + \mathrm{div}_M \bar{\mathbf{M}}. \qquad (8.14)$$

In contrast to the balance of momentum of an embedded particle in equation (8.9) that leads to a symmetric stress state on the particle level, equation (8.14) implies a non-symmetric stress $\mathbf{T}$ on the RVE level whenever couple stresses $\bar{\mathbf{M}}$ are present. From the definition of the couple stresses $\bar{\mathbf{M}}$ it is evident that $\bar{\mathbf{M}}$ vanishes with vanishing fluctuations $\bar{\mathbf{x}} \times \mathbf{t}$, i. e. for $|\bar{\mathbf{x}}| \to 0$. An RVE composed of individual particles embedded into a macroscopic body $\mathcal{B}$ represents a micropolar Cosserat continuum as long as $\bar{\mathbf{M}}$ exists and turns out to be a standard Boltzmann continuum for vanishing $\bar{\mathbf{M}}$. Thus, one of the key aims of this chapter, namely to motivate a micropolar continuum from the DEM methodology by providing a straightforward application of basic continuum mechanical principles and balance laws, was successful. If the RVE is considered as a continuum in the sense that it theoretically consists of a manifold of material points or particles, respectively, the number of boundary particles is independent of the size of $|\bar{\mathbf{x}}|$. This applies no matter whether or not $|\bar{\mathbf{x}}|$ tends to zero. On the other hand, realistic RVEs consist of a finite number of particles instead of a theoretical manifold of material points. Considering constant values of $|\bar{\mathbf{x}}|$, i. e. keeping the particle size fixed, a transition from a micropolar to a standard continuum can also be guaranteed. In this case the RVE volume has to be increased such that the ratio between the RVE radius and the particle radius increases. This is equivalent to an increasing ratio between the RVE volume and the RVE surface. Otherwise, the character of a micropolar continuum is maintained.

In order to apply the above results to the DEM model a transition from a continuous to a discrete representation is needed, i. e. the global balance equations $(8.12)_1$ are substituted by discrete statements. The boundary $\partial\mathcal{R}$ of the RVE consists of $N_{\partial\mathcal{R}}$ particles that have C^i outward oriented contacts and B^i outward oriented cohesive components (e. g. beams or interfaces). Thus, the balance of momentum with the force resultant $\mathbf{f}^{(i)}$ is constituted as a static force equilibrium at RVE level

$$\mathbf{0} = \int\limits_{\partial\mathcal{R}} \mathbf{t}\,\mathrm{d}a = \sum_{i=1}^{N_{\partial\mathcal{R}}} \mathbf{f}^{(i)}, \qquad \text{with} \qquad \mathbf{f}^{(i)} = \mathbf{f}_c^{(i)} + \mathbf{f}_{coh}^{(i)} = \sum_{c=1}^{C^i} \mathbf{f}^{(i)c} + \sum_{b=1}^{B^i} \mathbf{f}^{(i)b}. \qquad (8.15)$$

With the moment resultant $\bar{\mathbf{m}}^{(i)}$ represented by the sum of the contact (Cosserat) moments $\bar{\mathbf{m}}_c^{(i)}$ and the intrinsic moments of the cohesive components $\bar{\mathbf{m}}_{coh}^{(i)}$ per particle i

$$\bar{\mathbf{m}}^{(i)} = \bar{\mathbf{m}}_c^{(i)} + \bar{\mathbf{m}}_{coh}^{(i)} = \sum_{c=1}^{C^i} \mathbf{l}^{(i)c} \times \mathbf{f}^{(i)c} + \sum_{b=1}^{B^i} \bar{\mathbf{m}}^{(i)b} \qquad (8.16)$$

the balance of angular momentum in terms of discrete forces results

$$\mathbf{0} = \int\limits_{\partial\mathcal{R}} (\mathbf{x}_M \times \mathbf{t} + \bar{\mathbf{x}} \times \mathbf{t})\,\mathrm{d}a = \sum_{i=1}^{N_{\partial\mathcal{R}}} (\mathbf{x}_M^{(i)} \times \mathbf{f}_c^{(i)} + \bar{\mathbf{m}}^{(i)}). \qquad (8.17)$$

Therein, to be complete, in addition to the formulation presented in *D'Addetta et al.* [53] and *Ehlers et al.* [77] forces and moments of the cohesive components (beam or interface)

enter the formulation. The moments of the cohesive components that act on the boundary $\partial\mathcal{R}$ of the RVE are computed according to sections 4.3 and 5.2. It should be kept in mind that the contact moments $\bar{\mathbf{m}}_c^{(i)}$ per particle i are independent of the total force resultant $\mathbf{f}^{(i)}$ per particle i. In contrast to the image of a continuous body, where the abstract assumption $|\bar{\mathbf{x}}| \to 0$ led from a micropolar to a non-polar continuum, a limit analysis in the frame of particle ensembles (constituting the RVEs) generally exhibits non-vanishing moments $\bar{\mathbf{m}}_c^{(i)}$. Given realistic RVEs with constant reference volume this result is due to the following fact: Even if the particle size $|\mathbf{l}^{(i)c}|$ on the micro scale (order δ) is extremely small such that $|\mathbf{l}^{(i)c}|/d \to 0$ on the meso scale of the RVE (order d), the number $N_{\partial\mathcal{R}}$ of RVE boundary particles tends to infinity. Thereby, this applies whenever the RVE size does not shrink with the particle size. Hence, one generally obtains

$$\lim_{\substack{N_{\partial\mathcal{R}} \to \infty \\ |\mathbf{l}^{(i)c}|/d \to 0}} \sum_{i=1}^{N_{\partial\mathcal{R}}} \sum_{c=1}^{C^i} \mathbf{l}^{(i)c} \times \mathbf{f}^{(i)c} = a \quad \text{with} \quad a \neq 0 \,. \tag{8.18}$$

As a consequence, if the discontinuous microstructure of the RVE loaded by eccentric forces is replaced by an equivalent continuum loaded by discrete stresses and couple stresses, a Cosserat continuum is naturally obtained, compare *Diebels & Ehlers* [65] or *Ehlers et al.* [77].

8.3 Average quantities

The following sections are concerned with the derivation and definition of average quantities. Application of the results attained within the previous sections provides average dynamic quantities like stresses and couple stresses. This is supplemented by average kinematic and energetic quantities which are obtained by a straightforward transfer of the scale separation arguments introduced before.

8.3.1 Dynamic quantities

The presented chain of arguments allows for the usual homogenization approaches on the scale d of the RVE by relating average stress tensors to contact forces. Since the pioneering work of *Drescher & De Josseling De Jong* [74] on the calculation of average stresses and strains by photoelastic techniques (compare *Dantu* [56] on this topic) a variety of work in the context of averaging techniques coupled to the stress calculation of discrete media has been published. Since the introduction of the DEM in the 1970's immediately the question of mechanically funded expressions for average stresses and, later on, strains arose. The articles by *Christoffersen et al.* [39], *Cundall et al.* [47] and *Rothenburg & Selvadurai* [209] on the micromechanical definition of stresses in the early 1980's established the basis for a complete and coherent mechanical elaboration of the notion *average stress* in the course of the 1990's, compare among others *Bagi* [8], *Cambou et al.* [29], *Chang & Misra* [38] or *Kruyt* [134]. The process to find an equivalent definition of average kinematic quantities like the average strain has not come to an end yet, compare *Bagi & Bojtar* [9]. In the same manner as for the average stress, the average Cosserat couple stress tensor can be related to the boundary moments of the RVE. Starting from a generalized local form of equilibrium of forces and moments in equations $(8.12)_2$, via $\text{div}_M \mathbf{A} = \mathbf{0}$ and use of the

substitutes $\mathbf{A} = \mathbf{T}$ and $\mathbf{A} = \tilde{\mathbf{M}} + \bar{\mathbf{M}}$ one obtains the quasi-static balances of momentum and angular momentum. The combination of the two familiar calculation rules

$$\mathbf{A}^T = \mathbf{I} \cdot \mathbf{A}^T = (\text{grad}_M \mathbf{x}_M) \cdot \mathbf{A}^T , \quad \text{div}_M(\mathbf{x}_M \otimes \mathbf{A}) = (\text{grad}_M \mathbf{x}_M) \cdot \mathbf{A}^T + \mathbf{x}_M \otimes \text{div}_M \mathbf{A} \quad (8.19)$$

yields

$$\mathbf{A}^T = \text{div}_M(\mathbf{x}_M \otimes \mathbf{A}) - \mathbf{x}_M \otimes \text{div}_M \mathbf{A} \quad (8.20)$$

as starting point of the formal averaging process. The definition of $\text{div}_M(\cdot)$ and $\text{grad}_M(\cdot)$ is given in section 8.2.3. Application of *Hill's* [108] averaging definition in equation (2.38) in conjunction with the above calculation rule, an extended Gaussian theorem and the generalized form of equilibrium $\text{div}_M \mathbf{A} = \mathbf{0}$ results in

$$
\begin{aligned}
\langle \mathbf{A} \rangle^T &= \frac{1}{V_\mathcal{R}} \int_{\partial \mathcal{R}} (\mathbf{x}_M \otimes \mathbf{A}) \cdot \mathbf{n} \, da - \frac{1}{V_\mathcal{R}} \int_\mathcal{R} \mathbf{x}_M \otimes \underbrace{\text{div}_M \mathbf{A}}_{= \, 0} \, dv \\
&= \frac{1}{V_\mathcal{R}} \int_{\partial \mathcal{R}} \mathbf{x}_M \otimes (\mathbf{A} \cdot \mathbf{n}) \, da .
\end{aligned}
\quad (8.21)
$$

$V_\mathcal{R}$ represents the volume of the RVE under consideration. Identification of $\mathbf{A} = \mathbf{T}$, application of the transposition, use of the divergence theorem and the transition from the continuous to the discrete formulation by use of equation (8.15) leads to the well known average Cauchy stress tensor, see also *Cundall* [47] or *Drescher & De Josseling De Jong* [74]:

$$\langle \mathbf{T} \rangle = \frac{1}{V_\mathcal{R}} \sum_{i=1}^{N_{\partial \mathcal{R}}} \mathbf{f}^{(i)} \otimes \mathbf{x}_M^{(i)} . \quad (8.22)$$

Thus, the average RVE stress is given by the product of the resultant forces per particle $\mathbf{f}^{(i)}$ acting on the boundary of the RVE and the position vectors of the mass centers of the boundary particles $\mathbf{x}_M^{(i)}$. Note that in the general case $\mathbf{f}^{(i)}$ is composed by the contact and cohesive forces. The choice $\mathbf{A} = \tilde{\mathbf{M}} + \bar{\mathbf{M}}$, application of the transposition and use of the Cauchy theorem in equation (8.13) along with the Cauchy theorem applied to $\tilde{\mathbf{M}}$ by

$$\tilde{\mathbf{M}} \cdot \mathbf{n} = (\mathbf{x}_M \times \mathbf{T}) \cdot \mathbf{n} = \mathbf{x}_M \times \mathbf{t} \quad (8.23)$$

in analogy to the above procedure yields

$$
\begin{aligned}
\langle \tilde{\mathbf{M}} + \bar{\mathbf{M}} \rangle &= \frac{1}{V_\mathcal{R}} \int_{\partial \mathcal{R}} \left[(\tilde{\mathbf{M}} + \bar{\mathbf{M}}) \cdot \mathbf{n} \right] \otimes \mathbf{x}_M \, da \\
&= \frac{1}{V_\mathcal{R}} \int_{\partial \mathcal{R}} (\mathbf{x}_M \times \mathbf{t}) \otimes \mathbf{x}_M \, da + \frac{1}{V_\mathcal{R}} \int_{\partial \mathcal{R}} \bar{\mathbf{m}} \otimes \mathbf{x}_M \, da .
\end{aligned}
\quad (8.24)
$$

Recall that $\tilde{\mathbf{M}} = \mathbf{x}_M \times \mathbf{T}$ represents the stress or continuum moment (moment of the stress distribution), while $\bar{\mathbf{M}}$ represents the couple stress tensor of the Cosserat theory. Transition from the continuous formulation of equation (8.24) to a discrete formulation by use of equations (8.17) and (8.16) and subsequent extraction via a separation by reasons according to *Ehlers et al.* [77] leads to the stress moment and couple stresses in the

discrete form

$$\langle \tilde{\mathbf{M}} \rangle = \frac{1}{V_{\mathcal{R}}} \sum_{i=1}^{N_{\partial\mathcal{R}}} (\mathbf{x}_M^{(i)} \times \mathbf{f}^{(i)}) \otimes \mathbf{x}_M \,, \qquad \langle \bar{\mathbf{M}} \rangle = \frac{1}{V_{\mathcal{R}}} \sum_{i=1}^{N_{\partial\mathcal{R}}} \bar{\mathbf{m}}^{(i)} \otimes \mathbf{x}_M^{(i)} \,. \qquad (8.25)$$

Hence, the average RVE couple stresses are computed in a similar fashion as the average stresses in equation (8.22). $\langle \bar{\mathbf{M}} \rangle$ follows from the product of the resultant boundary moments $\bar{\mathbf{m}}^{(i)}$ per particle and the position vectors $\mathbf{x}_M^{(i)}$ of the mass centers of the boundary particles. Note again that in the general case $\bar{\mathbf{m}}^{(i)}$ is composed by the contribution of the contact and cohesive forces according to equation (8.16).

In conclusion, it has been shown that an independent couple stress tensor $\bar{\mathbf{M}}$ can be formally derived for an ensemble of particles. The derivation is based on the moments which result from the "reduction" of the distributed forces acting from outside of the RVE on the boundary particles. It becomes evident that moments on an intermediate scale are necessary in order to transfer the particle methodology via a homogenization procedure into a resulting enhanced continuum theory, namely a macroscopic Cosserat approach. This procedure is successful solely for the case that in addition to the MMM principle the inequality $\varepsilon_d \ll \varepsilon_\delta$ holds. The character of micropolarity is maintained even in the case of decreasing particle sizes as far as the RVE size does not decrease in the same manner, compare equation (8.18). Otherwise, if the RVE decreases to the particle size, i. e. the RVE is identified by a single particle, the stress tensor becomes symmetric and the couple stresses tend to zero, as the moments vanish. As result the micropolar continuum changes to a standard non-polar continuum.

If one plans to embed the above results into continuum mechanical problems on a macro scale, e. g. in form of a multiscale approach, the stresses $\mathbf{T}$ and couple stresses $\bar{\mathbf{M}}$ at a specific material point are replaced by the averages $\langle \mathbf{T} \rangle$ and $\langle \bar{\mathbf{M}} \rangle$ computed by an evaluation at the RVE level. For example, a multiscale approach based on a micropolar continuum may be solved by the FEM on the macro scale and by the DEM on the micro scale. This implies the solution of a boundary value problem on the macro scale which is based on the weak forms of equilibrium in equations (8.3)$_2$ and (8.8)$_2$. Thereby, the average stresses and couple stresses are computed by an evaluation of corresponding RVEs on the meso scale. This procedure gives a natural definition of occurring couple stresses and non-symmetric stress states without introducing debatable constitutive laws for the couple stresses as described in section 8.1, compare also *de Borst* [60] or *Dietsche* [69]. An example in the context of macroscopic gradient models has recently been reported by *Kouznetsova* [128, 129]. This approach is based on a FEM modeling on both the macro and the micro scale and seems to be fairly promising. A more detailed discussion on multiscale models is embedded in the next chapter.

8.3.2 Kinematic quantities

The same chain of arguments as presented above leads to average kinematic variables according to *D'Addetta et al.* [54]. In the context of the particle assembly kinematics the deformation and rotation of each particle on the boundary of a RVE is known. As the kinematic setting of the particle model includes rotational degrees of freedom, the kinematics of a micropolar continuum is resembled. Application of the known averaging principles yields definitions of volumetric averages of strain and curvature measures. The

formal procedure implies at first the formation of an integral over the volume $V_\mathcal{R}$ of the RVE. In a second step, a reformulation based on the divergence theorem leads to an integral over the boundary $\partial\mathcal{R}$ of the RVE.

In contrast to the calculation of the dynamic quantities, the calculation of the kinematic quantities is more expensive, since the formal integration over the boundary of the RVE is more sophisticated. Recall that in the case of the dynamic quantities also an integration over the boundary was involved, however, there the quantities have already been "discretized" prior to the integration. Under consideration of linear displacement and rotation fields the formal integration simplifies to a summation, as shown for the integration of the displacements in figure 8.4. In this figure the detail of the boundary of a RVE is shown along with the numbering used in the forthcoming equations. The unit normal $\mathbf{n}^i$ on the boundary segment i as well as the width of one boundary segment Δw^i are stored at the start of the simulation. Δw^i is the distance between the centers of two neighboring boundary particles. Following the outlined procedure one obtains the average symmetric and skew symmetric strains for a linear kinematics according to the general formulation in equation (2.32)

$$
\begin{aligned}
\langle \bar{\boldsymbol{\varepsilon}}_{sym} \rangle &= \frac{1}{V_\mathcal{R}} \int\limits_{\partial\mathcal{R}} \frac{1}{2} \left(\mathbf{u} \otimes \mathbf{n} + \mathbf{n} \otimes \mathbf{u} \right) \mathrm{d}a \\
&= \frac{1}{V_\mathcal{R}} \sum_{i=1}^{N_{\partial\mathcal{R}}} \frac{1}{4} \Delta w^i \left[(\mathbf{u}^i + \mathbf{u}^{i+1}) \otimes \mathbf{n}^i + \mathbf{n}^i \otimes (\mathbf{u}^i + \mathbf{u}^{i+1}) \right] ,
\end{aligned}
\tag{8.26}
$$

$$
\begin{aligned}
\langle \bar{\boldsymbol{\varepsilon}}_{skw} \rangle &= \frac{1}{V_\mathcal{R}} \int\limits_{\partial\mathcal{R}} \frac{1}{2} \left(\mathbf{u} \otimes \mathbf{n} - \mathbf{n} \otimes \mathbf{u} \right) \mathrm{d}a + \frac{1}{V_\mathcal{R}} \int\limits_{V_\mathcal{R}} \overset{3}{\mathbf{E}} \, \bar{\boldsymbol{\varphi}} \, \mathrm{d}v \\
&= \frac{1}{V_\mathcal{R}} \sum_{i=1}^{N_{\partial\mathcal{R}}} \frac{1}{4} \Delta w^i \left[(\mathbf{u}^i + \mathbf{u}^{i+1}) \otimes \mathbf{n}^i - \mathbf{n}^i \otimes (\mathbf{u}^i + \mathbf{u}^{i+1}) \right] + \frac{1}{V_\mathcal{R}} \overset{3}{\mathbf{E}} \sum_{i=1}^{N_\mathcal{R}} V^i \bar{\boldsymbol{\varphi}}^i .
\end{aligned}
\tag{8.27}
$$

$N_\mathcal{R}$ defines the number of particles within the RVE and $N_{\partial\mathcal{R}}$ denotes the number of segments of the polygon formed by the boundary of the RVE, i. e. the number of boundary particles. Note that the information (displacement, rotation etc.) of the first particle of the RVE boundary ($i = 1$) is saved twice for technical reasons, e. g. $\mathbf{u}^{i+1} = \mathbf{u}^1$ for $i = N_{\partial\mathcal{R}}$. Since the second term of the skew-symmetric part of the strain tensor contains
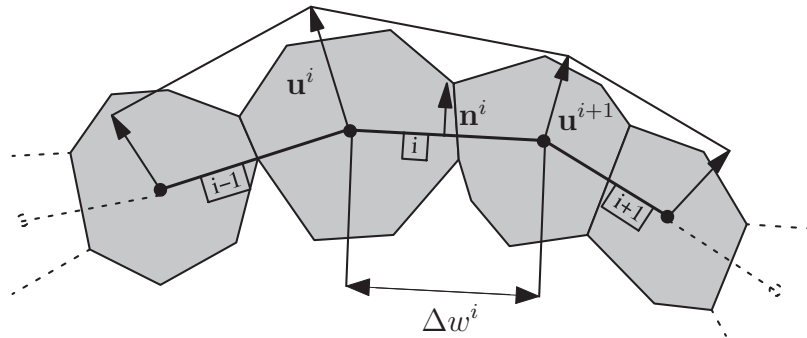
Figure 8.4: Integration over boundary of RVE, e. g. for the strains.

the independent rotation $\bar{\boldsymbol{\varphi}}^i$, this term cannot be transformed into a surface integral. Therefore, this part is calculated via a volumetric averaging over the RVE. The average curvature is computed based on an evaluation of equation (2.33) and application of the divergence theorem

$$\langle \bar{\boldsymbol{\kappa}} \rangle = \frac{1}{V_{\mathcal{R}}} \int\limits_{\partial \mathcal{R}} \bar{\boldsymbol{\varphi}} \otimes \mathbf{n} \, \mathrm{d}a = \frac{1}{V_{\mathcal{R}}} \sum_{i=1}^{N_{\partial \mathcal{R}}} \frac{1}{2} \Delta w^i (\bar{\boldsymbol{\varphi}}^i + \bar{\boldsymbol{\varphi}}^{i+1}) \otimes \mathbf{n}^i \, . \tag{8.28}$$

Strains and curvature directly follow from the displacement and rotation fields $\mathbf{u}$ and $\bar{\boldsymbol{\varphi}}$ known from the particle motion.

In order to calculate energetical quantities spatial velocity gradients are required. The average spatial velocity gradient $\langle \mathbf{L} \rangle$ follows with the definitions $\mathbf{x} = \mathbf{X} + \mathbf{u}$ and grad $\dot{\mathbf{x}}$ = grad $\dot{\mathbf{u}}$ = grad $\mathbf{v}$ from equation $(2.4)_2$ together with an application of the divergence theorem

$$\langle \mathbf{L} \rangle = \frac{1}{V_{\mathcal{R}}} \int\limits_{\partial \mathcal{R}} \dot{\mathbf{x}} \otimes \mathbf{n} \, \mathrm{d}a = \frac{1}{V_{\mathcal{R}}} \sum_{i=1}^{N_{\partial \mathcal{R}}} \frac{1}{2} \Delta w^i (\mathbf{v}^i + \mathbf{v}^{i+1}) \otimes \mathbf{n}^i \, . \tag{8.29}$$

In the same way the rate of the curvature $\langle \dot{\bar{\boldsymbol{\kappa}}} \rangle$, i. e. the spatial angular velocity gradient, is obtained

$$\langle \dot{\bar{\boldsymbol{\kappa}}} \rangle = \frac{1}{V_{\mathcal{R}}} \int\limits_{\partial \mathcal{R}} \dot{\bar{\boldsymbol{\varphi}}} \otimes \mathbf{n} \, \mathrm{d}a = \frac{1}{V_{\mathcal{R}}} \sum_{i=1}^{N_{\partial \mathcal{R}}} \frac{1}{2} \Delta w^i (\dot{\bar{\boldsymbol{\varphi}}}^i + \dot{\bar{\boldsymbol{\varphi}}}^{i+1}) \otimes \mathbf{n}^i \, . \tag{8.30}$$

The derivation of the average dynamic and kinematic quantities is based on the simplification that those terms defined at internal boundaries of the RVE like cracks and pores remain out of consideration, compare with *Nemat-Nasser & Hori* [185]. This proceeding is correct for the dynamic quantities, as the internal boundaries of the RVE are typically stress-free or a continuous stress distribution is present on internal cracks which does not contribute to the average measure. In contrast to this, for the kinematic quantities these considerations are assumptions, as the deformations of the internal boundaries are in general present, but neglected in the presented approach. In a more general form, the formulas of the kinematic quantities contain terms referring to internal pores (integral over surface of pore) and/or jump integrals that refer to internal cracks, see *Diebels* [64] or *Nemat-Nasser & Hori* [185]. However, the simulation results show that the present definition of average quantities by boundary data, also known as testing volume approach according to *Huet* [115], is valid in the evaluated regime.

A further remark is concerned with the formulation of energetically related average strain and stress tensors for granular assemblies. This point still marks an open question in the literature, cf. the discussion by *Bagi* [8] and *Bagi & Bojtar* [9]. It should be pointed out that in this thesis the strains are defined in the same domain as the stresses are defined in. Therefore, the definition of volume $V_{\mathcal{R}}$ of the RVE and of its boundary $\partial \mathcal{R}$ is identical for the stress and strain calculation. Based on the "reduction" of contact forces from the contact points onto the particle centers one naturally obtains the same boundary for the stress calculation as for the strain calculation. Therefore, the formulations at hand do not require the definition of different averaging volumes for conjugated stress and strain tensors as is usually found in the literature, see among others *Bagi* [8], *Bagi & Bojtar* [9], *Kruyt & Rothenburg* [135] or *Liao et al.* [149].

8.3.3   Energetic quantities

In a general framework the internal mechanical power, also known as stress power, is balanced by the external mechanical power and by the rate of the kinetic energy. The notion mechanical power can be substituted by the rate of mechanical work or mechanical energy. Taking into account translational as well as rotational motion one obtains an additive decomposition of the mechanical energy as presented in equation $(2.39)_2$. There, the stress power is expressed by products of so-called energetically conjugated (or dual) dynamic and kinematic variable pairs $\{\langle\mathbf{T}\rangle,\langle\bar{\mathbf{\Delta}}\rangle\}$ and $\{\langle\mathbf{M}\rangle,\langle\mathrm{grad}\,\bar{\boldsymbol{\omega}}\rangle\}$, compare with the remarks in *Diebels* [63]. The validity of the Hill condition represents an important premise for a consistent homogenization and is noted as follows

$$
\begin{aligned}
\mathcal{P}_{int} = \mathcal{P}^1_{int} + \mathcal{P}^2_{int} &= {\mathcal{P}^1_{int}}^* + {\mathcal{P}^2_{int}}^* = {\mathcal{P}_{int}}^* \\
\langle\mathbf{T}\rangle{:}\langle\bar{\mathbf{\Delta}}\rangle + \langle\mathbf{M}\rangle{:}\langle\mathrm{grad}\,\bar{\boldsymbol{\omega}}\rangle &= \langle\mathbf{T}{:}\bar{\mathbf{\Delta}}\rangle + \langle\mathbf{M}{:}\mathrm{grad}\,\bar{\boldsymbol{\omega}}\rangle\,.
\end{aligned}
\tag{8.31}
$$

The Hill condition states that the average rate of stress work equals the rate of work of the average stresses and average couple stresses. The first product on either sides of equation $(8.31)_2$, $\mathcal{P}^1_{int}$ and ${\mathcal{P}^1_{int}}^*$, may be transformed to

$$
\langle\mathbf{T}\rangle{:}\langle\bar{\mathbf{\Delta}}\rangle = \langle\mathbf{T}\rangle{:}\langle\mathbf{L}\rangle - \langle\mathbf{T}\rangle{:}\langle\bar{\mathbf{\Omega}}\rangle\,, \qquad\qquad \langle\mathbf{T}{:}\bar{\mathbf{\Delta}}\rangle = \langle\mathbf{T}{:}\mathbf{L}\rangle - \langle\mathbf{T}{:}\bar{\mathbf{\Omega}}\rangle\,,
\tag{8.32}
$$

by application of equation (2.34). As mentioned in section 2.3.2 in the context of a DEM implementation $\mathrm{grad}\,\bar{\boldsymbol{\omega}}$ is identified by $\dot{\bar{\boldsymbol{\kappa}}} = \mathrm{grad}\,\dot{\bar{\boldsymbol{\varphi}}}$. Due to numerical reasons in the present context the Hill condition is only examined in a restricted form. It is restricted in the sense that the contribution of the product of stresses and skew-symmetric gyration tensor $\langle\mathbf{T}\rangle{:}\langle\bar{\mathbf{\Omega}}\rangle$ according to equation (8.32) is neglected for simplicity reasons since $\langle\bar{\mathbf{\Omega}}\rangle$ cannot be resolved in terms of boundary data, comparable to the second term in equation (8.27). It is expected that the absence of this contribution has an effect, if any, only in zones where a high rotatory motion is active and most of the internal mechanical power $\mathcal{P}^1_{int}$ depends on the pure rotatory motion. The contribution of the continuum moment $\tilde{\mathbf{M}}$ to $\mathbf{M}$ according to equation (8.25) is also left out, since the energy terms containing $\tilde{\mathbf{M}}$ are not regarded as crucial for the check of the validity of the Hill condition. Finally, the inclusion of the above simplifications yields the restricted form of equation (8.31)

$$
\langle\mathbf{T}\rangle{:}\langle\mathbf{L}\rangle + \langle\mathbf{M}\rangle{:}\langle\dot{\bar{\boldsymbol{\kappa}}}\rangle = \langle\mathbf{T}{:}\mathbf{L}\rangle + \langle\mathbf{M}{:}\dot{\bar{\boldsymbol{\kappa}}}\rangle\,.
\tag{8.33}
$$

Application of the divergence and Gauss theorem leads to a formulation in terms of boundary data. For the average quantities on the right side of equation (8.33) one obtains

$$
\begin{aligned}
\langle\mathbf{T}{:}\mathbf{L}\rangle &= \frac{1}{V_\mathcal{R}} \int\limits_{\partial\mathcal{R}} \mathbf{t}\cdot\dot{\mathbf{x}}\ \mathrm{d}a = \frac{1}{V_\mathcal{R}} \sum_{i=1}^{N_{\partial\mathcal{R}}} \mathbf{f}^{(i)}\cdot\dot{\mathbf{x}}_M^{(i)}\,, \\
\langle\mathbf{M}{:}\dot{\bar{\boldsymbol{\kappa}}}\rangle &= \frac{1}{V_\mathcal{R}} \int\limits_{\partial\mathcal{R}} \bar{\mathbf{m}}\cdot\dot{\bar{\boldsymbol{\varphi}}}\ \mathrm{d}a = \frac{1}{V_\mathcal{R}} \sum_{i=1}^{N_{\partial\mathcal{R}}} \bar{\mathbf{m}}^{(i)}\cdot\dot{\bar{\boldsymbol{\varphi}}}^{(i)}\,.
\end{aligned}
\tag{8.34}
$$

The Hill condition is fulfilled if particular boundary conditions are met, compare with section 2.3.2. An evaluation of equations (8.31) or (8.33), respectively, in the form $P_{int} -$

$P_{int}{}^* = 0$ leads to the following restrictions

$$\frac{1}{V_{\mathcal{R}}} \int\limits_{N_{\partial\mathcal{R}}} (\mathbf{t} - \langle\mathbf{T}\rangle \cdot \mathbf{n}) \cdot (\dot{\mathbf{x}} - \langle\mathbf{L}\rangle \cdot \mathbf{x}) \, \mathrm{d}a \;=\; 0 \,, \qquad \frac{1}{V_{\mathcal{R}}} \int\limits_{N_{\partial\mathcal{R}}} (\mathbf{m} - \langle\mathbf{M}\rangle \cdot \mathbf{n}) \cdot (\dot{\boldsymbol{\varphi}} - \langle\dot{\boldsymbol{\kappa}}\rangle \cdot \mathbf{x}) \, \mathrm{d}a \;=\; 0 \,.$$

$$(8.35)$$

For those terms in equations (8.31) and (8.32) containing the average Cauchy stress $\langle\mathbf{T}\rangle$ and the average spatial velocity gradient $\langle\mathbf{L}\rangle$ the evaluation leads to equation $(8.35)_1$. This equation is only valid if boundary conditions like linear displacements or uniform tractions on the boundary of the RVE are set. Terms containing the couple stresses $\langle\mathbf{M}\rangle$ in equation (8.31) are restricted by the condition $(8.35)_2$. In analogy to equation $(8.35)_1$, this condition holds true, only if special boundary conditions like a linear distribution of the rotations or a uniform couple stress vector on the boundary of the RVE are met.

8.4 Numerical realization

Although the formal definition of a RVE plays an important role in the context of a DEM implementation, e. g. when computing stresses or strains, it received limited attention in the literature so far. But, the correct representation and numerical realization of a RVE constitutes an important task within the numerical representation of homogenization approaches. In this context the determination of those particles forming the boundary $\partial\mathcal{R}$ of the RVE represents a key operation. The forthcoming paragraphs are devoted to an exact and comprehensible procedure for the determination of a RVE. Furthermore, two different volume definitions of RVEs will be considered in view of a quantitative comparability of RVE and macroscopic results.

8.4.1 Definition of RVEs

Following the lines of *D'Addetta et al.* [54] the use of neighbor relations constitutes an array which contains the boundary particles of the RVE, see figure 8.5. The procedure is outlined as follows: (1) A circle with a specific radius is drawn around the mass center of a base particle. All particles cut by this circle (not shown in figure 8.5 (a) for simplicity) are saved in an array. Due to numerical reasons these particles represent the first particle row outside of the RVE. (2) Use of neighborhood lists and contact/bond relations provides an array of the RVE boundary particles: A boundary particle must have at least one contact partner outside and one inside of the RVE.

It should be kept in mind that this procedure is by far no one-step technique and, certainly, represents only one way of realization. Those particles marked in light grey in figure 8.5 (a) define the boundary of the RVE and those particles marked in white and light grey form the array of all RVE particles. The composition of each RVE is fixed at the start of the simulation and is not changed in the course of it. According to *Huet* [115] one could think of all particles within a RVE being surrounded by a flexible vessel allowing for internal deformation as well as interchange of forces with surrounding particles. Note, that since in the present thesis the composition of the RVE is fixed from the beginning, in the case of localization like e. g. shearing an unphysical separation of the RVE may be obtained. For example the particles in the upper part of the RVE in figure 8.5 may move in the opposite direction compared to those particles in the lower part of the RVE. Due to numerical
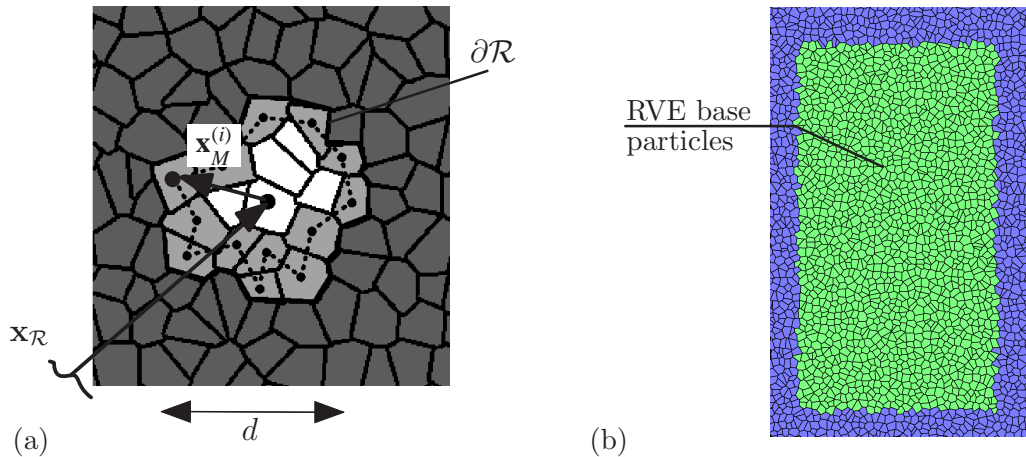
Figure 8.5: (a) Definition of RVE and (b) RVE base particles.

reasons only RVE base particles in a certain distance from the boundaries of the problem are chosen. For the sample used in the biaxial simulation later on, these base particles are shown in light grey in figure 8.5 (b). The evaluated quantities for each RVE will be projected on the corresponding base particles. Throughout the numerical simulations different RVE sizes have been investigated. Mostly the following two RVE sizes are used: RVE_5, where on average 5 particles as diameter of the RVE and 20 particles within the RVE volume result by the described technique. RVE_19, where on average 19 particles as diameter of the RVE result leading to approximately 280 particles within the RVE. The shape of an RVE can be coarsely approximated by a circle with a diameter of $2R-1$ particles. The RVE size is identified by RVE_$(2R-1)$.

The computation of the average quantities is realized by evaluation of RVE lists which include all particles on the boundary of a RVE. In general, each particle within a sample is contained in more than one RVE. Therefore, each particle contributes to the computation of RVE quantities of the RVEs it is contained in. Each RVE possesses a base particle where the RVE quantities are mapped onto, i. e. the base particle moves together with the complete RVE through the system. Thus, this realization represents a type of material description. For simplicity, the quantities are referred to the initial configuration in terms of the composition and volume of the RVE. On this account, and to be formally correct, the integration constants in the integral expressions introduced in the previous sections should contain capital letters $\mathrm{d}A, \mathrm{d}V$ instead of $\mathrm{d}a, \mathrm{d}v$.

8.4.2   Adjustment of RVE volume definition

The correct determination of the volume of the RVE with respect to different RVE sizes, e. g. RVE_5 or RVE_19, is an important task. Preliminary results using the proposed homogenization technique showed that the results of homogenized quantities like the stresses strongly depend on the computed size of the corresponding RVE volume. If, for example, a special stress tensor is calculated as an average of all average RVE stress tensors of a specific sample, the results are RVE size dependent, as it will be shown in figure 8.7 (a). This special tensor may be noted by $\langle\langle\cdot\rangle\rangle$ which formally represents an average of a RVE quantity $\langle\cdot\rangle$ over all RVEs within a sample. This size dependent
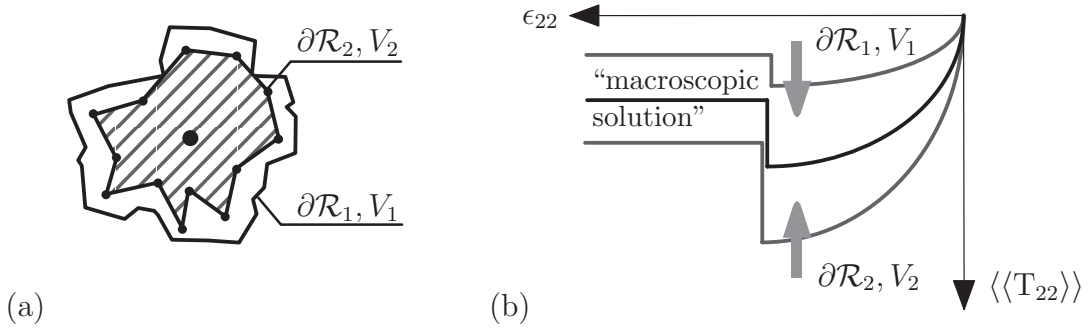
Figure 8.6: (a) Different RVE volume definitions and (b) schematic sketch of corresponding stress-strain diagram.

behavior is undesirable. The definition of the RVE volume should naturally account for the fact that an average of a specific quantity like the stress over all RVEs contained in a sample should on average give the same values irrespective how large the individual RVEs are chosen. This means that if a large RVE size is used for the calculation of the stresses, on average (over all available RVEs within a sample) the same results as if a small RVE size is used, should be obtained. It should be clarified that this effect is only obtained for that part of the stresses calculated from the contact forces, but not for that part resulting from the cohesive component, i. e. it represents an extra effect in addition to the above smearing effect. This is due to the fact that the cohesive forces and moments are naturally defined in the particle centers, but the contact forces and moments are transferred to the particle centers from the RVE boundary and, thus, involve the particle scale. Certainly, a measured quantity for a single RVE still fluctuates around the above average value, but the amplitude of fluctuation should decrease with increasing size of the RVE volume, as shown later on.

A closer investigation of an appropriate definition of RVE volumes reveals two different approaches, as shown in figure 8.6 (a) or within the detailed view in figure 8.5 (a). In the "traditional" definition, $\partial\mathcal{R}_1, V_1$ is based on the area enclosed by all particles of the RVE. The term "traditional" refers to the definition usually found in the literature, see *Bagi* [8], *Cambou et al.* [29], *Chang & Misra* [38], *Christoffersen et al.* [39], *Cundall et al.* [47], *Kruyt* [134] or *Rothenburg & Selvadurai* [209]. In contrast, the proposed alternative definition takes into account the area enclosed by a polygon connecting the centers of mass of all boundary particles of the RVE and leads to a definition $\partial\mathcal{R}_2, V_2$. This definition is consistent with the averaging procedure which is based on resultant forces and moments located in the particles' centers of mass. $\partial\mathcal{R}_2$ represents the natural reference line of the used homogenization approach, as the action of the contact forces is transferred from the particle boundary into its center of mass. Depending on which volume definition is utilized, lower or higher values are obtained compared to the macroscopic solution. On this account compare the schematic stress-strain diagrams within figure 8.6 (b) or the numerical evaluation using definition $\partial\mathcal{R}_2, V_2$ in figure 8.7 (a). The deviation increases with decreasing RVE size. Thus, a comparability of the stresses based on different RVE sizes is not given. The reason for this is the validity of the balance of angular momentum and, following this line, the relation between the occurrence of couple stresses and of non-symmetric Cauchy stresses. In order to maintain the balance of angular momentum in equation (8.17), the contribution of the contact forces is balanced by that of the external

moments. This gives rise to the shown results. In figure 8.6 (b) the term "macroscopic solution" refers to an evaluation of the stress tensor in the form of equation (8.22) using the appropriate volume definition for the whole sample. This graph is set as the limit solution for $d \to D$. This "macroscopic solution" is identical to the stress-strain behavior by means of a normalized load-displacement diagram, as introduced in section 4.5.

Based on the relation between the stress tensor and the difference of equivalent radii of different RVEs D'Addetta et al. [54] proposed a straightforward and theoretically coherent adjustment of the RVE volume. The calculation of radii from the RVE areas V_1 and V_2 leads to r_1 and r_2, respectively, and, correspondingly, to their difference $\Delta r = r_1 - r_2$. In the following, the index 2 is dropped, $r_2 = r$, since definition 2 is used. The average stress tensor (including only contact forces and no cohesive forces - see explanation above) can then be formulated by

$$
\begin{aligned}
\langle \mathbf{T} \rangle &= \frac{1}{V_2} \sum_{i=1}^{N_{\partial\mathcal{R}}} \sum_{c=1}^{C^i} \mathbf{f}^{(i)c} \otimes \mathbf{l}_M^{(i)} = \frac{1}{V_2} \sum_{i=1}^{N_{\partial\mathcal{R}}} \sum_{c=1}^{C^i} \mathbf{f}^{(i)c} \otimes (\mathbf{x}_M^{(i)} + \mathbf{l}^{(i)c}) \\
&\cong \frac{1}{V_2} \sum_{i=1}^{N_{\partial\mathcal{R}}} \left[\sum_{c=1}^{C^i} \mathbf{f}^{(i)c} \right] \otimes (1 + \frac{\Delta r}{r}) \mathbf{x}_M^{(i)} = \frac{1}{V_2} \sum_{i=1}^{N_{\partial\mathcal{R}}} \mathbf{f}_c^{(i)} \otimes (1 + \frac{\Delta r}{r}) \mathbf{x}_M^{(i)} \\
&\cong (1 + \frac{\Delta r}{r}) \frac{1}{V_2} \sum_{i=1}^{N_{\partial\mathcal{R}}} \mathbf{f}_c^{(i)} \otimes \mathbf{x}_M^{(i)} = \frac{\partial \mathcal{R}_1}{\partial \mathcal{R}_2} \frac{1}{V_2} \sum_{i=1}^{N_{\partial\mathcal{R}}} \mathbf{f}_c^{(i)} \otimes \mathbf{x}_M^{(i)} .
\end{aligned}
\tag{8.36}
$$

Therein, the identities $\mathbf{l}_M^{(i)} = \mathbf{x}_M^{(i)} + \mathbf{l}^{(i)c}$ as shown in figure 8.3 and the force definition introduced in equation $(8.15)_2$ was used. In equation (8.36) two approximations have been utilized: First, $(\mathbf{x}_M^{(i)} + \mathbf{l}^{(i)c})$ has been approximated by $(1 + \Delta r/r)\mathbf{x}_M^{(i)}$ with use of the relation $\Delta r/r = |\mathbf{l}^{(i)c}|/|\mathbf{x}_M^{(i)}|$. In a second step, the factor $(1 + \Delta r/r)$ is taken in front of the sum assuming that on average the relation $(1 + \Delta r/r)$ is constant for each RVE. Afterwards, the fraction $(1 + \Delta r/r)$ is further expanded to provide a relation that includes the circumferences of the polygonal RVE, $\partial \mathcal{R}_1/\partial \mathcal{R}_2$. Starting with the "traditional" RVE volume V_1 and utilizing the same arguments as in equation (8.36), an equivalent definition of the average stress on the RVE level is obtained:

$$
\langle \mathbf{T} \rangle = \frac{\partial \mathcal{R}_1}{\partial \mathcal{R}_2} \frac{1}{V_2} \sum_{i=1}^{N_{\partial\mathcal{R}}} \mathbf{f}_c^{(i)} \otimes \mathbf{x}_M^{(i)} = \frac{\partial \mathcal{R}_2}{\partial \mathcal{R}_1} \frac{1}{V_1} \sum_{i=1}^{N_{\partial\mathcal{R}}} \mathbf{f}_c^{(i)} \otimes \mathbf{x}_M^{(i)} .
\tag{8.37}
$$

For the absolute value of the stress, the multiplier in form of a function $f = f(\delta/d) = \partial \mathcal{R}_1/\partial \mathcal{R}_2$ becomes more important with decreasing size of the RVE, i. e. the more the postulated scale separation $d \gg \delta$ is violated. The interpretation is obvious: The multiplier couples the δ-scale on the particle level with the d-scale on the RVE level. For the biaxial simulation to be discussed in the next section, the stress-strain diagram using volume definition 2 and, thus, no volume adjustment is shown in figure 8.7 (a). As pointed out earlier, $\langle\langle T_{22} \rangle\rangle$ describes the average of all RVE (averaged) stresses within the sample and ϵ_{22} denotes the macroscopic nominal vertical strain of the sample. Two important observations are made: First, the curves for different RVE sizes do not coincide, e. g. the peak value of RVE_5 is 20 % higher than of RVE_19. Second, with increasing size of RVE the curves tend to the "macroscopic solution". If the RVE volume is adjusted via $\partial \mathcal{R}_1/\partial \mathcal{R}_2$, the situation in figure 8.7 (b) is obtained. The remarkable results are constituted by the
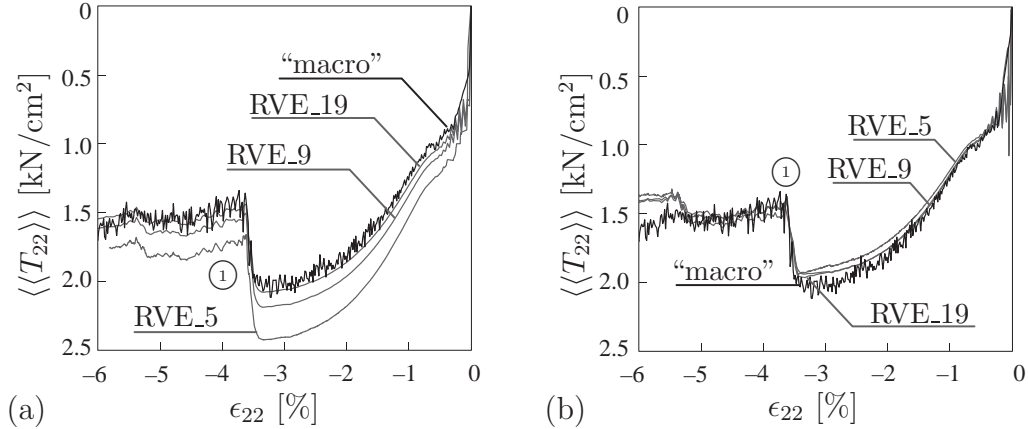
Figure 8.7: "Averaged" RVE stresses (a) without and (b) with adjustment of volume.

fact that nearly no difference between the three RVE sizes is visible. Furthermore, the RVE results are in good agreement with the "macroscopic solution" which was set as the reference solution approximating the result of an infinite RVE size. In conclusion, starting from the natural definition $\partial\mathcal{R}_2$, a coherent theoretical volume definition was obtained which is in agreement with the balance equations of the RVE. It should be noted that RVE quantities are different only for that part of the stress tensor that refers to the particle contact forces. For those parts of the stress tensor that refer to the cohesive components (like beam or interface forces), the couple stresses and the kinematic variables no adjustment of the RVE volume is needed. In these cases volume definition 2 without premultiplication of factors of the form $f(\delta/d)$ directly applies. This behavior is quite comprehensible: Since the couple stresses are defined on the mass centers of the RVE's boundary particles, the definition $V_2, \partial\mathcal{R}_2$ is used in the RVE volume definition for $V_\mathcal{R}$ in equation (8.25). Furthermore, since the formal definition of the kinematic variables involves solely the deformations of the boundary particles measured from the centers of mass, the volume definition V_2 without premultiplication is involved in the calculation of the strains, curvatures and their derivatives in equations (8.26) to (8.30).

8.5 Numerical results

The homogenization procedure introduced in the previous sections is validated by two-dimensional DEM simulations. The occurrence of non-symmetric stress tensors as well as couple stresses are studied with respect to different RVE sizes. The focus lies on one of the key questions in the framework of homogenization methods and their application, namely how large a RVE must be. This is equivalent with the question, how many particles have to be included within a RVE in order to represent a sample on the macro scale in terms of measurable quantities like stresses etc. An ideal size of a RVE on the meso scale d is studied that, on the one hand, guarantees a reliable quantitative comparability with the macro scale D and, on the other hand, includes the locality of the problem. The necessary size of the RVE is associated with the internal length scale in that it defines a measure $d > \delta$ for which microstructural effects are not smeared out. Biaxial tests as well as the extension of a granular layer are examined in the context of cohesionless samples. Finally,

the application to the Brazilian test setup shows the suitability of the homogenization method for cohesive samples.

8.5.1   Biaxial test

The benchmark problem used for the validation of the homogenization procedure is a strain driven Hambly-type biaxial simulation of a rectangular sample with rigid side walls introduced in section 3.6.1. The test sample consists of approximately 2500 non-cohesive particles (only based on contact forces) and is loaded by four non-deformable walls, compare the load setup in figure 3.12. The parameters and further information on the biaxial test can be found in section 3.6.1 and details of the failure mode are given in section 6.2.1. As remarked earlier, the biaxial test is a well known experimental setup in geotechnics. Based on this experience for not too large side pressures a failure evolution dominated by shear localization in zones of finite width is expected. In several FEM applications, see e. g. *Ehlers & Volk* [78] or *Volk* [251], the numerical treatment makes use of a Cosserat model. In these studies it is found that the occurrence of couple stresses is restricted to narrow but finite failure zones. Therefore, this problem represents an adequate benchmark for a validation of the proposed homogenization technique. At each time step of the biaxial simulation the average dynamic, kinematic and energetic quantities are evaluated for approximately 1500 RVEs shown via the base particles in figure 8.8. Two different RVE sizes are illustrated in a qualitative format together with the corresponding base particles colored in light and very dark grey in figure 8.8 (a). This figure presents the initial particle structure of the test. These two RVEs will be used for a comparative study later on. The failure behavior of the biaxial test is shortly summarized based on the results in sections 3.6.1 and 6.2.1: The deformed sample at a later stage of the simulation in figure 8.8 (b) shows the formation of shear zones, whereby the upper shear zone ① appears at first. The particles located above shear zone ① and below shear zone ② form
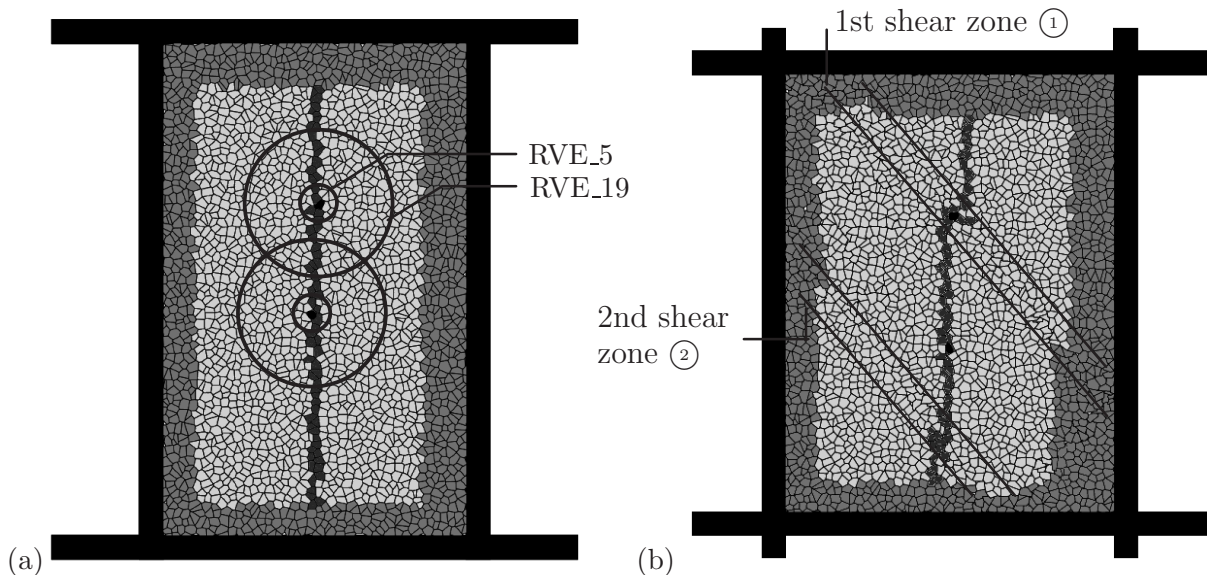
Figure 8.8:   Position of RVEs for comparative study in (a) initial and (b) deformed state of slender biaxial test.

wedges that undergo a rigid body translation with little visible internal deformation. The middle region between both shear zones behaves like a rectangular block sheared at the top and bottom. In between, a region of finite width represents the shear bands that are governed by dilation and particle rotation. The purely local deformation of the vertical line of dark shaded particles in figure 8.8 reveals the highly localized action and a re-organization of the particle structure. In principle, this line remains vertical except the "discontinuity" in the region of the shear zones.

The main focus of the following computations is directed to the influence of the RVE size: In the context of the dynamical quantities, on the one hand, the observation of fluctuations by means of the vertical stresses is examined. On the other hand, the determination of non-symmetric stresses along with the occurrence of couple stresses is exercised. In a second step, the kinematic quantities are used to resolve strain localization and pattern formation. Finally, the validity of a limited form of the Hill condition is proven by means of an evaluation of the energetic quantities.

Dynamic quantities - Fluctuations

The macroscopic stress-strain response in terms of the vertical coefficient of the stress tensor $\langle\langle T_{22}\rangle\rangle$ and the vertical strain coefficient ϵ_{22} has already been plotted within figure 8.7 (b), but is repeated for didactical reasons in figure 8.9. The $\langle T_{22}\rangle - \varepsilon_{22}$ diagram of one arbitrary RVE would principally follow the graph of the macroscopic stress-strain curve given in figures 8.7 or 8.9. Note that due to the increased absolute values of the nominal strains the definition range of a linear kinematics is formally left. However, this does not contradict the qualitative statements given below. Typically, the locality of the variables is expressed by fluctuations in the $\langle T_{22}\rangle$ values with respect to the position of the RVEs. The larger the RVE is, the smaller are the fluctuations encountered, cf. the remarks in *Bear & Bachmat* [19]. In the following, the fluctuations are examined in detail by the vertical stress amplitude $\langle T_{22}\rangle^i / \langle\langle T_{22}\rangle\rangle$ of different RVEs i. For this comparative study four different RVE sizes, namely RVE_3, RVE_7, RVE_13 and RVE_39, have been used to evaluate the average vertical stress of 72 RVEs. These RVEs lie on the vertical middle line of the tested sample. The dark shaded particles in figure 8.8 represent the base particles of the monitored RVEs ranging from the bottom RVE (near the sample
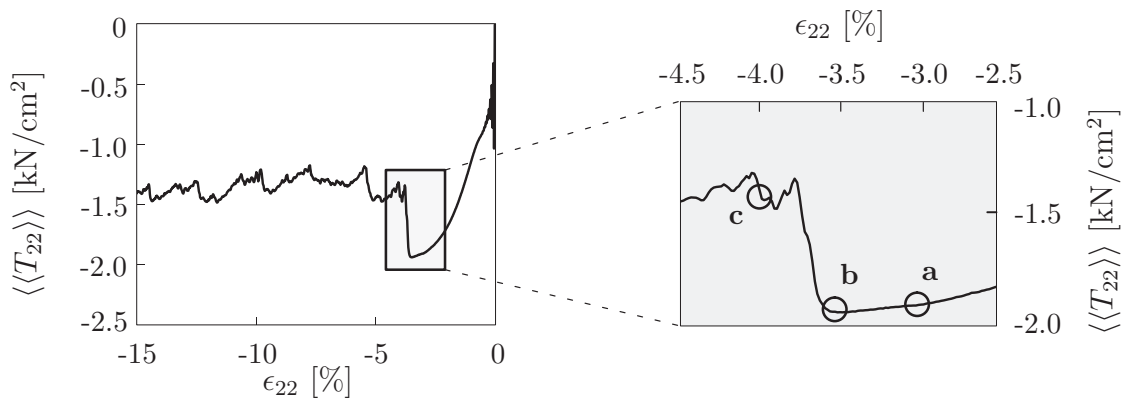
Figure 8.9: $\langle\langle T_{22}\rangle\rangle - \epsilon_{22}$ diagram of biaxial test with detail around localization onset.
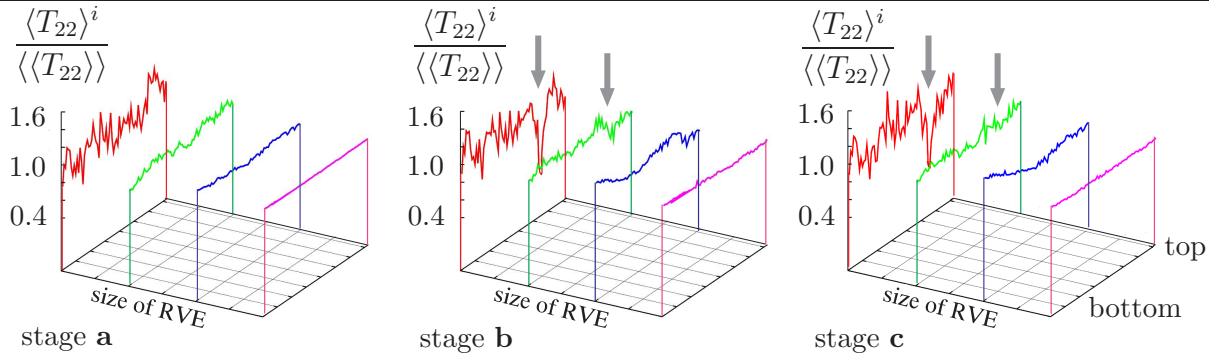
Figure 8.10: Fluctuation of stress amplitude with respect to RVE size.

bottom) to the top RVE (near the sample top). Three different time stages are shown in figure 8.10 according to the "macroscopic" stress-strain diagram in figure 8.9: stage **a** refers to a situation some time before the onset of localization, i. e. the evolution of the first shear zone, stage **b** represents the situation just at the start of localization and stage **c** expresses the situation after the development of the first shear band. The four curves within each of the three diagrams refer to the corresponding RVE size: the smallest one (RVE_3) at the left side of each diagram and the largest one (RVE_39) at the right side, with RVE_7 and RVE_13 in between. Hence, in the horizontal direction (from the left to the right) the RVE size is marked, while the backward direction refers to the spatial position of the RVE. The values in the foreground refer to the RVE at the bottom of the monitored area, the values in the background refer to the RVE at the top of the monitored area according to figure 8.8. The following effects are visible:

1. The larger the RVE size, the fewer the fluctuations. As expected, on average all curves fluctuate around 1.0 and the fluctuation amplitude decreases with larger averaging volume. In the case of RVE_3 an amplitude of ± 50 % is obtained that decreases to nearly 0 % for RVE_39.

2. With onset of localization the locality (here: the position of the first shear band) is obvious only for the case of the small RVEs (RVE_3 and RVE_7), while for the two larger RVEs (RVE_13 and RVE_39) nearly no effect is seen due to the large averaging radius. The fluctuations are simply smeared out in this case. The evolution of the first shear zone is expressed by a sharp jump in the corresponding curve, compare RVE_3 and RVE_7 at stages **b** and **c** in figure 8.10 (position marked by arrows).

3. In the last controlled time stage **c** in figure 8.10 the effect of the localization is additionally visible in the curve corresponding to RVE_13 (third curve from the left) by a rather smooth decay in the middle region.

The temporal progress of the vertical stress distribution shown in figure 8.11 gives an additional insight into the failure behavior of the sample and the fluctuating stresses. The coefficient $\langle T_{22} \rangle$ of the stress tensor is plotted for both investigated RVE sizes. The value computed for a certain RVE is projected on the corresponding base particle in the deformed state. The brightness of each base particle in figure 8.11 reflects the average quantity under study in a circular neighborhood around this base particle. Only those base particles indicated by light and dark grey shading in figure 8.8 are used for the

<center>RVE_5   RVE_19</center>

<center>-2.5   -2.0   -1.5   -1.0   -0.5   0 $\langle T_{22} \rangle$ [kN/cm^2]</center>
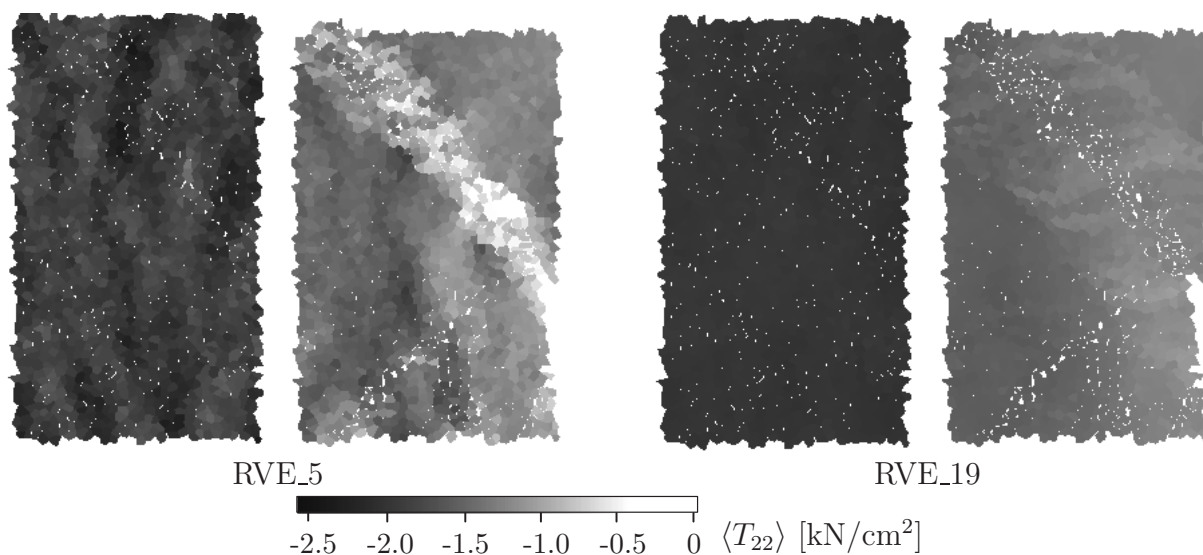
Figure 8.11: Distribution of vertical stresses before and after localization onset.

graphical representation. The respective left figure represents a situation short before localization onset and the right one a situation after localization onset. In agreement with the findings in the context of the fluctuation analysis in figure 8.10, for the smaller RVE (RVE_5) fluctuations in the stresses are observed before the first shear zone ① appears (left figure). The structure of the load transfer by force chains inside the sample is obvious in this case. After onset of localization (right figure) the vertical stress distribution expresses an unloading in parts of the sample. This effect becomes visible in particular within the localization band. In the case of the larger RVE (RVE_19) a uniform behavior is found for the vertical stresses before onset of failure. After localization the situation in terms of uniformity does not change drastically. The smearing-out effect becomes obvious as the stresses slightly drop in a broader band as is the case for RVE_5. One interesting result also known from geotechnical experiments concerns the stress transfer. Outside the shear zone the load is transferred mainly by a vertical stress T_{22} and within the shear zone by shear stresses T_{12} and T_{21}. This observation sheds some light on the relation between the dilatant behavior and the activation of shear stresses. This relation plays an important role for the motivation of macroscopic constitutive laws like those based on a Mohr-Coulomb plasticity model. A further interesting point in this context is an evaluation of the eigendirections of the stress tensor. With formation of the first shear band the eigendirections of the RVE stress tensors in the middle region of the sample change: They skip from a vertical/horizontal pattern to a pattern aligned with the inclination of the first shear zone. This sustains the remark in section 3.6.1 on the wedge formation and the resulting simple shear type loading of the particle block in between the two evolving shear zones. This observation supports and supplements the remarks by Åström et al [7] on the alignment of the grain skeleton in the context of the formation of shear bands.

Dynamic quantities - Stress asymmetry & couple stresses

Another aim of this section is to show that by application of the proposed homogenization technique effects of the microstructure related to the size and the shape of the grains are

preserved on the meso scale defined by the dimension of the RVE. Two different positions
of RVEs are chosen for the oncoming comparison: In the first case, the corresponding
base particle of the RVE lies within the first evolving shear band. In the second case,
the base particle is situated outside of the influence region of the primary shear zones.
Both base particles are marked in black in figure 8.8. Within the oncoming diagrams the
pointer ① marks the point in time when the first shear band occurs.
In figure 8.12 the norm of the couple stress tensor $|\langle \bar{\mathbf{M}} \rangle| = \sqrt{\langle \bar{M}_{31} \rangle^2 + \langle \bar{M}_{32} \rangle^2}$ is plotted
versus the vertical nominal strain for the two chosen RVEs with sizes RVE_5 and RVE_19.
Two effects become visible: As has been expected, couple stresses are only active in the
shear band zone, see figure 8.12 (a), while outside the shear band no couple stresses occur,
see figure 8.12 (b). Secondly, the homogenized couple stresses are only visible, if the RVE
size is small enough such that microscopic effects are not smeared out on the meso scale,
compare the different results of RVE_5 and RVE_19 given in figure 8.12 (a). Once again
these observations are in good agreement with both numerical simulations carried out on
the basis of the FEM by use of a micropolar Cosserat continuum, cf. *Ehlers & Volk* [78] or
Volk [251], as well as with experimental results on dry granular materials, cf. *Viggiani et
al.* [250]. Since the width of experimentally observable shear bands like in sand consists
of only a few grain diameters, see *Mühlhaus & Vardoulakis* [181] or *Viggiani et al.* [250],
a RVE should not be chosen too large in order to capture the influence of the microscopic
inhomogeneities on the macro scale.
Concerning the particle contact behavior included in this study, recall that only normal
stiffnesses have been taken into account and that the tangential forces as well as rotational
stiffnesses have not been considered. In contrast to articles where rotational stiffnesses
are used, see e. g. *Chang & Gao* [35], here, the couple stresses naturally result from the
eccentricities of the normal contact forces. Hence, they are neither a result of tangential
contact forces nor a result of an enhanced contact description through the introduction
of rotational stiffnesses.

In addition to the couple stresses, a further indicator for the existence of localization zones,
dual to the occurrence of couple stresses, is the existence of non-symmetric stress tensors,
i. e. a stress asymmetry. In the biaxial problem under study the stress asymmetry is given
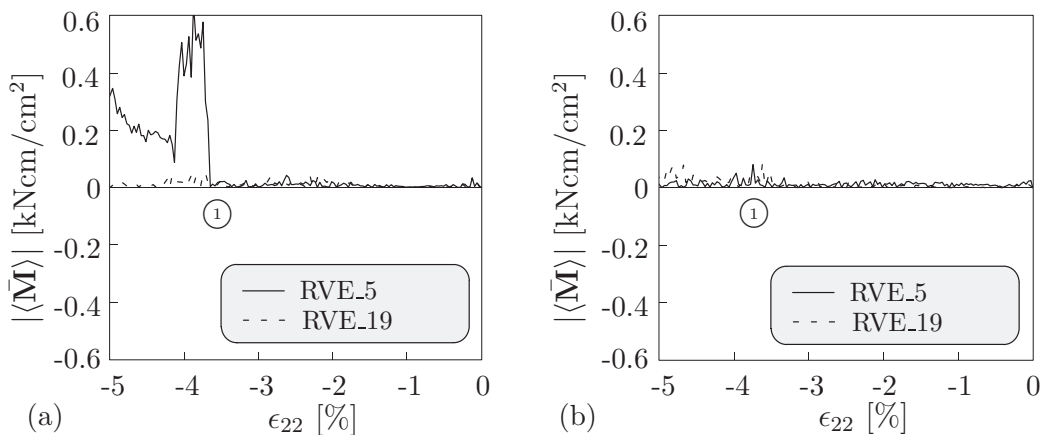
Figure 8.12: Norm of couple stress tensor for RVE (a) inside evolving shear zone and (b)
outside of it.
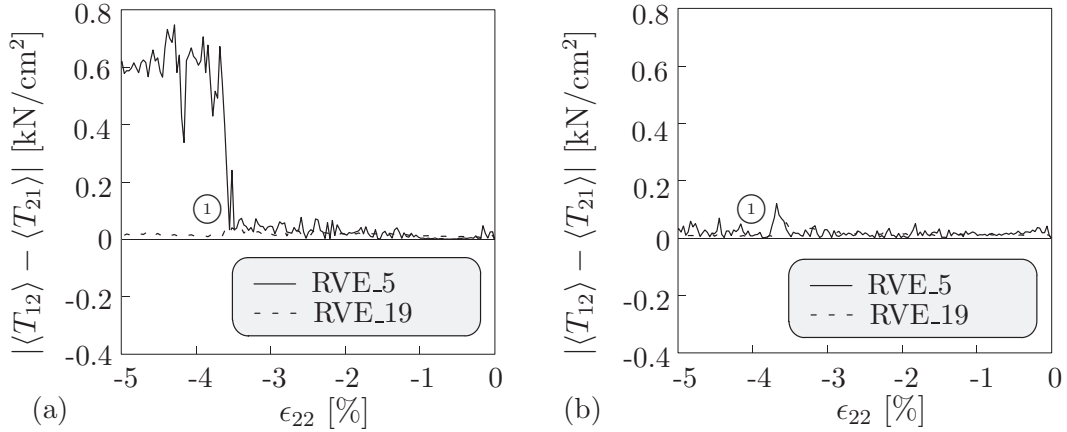
Figure 8.13: Difference of shear coefficients of stress tensor for RVE (a) inside evolving shear zone and (b) outside of it.

by non-vanishing differences between $\langle T_{12} \rangle$ and $\langle T_{21} \rangle$. Recall that if a couple stress exists, the stress tensor is not symmetric and, hence, $\langle T_{12} \rangle \neq \langle T_{21} \rangle$ is expected to hold in the localization zone. In figure 8.13 the difference between the shear stresses $|\langle T_{12} \rangle - \langle T_{21} \rangle|$ is plotted with respect to the size and position of the RVEs. From this figure it is clearly seen when $\langle \mathbf{T} \rangle$ becomes unsymmetric. In analogy to the detection of couple stresses, it is evident that the stress asymmetries are only obtained in the case of sufficiently small RVEs lying within the localization zone. Concerning the present example there is only a clear difference between $\langle T_{12} \rangle$ and $\langle T_{21} \rangle$ for the RVE with size RVE_5 located inside the shear band, compare figure 8.13 (a). Furthermore, it is seen that the RVE with size RVE_19 is unable to detect a shear zone by use of the proposed homogenization technique. In addition, it is obvious that the RVEs outside of the developing shear bands exhibit symmetric stresses like they exhibit vanishing couple stresses, compare figures 8.12 (b) and 8.13 (b).

Moreover, it is observed that the amplitude of stress asymmetry decreases with increasing volume of the RVEs. These findings do not only correspond to the remarks given in section 8.2.3, but they are also related to the observations made by *Bardet & Vardoulakis* [11]. In addition to their findings, the present procedure also provides a backbone for a sound numerical treatment of the proposed homogenization process.

The temporal progress of the couple stress distribution for the two RVE sizes in figures 8.14 and 8.15 gives additional insight into the activation of couple stresses in shear zones. The norm of the couple stress tensor is plotted for both RVE sizes with respect to four consecutive time stages ⓐ, ⓑ, ⓒ and ⓓ: The sequence covers the time interval from the development of the first shear zone by the time the second shear zone just starts to form. ⓐ denotes the situation just before onset of localization and the remaining stages denote three consecutive time stages within the first phase of localization. The RVE values are projected on the corresponding base particle in the deformed state. Again, only those base particles indicated by a light color in figure 8.5 (b) are used for the graphical representation in figures 8.14 and 8.15. A clear localization of the couple stresses becomes evident within the region of the first evolving shear zone for RVE_5. Different points of activity within the shear zone can be recognized during the course of the monitored

(a) $\epsilon_{22} = -3.2\%$ (b) $\epsilon_{22} = -3.8\%$ (c) $\epsilon_{22} = -4.2\%$ (d) $\epsilon_{22} = -4.8\%$

$|\langle \bar{\mathbf{M}} \rangle|$ [kNcm/cm^2]

0   0.1   0.2   0.3   0.4
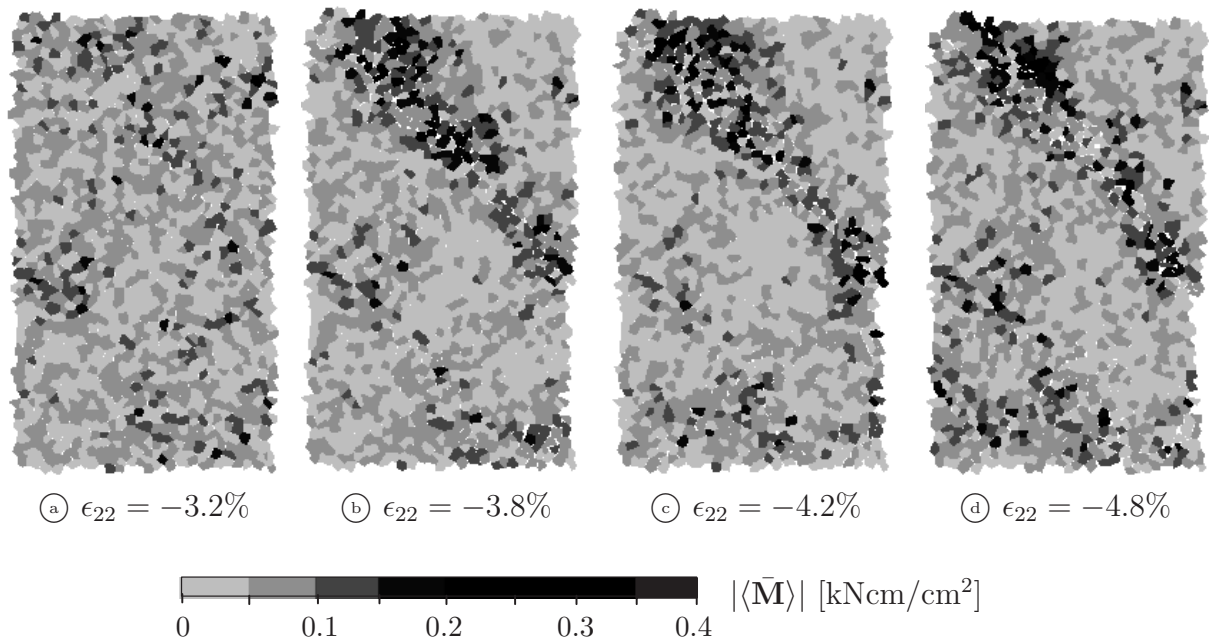
Figure 8.14:   Temporal progress of norm of couple stresses for RVE_5.

time interval. In contrast, the temporal progress for RVE_19 in figure 8.15 shows no pronounced activity within the first shear zone. This fact becomes more evident, if the scale in figure 8.15 would be fit to the maximum values of RVE_19 instead of that of RVE_5, as done here. As a consequence of the relative large RVE size, the norm of the couple stresses tends to zero and a smearing-out effect is obtained. Nevertheless, small local

(a) $\epsilon_{22} = -3.2\%$ (b) $\epsilon_{22} = -3.8\%$ (c) $\epsilon_{22} = -4.2\%$ (d) $\epsilon_{22} = -4.8\%$

$|\langle \bar{\mathbf{M}} \rangle|$ [kNcm/cm^2]

0   0.1   0.2   0.3   0.4
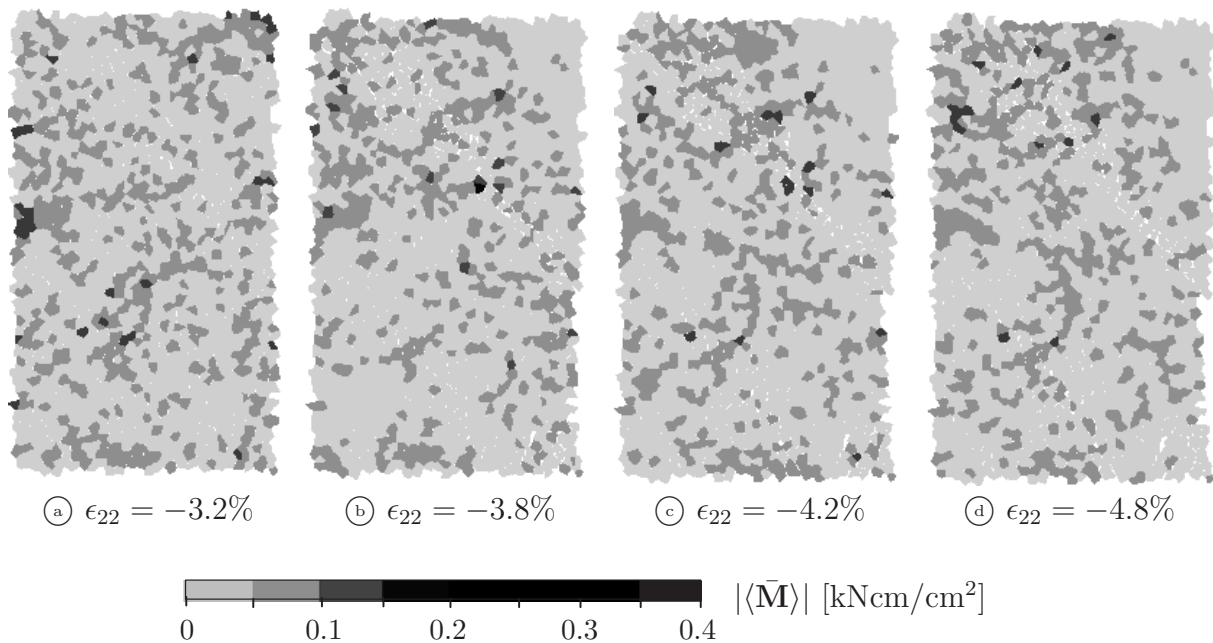
Figure 8.15:   Temporal progress of norm of couple stresses for RVE_19.

fluctuations are still present which are distributed in a statistical fashion rather than in the form of a strict localization, as for RVE_5.

Dynamic quantities - Effect of scale separation arguments

The last topic in the context of dynamic quantities concerns the effect of the body forces on the equilibrium and, therewith, on the stress calculation. Based on the arguments of scale separation $D \gg d \gg \delta$ volume terms were neglected with respect to surface terms in section 8.2.3. This means that for the purpose of homogenization and calculation of continuum mechanical quantities volume terms have been left out. Those integrals containing the body forces, e. g. gravitation, or the acceleration terms in the equation of motion are neglected. However, this does not mean that those terms do not influence the general numerical solution scheme by means of the DEM model and the corresponding evaluation of the equation of motion, compare equations (2.11) and (3.4). Quite the contrary is the case: The acceleration terms are the driving action in the numerical model, but are left out in the post-processing routine of homogenization due to the above considerations. One could hypothesize that the occurrence of couple stresses and stress asymmetries, as manifested in figures 8.12 and 8.13, is an outcome of neglected volumetric forces, e. g. by means of acceleration forces rather than being the result of the presented procedure itself. In order to show that the asymmetry of the stress tensor and the occurrence of couple stresses is still valid regardless of the assumptions of scale separation, the stress calculation is repeated with special consideration of the acceleration terms. Thus, the average stress tensor is derived anew by including the volume part of the stresses via an additional inclusion of the acceleration terms. This average stress tensor is numerically investigated in the context of the biaxial test.

Starting from the general local form of balance of momentum given in equation $(8.3)_2$, under consideration of vanishing gravitation forces, $\rho \mathbf{b} = 0$, one obtains $\operatorname{div} \mathbf{T} = \rho \, \ddot{\mathbf{x}}$. Insertion into the formal homogenization methodology introduced in section 8.3.1 yields

$$\langle \mathbf{T} \rangle^T = \frac{1}{V_\mathcal{R}} \int\limits_\mathcal{R} \operatorname{div} (\mathbf{x}_M \otimes \mathbf{T}) \, \mathrm{d}v - \frac{1}{V_\mathcal{R}} \int\limits_\mathcal{R} \mathbf{x}_M \otimes \rho \, \ddot{\mathbf{x}}_M \, \mathrm{d}v. \tag{8.38}$$

Further evaluation of the first term in equation (8.38) via an integral expression formulated over the boundary yields the average stress tensor in terms of contact forces (as in equation (8.22)). An additional term results from the transfer of the second term in equation (8.38) to a sum over all particles of a RVE. Thus, the complete stress tensor is decomposed into two parts, one related to the contact forces $\langle \mathbf{T}^c \rangle$ and another one related to the volume term $\langle \mathbf{T}^{vol} \rangle$

$$\langle \mathbf{T} \rangle = \underbrace{\frac{1}{V_\mathcal{R}} \sum_{i=1}^{N_{\partial\mathcal{R}}} \mathbf{f}^{(i)} \otimes \mathbf{x}_M^{(i)}}_{\langle \mathbf{T}^c \rangle} - \underbrace{\frac{1}{V_\mathcal{R}} \sum_{i=1}^{N_\mathcal{R}} m^{(i)} \, \ddot{\mathbf{x}}_M^{(i)} \otimes \mathbf{x}_M^{(i)}}_{\langle \mathbf{T}^{vol} \rangle} . \tag{8.39}$$

The evaluation of the two terms of equation (8.39) for two RVEs, one inside the evolving localization zone and one outside of it, is shown in figure 8.16. This pictures clearly the independence of the stress asymmetry of the body forces. As one can see for the RVE inside the shear zone, the volume part of the stress asymmetry fluctuates around the zero
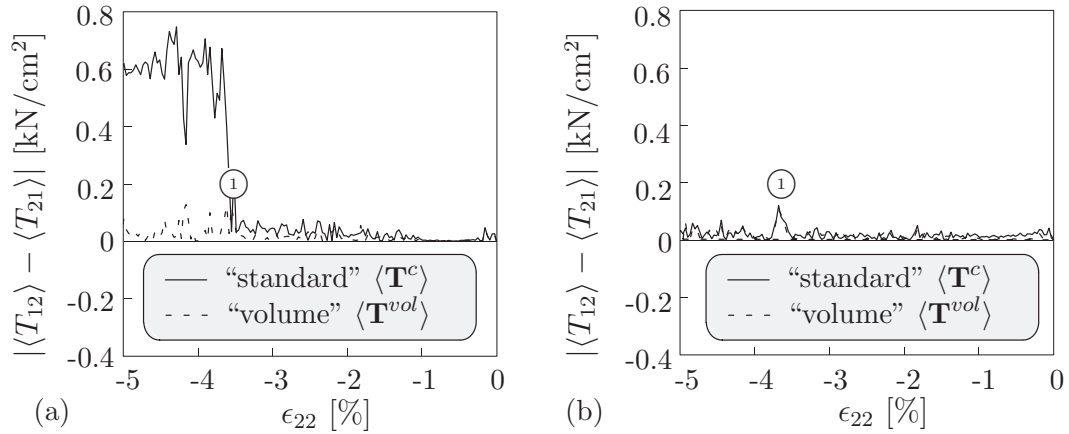
Figure 8.16:   Difference of shear coefficients of stress tensor (separation by reasons with respect to equation (8.39)) for RVE_5 (a) inside and (b) outside of evolving shear zone.

line in figure 8.16 (a). When the shear band zone appears in ① the stress asymmetry $|\langle T^c_{12}\rangle - \langle T^c_{21}\rangle|$ becomes apparent, while the additional part of the stress tensor $|\langle T^{vol}_{12}\rangle - \langle T^{vol}_{21}\rangle|$ remains close to the zero line. It is obvious that the volume part does not contribute to the complete stress tensor for a reasonable RVE size RVE_5. In figure 8.16 (b) for the RVE outside the shear zone the curves practically coincide, i. e. in the sum the stress asymmetry vanishes according to equation (8.39). In conclusion, it can be stated that the stress asymmetry is a pure outcome of the procedure itself rather than being the result of the neglected volumetric terms by means of the acceleration forces. Thus, the "complete" stress tensor according to equation (8.39) does not differ from the originally proposed stress tensor, compare the graphs for RVE_5 in figure 8.13 with figure 8.17. Please note that the notion "volume part of the stress" does not include the "dynamic stress" as introduced by *Lätzel* [144] or *Luding et al.* [157], i. e. in the case of slow motion terms
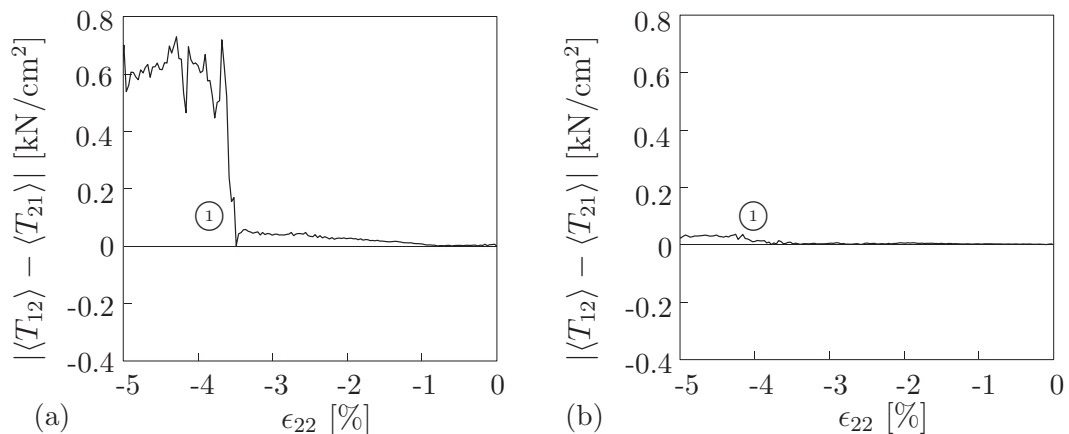
Figure 8.17:   Difference of shear coefficients of complete stress tensor according to equation (8.39) for RVE_5 (a) inside and (b) outside of evolving shear zone.

which include the dyadic product of velocities are neglected.

Kinematic quantities - Strains

The averaged strain tensor for two different RVE sizes is evaluated and the results are compared to the corresponding macroscopic or nominal strain. Again the term "averaged" $\langle\langle\cdot\rangle\rangle$ refers to an average of a RVE quantity $\langle\cdot\rangle$ over all RVEs within a specific sample. In figure 8.18 (a) the horizontal average strain is plotted versus the vertical nominal strain. No substantial difference between the "macro" strain and the corresponding coefficient of the averaged RVE strain tensor is obtained. The "macro" strain is determined by an evaluation of the distance of the two side walls. In the case of the vertical coefficient $\langle\epsilon_{22}\rangle$ the RVE strains show a small deviation from the macroscopic solution after localization onset. This observation represents the effect of the particle rotations that is explicitly accounted for by the skew-symmetric part of the strain tensor according to equation (8.27). Therefore, small deviations are obtained as outcome of a non-symmetric strain tensor. The results for RVE_5 and RVE_19 are nearly identical. Thus, on average the strain calculation is independent of the RVE size. Solely for a representation of the locality the RVE size plays a similar role, as described for the stress and couple stress calculation in the previous paragraphs. This fact is envisioned in figure 8.19 where the evolution of the vertical component of the average strain tensor is depicted. For clearness, different scales are given for each plot in order to demonstrate the behavior for two different points in time, just before and right after localization. The left picture of one figure set refers to the situation before and the right one to the situation after the localization in one primary shear band zone has occurred. For RVE_5 before onset of the dominant fault zone a clear pattern with various crossing diagonals of higher strain values is obtained. Afterwards, one of these zones becomes dominant and proceeds in terms of deformation, while the other patterns do not evolve further. These numerical results are in good agreement with experimental observations of the strain distribution, as obtained e. g. by stereophotogrammetry, particle image velocimetry or x-ray tomography of granular materials, see *Desrues et al.* [62], *Nübel* [188] or *Viggiani et al.* [250]. For RVE_19 before localization onset a more or less homogeneous deformation behavior within the sample is
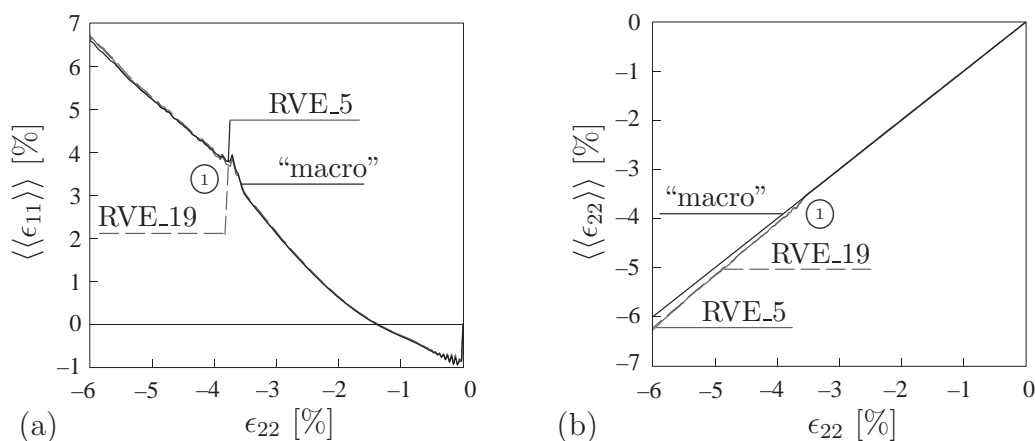
Figure 8.18: (a) Averaged horizontal and (b) vertical RVE strains compared to nominal "macro" strains.
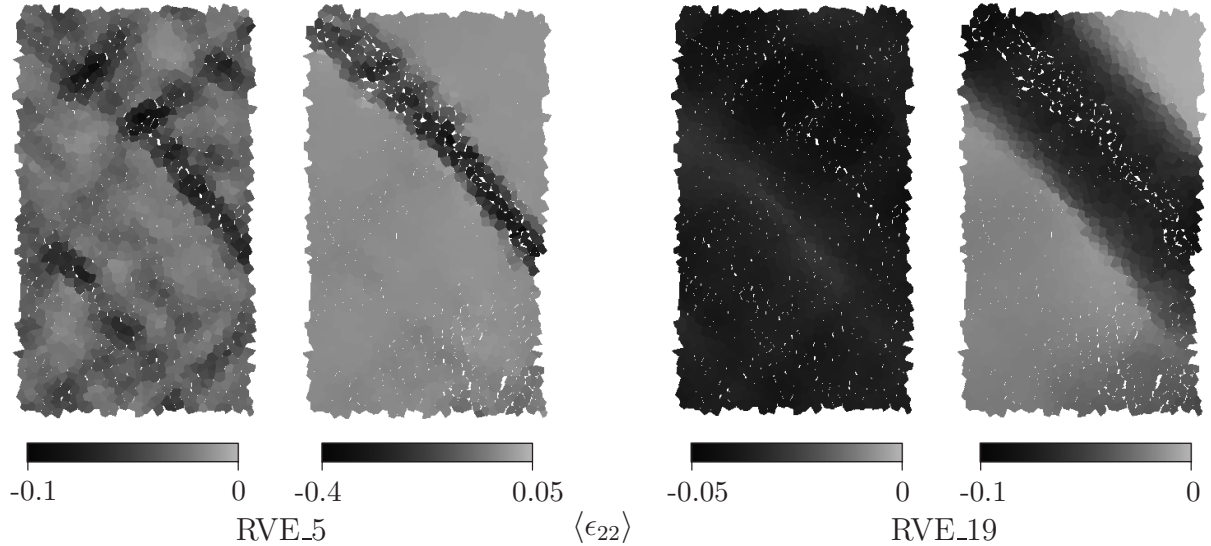
Figure 8.19: Distribution of vertical strains before and after localization.

encountered due to the large averaging volume. The occurrence of the dominant shear fault is qualitatively correctly represented, although the width of the shear band is 5 times larger compared to the corresponding situation for RVE_5 due to a smearing effect.

Kinematic quantities - Pattern formation

The evaluation of the average strain distribution leads to a more fundamental understanding of this kind of model material which is closely related to real granular materials. The homogenization method provides the opportunity to study the pattern formation in combination with the self-organization of the granular body. Figures 8.8, 8.11 or 8.14 reveal the formation of one primary shear zone. However, this is only half the truth, because the formation of one or two dominating shear band zones is anticipated by a relatively large amount of competing secondary zones. The pre-localization phase shown for RVE_5 in figure 8.19 pictures this situation quite good. The pattern formation in the pre-localization regime is an accepted feature of geomaterials like dry sands, compare *Nübel* [188], or rocks and soft sediments, compare *Poliakov & Herrmann* [199]. If the size of the biaxial test sample is increased by keeping the height to width ratio constant, an interesting feature of the DEM model in combination with the homogenization procedure is obtained. In addition to the 40 cm × 64 cm sample, denoted as sample A, twice and thrice as high samples, termed sample B and C, have been simulated. Consequential, samples B and C posses the spatial dimensions 80 cm × 128 cm and 120 cm × 192 cm. Sample A consists of 2560 particles, sample B of 10240 particles and sample C of 23040 particles. The distribution of the average vertical strain $\langle \epsilon_{22} \rangle$ is illustrated in figure 8.20. Note that although this figure suggests a size effect, this does not represent the point of interest of the present study, since here the focus lies on the size independent pattern formation. For all three samples the pattern formation reflected by the strain distribution is practically identical with respect to the following key features: localization band inclination, band width and band distance. First, the inclination of the (secondary) bands is the same in all three cases, namely, as expected for the case of vanishing tangential forces,
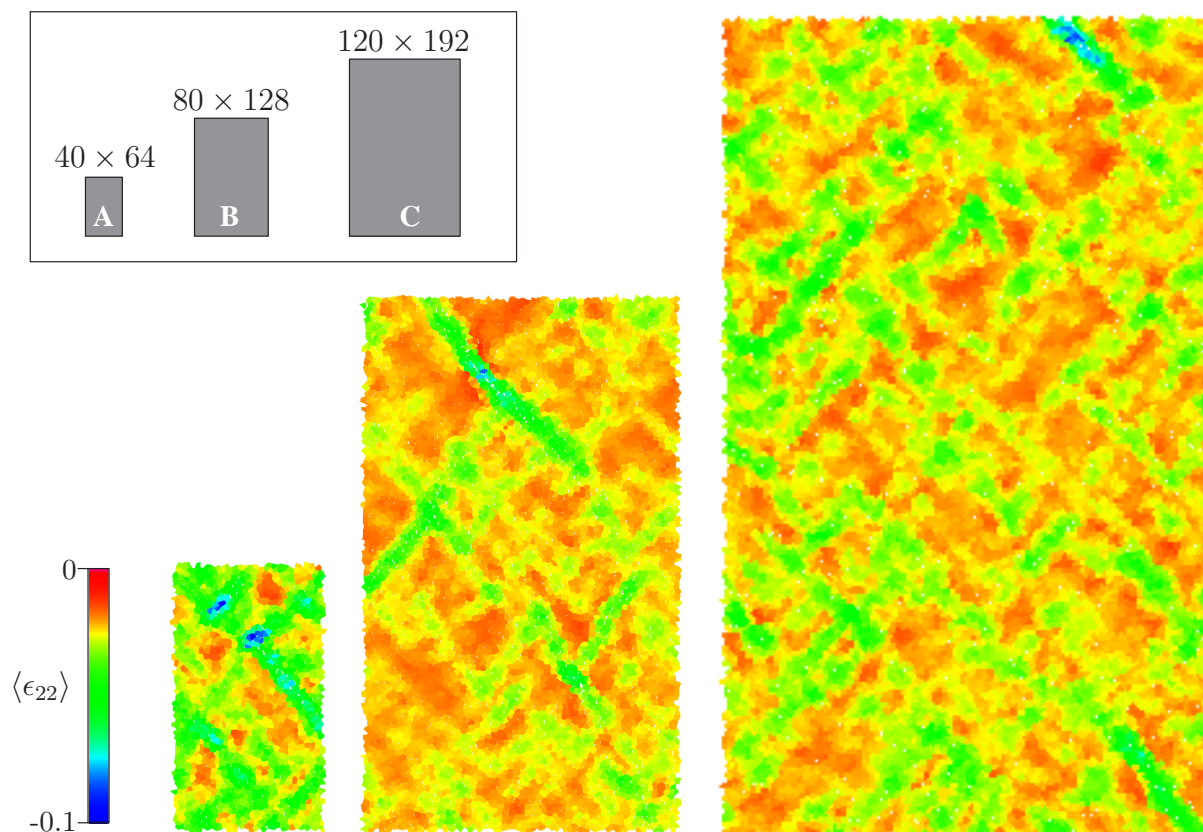
Figure 8.20: Pattern formation by means of vertical strains in the pre-localization regime.

45°. Second, the band is approximately 5 particles thick for all cases. Finally, the distance of parallel competing shear bands ranges from a measured minimum of approximately 4 to a maximum of approximately 16 particles. The band inclination is obviously independent of the RVE size, compare the situation after localization of the 40 cm × 64 cm sample for RVE_5 and RVE_19 in figure 8.19. Certainly, the band width as well as the distance of the localization bands depend to a high degree on the RVE size, compare also figure 8.19. As stated before, the RVE size is bound by the microstructural effect that ought to be described and visualized. This applies even for the case of kinematic quantities. In view of this remark, a RVE size RVE_19, as used for the comparative study of the 40 cm × 64 cm sample, is too large in order to resolve this pattern formation. However, this is exactly the same conclusion drawn from the case of the dynamic quantities, e. g. the evaluation of the couple stresses.

Energetical quantities - Hill condition

A closer look on the stress power of the sample helps to understand the process of failure and its time evolution, e. g. the appearance of the first dominant shear zone ①. At first, one is interested in the part of the stress power caused by the curvature and the couple stresses, named $\mathcal{P}_{int}^2$ in equation (8.31). As the rotational degree of freedom plays an important role for the development of this first dominant fault, the quantity $\mathcal{P}_{int}^2$ was recorded in a time period ranging from just before the localization appears up to a situation right after the formation of this zone has ended. Note that for didactical reasons
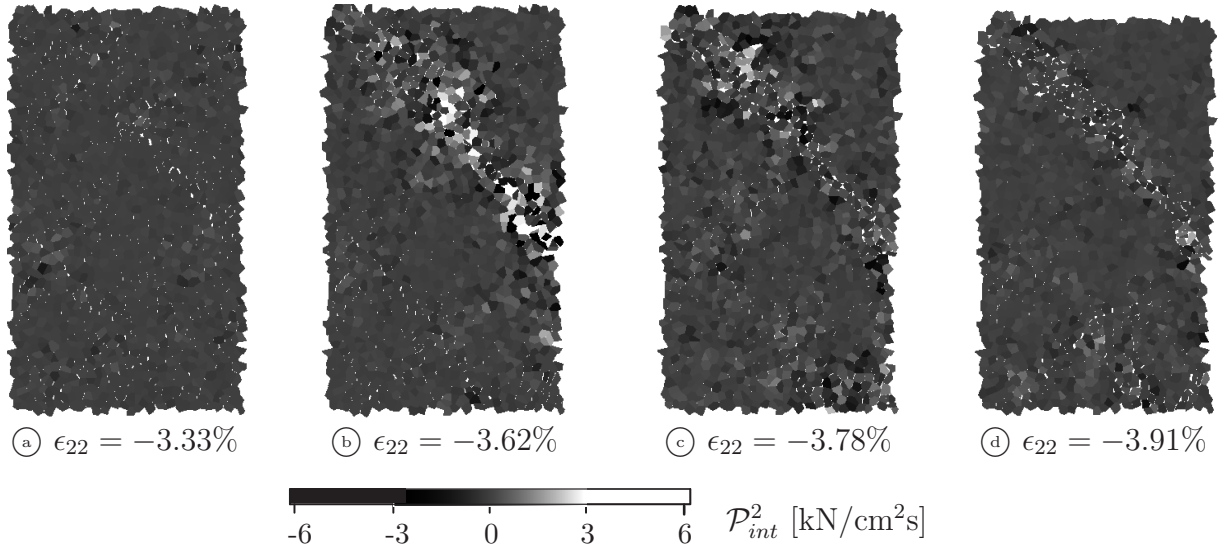
Figure 8.21: Distribution of $\mathcal{P}_{int}^2$ for RVE_5 in a period covering the formation of the first shear band zone.

a shorter time period ⓐ to ⓓ compared to figures 8.14 and 8.15 is utilized and in turn different time stages compared to the above ones are used for the visualization. As one can see in situation ⓐ in figure 8.21 no outstanding activity is visible, as the mass of the middle grey shaded particles represents a neutral situation ($\mathcal{P}_{int}^2 \approx 0$). Against it, in situation ⓑ the stress power localizes in the lower part of the shear zone expressed by the white and black regions. Afterwards, in ⓒ the zone of activity is slightly moving upwards in diagonal direction of the shear zone accompanied by a decrease of the average amount of power. The last scene ⓓ in figure 8.21 represents the situation after formation
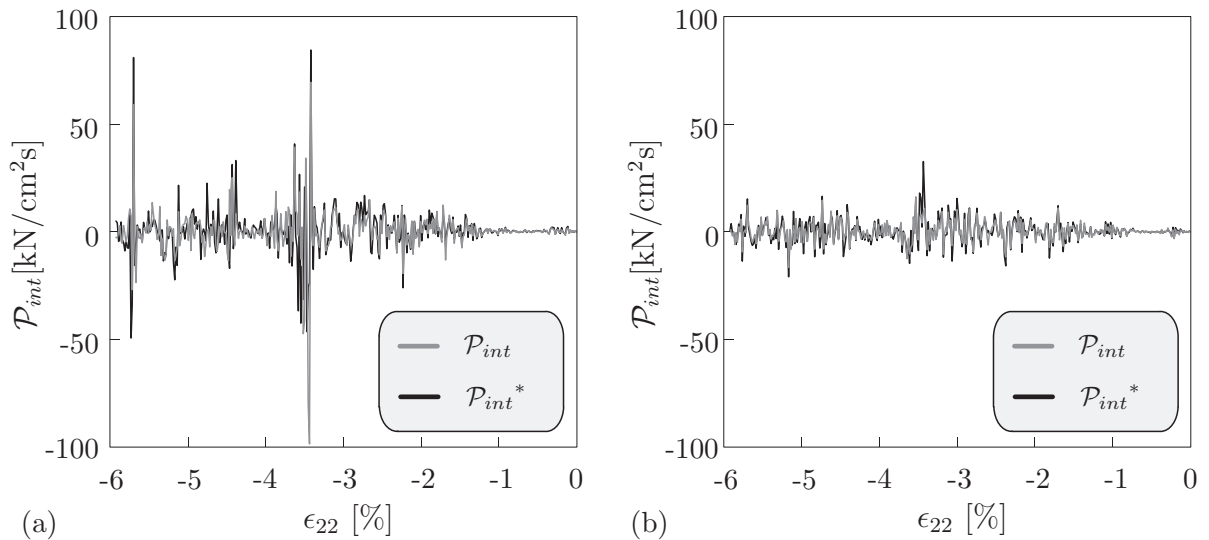
Figure 8.22: Check of validity of restricted Hill criterion for RVE_5 by means of $\mathcal{P}_{int}$ and $\mathcal{P}_{int}^*$ for an RVE (a) inside evolving shear band and (b) outside evolving shear band.
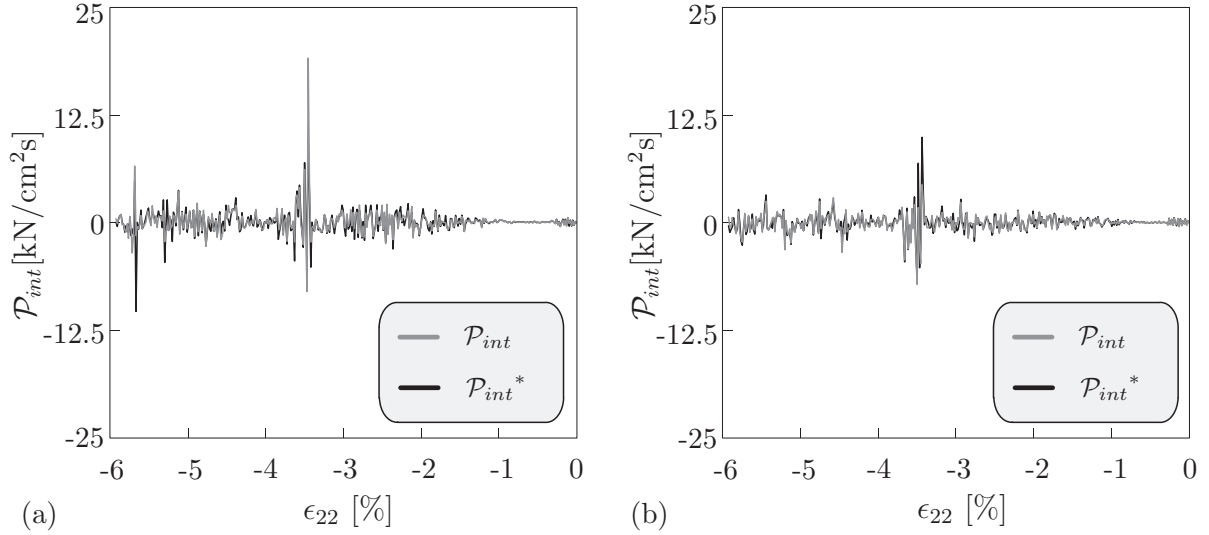
Figure 8.23: Check of validity of restricted Hill criterion for RVE_19 by means of $\mathcal{P}_{int}$ and $\mathcal{P}_{int}{}^*$ for an RVE (a) inside evolving shear band and (b) outside evolving shear band.

of the shear band. It becomes apparent that only a negligible rotational activity is present within the sample. The results in figure 8.21 and, in particular at stage ⓑ, agree quite well with the findings of Åström et al [7] on the energy release in shear zones.

An investigation of the validity of a restricted form of the Hill criterion of equation (8.33) is plotted in figures 8.22 and 8.23 for different RVE sizes RVE_5 and RVE_19. The result is that for both RVE sizes the simplified relation (8.31) holds, as both curves $\mathcal{P}_{int}$ (grey) and $\mathcal{P}_{int}{}^*$ (black) almost coincide and lie one on another. Therefore, nearly no difference between the grey and black curves is visible in most parts, except at that time stages when a highly localized action occurs in the vicinity or within the monitored RVEs, i. e. in the peak region. This behavior is seen for RVEs either inside or outside of the evolving shear band. By comparing the results of the different RVE sizes it becomes clear that irrespective of the size of the RVE the evolution of the shear zone is reflected. However, the maximum values of the stress power are four times smaller for RVE_5 than for RVE_19. This is an indirect consequence of the effect of the larger smearing radius on the average strain calculation, compare figure 8.19. The onset of the shear band zone is apparent for both RVE sizes, as shown in figures 8.22 and 8.23. The action is more visible in terms of time duration for RVE_5 than RVE_19. Even for RVEs outside of the evolving localization band a small peak is measured for both RVE sizes, see figures 8.22 (b) and 8.23 (b).

Summary

In conclusion, based on the evaluation of dynamical, kinematical and energetical quantities an "ideal" RVE size was found: RVE_5, containing approximately 20 particles and having 5 particles as diameter.

In the case of energetical values the locality is still reflected in a qualitative manner for RVE_19. However, for a reflection of the locality of the couple stresses or the pattern formation in the pre-localization regime the RVE size RVE_19 is too large. A size RVE_5 guarantees comparable values of the stress tensor $\langle \mathbf{T} \rangle$ with respect to a macro-

scopic measurable stress response as well as comparable values of strains. Therewith, the homogenization is possible without a loss of the locality of the problem, expressed by the occurrence of couple stresses as well as a non symmetric stress tensor. Certainly, the found "ideal" size is only exemplary for the shown boundary value problem and under consideration of the given particle shape and size. A check of a restricted form of the Hill condition showed the generality of the found results. Furthermore, it was shown that the scale separation arguments which imply a neglect of the volume terms (e. g. acceleration terms) in the corresponding balance equations have no effect on the calculation of stresses and couple stresses for the "ideal" RVE size. In particular, the presented example emphasized that couple stresses as well as a non-symmetric stress tensor are an outcome of the introduced homogenization procedure rather than being a result of the simplification along with the neglect of the volumetric terms in the balance laws.

8.5.2   Compact biaxial test

The next example considers the compact biaxial test introduced in section 3.6.1 with a height to width ratio of 1:0.37 and 3800 particles that resemble the 38 cm × 102 cm large sample. 2600 RVEs are used for the evaluation of the considered variables. Again, for simplicity, no base particles are placed in the boundary region of the sample, compare the procedure for the slender biaxial test, e. g. the valid base particles in figure 8.5 (b). As a result from the first example the "ideal" RVE size RVE_5 is used. In comparison to the slender specimen a higher amount of dominant shear zones appears, compare figure 3.15. In figure 8.24 the horizontal strain distribution before and after localization of the primary fracture pattern is presented. In order to visualize the pre-localization behavior in a detailed form the scale is fit appropriately. For the pre-localization behavior on the left side of figure 8.24 a maximum strain of 7 % is reached, while afterwards a maximum strain of 28 % is obtained. Note again that the application range of a linear kinematics which underlies the present homogenization procedure is left, since the particle sample exhibits gross discontinuous material and geometrical behavior. Thus, the continuity constraints included within the presented homogenization procedure are relaxed because of the physics of the problem, i. e. in the post-localization regime of the present and the oncoming examples the homogenization procedure is used rather as visualization than as quantification tool. As expected a pattern with crossing diagonal bands becomes visible in the pre-localization regime, whereas a dominant failure pattern with non-crossing bands is obtained after localization. The picture does not significantly change, if the vertical component of the average strain tensor is plotted. The various bands formed in the pre-
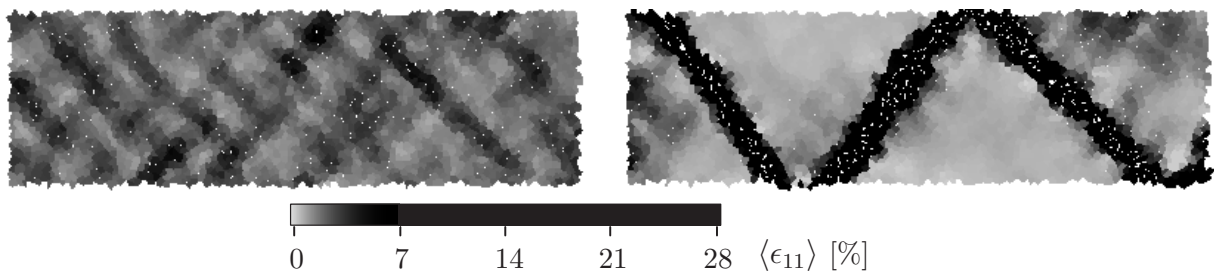
Figure 8.24:   Distribution of horizontal strains before and after localization.
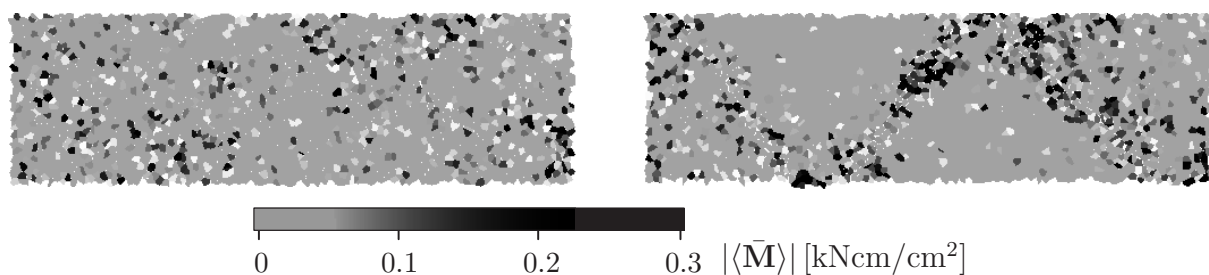
Figure 8.25: Distribution of norm of couple stress tensor before and after localization.

localization regime are completely relaxed after onset of localization. The investigation of the evolution of the couple stresses in figure 8.25 gives an additional insight into the activation of the particle rotations in the shear zones. The norm of the couple stress tensor is plotted with respect to a point in time before and after the onset of shear band formation. Small local fluctuations in a statistically distributed fashion are present before the shear band forms. During the formation of the band a clear accumulation of high couple stresses is obtained in the corresponding diagonal bands, as shown in figure 8.25, right. A computation by use of larger RVE sizes like RVE_19 shows no pronounced activity within the evolving shear zone, as already illustrated for the slender biaxial test in the previous section.

8.5.3 Extension of granular layer

The third example is concerned with the extension of a granular layer according to *Nübel's* [188] setup already introduced in section 3.6.2. An elastic strip attached between a fixed and a movable vertical side wall is placed at the bottom of a particle filled box and by shifting the right wall a linear stretch at the bottom is attained. The induced failure within the sample is shown in figure 3.18. The basic failure mechanism is developed by the formation of a wedge limited by two inclined fault zones. Here, the example with the smaller boundary velocity v_B is used. 2600 RVEs of size RVE_5 are utilized for the evaluation. The pre-localization behavior becomes obvious, if one considers the distribution of the average strain tensor $\langle \epsilon_{11} \rangle$ in figure 8.26, left. Again, comparable to the previous biaxial tests the pattern formation dominates the pre-localization regime, while the wedge formation becomes obvious after localization onset. A broad spectrum of inclined zones forms in the region of the wedge. In the pre-localization regime a similar
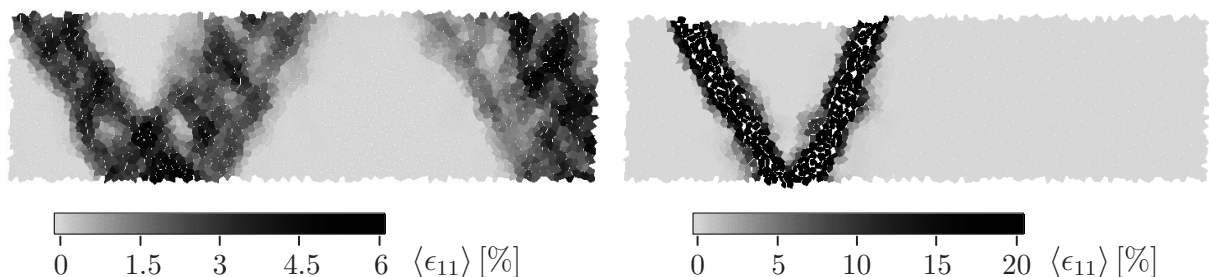
Figure 8.26: Distribution of horizontal strains before and after final localization.
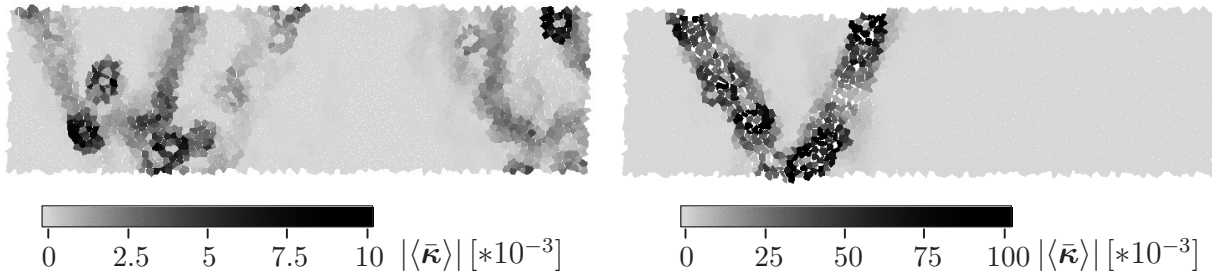
Figure 8.27: Distribution of norm of curvature before and after final localization.

localization pattern as for the biaxial simulations is visible, i. e. crossing secondary shear zones develop in the region of the boundary and the wedge to form, compare figure 8.26, left. At this stage it seems that two wedges may form, one inside the sample and one at the right boundary. The decision of the final failure is a matter of the velocity v_B. After onset of localization two zones become dominant and lead to the wedge formation and downward wedge motion, as visible in figure 8.26, right. Further insight into the temporal progress of failure is obtained through an evaluation of the norm of the curvature $|\langle \bar{\kappa} \rangle|$. This measure represents an average expression of the activation of the rotational degree of freedom of the RVEs. The plots in figure 8.27 refer to the same time stages, as the strain distribution plotted before, namely just before and after localization. The curvature distribution provides a more detailed picture of the points of activity within the sample, especially the snapshot of the pre-localization regime. For example, in the region of the wedge to form three distinct "lines of action" and some isolated zones with dominant rotational activity stand out.

8.5.4 Brazilian test

In the Brazilian test a failure evolution dominated by tensile splitting in a zone of finite width through the whole sample is obtained, compare the simulation output in figure 4.11 (b). The average dynamic and kinematic quantities are evaluated for approximately 1800 RVEs using a RVE size RVE_5. The parameters of the simulation and, in particular, the beam parameters representing the cohesive component are summarized in sections 4.5.1 and 4.5.2. The evolution of the horizontal stresses in figure 8.28 shows a gradual decrease of the stresses towards the non loaded upper and lower boundary of the sample throughout steps (1) to (3). After completion of localization in (3) tensile horizontal stresses are possible that, depending on the chosen beam parameters, may lead to cracking at the top and bottom boundary. The triangular zones at the left and right hand side of the corresponding bearing strip are highly compressed both in the horizontal, as visualized by the light grey zone in figure 8.28, and vertical direction. In accordance with experimental observations no beam breaking occurs in this region.

The evolution of the vertical strains is presented in figure 8.29. Comparable to the biaxial simulation results before the onset of visible failure in (1) a pattern of crossing zones with higher strains in the center region of the sample is obtained. The cracking starts nearly simultaneously at the top border of the bearing zones and in the center region, as visible in situation (2), and drives in horizontal direction through the complete sample. In the meantime cracking at the bottom border of the bearing strips starts and merges into the
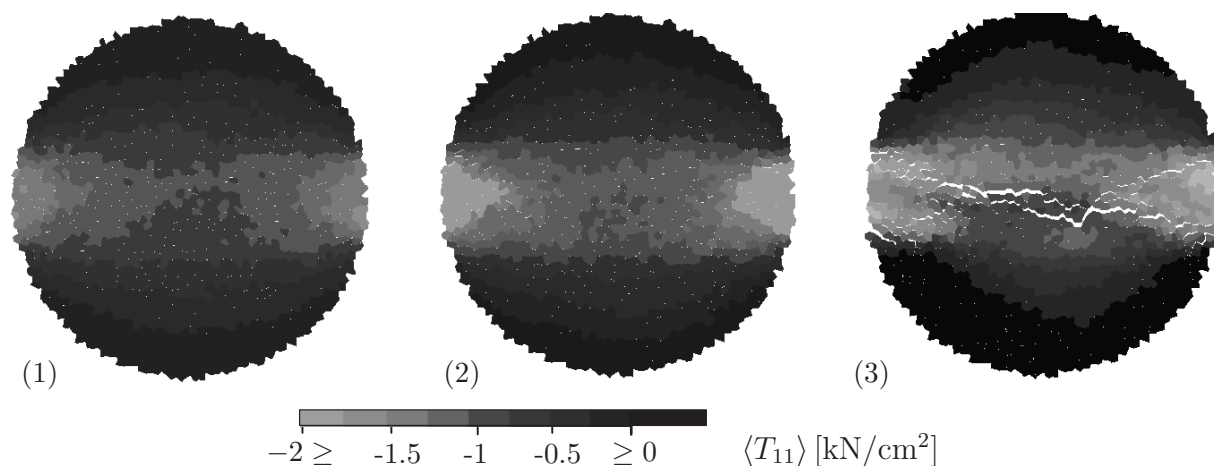
Figure 8.28: Distribution of horizontal stress before (1), during (2) and after completion (3) of localization.

horizontal main crack in the center, compare situation (3). The stress and strain evolution agree qualitatively very well with the experimental observations of *Castro et al.* [32] and *Rocco et al.* [208]. Comparable to the experiments a constant vertical stress state in the center region of the specimen along 80 % of the horizontal plane is obtained which is not shown here for brevity.

Finally, this example shows that the proposed homogenization technique is not restricted to cohesionless particle systems, but can be applied to bonded granulates as well as pure beam lattices, too, see also *Diebels & Steeb* [66, 67]. On the other hand, this example also expresses the limit of homogenization theories: In the process of localization, a macroscopically visible crack appears that represents a strong discontinuity of the strain field, compare figure 8.29. It makes no sense, in particular for kinematic variables, to calculate average quantities in these regions, as this mode I crack yields unmeaning values of the RVE quantities.
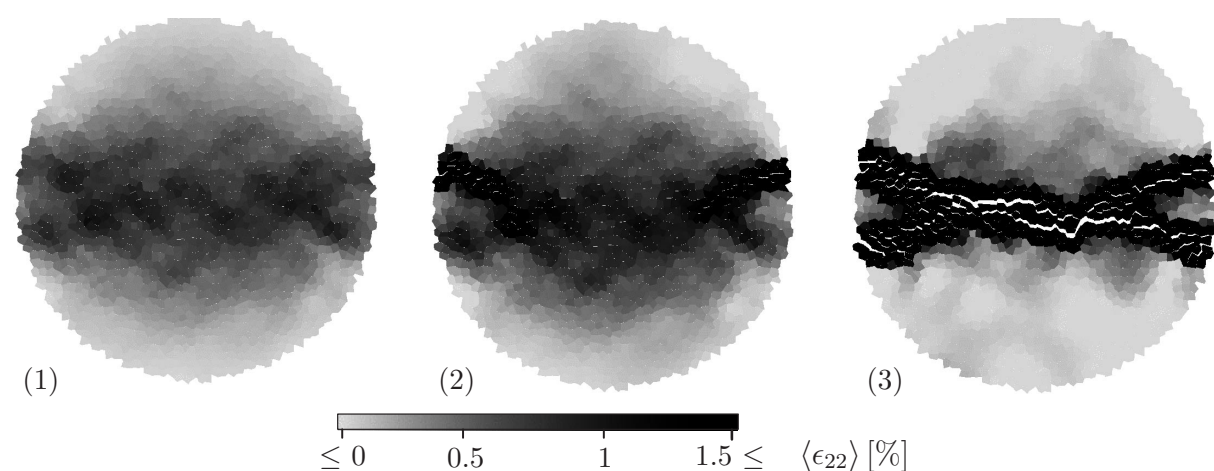
Figure 8.29: Distribution of vertical strains before (1), during (2) and after completion (3) of localization.

8.6 Identification of material parameters

Apparently, if dynamic and kinematic quantities are known, an identification of macroscopic material properties seems conceivable. Thus, it makes sense to devote further discussion on this subject. In this context the following two central points are detailed below: first, the relation of the RVE size to the internal length scale, and second, a possible determination of material parameters.

The first point refers to the relation between the size of the RVE by means of the averaging radius and the so-called internal length scale in the context of an implementation of enhanced continuum theories in FEM models: Although similar from the terminology, these two lengths are very different from their definition. The "internal length" of an enhanced continuum model denotes a parameter that approximatively represents the neighborhood of a material point and among other things is influenced by the effect of the corresponding stiffnesses of the numerical model, e. g. the Lamé parameters. The fact, that this parameter has a relation to the microstructure or is at least motivated by it, is widespread in the literature. However, so far no clear analytical relation between ingredients of a microstructure and this length scale has been proposed and methodological evidence about this relation is still missing in the relevant literature. Mostly the choice of this length scale is of heuristic nature, by e. g. fixing a relation between average grain diameters and the internal length, see e. g. *Marcher* [163] or *Mühlhaus & Vardoulakis* [181], or can be determined by inverse modeling, see *Mahnken & Kuhl* [160], which definitely represents a non-physical approach and is highly problem dependent. As in most numerical applications the "internal length" is used to control or scale, respectively, the thickness of the determinable localization zone width, at the present stage of research this parameter can rather be attributed as a numerical parameter than a microstructural one. The RVE size is by definition a numerical parameter and represents a length with a direct link to the underlying microstructure. Upon consideration of the insights attained in the previous sections, depending on the used RVE size microstructural effects can be observed. In analogy to the non-local theories realized in the context of enhanced continuum models, if the averaging radius becomes too large, these effects are no longer detectable. Recall, that the target "ideal" RVE size which allows to extract the locality of the solution, e. g. the microstructural effects like the evolution of couple stresses or the stress asymmetry, is by no means a numerical parameter, but represents the inherently included length scale. These two lengths, the "internal length scale" of enhanced continuum theories and the "ideal" RVE size of the homogenization procedure, can be related to each other, e. g. by following the remarks in *Diebels & Steeb* [66, 67]. There, the information attained through the observation of boundary layer effects when performing simple shear simulations of foams with a discrete beam lattice model were utilized for an inverse modeling of the shear band thickness in continuum models. In the linear elastic regime a functional dependence of the localization band thickness and, therewith, of the "internal length scale" l_c^2 of the macro model on the following parameters is obtained: the stiffness parameters of the micropolar-type macro model, i. e. the Lamé parameter μ and the Cosserat parameter μ_c, and the length scale of the micro model, i. e. the particle size. In the above considerations the RVE size is intrinsically included due to the general restriction on its size to be smaller than the size of the boundary layer. Thereby, a macro model may be represented by an enhanced continuum model within a FEM framework and a micro model by a particle model or as done in *Diebels & Steeb* [66, 67] by a beam

lattice model.

The second topic concerns the determination of elastic material parameters by use of the relation of average dynamic and kinematic quantities to each other. Note that this kind of relations are only valid in the initial, elastic regime since typically in particle composites starting from the pre-failure stage a highly nonlinear behavior is obtained. In principle, the present definition of the RVE implies a "testing volume" which is small enough to represent microstructural effects, e. g. to represent couple stresses on an intermediate scale, rather than being a "representative" element as stated by the terminology "RVE". The standard average quantities determined for one RVE are not representative for the complete sample. Both dynamic as well as kinematic quantities fluctuate subject to the corresponding RVE size. It is not clear, whether the sensitivities of the dynamic and kinematic quantities with respect to the RVE size are the same. This means that in the present case the corresponding quantities may not be correlated to each other, i. e.

$$\frac{\langle \mathbf{T} \rangle^i_{\mathcal{R}_1}}{\langle \langle \mathbf{T} \rangle_{\mathcal{R}_1} \rangle} \not\approx \frac{\langle \boldsymbol{\varepsilon} \rangle^i_{\mathcal{R}_1}}{\langle \langle \boldsymbol{\varepsilon} \rangle_{\mathcal{R}_1} \rangle} , \qquad \text{with} \qquad \max_{1 \leq i \leq n_{\mathcal{R}}} \left[\frac{\langle \mathbf{T} \rangle^i_{\mathcal{R}_1}}{\langle \langle \mathbf{T} \rangle_{\mathcal{R}_1} \rangle} \right] \not\approx \max_{1 \leq i \leq n_{\mathcal{R}}} \left[\frac{\langle \boldsymbol{\varepsilon} \rangle^i_{\mathcal{R}_1}}{\langle \langle \boldsymbol{\varepsilon} \rangle_{\mathcal{R}_1} \rangle} \right] . \qquad (8.40)$$

Therein, $n_{\mathcal{R}}$ denotes the number of RVEs in a sample and the notion $\langle \cdot \rangle_{\mathcal{R}_1}$ refers to an average quantity of a certain RVE $\mathcal{R}_1$. This fact renders the determination of the elastic stiffness parameters that combine stresses with strains via $\langle \mathbf{T} \rangle = \mathbf{C} \langle \boldsymbol{\varepsilon} \rangle$ and couple stresses with curvatures via $\langle \bar{\mathbf{M}} \rangle = 2 \mu_c l_c^2 \langle \bar{\boldsymbol{\kappa}} \rangle$ impossible. It makes no sense to compute RVE specific elastic material parameters by use of these relations, as the meaning of this kind of material quantities would be unclear in the present context. In order to determine reasonable elastic material parameters one has either to increase the RVE size or to average over the available average quantities. In this context the term "reasonable" refers to equivalent elastic macroscopic parameters. This means that in order to adapt realistic material parameters of e. g. granular materials for simulations with a predictive character, at least in the elastic regime the material parameters of the target material have to be fit. If the RVE size is increased, average quantities will no longer represent microstructural effects like a stress asymmetry or couple stresses. However, if the average over all average quantities is carried out, at least reasonable effective elastic stiffness parameters for the standard continuum theory may be obtained via $\langle \langle \mathbf{T} \rangle \rangle = \langle \mathbf{C} \rangle \langle \langle \boldsymbol{\varepsilon} \rangle \rangle$, compare also *Lätzel* [144], *Lätzel et al.* [145] or *Luding* [154]. In the case of the additional (micropolar) parameters this procedure cannot succeed. The reason is obvious: The average couple stresses as well as the average curvatures localize only in narrow zones within a sample. An additional averaging over the complete sample would smear out the microstructural effects coupled with a localization of these variables. Thus, no reasonable result can be expected. The same applies for the stress asymmetry which is only detectable in the same narrow zones.

In the following, an alternative idea is proposed which enables to capture the additional parameters of the enhanced continuum theory, i. e. Cosserat stiffness μ_c and internal length l_c^2 in the elastic pre-localization regime, i. e. before failure takes place. This alternative approach where the average quantities are averaged over a predefined part of the sample seems more promising than the procedure described above. The control volume (to be averaged over) includes only those zones where microstructural effects appear. In the case of the biaxial test one may define the control volume to cover the region of the first shear zone, compare figure 8.30 (a). All RVEs are considered whose extension of
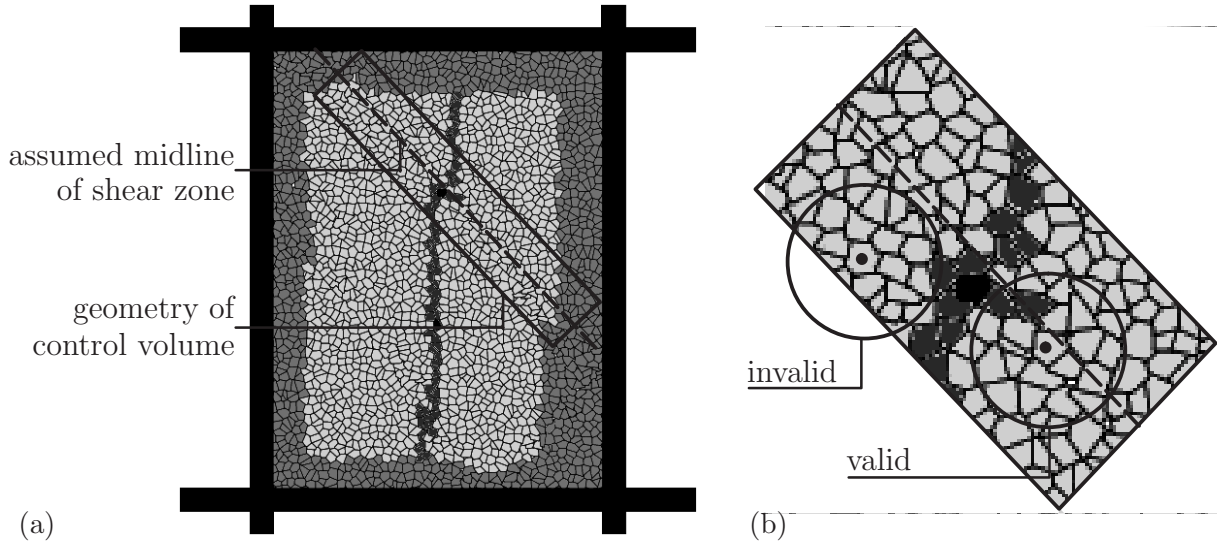
Figure 8.30:   (a) Definition of control volume for computation of effective material parameters and (b) detail of control volume with examples of valid and invalid RVEs.

the corresponding averaging circles is completely included in this monitored area, see the examples of valid and invalid RVEs in figure 8.30 (b). Then, an evaluation by means of $\langle \bar{\mathbf{M}} \rangle_* = 2\mu_c l_c^2 \langle \bar{\boldsymbol{\kappa}} \rangle_*$ seems reasonable. $\langle\langle \cdot \rangle\rangle_*$ denotes an averaging of average quantities over the control volume. A further specification of this idea leads to a definition where only RVEs are included in the control volume that posses a diameter that equals the width of the localization zone. This implies that those particles that are cut by the dotted line in figure 8.30 represent the base particles of corresponding RVEs, while the diameter of the RVE is identified with the smallest dimension of the control volume, i. e. its width. In order to validate the detailed procedures exemplary simulation setups should be considered. Corresponding setups should ensure that the position of the zones where microstructural effects occur are known in advance. An adequate example is the shearing of a narrow granular layer between very rough boundaries by *Tejchman & Gudehus* [236]. The position of the shear zone is known a-priori to occur parallel to the loading direction in the middle of the specimen. In micropolar FE computations the thickness of the shear zone depends among other parameters on the internal length scale which is inserted as input parameter. This thickness and the according relation to the parameters of a microscopic model like the DEM model represent the starting point of a corresponding parameter identification. Thereby, the ideas presented above and at the beginning of this section denote a promising way to realize this identification.

8.7   Validation of homogenization procedure

A homogenization method was presented that allows for the modeling of couple stresses and non-symmetric stress states in a straightforward way. One of the key ideas that lead to this characteristic is the statically equivalent transfer of the contact forces from the boundary of representative volume elements to the centers of mass of the corresponding boundary. Based on this approach a micropolar theory was motivated either by means

of a theoretical derivation of balance laws on the basis of the assumptions of particle (rigid body) mechanics and, on the other hand, by numerical simulations on the basis of the DEM. The following general dilemma in the context of homogenization is persistent: The use of a discrete model naturally aims at the description of local effects along with the computation of corresponding local quantities. But, a homogenization smears this information in a certain averaging radius, what is in contradiction with the usual thought behind the use of discrete models. However, the presented procedure combines the advantages of the locality (by the DEM) and the "continuumization" (by the homogenization) and shows advantageous characteristics: On the one hand, the discrete model can be used in order to properly represent the locality of certain mechanical quantities. On the other hand, the averaging procedure along with the volume adjustment yields comparable continuum mechanical quantities, whereby the locality is not completely lost. As a result the described procedure reflects a filtering of the relevant results without the loss of comparability with continuum models.

The biaxial simulation results showed that the diameter of the RVEs should be of the order of around 5 times the typical particle diameter in order to reproduce the macroscopic stress response together with localization effects occurring when strong inhomogeneities dominate the local behavior. Increasing the diameter of the RVEs yields a smearing out of the results in the sense that localization becomes invisible. In particular, it was found that micropolar effects occurring in the shear band zones are governed by the existence of couple stresses and non-symmetric stress tensors. These effects are of boundary layer type and are, therefore, only detected by sufficiently small RVEs, while they are shrinking with increasing RVE size. From the biaxial simulations under study the thickness of the shear band was found to be of the order of only several grain diameters. Upon consideration of the general dilemma, the RVE size is obviously limited by the size of the effects to be described rather than by the theoretical requirement of containing a manifold of particles.

In short, the following conclusions can be drawn:

- Micropolar formulations can be motivated by means of a discrete particle method on the basis of the DEM via an explicit inclusion of the rotational degree of freedom and the procedure of a statically equivalent transfer of the contact forces.

- A volume adjustment technique enables the comparability between RVE average stresses with the macroscopic stress answer. The general feature of homogenization techniques, namely that the fluctuations of average quantities decrease with increasing average diameter, is correctly resembled.

- The localization of the couple stress as well as the stress asymmetry point to the position and inclination of the shear band development.

- The assumption of scale separation, which implies a neglect of the volume integrals with respect to surface ones in the balance laws, is valid. Furthermore, the evaluation of a restricted form of the Hill condition suggests a consistent derivation of the homogenization.

- The procedure for derivation of dynamic quantities can be straightforward transferred to kinematic quantities. Therewith, experimentally motivated strain localization pattern can be obtained.

- Promising ideas for the identification of (elastic) macroscopic material parameters have been mentioned. The estimation of the internal length scale parameter l_c^2 or the Cosserat parameter μ_c which are needed for a FEM implementation of a micropolar model are conceivable.

In contrast to articles where rotational stiffnesses are introduced "by hand" via local constitutive laws at the contact in form of a moment spring, e. g. see *Chang & Gao* [35], here, couple stresses naturally result from the eccentricities of the normal contact forces. Thus, the physical evidence of couple stresses can be motivated. No additional constitutive parameters, that generally are not directly detectable by experiments, have to be introduced in order to represent the feature of micropolarity within a DEM model. Certainly, as will be shown in the next chapter, the micropolar theory represents only one possibility of an enhanced continuum theory which can be motivated by particle models.

A further remark concerns the applicability of the present homogenization theory: This procedure is not restricted to test setups where micropolar effects are expected like in the case of the biaxial test. Quite the contrary is the case, as the procedure provides a general framework for a coherent numerical treatment of homogenization in the context of DEM models. The "micropolar effects" discussed before may simply be seen as an inherent feature of this type of homogenization approach and are mainly based on the elegant way to transfer the boundary forces into the mass centers in a statically equivalent way.

Chapter 9

From particle models to gradient continua

9.1 General

Starting from the formulation of a *continuum with microstructure* according to *Mindlin* [172], the special case of a second gradient (of displacement) theory was obtained in chapter 2: Thereby, the assumption was made that a particle on the micro scale δ is subjected to the same deformation as the general continuum on the meso scale d or macro scale D. Elaborated in the 1960's, e. g. by *Eringen* [79], *Green & Rivlin* [94] or *Mindlin* [172], gradient-type theories have been increasingly utilized in the context of regularization techniques for FEM models since the 1990's, see section 2.2.4 for a general discussion of gradient-type theories in the context of a non-local continuum. The basis of this development were the seminal articles by *Aifantis* [1, 2]. Increasing computational power at the beginning of the 1990's allowed the mathematical elaboration and numerical realization of his ideas to include gradients into the FEM, cf. e. g. *de Borst & Mühlhaus* [59], *Mühlhaus & Aifantis* [179], *Pamin* [195] or *Vardoulakis & Aifantis* [246]. Experimental evidence of general non-local continua (gradient- or integral-type) by detection of displacement or strain gradients has been found in materials where an interplay between different length scales is present. The microstructural length scale is significant in the analysis of the material at a scale where it is greater than or equal to the required resolution length or the length scale of the deformation field. In these cases, strain gradient effects may play a dominating role. Laboratory experiments and field observations suggest that the spatial periodicity is the underlying common feature of typical failure phenomena in geomaterials. Thereby, the spatial periodicity is expressed by a characteristic wavelength which yields a consistently reproducible pattern formation, compare the simulation results in figure 8.20 or 8.26. The most prominent physical motivation for non-local material behavior is the heterogeneity of the microstructure and corresponding implications of it, cf. the surveys of *Aifantis* [3] and *Bažant & Jirásek* [15]. The macroscopic or averaged stress answer depends on the average strain of the RVE, i. e. the finite volume surrounding a certain point, instead of the strain at this point.

The scope of this chapter comprises the extension of the homogenization procedure presented in the previous chapter towards the inclusion of gradient terms. The original ideas of *Mindlin* [172] incorporating a second gradient theory are extended up to the third gradient of displacement. Furthermore, a method is incorporated that enables the computation of displacement gradients based on local measurements of the particle movement within the RVE. This includes a statistical "best-fit" routine that represents the core operation for the determination of the gradients. Energetical considerations yield conjugated higher

order stresses as additional dynamic quantities and substitute the couple stresses derived in the previous chapter. In addition, interesting similarities of the presented methodology and computational multiscale methods based on minimizing fluctuation fields, compare *Kouznetsova et al.* [129], *Miehe et al.* [171] or *van der Sluis* [242], are outlined. The procedure is validated by means of numerical simulations where, again, the question on the size of a representative volume element is picked up.

9.2   Kinematic quantities

The determination of displacement gradients is not a straightforward task as the determination of the additional degree of freedom, rotation, was in the previous chapter. The displacement gradients are no directly measurable quantity and their visualization in experiments poses a constraint on the testing facility. However, the displacement gradients (of first, second and even higher order) may be computed in an indirect manner from the discrete displacements using a statistical technique.

The procedure that will be introduced in the following is influenced by the analysis of experimental measurements by means of measured discrete displacements in form of a post processing technique. The original idea behind this procedure can be traced back to the thesis of *Peters* [196] and intense elaborations by *Geers et al.* [91], see also his thesis, *Geers* [89], for a more detailed overview. Essentially, in the context of a particle assembly the local distances between the center points of particles contained within an averaging volume are utilized. Comparable to the procedure introduced in the previous chapter the distances are referred to the center point of the base particle. On the other hand, these distances can be approximated via a Taylor expansion. The comparison of approximated and measured values, then, yields an approximation of the displacement gradients. Within the homogenization procedure in chapter 8 only the displacement and rotation of the boundary particles contributed to the average quantities. In contrast, here, for methodical reasons the displacements of all particles within a RVE contribute to the average quantities. However, the basic arguments of chapter 8 in the context of scale separation and averaging theorems are still valid.

9.2.1   Approximation through Taylor series

In order to picture the situation of an arbitrary RVE containing a finite number of particles in the initial configuration at $t = t_0$ and actual configuration $t = t_1$, figure 9.1 is considered. Two particles $\mathcal{M}$ and $\mathcal{N}$ contained within the RVE are connected by the vector $\mathbf{\Delta x}_0$ in the initial and by $\mathbf{\Delta x}_t$ in the actual configuration. $\mathcal{M}$ represents the base particle of the RVE. In-between t_0 and t_1 the RVE is driven by a deformation and, thus, the position of the particles has changed. The position vectors of the particles in both configurations are included in figure 9.1. The principal methodology that underlies the procedure to be presented here was introduced in an experiment-based framework by *Peters* [196] and advanced by *Geers et al.* [91]. If one considers $\mathbf{\Delta x}_0$ and $\mathbf{\Delta x}_t$ as line elements, the deformation tensor of the corresponding line element at time $t = t_1$ is represented by

$$\mathbf{F} = \frac{\partial \mathbf{\Delta x}_t}{\partial \mathbf{\Delta x}_0} \, . \tag{9.1}$$

Correspondingly, the position vector of a neighboring particle $\mathcal{N}$ can be approximated by a vectorial Taylor expansion via

$$
\begin{aligned}
\mathbf{x}_t^{\mathcal{N}} &= \sum_{k=0}^{\infty} \frac{1}{k!} \frac{\partial^k \left(\mathbf{x}_t^{\mathcal{M}}\right)}{\partial \left(\mathbf{x}_0^{\mathcal{M}}\right)^k} \left(\mathbf{x}_0^{\mathcal{N}} - \mathbf{x}_0^{\mathcal{M}}\right)^k = \sum_{k=0}^{\infty} \frac{1}{k!} \frac{\partial^k \left(\mathbf{x}_t^{\mathcal{M}}\right)}{\partial \left(\mathbf{x}_0^{\mathcal{M}}\right)^k} \mathbf{\Delta x}_0^k \\[2mm]
&= \frac{1}{0!} \mathbf{x}_t^{\mathcal{M}} + \frac{1}{1!} \frac{\partial \mathbf{x}_t^{\mathcal{M}}}{\partial \left(\mathbf{x}_0^{\mathcal{M}}\right)} \cdot \mathbf{\Delta x}_0 + \frac{1}{2!} \frac{\partial^2 \mathbf{x}_t^{\mathcal{M}}}{\partial \left(\mathbf{x}_0^{\mathcal{M}}\right)^2} : \mathbf{\Delta x}_0 \otimes \mathbf{\Delta x}_0 + \\[2mm]
&\quad \frac{1}{3!} \frac{\partial^3 \mathbf{x}_t^{\mathcal{M}}}{\partial \left(\mathbf{x}_0^{\mathcal{M}}\right)^3} \vdots \mathbf{\Delta x}_0 \otimes \mathbf{\Delta x}_0 \otimes \mathbf{\Delta x}_0 + \tilde{\mathbf{w}} \\[2mm]
&= \mathbf{x}_t^{\mathcal{M}} + \underbrace{\mathbf{F} \cdot \mathbf{\Delta x}_0 + \mathbf{G} : \mathbf{\Delta x}_0 \otimes \mathbf{\Delta x}_0 + \mathbf{K} \vdots \mathbf{\Delta x}_0 \otimes \mathbf{\Delta x}_0 \otimes \mathbf{\Delta x}_0 + \tilde{\mathbf{w}}}_{\mathbf{\Delta x}_t} \ .
\end{aligned}
\tag{9.2}
$$

Indices $\mathcal{M}$ and $\mathcal{N}$ refer to the corresponding base and target particles. In this thesis the series is truncated after the terms of third order, i. e. terms of higher order are collected in the vectorial expression $\tilde{\mathbf{w}}$. Equation (9.2) intrinsically contains the deformation gradient tensor $\mathbf{F}$ and the second and third deformation gradient tensors $\mathbf{G}$ and $\mathbf{K}$. $\mathbf{F}$, $\mathbf{G}$ and $\mathbf{K}$ are general place holders and represent average quantities on the RVE level in the form $\langle \mathbf{F} \rangle_{\mathcal{R}}$, $\langle \mathbf{G} \rangle_{\mathcal{R}}$ and $\langle \mathbf{K} \rangle_{\mathcal{R}}$ with the index $\mathcal{R}$ referring to the RVE level. For simplicity, the notation $\mathbf{F}$, $\mathbf{G}$ and $\mathbf{K}$ is used throughout sections 9.2.1 and 9.2.2. The position vector of particle $\mathcal{N}$ at time $t = t_1$ is expressed solely based on the position vector of base particle $\mathcal{M}$ and the combination of the displacement gradients with the initial distance $\mathbf{\Delta x}_0$ of particles $\mathcal{N}$ and $\mathcal{M}$. Imagine now, not only one neighboring particle $\mathcal{N}$ of base particle $\mathcal{M}$, but a finite number p of particles $\mathcal{N}^p$ surround the base particle within the RVE, as shown in figure 9.1. Then, equation (9.2) can be set up for each of these p particles and corresponding distances between them and the base particle. As the position of each particle is known at each time step of a simulation, so are the distances $[\mathbf{\Delta x}_t]^{meas}$ between the particles. The average displacement gradient tensors $\mathbf{F}$, $\mathbf{G}$ and $\mathbf{K}$ and the higher or-
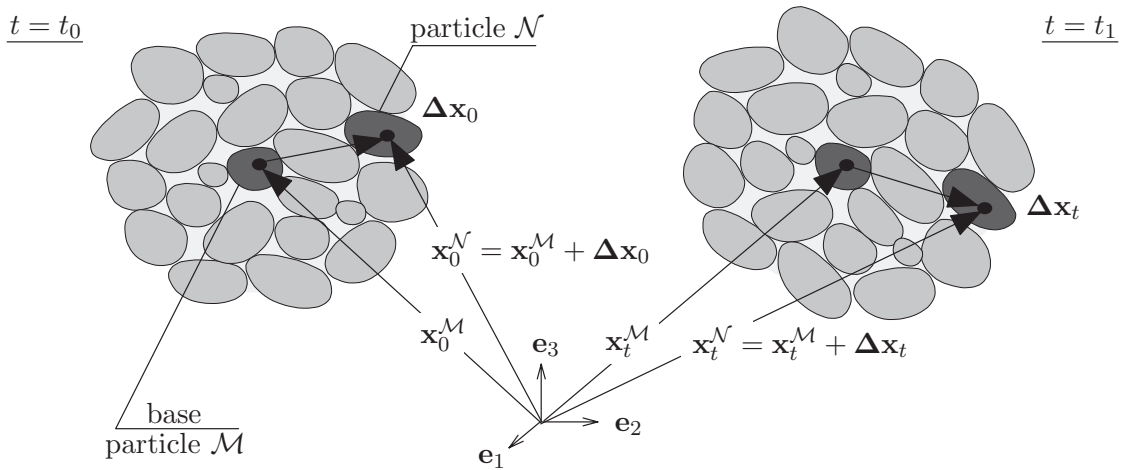
Figure 9.1: Sample in undeformed initial configuration at $t = t_0$ and deformed actual configuration at $t = t_1$.

der term $\tilde{\mathbf{w}}$ according to equation (9.2) are the unknowns. Through the known (because measured) distances these displacement gradient tensors can be evaluated in an approximated format. This is done in an inverse manner by minimizing the difference $\mathbf{d}$ between the "real" measured distance $[\mathbf{\Delta x}_t]^{meas}$ and the approximated distance $[\mathbf{\Delta x}_t]^{approx}$ via

$$
\begin{aligned}
\mathbf{d}^j &= [\mathbf{\Delta x}_t]^{j,meas} - [\mathbf{\Delta x}_t]^{j,approx} \\
&= [\mathbf{\Delta x}_t]^{j,meas} - \mathbf{F} \cdot \mathbf{\Delta x}_0 - \mathbf{G} : \mathbf{\Delta x}_0 \otimes \mathbf{\Delta x}_0 - \mathbf{K} \vdots \mathbf{\Delta x}_0 \otimes \mathbf{\Delta x}_0 \otimes \mathbf{\Delta x}_0 - \tilde{\mathbf{w}}^j \,,
\end{aligned}
\tag{9.3}
$$

with $j \in 1...p$. In the general two-dimensional case $\mathbf{F}$ contains 4, $\mathbf{G}$ 8, $\mathbf{K}$ 16 and, finally, $\tilde{\mathbf{w}}^j$ 2 unknown coefficients. In the case at hand, where the Taylor series is truncated after the third order term, one generally has 30 unknowns. As generally for each particle pair j two equations are provided, a minimum of 15 particle pairs is necessary for a mathematically well-posed evaluation.

If equation (9.2) is evaluated for each $(\mathcal{M}, \mathcal{N}^j)$ particle pair, one obtains a different systematic error $\tilde{\mathbf{w}}^j$ for each of these particle pairs. This systematic error can be decomposed into two parts: a constant average error $\tilde{\mathbf{w}} = \langle \tilde{\mathbf{w}}^j \rangle$, constant for each particle pair within the RVE, and an approximation error $\delta\tilde{\mathbf{w}}^j$, fluctuating for each particle pair within the RVE. Thus, the higher order term contained in the Taylor series in equation (9.2) is identified as

$$
\tilde{\mathbf{w}}^j = \tilde{\mathbf{w}} + \delta\tilde{\mathbf{w}}^j = \langle \tilde{\mathbf{w}}^j \rangle + \delta\tilde{\mathbf{w}}^j \,.
\tag{9.4}
$$

Thereby, the approximation error $\delta\tilde{\mathbf{w}}^j$ can be considered as fluctuation of $\tilde{\mathbf{w}} = \langle \tilde{\mathbf{w}}^j \rangle$. The further derivation is based on the assumption that the fluctuation term $\delta\tilde{\mathbf{w}}^j$ is normally distributed around zero, i. e. its average contribution on the RVE level is zero. Hence, it does not contribute to the subsequent solution method. The complete error $\tilde{\mathbf{w}}^j$ may be interpreted as a microstructural fluctuation field (on the particle level) that accounts for the superposition of the local (per particle pair) micro displacement field on the displacement field on the RVE level. A more detailed discussion on this topic is postponed to section 9.4.

The statistical approach is based on the fact that the deviations $\mathbf{d}^j$ are non correlated and normally distributed around the null vector. The probability density function for the j observed deviations $\mathbf{d}^j$ depends on the unknown average displacement gradients and the fluctuation term

$$
P = P\left[\tilde{\mathbf{w}}, \mathbf{F}, \mathbf{G}, \mathbf{K}\right] = (2\pi\sigma)^{-p} \, e^{-\frac{1}{2\sigma^2} J} \,, \qquad \text{with} \qquad J = \sum_{j=1}^{p} \mathbf{d}^j \cdot \mathbf{d}^j \,.
\tag{9.5}
$$

The Cartesian components of the standard deviation in the 2D case are the same, $\sigma^2 = \sigma_x^2 = \sigma_y^2$. Upon consideration of the maximum likelihood method, the unknown gradients $\mathbf{F}$, $\mathbf{G}$ and $\mathbf{K}$ and the stochastic deviation $\tilde{\mathbf{w}}$ can be predicted by maximizing the probability density function with respect to the unknowns. This implies the least-square minimization of J in equation (9.5). The statistical approach involves the deviations $\mathbf{d}^j$ of all particle pairs within the RVE in an integral sense. For one particle pair one obtains the expression

$$
\begin{aligned}
\mathbf{d} \cdot \mathbf{d} \;=\; & \mathbf{\Delta x}_t \cdot \mathbf{\Delta x}_t - \mathbf{\Delta x}_t \cdot (\mathbf{F} \cdot \mathbf{\Delta x}_0) - \mathbf{\Delta x}_t \cdot (\mathbf{G}{:}\mathbf{\Delta x}_0 \otimes \mathbf{\Delta x}_0) \\
& - \; \mathbf{\Delta x}_t \cdot (\mathbf{K}\vdots\mathbf{\Delta x}_0 \otimes \mathbf{\Delta x}_0 \otimes \mathbf{\Delta x}_0) - \mathbf{\Delta x}_t \cdot \tilde{\mathbf{w}} - (\mathbf{F} \cdot \mathbf{\Delta x}_0) \cdot \mathbf{\Delta x}_t \\
& + \; (\mathbf{F} \cdot \mathbf{\Delta x}_0) \cdot (\mathbf{F} \cdot \mathbf{\Delta x}_0) + (\mathbf{F} \cdot \mathbf{\Delta x}_0) \cdot (\mathbf{G}{:}\mathbf{\Delta x}_0 \otimes \mathbf{\Delta x}_0) \\
& + \; (\mathbf{F} \cdot \mathbf{\Delta x}_0) \cdot (\mathbf{K}\vdots\mathbf{\Delta x}_0 \otimes \mathbf{\Delta x}_0 \otimes \mathbf{\Delta x}_0) + (\mathbf{F} \cdot \mathbf{\Delta x}_0) \cdot \tilde{\mathbf{w}} \\
& - \; (\mathbf{G}{:}\mathbf{\Delta x}_0 \otimes \mathbf{\Delta x}_0) \cdot \mathbf{\Delta x}_t + (\mathbf{G}{:}\mathbf{\Delta x}_0 \otimes \mathbf{\Delta x}_0) \cdot (\mathbf{F} \cdot \mathbf{\Delta x}_0) \\
& + \; (\mathbf{G}{:}\mathbf{\Delta x}_0 \otimes \mathbf{\Delta x}_0) \cdot (\mathbf{G}{:}\mathbf{\Delta x}_0 \otimes \mathbf{\Delta x}_0) + \\
& + \; (\mathbf{G}{:}\mathbf{\Delta x}_0 \otimes \mathbf{\Delta x}_0) \cdot (\mathbf{K}\vdots\mathbf{\Delta x}_0 \otimes \mathbf{\Delta x}_0 \otimes \mathbf{\Delta x}_0) + (\mathbf{G}{:}\mathbf{\Delta x}_0 \otimes \mathbf{\Delta x}_0) \cdot \tilde{\mathbf{w}} \\
& - \; (\mathbf{K}\vdots\mathbf{\Delta x}_0 \otimes \mathbf{\Delta x}_0 \otimes \mathbf{\Delta x}_0) \cdot \mathbf{\Delta x}_t + (\mathbf{K}\vdots\mathbf{\Delta x}_0 \otimes \mathbf{\Delta x}_0 \otimes \mathbf{\Delta x}_0) \cdot (\mathbf{F} \cdot \mathbf{\Delta x}_0) \\
& + \; (\mathbf{K}\vdots\mathbf{\Delta x}_0 \otimes \mathbf{\Delta x}_0 \otimes \mathbf{\Delta x}_0) \cdot (\mathbf{G}{:}\mathbf{\Delta x}_0 \otimes \mathbf{\Delta x}_0) \\
& + \; (\mathbf{K}\vdots\mathbf{\Delta x}_0 \otimes \mathbf{\Delta x}_0 \otimes \mathbf{\Delta x}_0) \cdot (\mathbf{K}\vdots\mathbf{\Delta x}_0 \otimes \mathbf{\Delta x}_0 \otimes \mathbf{\Delta x}_0) \\
& + \; (\mathbf{K}\vdots\mathbf{\Delta x}_0 \otimes \mathbf{\Delta x}_0 \otimes \mathbf{\Delta x}_0) \cdot \tilde{\mathbf{w}} \\
& - \; \tilde{\mathbf{w}} \cdot \mathbf{\Delta x}_t + \tilde{\mathbf{w}} \cdot (\mathbf{F} \cdot \mathbf{\Delta x}_0) + \tilde{\mathbf{w}} \cdot (\mathbf{G}{:}\mathbf{\Delta x}_0 \otimes \mathbf{\Delta x}_0) \\
& + \; \tilde{\mathbf{w}} \cdot (\mathbf{K}\vdots\mathbf{\Delta x}_0 \otimes \mathbf{\Delta x}_0 \otimes \mathbf{\Delta x}_0) + \tilde{\mathbf{w}} \cdot \tilde{\mathbf{w}} \,.
\end{aligned}
\tag{9.6}
$$

Recall that $\mathbf{\Delta x}_t$ and $\mathbf{\Delta x}_0$ represent the measured distances of the particle pairs within the RVE. If one considers the summation over all particle pairs p in the RVE and introduces the following abbreviations

$$
\begin{aligned}
s \;&=\; \sum_{j=1}^{p} \mathbf{\Delta x}_t^j \cdot \mathbf{\Delta x}_t^j \,, \\
\mathbf{i} \;&=\; \sum_{j=1}^{p} \mathbf{\Delta x}_0^j \,, && \mathbf{j} \;=\; \sum_{j=1}^{p} \mathbf{\Delta x}_t^j \,, \\
\mathbf{X} \;&=\; \sum_{j=1}^{p} \mathbf{\Delta x}_0^j \otimes \mathbf{\Delta x}_0^j \,, && \mathbf{W} \;=\; \sum_{j=1}^{p} \mathbf{\Delta x}_0^j \otimes \mathbf{\Delta x}_t^j \,, \\
\mathbf{Y} \;&=\; \sum_{j=1}^{p} \mathbf{\Delta x}_0^j \otimes \mathbf{\Delta x}_0^j \otimes \mathbf{\Delta x}_0^j \,, && \mathbf{H} \;=\; \sum_{j=1}^{p} \mathbf{\Delta x}_0^j \otimes \mathbf{\Delta x}_0^j \otimes \mathbf{\Delta x}_t^j \,, \\
\mathbf{Z} \;&=\; \sum_{j=1}^{p} \mathbf{\Delta x}_0^j \otimes \mathbf{\Delta x}_0^j \otimes \mathbf{\Delta x}_0^j \otimes \mathbf{\Delta x}_0^j \,, && \mathbf{J} \;=\; \sum_{j=1}^{p} \mathbf{\Delta x}_0^j \otimes \mathbf{\Delta x}_0^j \otimes \mathbf{\Delta x}_0^j \otimes \mathbf{\Delta x}_t^j \,, \\
\mathbf{L} \;&=\; \sum_{j=1}^{p} \mathbf{\Delta x}_0^j \otimes \mathbf{\Delta x}_0^j \otimes \mathbf{\Delta x}_0^j \otimes \mathbf{\Delta x}_0^j \otimes \mathbf{\Delta x}_0^j \,, \\
\mathbf{V} \;&=\; \sum_{j=1}^{p} \mathbf{\Delta x}_0^j \otimes \mathbf{\Delta x}_0^j \otimes \mathbf{\Delta x}_0^j \otimes \mathbf{\Delta x}_0^j \otimes \mathbf{\Delta x}_0^j \otimes \mathbf{\Delta x}_0^j \,,
\end{aligned}
\tag{9.7}
$$

a more compact form of $J = \sum_{j=1}^{p} \mathbf{d}^j \cdot \mathbf{d}^j$ in equation (9.5) is obtained:

$$
\begin{aligned}
J \;=\; & s - 2\mathbf{F}{:}\mathbf{W} - 2\mathbf{G}\vdots\mathbf{H} - 2\mathbf{K}{::}\mathbf{J} - 2\mathbf{j} \cdot \tilde{\mathbf{w}} + (\mathbf{F}^T \cdot \mathbf{F}){:}\mathbf{X} + 2(\mathbf{G}^T \cdot \mathbf{F})\vdots\mathbf{Y} \\
& + \; 2(\mathbf{K}^T \cdot \mathbf{F}){::}\mathbf{Z} + (\mathbf{G}^T \cdot \mathbf{G}){::}\mathbf{Z} + 2(\mathbf{K}^T \cdot \mathbf{G}){::}\mathbf{L} + (\mathbf{K}^T \cdot \mathbf{K})\vdots\!{::}\mathbf{V} + 2\mathbf{F}{:}\mathbf{i} \otimes \tilde{\mathbf{w}} \\
& + \; 2\mathbf{K}{::}\mathbf{Y} \otimes \tilde{\mathbf{w}} + 2\mathbf{G}\vdots\mathbf{X} \otimes \tilde{\mathbf{w}} + p\,\tilde{\mathbf{w}} \cdot \tilde{\mathbf{w}} \,.
\end{aligned}
\tag{9.8}
$$

Therein, use was made of the transposition rules according to appendix A and the symmetries $\mathbf{X} = \mathbf{X}^T$, $\mathbf{Y} = \mathbf{Y}^T$ and $\mathbf{Z} = \mathbf{Z}^T$. The minimization of J in equation (9.8) implies that this equation is differentiated with respect to the unknowns $\mathbf{F}$, $\mathbf{G}$, $\mathbf{K}$ and $\tilde{\mathbf{w}}$ and the resulting equations are set to zero. In turn this provides a set of 4 separate equations:

$$
\begin{aligned}
\frac{\partial J}{\partial \mathbf{F}} &= \mathbf{0} & \rightarrow & & \mathbf{X}\cdot\mathbf{F}^T &+& \mathbf{Y}{:}\mathbf{G}^T &+& \mathbf{Z}{\vdots}\mathbf{K}^T &+& \mathbf{i}\otimes\tilde{\mathbf{w}} &=& \mathbf{W}\,, \\
\frac{\partial J}{\partial \mathbf{G}} &= \mathbf{0} & \rightarrow & & \mathbf{Y}^T{\cdot}\mathbf{F}^T &+& \mathbf{Z}{:}\mathbf{G}^T &+& \mathbf{L}{\vdots}\mathbf{K}^T &+& \mathbf{X}\otimes\tilde{\mathbf{w}} &=& \mathbf{H}\,, \\
\frac{\partial J}{\partial \mathbf{K}} &= \mathbf{0} & \rightarrow & & \mathbf{Z}^T{\cdot}\mathbf{F}^T &+& \mathbf{L}^T{:}\mathbf{G}^T &+& \mathbf{V}{\vdots}\mathbf{K}^T &+& \mathbf{Y}\otimes\tilde{\mathbf{w}} &=& \mathbf{J}\,, \\
\frac{\partial J}{\partial \tilde{\mathbf{w}}} &= \mathbf{0} & \rightarrow & & \mathbf{i}\cdot\mathbf{F}^T &+& \mathbf{X}^T{:}\mathbf{G}^T &+& \mathbf{Y}^T{\vdots}\mathbf{K}^T &+& p\,\tilde{\mathbf{w}} &=& \mathbf{j}\,.
\end{aligned}
\tag{9.9}
$$

In order to determine the unknown average displacement gradients all equations of the above system are written explicitly and can be reformulated in the following matrix form

$$
\mathbf{K}^* \cdot \mathbf{u}^* = \mathbf{P}^* \qquad \rightarrow \qquad \mathbf{u}^* = [\mathbf{K}^*]^{-1} \cdot \mathbf{P}^* \,.
\tag{9.10}
$$

In the general form one has 30 equations: 4 from $(9.9)_1$, 8 from $(9.9)_2$, 16 from $(9.9)_3$ and 2 from $(9.9)_4$. In equation (9.10) $\mathbf{K}^*$ includes the coefficients of the tensors which contain products of the distance vectors of the initial configuration $\mathbf{\Delta x}_0$. $\mathbf{P}^*$ includes the coefficients of the right hand sides of the equation set (9.9) and, therewith, the tensors containing the products of the distance vectors of initial and actual configuration $\mathbf{\Delta x}_0$ and $\mathbf{\Delta x}_t$. Hence, the geometrical information of the actual time step is solely included in $\mathbf{P}^*$, while $\mathbf{K}^*$ includes only the geometrical information of the initial stage. $\mathbf{u}^*$ contains the coefficients of all unknown displacement gradients. Finally, the matrices in equation (9.10) show the following functional dependencies: $\mathbf{K}^* = \mathbf{K}^*(\mathbf{i}, \mathbf{X}, \mathbf{Y}, \mathbf{Z}, \mathbf{L}, \mathbf{V})$, $\mathbf{u}^* = \mathbf{u}^*(\tilde{\mathbf{w}}, \mathbf{F}, \mathbf{G}, \mathbf{K})$ and $\mathbf{P}^* = \mathbf{P}^*(\mathbf{j}, \mathbf{W}, \mathbf{H}, \mathbf{J})$. Upon use of the following symmetries for the displacement gradients of second and third order

$$
\begin{aligned}
G_{212} &= G_{221}\,, & G_{112} &= G_{121}\,, \\
K_{1211} &= K_{1121} = K_{1112}\,, & K_{2211} &= K_{2121} = K_{2112}\,, \\
K_{1221} &= K_{1212} = K_{1122}\,, & K_{2221} &= K_{2212} = K_{2122}\,,
\end{aligned}
\tag{9.11}
$$

the number of equations in the equation set (9.10) can be reduced from 30 to 20. Note that the above symmetries are a result of the symmetries contained in the tensors of the geometrical properties introduced in equations (9.7). The complete matrix $\mathbf{K}^*$ is non-symmetric what poses a constraint on the choice of the inversion procedure. From the technical point of view, if no reduction of the size of $\mathbf{K}^*$, $\mathbf{u}^*$ and $\mathbf{P}^*$ is performed, the inversion of $\mathbf{K}^*$ is not possible due to 10 linear dependent equations within the system of equations in (9.10). After reduction $\mathbf{K}^*$ is represented by a 20×20 matrix, while $\mathbf{u}^*$ and $\mathbf{P}^*$ are given as 1×20 column matrices. The solution of equation (9.10) is realized by a solver capable of non-symmetric matrices via a LU decomposition and is included in the *LAPACK package* [6]. After solution of the equation set the entries of the resulting vector $\mathbf{u}^*$ constitute the average displacement gradients.

In summary, the proposed approximation model includes the simplified models (in terms of approximation order) by *Geers et al.* [91] and *Peters* [196]. Thus, it represents a generalization of these models. The described procedure deviates in various points from the procedure proposed by *Geers* [89] and *Geers et al.* [91]. First, the order of the Taylor approximation is higher by the order of one. Second, the general handling of the system of equations in (9.9) is different: Equation $(9.9)_4$ is not used for a further reduction of

the equation set, but is included into the solution system in the form of equation (9.10). Furthermore, the numerical realization of the solution algorithm differs from the way followed by *Geers* [90]. Instead of obtaining the inverse of a symmetric fourth order tensor by direct inversion after a condensation to a 3×3 matrix according to *Geers* [90], here, the matrix type formulation in equation (9.10) is used. *Geers'* [90] way is not applicable in the present context, as, on the one hand, the contained maximum tensorial order is 6 and, on the other hand, the condensation to a matrix is not realizable. A further deviation compared to the approach by *Geers* [89] and *Geers et al.* [91] considers the motivation of the higher order term $\tilde{\mathbf{w}}$: Application of this technique in the context of an experimental measuring implies an erroneous influence of the measurement itself which according to *Geers* must be additionally included in the error in equation (9.4). In contrast to that, in the present case the position vectors of the particles are determined exactly and do not include any further error. Thus, $\tilde{\mathbf{w}}$ represents a pure microstructural fluctuation field.

In the context of a DEM implementation the formal advantage of a higher approximation order is a more exact description of the distribution of the displacement gradients. On this account compare the analogy to the approximation of the beam fabric in section 6.3 and, in particular, figure 6.10. In the context of a FEM multiscale implementation a higher approximation order than the linear one shows several additional advantages, compare *Kouznetsova* [128] or *Kouznetsova et al.* [129]: First, the absolute size of the microstructure is formally included (this is not the case for the linear approximation model), i. e. geometrical size effects can be captured. Second, it is more appropriate for a homogenization in critical regions where high deformation fields appear, i. e. the macro fields vary considerably. However, these points will not be examined in detail in the context of the DEM model.

9.2.2 Transition to simplified models

The general difference between the models of *Geers et al.* [91] and *Peters* [196] and the present one lies in the order of approximation used within the Taylor expansion in equation (9.2).
The linear model by *Peters* [196] contains only the linear terms in equation (9.2) and, thus, equations (9.3) and (9.8), respectively, reduce to

$$
\mathbf{d}^j = [\mathbf{\Delta x}_t]^{j,meas} - \mathbf{F} \cdot \mathbf{\Delta x}_0 - \tilde{\mathbf{w}}^j\,, \tag{9.12}
$$
$$
J = s - 2\mathbf{F}{:}\mathbf{W} - 2\mathbf{j} \cdot \tilde{\mathbf{w}} + (\mathbf{F}^T \cdot \mathbf{F}){:}\mathbf{X} + 2\mathbf{F}{:}\mathbf{i} \otimes \tilde{\mathbf{w}} + p\tilde{\mathbf{w}} \cdot \tilde{\mathbf{w}}\,. \tag{9.13}
$$

The minimization procedure in equations (9.9) yields only the two equations

$$
\begin{aligned}
\frac{\partial J}{\partial \mathbf{F}} &= \mathbf{0} &\rightarrow \qquad \mathbf{X}{\cdot}\mathbf{F}^T &+ \mathbf{i}{\otimes}\tilde{\mathbf{w}} &= \mathbf{W}\,, \\
\frac{\partial J}{\partial \tilde{\mathbf{w}}} &= \mathbf{0} &\rightarrow \qquad \mathbf{i}{\cdot}\mathbf{F}^T &+ p\tilde{\mathbf{w}} &= \mathbf{j}\,.
\end{aligned}
\tag{9.14}
$$

The system of equations (9.10) is then resembled by a 6×6 matrix $\mathbf{K}^*$ and the 1×6 column matrices $\mathbf{u}^*$ and $\mathbf{P}^*$. The further proceeding is analogous to that in section 9.2.1, whereas the numerical expense is by far smaller in amount compared to that of the third order approximation.

The quadratic model by *Geers et al.* [91] truncates the Taylor series in equation (9.2) after the quadratic term. The difference $\mathbf{d}^j$ and the compact form of $J = \sum_{j=1}^{p} \mathbf{d}^j \cdot \mathbf{d}^j$ according to equation (9.5) are obtained as

$$\mathbf{d}^j = [\mathbf{\Delta x}_t]^{j,meas} - \mathbf{F} \cdot \mathbf{\Delta x}_0 - \mathbf{G} : \mathbf{\Delta x}_0 \otimes \mathbf{\Delta x}_0 - \tilde{\mathbf{w}}^j \,, \tag{9.15}$$

$$\begin{aligned} J = \; & s - 2\mathbf{F} : \mathbf{W} - 2\mathbf{G} \vdots \mathbf{H} - 2\mathbf{j} \cdot \tilde{\mathbf{w}} + (\mathbf{F}^T \cdot \mathbf{F}) : \mathbf{X} + 2(\mathbf{G}^T \cdot \mathbf{F}) \vdots \mathbf{Y} \\ & + \; (\mathbf{G}^T \cdot \mathbf{G}) :: \mathbf{Z} + 2\mathbf{F} : \mathbf{i} \otimes \tilde{\mathbf{w}} + 2\mathbf{G} \vdots \mathbf{X} \otimes \tilde{\mathbf{w}} + p \tilde{\mathbf{w}} \cdot \tilde{\mathbf{w}} \,. \end{aligned} \tag{9.16}$$

Again, this represents the starting point of the differentiation which results in the following three equations:

$$\begin{aligned} \frac{\partial J}{\partial \mathbf{F}} &= \mathbf{0} & \rightarrow & \quad \mathbf{X} \cdot \mathbf{F}^T &+& \quad \mathbf{Y} : \mathbf{G}^T &+& \quad \mathbf{i} \otimes \tilde{\mathbf{w}} &=& \mathbf{W} \,, \\ \frac{\partial J}{\partial \mathbf{G}} &= \mathbf{0} & \rightarrow & \quad \mathbf{Y}^T \cdot \mathbf{F}^T &+& \quad \mathbf{Z} : \mathbf{G}^T &+& \quad \mathbf{X} \otimes \tilde{\mathbf{w}} &=& \mathbf{H} \,, \\ \frac{\partial J}{\partial \tilde{\mathbf{w}}} &= \mathbf{0} & \rightarrow & \quad \mathbf{i} \cdot \mathbf{F}^T &+& \quad \mathbf{X}^T : \mathbf{G}^T &+& \quad p \, \tilde{\mathbf{w}} &=& \mathbf{j} \,. \end{aligned} \tag{9.17}$$

Upon consideration of the symmetries in equation $(9.11)_1$, the system of equations (9.10) is resembled by a 12×12 matrix $\mathbf{K}^*$ and the 1×12 column matrices $\mathbf{u}^*$ and $\mathbf{P}^*$. The analogous procedure as in section 9.2.1 yields a solution for the unknown gradient terms. Alternatively, one can follow the solution approach by *Geers et al.* [91]: A further condensation of equation set (9.17) by elimination of the constant average error $\tilde{\mathbf{w}}$ yields only two equations. By application of simple algebra and reformulation one ends up with one final equation that contains several inverse tensors of fourth order. Due to the tensorial symmetry these inverses can be computed by standard matrix inversion, compare *Geers* [90]. Therefore, the symmetric tensors are condensed to matrices which can be further processed.

Note that the average displacement gradients will differ from each other depending on the approximation order used. For example, the statistical approach used herein does not yield the same displacement gradient $\mathbf{F}$ for the linear, quadratic or cubic model. In particular, the higher order term $\tilde{\mathbf{w}}$ in the linear model is not supposed to represent the contribution of the average second and third displacement gradient $\mathbf{G}$ and $\mathbf{K}$ of the cubic model. This is due to the kind of "balancing" included inherently within the statistical approach.
However, one would expect that the size of the constant systematic error $\tilde{\mathbf{w}}$ decreases with increasing approximation order. In the same manner the absolute value of the fluctuation $\delta \tilde{\mathbf{w}}^j$ according to equation (9.4) will certainly decrease with a higher approximation order. These points will be highlighted in the context of a comparison in section 9.5.

9.2.3   Constraint of boundary conditions

The formal completion of the kinematical formulation of the boundary value problem calls for a closer look on the deformation of the boundary $\partial \mathcal{R}$ of the RVE. In particular, the role of the error or fluctuation term $\tilde{\mathbf{w}}$, compare equation (9.4), is further elucidated. As mentioned above, $\tilde{\mathbf{w}}$ represents the local microstructural fluctuation field. Since the objective in mind is the motivation of gradient theories through particle methods and

not the replacement of macroscopic constitutive relations like in FEM implementations of gradient models either as standard one-scale approach, see *Chambon et al.* [33], *Fleck & Hutchinson* [87], *Sulem et al.* [232] or *Zervos et al.* [264], or as multiscale approach, see *Kouznetsova et al.* [129], *Miehe et al.* [171] or *van der Sluis* [242], the boundary conditions are treated differently here. As outlined in chapter 8, in the context of a DEM model combined with a homogenization procedure the boundary conditions of the RVEs are not prescribed. They are a naturally outcome of the geometric structure of the particle sample and, thus, of the RVE. A comparison between the presumed (for formal derivation due to boundary conditions) and the numerically present deformation of the boundary provides the opportunity to check the validity of the constraints in the context of the particle model. Furthermore, they enable a more detailed discussion and motivation of the present model in the context of models based on the concept of microstructural fluctuation fields, like those introduced by *Kouznetsova et al.* [129] or *Miehe et al.* [171].

If the displacement gradient on the particle level $\mathbf{F}_{\mathcal{P}}$ is evaluated by insertion of $\mathbf{\Delta x}_t$ according to equation (9.2) into equation (9.1), one obtains a relation between the displacement gradients on the particle (micro) and RVE (meso/macro) level

$$\mathbf{F}_{\mathcal{P}} = \frac{\partial \mathbf{\Delta x}_t}{\partial \mathbf{\Delta x}_0} = \langle \mathbf{F} \rangle_{\mathcal{R}} + \langle \mathbf{G} \rangle_{\mathcal{R}} \cdot \mathbf{\Delta x}_0 + \langle \mathbf{K} \rangle_{\mathcal{R}} {:} \mathbf{\Delta x}_0 \otimes \mathbf{\Delta x}_0 + \frac{\partial \tilde{\mathbf{w}}}{\partial \mathbf{\Delta x}_0} \,. \tag{9.18}$$

The integration of equation (9.18) over the RVE $\mathcal{R}$ yields

$$\frac{1}{V_{\mathcal{R}}} \int_{\mathcal{R}} \mathbf{F}_{\mathcal{P}} \, \mathrm{d}v = \langle \mathbf{F} \rangle_{\mathcal{R}} + \langle \mathbf{G} \rangle_{\mathcal{R}} \cdot \frac{1}{V_{\mathcal{R}}} \int_{\mathcal{R}} \mathbf{\Delta x}_0 \, \mathrm{d}v + \langle \mathbf{K} \rangle_{\mathcal{R}} {:} \frac{1}{V_{\mathcal{R}}} \int_{\mathcal{R}} \mathbf{\Delta x}_0 \otimes \mathbf{\Delta x}_0 \, \mathrm{d}v$$

$$+ \quad \frac{1}{V_{\mathcal{R}}} \int_{\mathcal{R}} \frac{\partial \tilde{\mathbf{w}}}{\partial \mathbf{\Delta x}_0} \, \mathrm{d}v \,. \tag{9.19}$$

The average displacement gradients are independent of the integration over the volume, $\int_{\mathcal{R}} \mathrm{d}v$, and are, therefore, set in front of the integral. In the general case the shape of the RVE is symmetric and the center of the base particle represents the center of the RVE. Then, the terms containing the integrals $1/V_{\mathcal{R}} \int_{\mathcal{R}} \mathbf{\Delta x}_0 \, \mathrm{d}v$ and $1/V_{\mathcal{R}} \int_{\mathcal{R}} \mathbf{\Delta x}_0 \otimes \mathbf{\Delta x}_0 \, \mathrm{d}v$ in equation (9.19) on average vanish. If the transition of equation (9.19) to a discrete DEM-based formulation is performed, some inaccuracies are obtained: Neither the shape of the polygon through the center points of the boundary particles is completely circular and symmetric, nor the center of the base particle defines exactly the center of the RVE. Thus, the above remark that the terms in equation (9.19) vanish approximately holds. Numerical simulations with the DEM model using different RVE sizes proved the approximative validity of this assumption on a trial basis. Application of the known averaging theorem, compare equation (2.38) in section 2.3.1, to the displacement gradient yields

$$\langle \mathbf{F} \rangle_{\mathcal{R}} = \frac{1}{V_{\mathcal{R}}} \int_{\mathcal{R}} \mathbf{F}_{\mathcal{P}} \, \mathrm{d}v \,. \tag{9.20}$$

Insertion of equation (9.20) in equation (9.19) under consideration of the divergence theorem and the fact that the integrals containing products of $\mathbf{\Delta x}_0$ vanish, leads to the following condition for the fluctuations

$$\frac{1}{V_{\mathcal{R}}} \int_{\mathcal{R}} \frac{\partial \tilde{\mathbf{w}}}{\partial \mathbf{\Delta x}_0} \, \mathrm{d}v = \frac{1}{V_{\mathcal{R}}} \int_{\mathcal{R}} \mathrm{div}_{\Delta} \tilde{\mathbf{w}} \, \mathrm{d}v = \frac{1}{V_{\mathcal{R}}} \int_{\partial \mathcal{R}} \tilde{\mathbf{w}} \otimes \mathbf{n} \, \mathrm{d}a = \mathbf{0} \,. \tag{9.21}$$

Thereby, $\operatorname{div}_\Delta(\cdot)$ denotes the divergence operator with respect to the center of the RVE. In analogy to the comments in *Kouznetsova et al.* [129], the boundary condition for the fluctuation field in equation (9.21) must be fulfilled by one of the following three different constraints:

a) $\tilde{\mathbf{w}} = \mathbf{0}$ in $\mathcal{R}$: The fluctuations vanish in the complete volume $V_\mathcal{R}$ of $\mathcal{R}$. This is the case if the RVE deforms completely according to the average displacement gradients $\langle \mathbf{F} \rangle_\mathcal{R}$, $\langle \mathbf{G} \rangle_\mathcal{R}$ and $\langle \mathbf{K} \rangle_\mathcal{R}$.

b) $\tilde{\mathbf{w}} = \mathbf{0}$ on $\partial \mathcal{R}$: The fluctuations vanish on the complete boundary $\partial \mathcal{R}$, i. e. the fluctuations within the RVE are not concerned.

c) Periodic boundary condition type: The displacements of two corresponding points on the boundary of the RVE $\partial \mathcal{R}$ (opposite with respect to the center of the RVE) are identical. Thereby, besides the requirement of a symmetric form, the shape of the RVE is irrelevant, e. g. circular or rectangular RVEs may be used.

In the case of a linear model, like that introduced by *Peters* [196] or utilized by *Miehe et al.* [171], case a) is typically referred as Taylor or Voigt assumption. It enforces a homogeneous deformation of the RVE and refers to displacement or Dirichlet boundary condition. Then, case b) is referred to as uniform displacement boundary condition requiring linear deformations on the boundary of the RVE. This condition is closely related to the traction or Neumann boundary condition.

For a Taylor series truncated after the quadratic or cubic term and including an error term in form of the fluctuation field $\tilde{\mathbf{w}}$, cases a) to c) represent generalized boundary conditions. In analogy to the given procedure, relations between the displacement gradients $\mathbf{G}_\mathcal{P}$ and $\mathbf{K}_\mathcal{P}$ on the particle (micro) and $\langle \mathbf{G} \rangle_\mathcal{R}$ and $\langle \mathbf{K} \rangle_\mathcal{R}$ on the RVE (meso/macro) level may be derived. For example, in order to relate $\mathbf{G}_\mathcal{P}$ to $\langle \mathbf{G} \rangle_\mathcal{R}$ normal and surface gradients of the fluctuation field $\tilde{\mathbf{w}}$ are implied. Therefore, higher order boundary conditions are obtained. This fact has already been discussed in the context of a second gradient continuum in section 2.2.4 or by *Germain* [92] or *Mindlin* [172]. In the context of a FEM implementation higher order boundary conditions represent complex constraints of the boundary value problem, compare the approach by *Kouznetsova et al.* [129]. However, for brevity higher order boundary conditions are skipped here. Recall that in contrast to the realization of typical FEM multiscale implementations, in the case of the present DEM implication the boundary conditions on the RVE level are not prescribed: They are an outcome of the geometric structure of the RVE. Note that this is generally not a matter of the models, but a matter of the objective in mind, i. e. the focus of the particle model is to motivate gradient theories and that of typical FEM multiscale models to formally represent macroscopic constitutive relations.

9.3 Dynamic quantities

A thermodynamically consistent framework calls for energetically equivalent dynamic quantities corresponding to the previously introduced higher displacement gradients $\mathbf{F}$, $\mathbf{G}$ and $\mathbf{K}$. In order to derive these energetically conjugated quantities the general form of the Hill condition according to section 2.3.2 is utilized. The Hill condition requires the volume average of the work on the micro level (particle scale) to equal the work on

the meso (RVE scale) or macro level. Starting from a microscopic particle model and using an enhanced displacement description along with a subsequent homogenization, an enhanced (gradient-type) continuum description is obtained. The enhanced displacement description was accommodated by the introduction of higher order displacement gradients on the RVE level. Thus, the procedure is quite similar to that introduced in the previous chapter where starting from a standard continuum on the particle level an enhanced (micropolar-type) continuum on the RVE level was obtained. The starting points for an evaluation of the Hill condition are the quasi-static balances of momentum on the micro level $\operatorname{div} \mathbf{T}_{\mathcal{P}} = \mathbf{0}$ and meso level $\operatorname{div} \langle \mathbf{T} \rangle_{\mathcal{R}} = \mathbf{0}$. The index $\mathcal{P}$ refers to an evaluation of the Cauchy stress tensor on the particle level, i. e. based on the contact forces on a single particle a stress tensor may be formulated, compare also equation (8.3). The index $\mathcal{R}$ refers to an evaluation on the RVE level (average quantity $\langle \cdot \rangle$). In the following the meso (RVE scale d) and macro scale (D) according to figure 8.2 are assumed to be virtually identical.

The extended Hill condition is identified as

$$\frac{1}{V_{\mathcal{R}}} \int_{\mathcal{R}} \mathbf{T}_{\mathcal{P}} {:} \mathbf{F}_{\mathcal{P}} \, \mathrm{d}v = \langle \mathbf{T} \rangle_{\mathcal{R}} {:} \langle \mathbf{F}^T \rangle_{\mathcal{R}} + \langle \mathbf{Q} \rangle_{\mathcal{R}} \vdots \langle \mathbf{G}^T \rangle_{\mathcal{R}} + \langle \mathbf{R} \rangle_{\mathcal{R}} {::} \langle \mathbf{K}^T \rangle_{\mathcal{R}} \, . \tag{9.22}$$

$\langle \mathbf{T} \rangle_{\mathcal{R}}$ represents the average Cauchy stress and $\langle \mathbf{Q} \rangle_{\mathcal{R}}$ and $\langle \mathbf{R} \rangle_{\mathcal{R}}$ denote the average higher order stresses. With the aid of the balance of momentum on the particle level, the divergence theorem and partial integration, the left hand side of equation (9.22) is reformulated

$$\delta W_{\mathcal{R}} = \frac{1}{V_{\mathcal{R}}} \int_{\mathcal{R}} \mathbf{T}_{\mathcal{P}} {:} \mathbf{F}_{\mathcal{P}} \, \mathrm{d}v = \frac{1}{V_{\mathcal{R}}} \int_{\partial \mathcal{R}} \mathbf{t} \cdot \boldsymbol{\Delta} \mathbf{x}_t \, \mathrm{d}a \, . \tag{9.23}$$

The tractions $\mathbf{t}$ will be represented by contact forces when transferring equation (9.23) to a discrete form. Note that the stress tensor for the gradient-type model is symmetric and Cauchy's theorem is resembled by $\mathbf{t} = \mathbf{T} \cdot \mathbf{n} = \mathbf{n} \cdot \mathbf{T}^T$. Thus, the microstructural stress state within the RVE $\mathbf{T}_{\mathcal{P}}$ is defined by the present particle contact forces. Upon insertion of $\boldsymbol{\Delta} \mathbf{x}_t$ according to equation (9.2) in equation (9.23), an exploitation of the symmetry with respect to products of the $\boldsymbol{\Delta} \mathbf{x}_0$ yields

$$\begin{aligned} \delta W_{\mathcal{R}} \ = \ & \frac{1}{V_{\mathcal{R}}} \int_{\partial \mathcal{R}} \mathbf{t} \otimes \boldsymbol{\Delta} \mathbf{x}_0 \, \mathrm{d}a : \langle \mathbf{F}^T \rangle_{\mathcal{R}} + \frac{1}{V_{\mathcal{R}}} \int_{\partial \mathcal{R}} \mathbf{t} \otimes \boldsymbol{\Delta} \mathbf{x}_0 \otimes \boldsymbol{\Delta} \mathbf{x}_0 \, \mathrm{d}a \vdots \langle \mathbf{G}^T \rangle_{\mathcal{R}} \\ + \ & \frac{1}{V_{\mathcal{R}}} \int_{\partial \mathcal{R}} \mathbf{t} \otimes \boldsymbol{\Delta} \mathbf{x}_0 \otimes \boldsymbol{\Delta} \mathbf{x}_0 \otimes \boldsymbol{\Delta} \mathbf{x}_0 \, \mathrm{d}a :: \langle \mathbf{K}^T \rangle_{\mathcal{R}} + \frac{1}{V_{\mathcal{R}}} \int_{\partial \mathcal{R}} \mathbf{t} \cdot \tilde{\mathbf{w}} \, \mathrm{d}a \, . \end{aligned} \tag{9.24}$$

The last term in equation (9.24) which contains the fluctuations of the deformations vanishes in the context of valid boundary conditions, i. e. $\tilde{\mathbf{w}}$ has no influence on the work on the micro level

$$\frac{1}{V_{\mathcal{R}}} \int_{\partial \mathcal{R}} \mathbf{t} \cdot \tilde{\mathbf{w}} \, \mathrm{d}a = 0 \, . \tag{9.25}$$

Comparison of equations (9.22) and (9.24) leads to an identification of the average Cauchy and average higher order stresses:

$$
\langle \mathbf{T} \rangle_{\mathcal{R}} = \frac{1}{V_{\mathcal{R}}} \int_{\partial \mathcal{R}} \mathbf{t} \otimes \mathbf{\Delta x}_0 \, \mathrm{d}a = \frac{1}{V_{\mathcal{R}}} \sum_{i=1}^{N_{\partial \mathcal{R}}} \mathbf{f}^{(i)} \otimes \mathbf{\Delta x}_0^{(i)} \, ,
$$

$$
\langle \mathbf{Q} \rangle_{\mathcal{R}} = \frac{1}{V_{\mathcal{R}}} \int_{\partial \mathcal{R}} \mathbf{t} \otimes \mathbf{\Delta x}_0 \otimes \mathbf{\Delta x}_0 \, \mathrm{d}a = \frac{1}{V_{\mathcal{R}}} \sum_{i=1}^{N_{\partial \mathcal{R}}} \mathbf{f}^{(i)} \otimes \mathbf{\Delta x}_0^{(i)} \otimes \mathbf{\Delta x}_0^{(i)} \, , \tag{9.26}
$$

$$
\langle \mathbf{R} \rangle_{\mathcal{R}} = \frac{1}{V_{\mathcal{R}}} \int_{\partial \mathcal{R}} \mathbf{t} \otimes \mathbf{\Delta x}_0 \otimes \mathbf{\Delta x}_0 \otimes \mathbf{\Delta x}_0 \, \mathrm{d}a = \frac{1}{V_{\mathcal{R}}} \sum_{i=1}^{N_{\partial \mathcal{R}}} \mathbf{f}^{(i)} \otimes \mathbf{\Delta x}_0^{(i)} \otimes \mathbf{\Delta x}_0^{(i)} \otimes \mathbf{\Delta x}_0^{(i)} \, .
$$

The average RVE stresses are given as products of the resultant force per particle $\mathbf{f}^{(i)}$ acting on the boundary of the RVE and the initial distance vector $\mathbf{\Delta x}_0^{(i)}$ between the mass centers of the boundary particles and the base particle. The resultant forces $\mathbf{f}^{(i)}$ are obtained according to equation (8.15) and $N_{\partial \mathcal{R}}$ denotes the number of RVE boundary particles. Note that a transformation of the boundary integral to a volume-based formulation in equation (9.26) is also possible, compare *Kouznetsova et al.* [129]. Indeed, this way is not followed here as the generally unknown stress tensor at the particle level is needed for a volume definition. The higher order stresses can be interpreted as first and second moment of the stress tensor (with respect to the RVE center). The average Cauchy stress tensor in equation $(9.26)_1$ formally compares to the formulation in the context of the micropolar model in equation (8.22). However, as mentioned above the Cauchy stress tensor is symmetric.

9.4   Concept of microstructural fluctuation field

The procedure introduced so far provides a physical and numerical motivation for the concept of microstructural fluctuation field. This concept evolved at the end of the 1990's in the context of FEM multiscale approaches, compare *Kouznetsova* [128], *Kouznetsova et al.* [129], *Miehe & Koch* [169], *Miehe et al.* [170], *Miehe et al.* [171], *Smit et al.* [225] and others. Starting from very basic comments by *Mohr* [175] or *Taylor* [235] on the consideration of a microstructure and following the remarks by *Mindlin* [172] on a continuum with microstructure, a homogenized continuum at the macro scale with a locally attached microstructure is considered. This includes two locally coupled boundary value problems on the macro and micro scale, respectively: Each material point of the body defined on the macro scale transports a known and discretized microstructure defined on the micro scale. Usually, the mentioned multiscale approaches make use of a FEM model for the discretization on both scales. It is obvious that the increasing computer power in the last decades provided the foundation for a numerical realization of this kind of models. The aim of the following two sections is the development and application of a procedure that enables a numerical motivation of microstructural fluctuation fields in the context of the DEM.

Summarizing the results of section 9.2, the key ingredient of a multiscale approach (based on the concept of microstructural fluctuation fields) is the description of the RVE geometry by an approximative treatment of the fluctuation fields. In that, higher order terms of a Taylor series are identified as fluctuation. In the general form the position of a particle

within a RVE may be described solely by the displacement gradients on the macro scale and an additional fluctuation term $\tilde{\mathbf{w}}$ according to

$$\boldsymbol{\Delta}\mathbf{x}_t = \langle\mathbf{F}\rangle_\mathcal{R} \cdot \boldsymbol{\Delta}\mathbf{x}_0 + \langle\mathbf{G}\rangle_\mathcal{R}\mathord{:}\boldsymbol{\Delta}\mathbf{x}_0 \otimes \boldsymbol{\Delta}\mathbf{x}_0 + \langle\mathbf{K}\rangle_\mathcal{R}\mathord{\vdots}\boldsymbol{\Delta}\mathbf{x}_0 \otimes \boldsymbol{\Delta}\mathbf{x}_0 \otimes \boldsymbol{\Delta}\mathbf{x}_0 + \tilde{\mathbf{w}}\,, \qquad (9.27)$$

compare also equation (9.2). In the literature the tensors $\langle\mathbf{F}\rangle_\mathcal{R}$, $\langle\mathbf{G}\rangle_\mathcal{R}$ and $\langle\mathbf{K}\rangle_\mathcal{R}$ denote the macro displacement gradients and are usually known at the material point level. Procedures along the lines of *Miehe et al.* [171] consider only the first and fourth term, while procedures along the lines of *Kouznetsova et al.* [129] consider the first, second and fourth term. Thereby, the fluctuation $\tilde{\mathbf{w}}$ stands for the higher order terms of a Taylor series. As an example for a geometrical interpretation of the fluctuations, the deformation of an initially quadratic RVE is schematically depicted in figure 9.2. The boundary of the RVE by means of the dotted line in figure 9.2, right, represents the situation for a linear model, i. e. as if the Taylor series in equation (9.27) contains only the first and the last term according to *Miehe et al.* [171]. Inclusion of the fluctuations for the linear case yields the continuous line in figure 9.2 as boundary of the deformed RVE. In the figurative sense, the fluctuation field is represented by the difference between the dotted and the continuous line. The fluctuations represent the superimposed higher order kinematic of the boundary. The interpretation of the deformation by *Miehe et al.* [171] denotes the first term of equation (9.27) as the homogeneous part of the deformation and the fluctuation term as a non-homogeneous superimposed field of the deformation.

As by definition no conditions and constraints are imposed on the RVE boundary, it is of special interest, whether an arbitrary RVE deforms in the manner typically prescribed by boundary conditions of the form considered in section 9.2.3. Recall that only the choice of special boundary conditions for the fluctuation field $\tilde{\mathbf{w}}$ enables a consistent derivation of a gradient-type continuum on the RVE scale starting from a local standard continuum on the particle scale. To be consistent with *Kouznetsova et al.* [129] and *Miehe et al.*
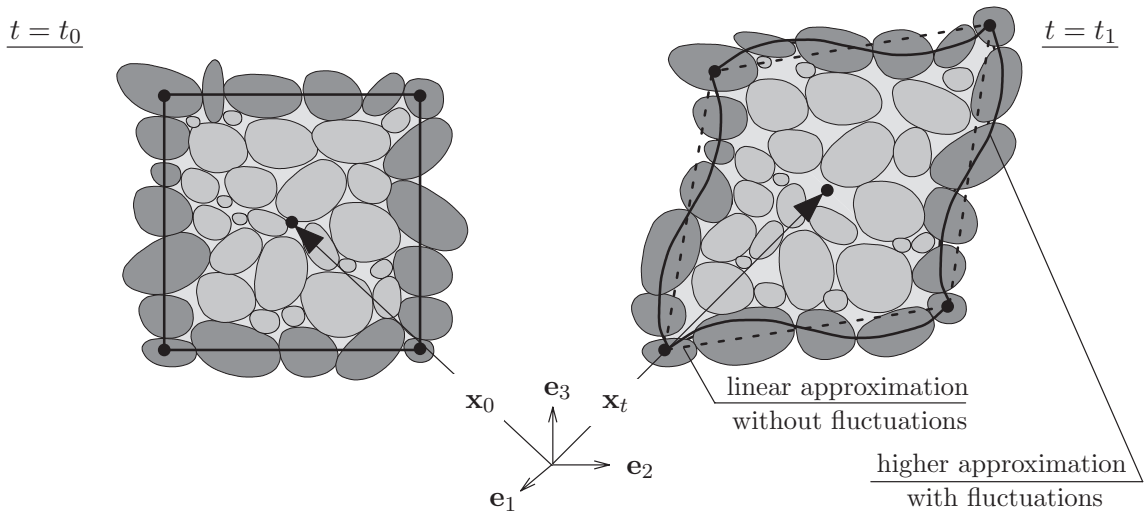
Figure 9.2: Effect of approximation order on boundary $\partial\mathcal{R}$ of RVE in initial and actual configuration.

[171], the following two key assumptions have to be numerically proven

$$
\begin{aligned}
\langle \tilde{\mathbf{W}} \rangle_{\mathcal{R}} &= \frac{1}{V_{\mathcal{R}}} \int_{\partial \mathcal{R}} \tilde{\mathbf{w}} \otimes \mathbf{n} \, \mathrm{d}a = \frac{1}{V_{\mathcal{R}}} \sum_{i=1}^{N_{\partial \mathcal{R}}} \frac{1}{2} \Delta w^i \left(\tilde{\mathbf{w}}^i + \tilde{\mathbf{w}}^{i+1} \right) \otimes \mathbf{n}^i = \mathbf{0} \,, \\
\langle \tilde{T} \rangle_{\mathcal{R}} &= \frac{1}{V_{\mathcal{R}}} \int_{\partial \mathcal{R}} \mathbf{t} \cdot \tilde{\mathbf{w}} \, \mathrm{d}a = \frac{1}{V_{\mathcal{R}}} \sum_{i=1}^{N_{\partial \mathcal{R}}} \mathbf{f}^{(i)} \cdot \frac{1}{2} \Delta w^i \left(\tilde{\mathbf{w}}^i + \tilde{\mathbf{w}}^{i+1} \right) = 0 \,.
\end{aligned}
\tag{9.28}
$$

The first assumption stems from the derivation of the higher order kinematics and was noted in equation (9.21). The second assumption poses a constraint on the work of the fluctuations and appeared in equation (9.25). For a numerical implementation the integrals over the RVE boundary have been transferred to sums including the discrete fluctuations and forces. Thus, the integration over the boundary of the RVE is formally carried out by including the width Δw^i of a RVE boundary segment i as shown in figure 8.4 and detailed within equations (8.26) to (8.30). In analogy to section 8.3.2 the information of the first particle of the RVE boundary ($i = 1$) is saved twice for technical reasons, i. e. $\tilde{\mathbf{w}}^{i+1} = \tilde{\mathbf{w}}^1$ for $i = N_{\partial \mathcal{R}}$.

A further fundamental difference compared to multiscale FEM realizations is the motivation of the fluctuations: In the present case the fluctuations $\tilde{\mathbf{w}}$ represent the collection of all neglected terms of higher order in the Taylor series. A comparison between the measured and approximated values of the distances of each particle pair provides an individual difference per pair. This individual difference is identified as the variable fluctuation $\delta \tilde{\mathbf{w}}^j$ of the displacement field according to equation (9.4).

The determination of the average displacement gradients and the average fluctuations implied the variable fluctuations $\delta \tilde{\mathbf{w}}$ to fluctuate around the zero value, compare section 9.2.1. $\delta \tilde{\mathbf{w}}^j$ was assumed normally distributed around the zero value, i. e. its average over the RVE or its boundary is expected to vanish. In order to check the validity of this assumption the average variable fluctuations over the RVE or its boundary $\langle \delta \tilde{\mathbf{w}} \rangle$ have to be evaluated. This is realized in two ways here: First, the absolute values are computed in vectorial form which yields $\langle \delta \tilde{\mathbf{w}} \rangle$, i. e. for each particle pair in the RVE or its boundary the corresponding fluctuation vectors $\delta \tilde{\mathbf{w}}$ are vectorially summed up. Second, the normalized values are computed in scalar form which yields $\langle \delta \tilde{w}_{norm} \rangle$, i. e. for each particle pair in the RVE or its boundary the corresponding norms of the fluctuation vectors $|\delta \tilde{\mathbf{w}}|$ are summed up. Finally, one obtains

$$
\begin{aligned}
\langle \delta \tilde{\mathbf{w}} \rangle_* &= \frac{1}{N_*} \sum_{i=1}^{N_*} \left[[\boldsymbol{\Delta} \mathbf{x}_t]^{i,meas} - [\boldsymbol{\Delta} \mathbf{x}_t]^{i,approx} \right] \,, \\
\langle \delta \tilde{w}_{norm} \rangle_* &= \frac{1}{N_*} \sum_{i=1}^{N_*} \left[\left| [\boldsymbol{\Delta} \mathbf{x}_t]^{i,meas} \right| - \left| [\boldsymbol{\Delta} \mathbf{x}_t]^{i,approx,sc} \right| \right] \,,
\end{aligned}
\tag{9.29}
$$

with

$$
[\boldsymbol{\Delta} \mathbf{x}_t]^{i,approx,sc} = [\boldsymbol{\Delta} \mathbf{x}_t]^{i,approx} \cos \alpha \,, \quad \alpha = \arccos \left[\frac{[\boldsymbol{\Delta} \mathbf{x}_t]^{i,meas} \cdot [\boldsymbol{\Delta} \mathbf{x}_t]^{i,approx}}{|[\boldsymbol{\Delta} \mathbf{x}_t]^{i,meas}| \cdot |[\boldsymbol{\Delta} \mathbf{x}_t]^{i,approx}|} \right] \,. \tag{9.30}
$$

Thereby, the summations in equations (9.29) are either taken over the boundary of the RVE $\partial \mathcal{R}$ with $N_* = N_{\partial \mathcal{R}}$ which yields $\langle \delta \tilde{\mathbf{w}} \rangle_{\partial \mathcal{R}}$, $\langle \delta \tilde{w}_{norm} \rangle_{\partial \mathcal{R}}$. Alternatively, a summation over the complete RVE $\mathcal{R}$ with $N_* = N_{\mathcal{R}}$ can be considered which yields $\langle \delta \tilde{\mathbf{w}} \rangle_{\mathcal{R}}$, $\langle \delta \tilde{w}_{norm} \rangle_{\mathcal{R}}$.

9.5 Numerical results

The homogenization procedure introduced in chapter 8 and adapted to capture gradient effects in the present chapter is validated by two-dimensional DEM simulations. The occurrence of strain gradients and the corresponding pattern formation as well as an evaluation of the fluctuation fields are studied with respect to different RVE sizes. Basically, the numerical implementation of the model is similar to that proposed in section 8.4. For a graphical representation the average quantities are mapped onto the base particles in the center of the RVEs. Composition and volume of the RVEs are fixed at the beginning and not changed throughout the simulations. The only obvious difference compared to the realization of the first homogenization version is that the computation of the average kinematic quantities comprises a summation over the complete RVE and not only over the boundary of the RVE. As example a notched tension simulation using the beam enhanced DEM model is examined.

9.5.1 Comparison of different approximation orders

The benchmark example used herein is the notched tension simulation discussed in section 4.5.2. The simulations are carried out with the beam enhanced DEM model according to chapter 4, see the failure evolution in figure 4.12. The advantage of a notched over an unnotched specimen is that the notch controls the position where a crack nucleates. This test is a well known experimental setup in the context of cohesive geomaterials. Based on this experience a failure evolution dominated by a mode I localization in a zone of finite width is expected. In several applications the numerical treatment on a macro scale by means of a FEM model makes use of a gradient enhanced model. In those studies uniaxial tension simulations are used as benchmark problem, compare e. g. *Kuhl* [137] or *Pamin* [195]. Thereby, the occurrence of displacement gradients is restricted to narrow and finite failure zones. Therefore, this problem represents an adequate benchmark for a validation of the proposed homogenization technique. Simulations with a rectangular 40 cm × 64 cm sample composed of 2560 particles have been carried out. The notch is positioned in the middle of the right border of the specimen with a width of 3 cm, compare figure 4.12 (a). A horizontal crack perpendicular to the loading direction and starting from the notch tip is obtained, compare figure 4.12 (b). At each time step of the simulation the average dynamic and kinematic quantities (stresses, strains and fluctuations) are evaluated for approximately 1500 RVEs. The base particles of this simulation are identical to those ones in the biaxial test, compare figure 8.5 (b). This means that in analogy to the visualization procedure detailed in the previous chapter, a small boundary region is neglected and, thus, not represented in the corresponding figures. Three different RVE sizes (RVE_5, RVE_9 and RVE_19) are utilized and three approximation orders are examined: linear, quadratic and cubic models. Hence, the Taylor series in equation (9.2) is either truncated after the linear, quadratic or cubic term and the corresponding higher order terms are collected in the fluctuation term.

The key quantities under observation in the present context are the norms of the second and third displacement gradients $\langle \mathbf{G} \rangle_{\mathcal{R}}$ and $\langle \mathbf{K} \rangle_{\mathcal{R}}$. As the corresponding gradient tensors contain 8 or 16 coefficients, it is convenient to plot the L_2 norm for a visualization of the localization of the gradients. As example, the results for RVE_19 are plotted in figure 9.3. The left figure set denotes $\langle \mathbf{G} \rangle_{\mathcal{R}}$. Thereby, the corresponding left figure shows the result

based on the quadratic approximation and the right one shows that based on the cubic approximation. The right figure denotes $\langle \mathbf{K} \rangle_{\mathcal{R}}$ applying the cubic approximation model. One can clearly see that even for a large RVE the upcoming localization zone is visible long before the macroscopic crack appears and, thus, basically represents the stress intensity effects at the notch tip. The radiation from the notch tip in radial direction is visible for the gradients of second and third order $\langle \mathbf{G} \rangle_{\mathcal{R}}$ and $\langle \mathbf{K} \rangle_{\mathcal{R}}$, respectively. For example, four lines with a slightly higher norm of the gradient tensor $|\langle \mathbf{G} \rangle_{\mathcal{R}}|$ form left of the notch tip and characterize the wave propagation. In the further course of simulation the qualitative picture of the strain gradient distribution does not change, besides an increase of the maximum values. When the macroscopic crack appears, the situation changes drastically and the displacement gradients of all orders localize in the crack region.

The distribution of the norm of various displacement gradients for three different RVE sizes are evaluated by means of 62 RVEs on a vertical line in the right region of the sample, compare the corresponding description in section 8.5.1. Similar as the dark shaded particles in figure 8.8, here, a vertical row of particles positioned between the center and the right border of the valid base particles represent the base particles of the monitored RVEs. On account of the valid base particles compare figure 8.5 (b). The corresponding base particles range from the bottom RVE ($y \to 0$ cm) to the top RVE ($y \to 60$ cm). For a comparative view the norms are scaled to the constant regime appearing outside the localization zone. Hence, the star symbol is used in the notation of the average quantity according to $|\langle \cdot \rangle|^*$. The displacement gradient of first order in figure 9.4 (a) shows a peak at the center of the crack region, whereas the displacement gradient of second order in figure 9.4 (b) develops two symmetric peaks in the direct neighborhood of the crack. The displacement gradient of third order possesses again one peak in the center region and two smaller symmetric peaks in the neighboring region, compare figure 9.4 (c). In the last case, for RVE_5 the averaging radius is too small in order to reproduce the secondary peaks. Upon consideration of the last remark, these general observations apply for all three RVE
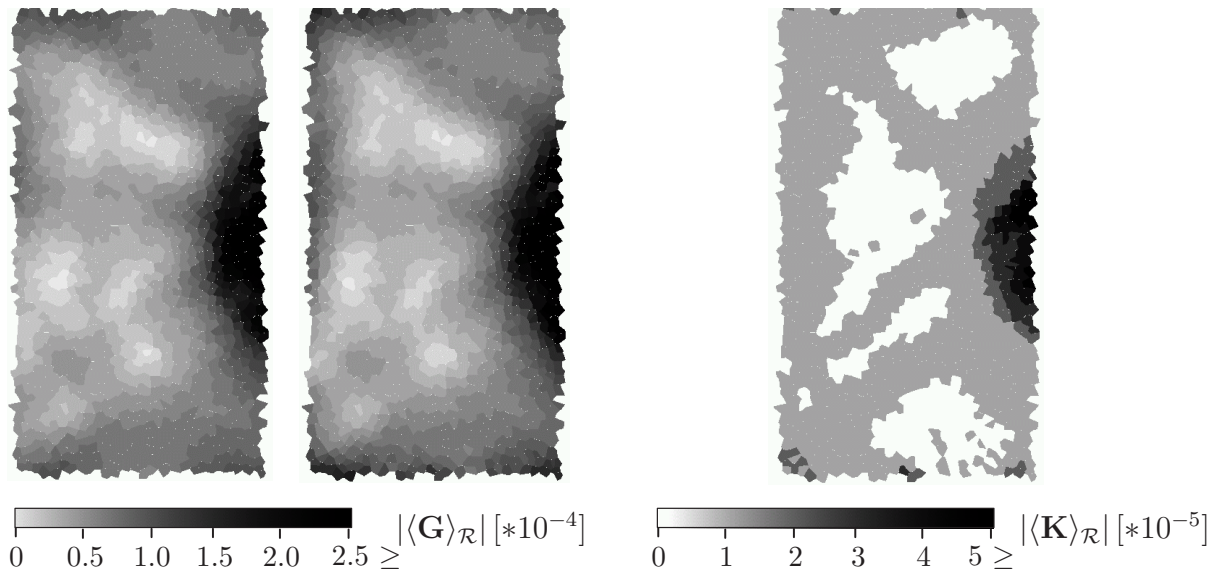
Figure 9.3: Distribution of norm of displacement gradient tensors $\langle \mathbf{G} \rangle_{\mathcal{R}}$ and $\langle \mathbf{K} \rangle_{\mathcal{R}}$ long before localization for RVE_19.
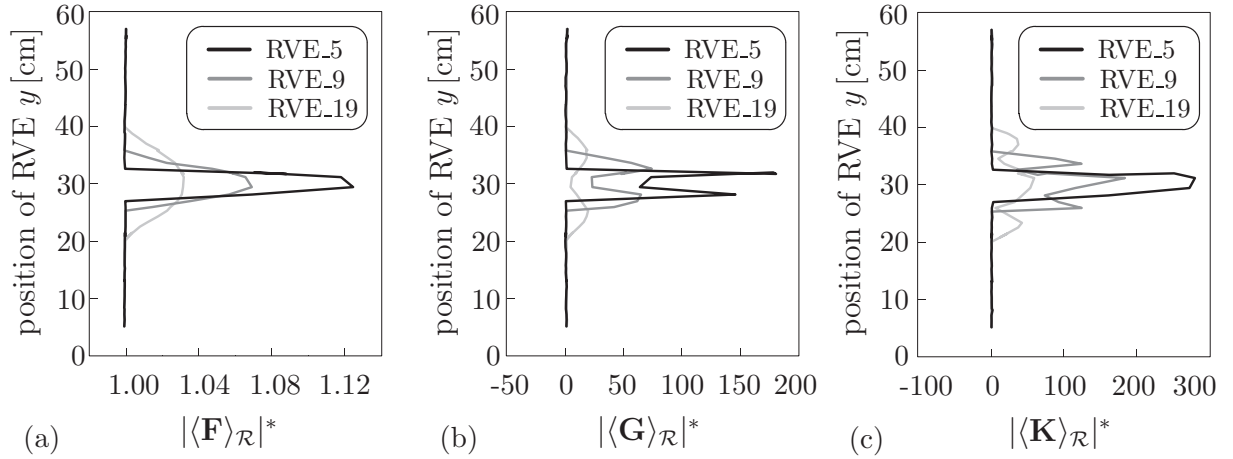
Figure 9.4: Norm of (a) first, (b) second and (c) third gradients of displacement over height of specimen short after localization onset.

sizes. To maintain consistency all displacement gradients have been computed on the basis of the cubic approximation model. Indeed, for the linear and the quadratic approximation model the distributions of $|\langle \mathbf{F} \rangle_{\mathcal{R}}|^*$ or $|\langle \mathbf{G} \rangle_{\mathcal{R}}|^*$ look very similar. On this account compare also the similarity of the distributions of $|\langle \mathbf{G} \rangle_{\mathcal{R}}|^*$ for the quadratic and cubic models in figure 9.3, left. Figure 9.4 documents that the distributions of $|\langle \mathbf{F} \rangle_{\mathcal{R}}|^*$, $|\langle \mathbf{G} \rangle_{\mathcal{R}}|^*$ and $|\langle \mathbf{K} \rangle_{\mathcal{R}}|^*$ represent the mathematical context in a qualitative correct manner, i. e. $\mathbf{G}$ is the derivative of $\mathbf{F}$ and $\mathbf{K}$ is the derivative of $\mathbf{G}$. This means that at those positions where the distributions show peaks, the corresponding higher derivative tends to vanish and in an approximate sense expresses a vertical tangent of the lower derivative distribution. For example, for RVE_19 in figure 9.3 the distribution of $|\langle \mathbf{G} \rangle_{\mathcal{R}}|^*$ vanishes in the middle of the specimen, since $|\langle \mathbf{F} \rangle_{\mathcal{R}}|^*$ is maximal there. Similar qualitative relations are also obtained for the other RVE sizes and for the relation between $|\langle \mathbf{G} \rangle_{\mathcal{R}}|^*$ and $|\langle \mathbf{K} \rangle_{\mathcal{R}}|^*$. However, with decreasing RVE size they are not so clearly recognizable in this figure. These distributions give a further insight into the "width" of the zone, as the observable width is directly reflected by the size of the RVE: RVE_5 yields a zone width of ca. 5 particles, RVE_9 of ca. 9 particles and RVE_19 of ca. 19 particles. Thereby, it should be kept in mind that on average one particle possesses a diameter of 1 cm. Similar to the kinematic quantities in the context of the simulation results in chapter 8, e. g. compare figure 8.19, the distribution of average kinematic measures yields RVE size dependent localization zone widths, if this width is defined by means of an evaluation of the displacement gradients.

The norm of $\langle \tilde{\mathbf{w}} \rangle_{\mathcal{R}}$ for RVE size RVE_19 in figure 9.5 pictures the influence of the approximation order on the statistical procedure. Again, the situation long before localization onset is illustrated. From the lowest approximation order (linear) in figure 9.5 (a) to the highest order (cubic) in figure 9.5 (c) the maximum value of the norm decreases from $9 * 10^{-3}$ to $5 * 10^{-3}$. $\langle \tilde{\mathbf{w}} \rangle_{\mathcal{R}}$ primarily localizes in the notch tip region, as there the highest deformations within the sample are present. From the technical point of view higher deformations in turn imply higher average fluctuations. It can be concluded that $\langle \tilde{\mathbf{w}} \rangle_{\mathcal{R}}$ represents an inherent approximation error which not only depends on the order of approximation, but also on the RVE size. This approximation error should vanish in the limit of an infinite RVE size and an infinite approximation order.
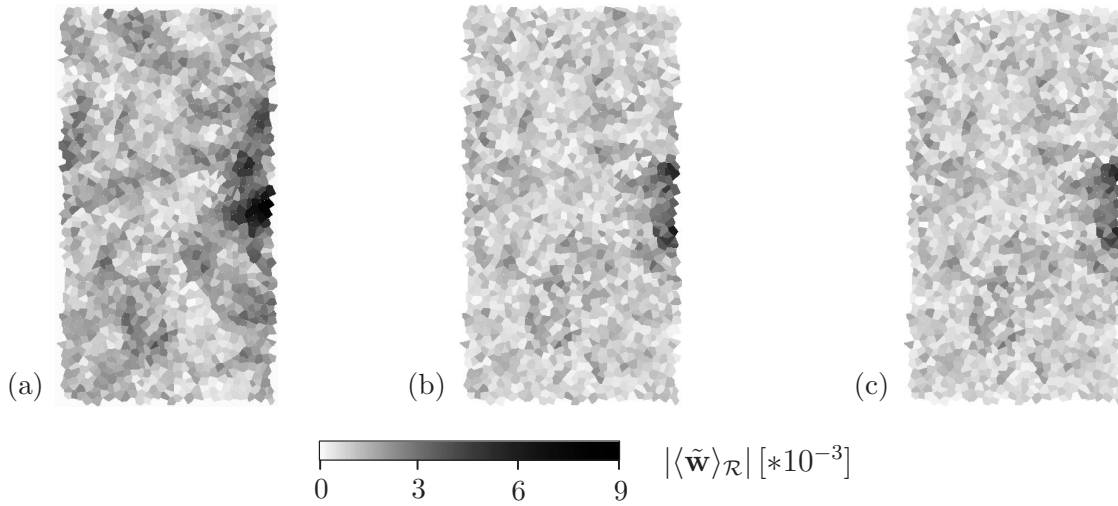
Figure 9.5: Distribution of norm of $\langle\tilde{\mathbf{w}}\rangle_\mathcal{R}$ long before localization for RVE_19.

9.5.2   Fluctuations on RVE level

As mentioned in section 9.4, it is of special interest whether the assumptions utilized during the process of derivation of the average quantities are valid or not. Therefore, the constraints imposed by the formulation of the boundary conditions have to be checked via the validity of equation set (9.28). In this context equation $(9.28)_1$, which was introduced for the derivation of the higher order kinematics, is evaluated in the form of a summation over the boundary of the RVE: The coefficients $\langle\tilde{W}_{11}\rangle_\mathcal{R}$ and $\langle\tilde{W}_{22}\rangle_\mathcal{R}$ of $\langle\tilde{\mathbf{W}}\rangle_\mathcal{R}$ are computed. In order to estimate if equation $(9.28)_1$ is valid or not, i. e. $\langle\tilde{\mathbf{W}}\rangle_\mathcal{R} = 0$, a quantitative comparison with the corresponding entries of the deformation gradient tensor $\langle\mathbf{F}\rangle_\mathcal{R}$ is carried out. Since it is not expected that the distribution of $\langle\tilde{\mathbf{W}}\rangle_\mathcal{R}$ yields pure zero values, an approximated way of checking is applied here, i. e. $\langle\tilde{\mathbf{W}}\rangle_\mathcal{R} \approx 0$. In order to be able to categorize whether this is sufficiently valid or not, a calibration with respect to $\langle\mathbf{F}\rangle_\mathcal{R}$ is utilized. The reason for a comparison with $\langle\mathbf{F}\rangle_\mathcal{R}$ can be traced back to the introduction of assumption $(9.28)_1$ in the context of equation (9.19). This means that the basis of computation of $\langle\tilde{\mathbf{W}}\rangle_\mathcal{R}$ and $\langle\mathbf{F}\rangle_\mathcal{R}$ is the same. Comparison of figure 9.6 (a) with (b) and figure 9.6 (c) with (d) leads to the conclusion that the assumption of a vanishing tensor $\langle\tilde{\mathbf{W}}\rangle_\mathcal{R}$ is sufficiently valid: On the one hand, the local absolute values of $\langle\tilde{\mathbf{W}}\rangle_\mathcal{R}$ are small compared to the variable part of the deformation tensor. Thereby, the variable part of the deformation tensor $\langle\mathbf{F}\rangle_\mathcal{R}$ is expressed by the difference between the minimum and maximum values of the corresponding scale. On the other hand, the fluctuation contribution is distributed over the complete sample instead of being localized in a certain zone. Thereby, the values are mostly near to zero (middle grey color in scales of figures 9.6 (a) and (c)).

Another instructive representation is given by the average variable fluctuations $\delta\tilde{\mathbf{w}}$. As mentioned earlier, these variable fluctuations have been assumed to fluctuate around the zero value in the preceding statistical routine. As an example, the normalized values of $\delta\tilde{\mathbf{w}}$ for a quadratic approximation order and a situation just before the start of the crack formation are evaluated according to equation $(9.29)_2$. In figure 9.7 (a) the evaluation based on the complete RVE volume data (i. e. all particle pairs $\rightarrow N_* = N_\mathcal{R}$) and in

(a) $\langle \tilde{W}_{11} \rangle_{\mathcal{R}}$ $[*10^{-4}]$ (b) $\langle F_{11} \rangle_{\mathcal{R}}$ (c) $\langle \tilde{W}_{22} \rangle_{\mathcal{R}}$ $[*10^{-4}]$ (d) $\langle F_{22} \rangle_{\mathcal{R}}$
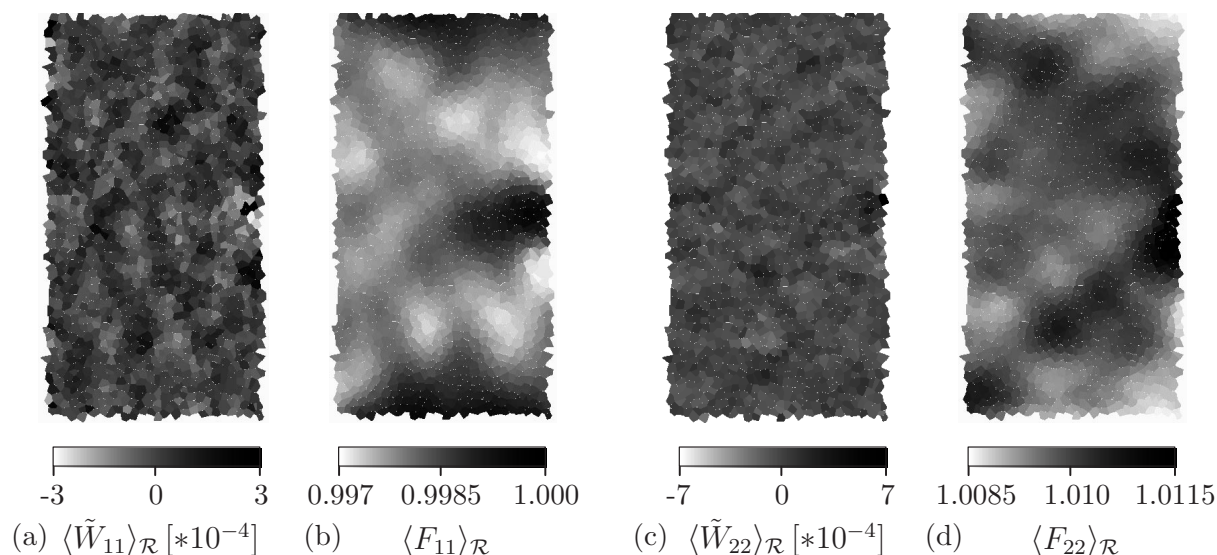
Figure 9.6: Evaluation of $\langle \tilde{\mathbf{W}} \rangle_{\mathcal{R}}$ and comparison with corresponding coefficients of displacement gradient $\langle \mathbf{F} \rangle_{\mathcal{R}}$ for RVE_9 short before localization onset.

figure 9.7 (b) the corresponding evaluation over the boundary of the RVE (i. e. all boundary particle pairs $\rightarrow N_* = N_{\partial \mathcal{R}}$) are shown. It is obvious that the variable fluctuations are equally distributed over the complete monitored part of the sample. The distribution in figure 9.7 suggests that the average over all average variable fluctuations vanishes for both cases, $\langle \langle \delta \mathbf{w}_{norm} \rangle_{\mathcal{R}} \rangle \approx 0$ and $\langle \langle \delta \mathbf{w}_{norm} \rangle_{\partial \mathcal{R}} \rangle \approx 0$. Remarkably, three times higher fluctuations are obtained, if only boundary particles are considered, compare figure 9.7 (a) with (b). This fact is not surprising, since a higher number of evaluated particle pairs is known to smooth out the solution. This is the case when all pairs are used instead of only the boundary pairs.

Finally, the following conclusions can be drawn: These observations show that fluctuations are physically motivated, if the kinematic description is enhanced accordingly. Strictly speaking, the DEM simulations have shown that the fluctuation fields are present and can be characterized as a representative characteristic of a specific microstructure. These models can be seen in the tradition of *Mindlin's* idea to represent a microstructure. Thus, models based on the concept of microstructural fluctuation field represent an alternative method in the context of enhanced continuum theories, like integral-, gradient- or micropolar-type ones.

9.6   Validation of procedure

A homogenization method was presented that allows for the modeling of higher displacement gradients and higher order stresses in a straightforward and natural way. One of the key ideas that led to this characteristic is the introduction of a physically motivated characterization of the displacement field via a truncated Taylor series. Based on this characteristic a gradient theory was motivated by means of a theoretical derivation in form of a statistical approach. Numerical simulations on the basis of the DEM supplemented this theoretical framework. Admittedly, the general dilemma discussed already in
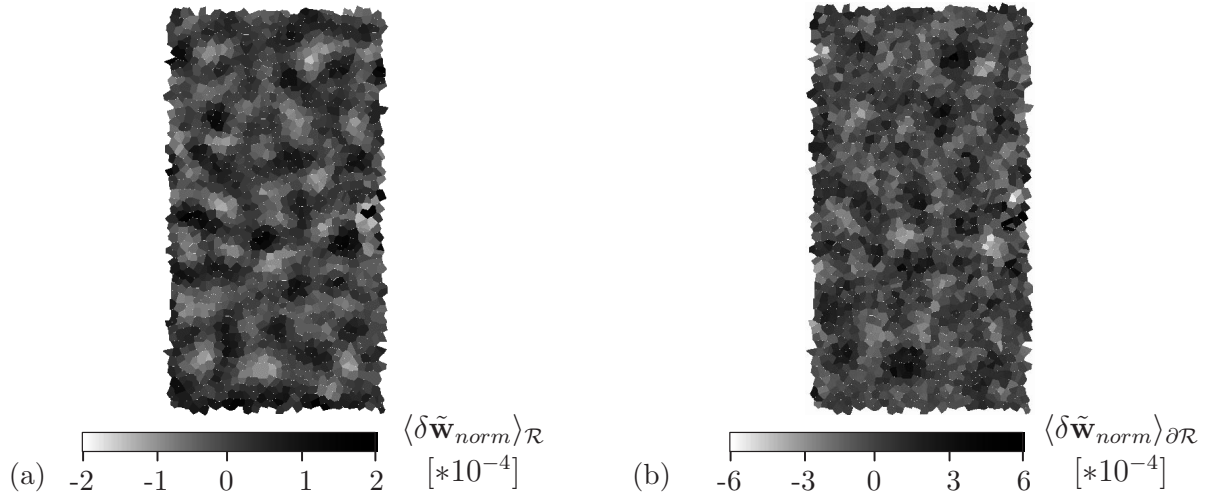
Figure 9.7:   Evaluation of variable fluctuations $\delta \tilde{\mathbf{w}}$ for RVE_9 short before localization onset.

the context of chapter 8 is still persistent: A discrete model naturally aims at the description of local effects, while the homogenization smears out this information in a certain averaging radius. The simulation results suggest that the averaging diameter of the RVEs are not restricted in the same manner as in the context of the homogenization procedure of the micropolar model due to the employed statistics approach. Therefore, it seems that the necessary RVE size to reproduce microstructural effects, i. e. displacement gradients and, therewith, the gradient effects, on the RVE or macro scale is higher compared to that found in the previous chapter. However, further examples are needed for a more detailed verification. The presented example showed that a RVE size RVE_9 can be considered as "ideal" size when a gradient model including displacement gradients up to the order 2 shall be represented.

In short, the DEM simulations lead to the following conclusions:

- Gradient formulations can be motivated by means of discrete particle methods on the basis of the DEM via an enhancement of the kinematic description utilizing a truncated Taylor series.

- Higher order displacement gradients as well as higher order stresses of cohesive and non-cohesive particle samples can be computed.

- The distribution of the displacement gradients over the height short after localization onset suggests that the mathematical context is represented in a qualitative correct manner.

- The assumptions used for the derivation of the average quantities are sufficiently valid, i. e. on average the corresponding products containing the fluctuation terms (higher order term in Taylor series) vanish.

- Fluctuations, as for example introduced in FEM multiscale approaches via the concept of microstructural fluctuation fields, are physically motivated on the basis of a higher order kinematics.

The inclusion of gradients in the context of particle mechanics and corresponding homogenization of particle composites is not new. Various authors introduced higher order gradients for a kind of "analytical" homogenization approach, see appendix E. In this context the term "analytical" homogenization denotes the proceeding for a derivation of macroscopic moduli of idealized granular samples in terms of particle contact stiffnesses. This can be realized along the lines of *Chang and co-workers* [34, 35, 36] or *Kuhl et al.* [138], compare also the discussion in *Ramm et al.* [206]. The essential result of appendix E is that the formal bases of the displacement gradient formulation followed in this thesis and the procedure usually followed in the context of "analytical" homogenization approaches are identical. However, one of the key differences between these approaches and the one presented in this chapter is given as follows: For example, *Chang and co-workers* [34, 35, 36] enhance the contact kinematics between two particles, i. e. a gradient model is "inserted by hand" on the particle scale. Thus, it is not surprising at all that after homogenization on the RVE or macro level also a gradient model is obtained. In contrast to that, in the present thesis the particle kinematic is kept in the standard form and the gradient model results naturally from the homogenization. This approach, in the author's opinion, represents a more coherent way from the physical point of view, if a gradient model ought to be included in a DEM context.

Chapter 10

Conclusion

10.1 Concluding validation

The goal of this thesis was the further development and advancement of discrete models for an application to cohesive as well as non-cohesive frictional materials. The derivation and supply of adequate homogenization methods aimed, on the one hand, at a continuum mechanical description of disintegrating particle assemblies in terms of averages, and on the other hand, at a thorough physical motivation of enhanced continuum theories like micropolar or gradient ones. A validation of these discrete models and the corresponding homogenization procedures, respectively, with regard to qualitative and quantitative aspects enriched the plan of the thesis. Thereby, an extensive simulation program has been carried out in order to clarify the respective subject matter.

The development and implementation of a polygonal two-dimensional discrete element model (DEM) has been carried out in a structured form. Starting from a basic DEM model for non-cohesive polygonal particles, the complexity of the model was successively increased in order to include a coherent representation of cohesive particle assemblies. This coherent representation implied a qualitative as well as quantitative reproduction of characteristic features of geomaterials. The formal realization of the particle model was further advanced by, first, including beam elements to represent the cohesion. Since a quantification of this type of beam enhanced DEM model is an arduous task, alternatively, interface elements between the particles have been inserted in order to model a cohesive bond. The last step in the series of increasing complexity was the realization of a microstructure-based simulation environment which utilizes the foregoing enhanced DEM models. With growing intricacy and, therewith, freedom of the models a wide variety of features typically observed in cohesive frictional materials could be represented in a satisfactory manner. Simulations in the context of non-cohesive and cohesive particle samples showed various characteristics and are validated as follows:

Basic DEM model
The application of the basic (non-cohesive) DEM model adopted from *Tillemans & Herrmann* [237] has proven to be capable to qualitatively picture the behavior of cohesionless granular materials like sand. The localization of shear bands along with the formation of complex failure pattern was studied by means of dense and porous samples and reflected experimental observations in an astonishing manner. Although a quantification of the model was not intended, based on the present knowledge its realization seems a manageable task.

→   *The qualitative picture of the basic DEM model is satisfactory and a quantification is conceivable.*

Beam enhanced DEM model

The general failure behavior using the beam enhanced DEM model adopted from *Kun & Herrmann* [141] is well represented when compared to the fracture of cohesive frictional materials like concrete, i. e. the model is capable to reproduce the typical inherent failure mechanisms. This form of the model has proven to be very well suited for a visualization of these mechanisms which are technically difficult to observe in experiments. Admittedly, a realistic softening behavior could not be obtained in the simulations due to the applied breaking criterion, i. e. the failure appears mostly brittle in the context of normalized load-displacement diagrams.

→   *The qualitative picture of the model is satisfactory, but the quantification remains still a demanding task.*

Interface enhanced DEM model

In order to picture the real physics of the cohesive bond better than by the previous model an interface enhanced DEM model was introduced. A numerical implementation was devised which incorporates a finite number of integration points attached along a common particle edge, i. e. the interface. This more complex bond representation favored the quantification of the model with respect to experiments. As a result, the post-peak softening in the corresponding simulations was by far better reproduced than for the beam enhanced model. However, the feature of a less pronounced softening in compression is to be clarified.

→   *The qualitative picture of the interface enhanced DEM model is similar to that of the beam enhanced DEM model and, in addition, the quantification seems by far more promising.*

Microstructure-based enhanced DEM model

The quality of the quantification process, in particular for the case of softening in compression, increases with a growing complexity by means of an explicit inclusion of a microstructure. In this context a generation algorithm for an artificial microstructure was developed where a mesh controlled distribution of stiffnesses and yield stresses is obtained as final result. Consequentially, a realistic representation of the post-peak softening behavior in terms of the stress-strain relation results as simulation output.

→   *The interface enhanced DEM simulations of microstructure-based particle meshes have proven to effectively remedy in a qualitative as well as quantitative manner the deficiencies of the non-microstructure simulation approaches.*

The second part of the thesis was devoted to the development of homogenization procedures which allow for a transfer from a particle model, which is based on a simple Boltzmann continuum framework, to a more complex continuum with microstructure. The numerical realization and verification of the transitions towards micropolar and gradient models have been presented. Thereby, the enhanced continuum theories have been viewed as special cases of Mindlin's continuum. The goal behind this topic was twofold: On the one hand, formulations of continuum mechanical quantities like average stresses, strains and corresponding higher order stress or strain measures are developed. In doing so, the higher order quantities are the natural result of this transition. As a vehicle to formally perform this micro to macro transition, the concept of a representative volume element (RVE) was adopted. The consideration of scale separation arguments in the context of rigid body mechanics led to simplifications of the key balance laws. These

balances denoted the point of origin for the further derivation towards the consistent definition of average quantities. On the other hand, a micromechanical motivation of these enhanced continuum theories was emphasized. The emergence of higher order quantities implicitly accounted for the microstructural effects which are related to the micropolar or gradient theories. Therefore, the corresponding averaging volume which was introduced in the context of RVEs showed a distinct relationship to the internal length scale. In this connection, the question of the necessary RVE size was highlighted. Possible RVE sizes - for the problems in mind - were estimated. These sizes allow the computation of continuum mechanical quantities (comparable to macroscopic ones) and account for the locality of a discrete system at the same time. Therefore, as one of the most fundamental results of the present work, the realized procedures reflect a filtering of the relevant results without the loss of comparability with continuum models. The validation of the homogenization procedures along with the corresponding simulation-based evaluation of homogenized quantities is expressed by the following general statements:

Numerical verification of transition to micropolar continuum
The simulation results showed that the diameter of the RVEs should be of the order of around 5 times the typical particle diameter. This size is necessary in order to reproduce the macroscopic stress response together with localization effects occurring when strong inhomogeneities dominate the local behavior. The localization of the couple stresses as well as the stress asymmetry point to the position and inclination of the shear band. Furthermore, the general feature of homogenization techniques, that the fluctuations of average quantities decrease with increasing average diameter, could be correctly represented. In this context the validity of the scale separation assumptions was shown. In a second step, the procedure for the derivation of dynamic quantities was straightforwardly transferred to kinematic quantities which for example yielded an experimentally motivated strain localization pattern. The same line was taken for the energetic quantities and suggested that the homogenization is consistent.

→ *Micropolar formulations can be motivated by means of a discrete particle method on the basis of the DEM via an explicit inclusion of the rotational degree of freedom and the procedure of a statically equivalent transfer of the contact forces.*

Numerical verification of transition to gradient continuum
The simulation results showed that due to the technical realization of the homogenization procedure the necessary RVE size to reproduce gradient effects on the macro scale is higher compared to the previous case. A RVE size of the order of around 9 times the typical particle diameter can be considered as necessary size for representing a model which includes displacement gradients up to the order 2. Gradient effects are apparent by a localization of the first, second or third order displacement gradients which also point to the position of an evolving failure zone. It was shown that the assumptions used for the derivation of the higher order quantities are sufficiently valid, i. e. the corresponding products containing the fluctuation terms vanish. Finally, a physical motivation of microstructural fluctuation fields was presented. Thereby, these microstructural fluctuation fields are typically encountered in multiscale approaches on the basis of continuum mechanical discretization methods like the FEM.

→ *Gradient formulations can be motivated by means of discrete particle methods via an introduction of a physically sound characterization of the displacements through a truncated Taylor series.*

Identification of macroscopic material parameters

A detailed discussion of a feasible identification of macroscopic material parameters was carried out. First, the relation that connects the RVE size in particle models to the internal length scale in enhanced continuum models was addressed. It was shown that these two lengths are very different from their definition, although their terminology is similar. An approach for an inverse modeling of the internal length scale of enhanced continuum models via the size of the microstructural constituents, i. e. the particle size, the RVE size and the corresponding stiffness parameters was briefly outlined. Second, different possibilities to determine effective stiffnesses were examined. In this context the difficulties in the computation of effective stiffnesses at RVE level have been pointed out. As remedy, an approach for the determination of macroscopic material parameters has been presented where the averaged (i. e. average of the average) RVE dynamic and kinematic quantities are related to each other. Furthermore, in the context of the micropolar model two approaches have been developed which should yield a reasonable relation between curvatures and couple stresses. The application of these procedures for a determination of the micropolar stiffness as well as the internal length parameter seems quite promising. Based on the introduction of a predefined control volume a coherent relation between averaged curvatures and couple stresses might be constituted. Thereby, the control volume covers the area where microstructural effects appear.

$\rightarrow$ *An identification of the material parameters of standard and enhanced continuum models by DEM simulations supplemented by adapted averaging procedures seems to be promising.*

10.2   Outlook

Several types of discrete element models and corresponding transitions towards a continuum mechanical description have been presented. Although various topics in the context of discontinuous simulation models have been touched throughout the thesis, a variety of issues has been left unexplored. From the author's point of view the following topics in the context of improvements of the models and the homogenization procedures are worth to receive further attention:

- Above all, the quantification of the parameters has to be advanced. In this sense, the relation between the micromechanical properties of geomaterials and the corresponding model parameters has to be further elaborated. This implies a consideration of special experimental setups to gain more knowledge on parameters like the micromechanical yield strength or the corresponding ratios for the aggregate, matrix and "interface" components. In order to achieve this simple composite (model) materials could be created, e. g. regular polygonal particles embedded in a soft matrix with glue between matrix and particles. Due to the clear knowledge of all micromechanical material=model parameters, a comparison of simulation and experiment could be much easier.

- An advancement to a three-dimensional modeling is not advisable until the previous point has been satisfactorily solved. With increasing computational power in the near future the 3D modeling and the corresponding application of homogenization procedures should be addressed. Particularly, microstructure-based 3D simulations

including irregular shaped particles like polyhedra may provide additional valuable insights into failure and post-peak behavior of geomaterials.

- A realization should be tackled where the composition of the RVEs is newly updated at each time step and the corresponding quantities are mapped onto a fixed background mesh instead of moving base particles. Although this procedure is numerically more demanding, an obvious advantage is obtained: Even after occurrence of localization zones a clear definition and interpretation of the RVE data is possible. This means that the flow-type failure which occurs after shear band formation can be followed in a physically more substantiated way. Strictly speaking, within the present numerical approach the assumption of a flexible vessel surrounding the RVE may be violated after shear band formation, e. g. one part of the particles within the RVE may move in the opposite direction compared to the other part. Newly updated RVEs could remedy this problem.

- A further quantification of the homogenization procedures directed towards a determination of effective stiffness parameters should be undertaken. The ideas presented in section 8.6 seem very promising. In particular, an evaluation of those stiffnesses which combine the higher order stresses with the additional kinematic degrees of freedom is conceivable. Therefore, these ideas should be put into practice and validated by according simulation setups. Corresponding setups should ensure that the position of the zones where microstructural effects occur are known in advance, e. g. like the simple shearing of a granular layer.

- Further attention should be paid to an embedding of a DEM model into a multiscale framework via the use of homogenization procedures like those introduced herein. For example, a combined approach based on a FEM model on the macro scale and a DEM model on the micro scale may be pursued. This can be realized for example by extending and enriching ideas like those presented by *Munjiza et al.* [182] with corresponding homogenization principles.

- Finally, by use of Microplane-based FEM formulations, an alternative way of transferring the information of the micro scale, by means of a DEM model, to the macro scale may be achieved: The anisotropy information of a (deformed) discrete particle assembly by means of an anisotropic damage or contact density distribution may be transported to the integration point level of a Microplane FEM model. The realization implies a "continuumization" of the discontinuous distributions according to section 6.3 and insertion into the continuum model as input, compare the schematic picture of the approach by *Kuhl et al.* [136].

As the interest in geomaterials is sure to remain at least constant in the next decades, the perspectives of a disproportionate increase of computational power lends the DEM a promising future when the aim is to describe a geomaterial with simple parameters and fully discontinuous characteristics. Some authors, among others *Peter Cundall* [46], one of the "inventors" of the DEM, argue that within 10-20 years in geomechanics continuum models such as the FEM may be completely replaced by particle models such as the DEM. Based on six years of DEM development and simulation experience, in the author's point of view, this argument is highly provocative and sets the sights too high. Which model will actually gain more acceptance for the simulation of geomaterials is vague tough.

If for example one compares the variety of concurring models presented in section 3.1, it is obvious that it is impossible to give a reasonable future perspective on the advancement of simulation models. Insofar, the author is hopeful that this contribution may lend more credence to discrete element methods in general and may stimulate further intensive investigations on the way to the best simulation method for geomaterials.

Appendix A

Notation & tensor calculus

In the following section the general notation used throughout this thesis is summarized by means of some fundamental topics in the context of tensor calculus. The content of this chapter is related to the proper Euclidean vector space $\mathcal{V}^3$ and the corresponding dyadic product space $\mathcal{V}^3 \otimes \mathcal{V}^3 \otimes \cdots \otimes \mathcal{V}^3$ (n times) of n-th order.

Notation

Usually, tensor notation is applied and tensors up to the sixth order appear throughout the thesis. If needed, e. g. for clarity, index notation is additionally specified, as done in equations (A.1) to (A.7) and (A.11). For simplicity, a normalized cartesian basis system is utilized, so that no distinction between co- and contravariant bases is needed. In the general form the tensorial quantities are constituted as follows:

$$
\begin{aligned}
a &= a & \mathbf{A} &= A_{ijk}\mathbf{e}_i \otimes \mathbf{e}_j \otimes \mathbf{e}_k \\
\mathbf{a} &= a_i\mathbf{e}_i & \mathbf{A} &= A_{ijkl}\mathbf{e}_i \otimes \mathbf{e}_j \otimes \mathbf{e}_k \otimes \mathbf{e}_l \quad\quad \text{(A.1)} \\
\mathbf{A} &= A_{ij}\mathbf{e}_i \otimes \mathbf{e}_j & &\;\vdots
\end{aligned}
$$

Thereby, a scalar is represented by a non bold small letter, a vector by a bold lower case letter and tensors starting from the second order with a bold capital letter. The order of higher order tensors becomes clear from the context or is denoted separately in the text. For simplicity, the base systems of the tensors are skipped within the notation in the following.

Scalar products

A scalar product is denoted by the operators $\cdot, :, \vdots, ::, \vdots\!\vdots$ and $\vdots\!\vdots$, whereby the amount of dots k denotes the order of the contraction. A scalar product of two tensors of order n and m yields an order of the resulting tensor of $n + m - 2k$, compare the following examples:

$$
\begin{aligned}
c &= \mathbf{a} \cdot \mathbf{b} = a_i b_i & c_i &= \mathbf{c} = \mathbf{A}::\mathbf{B} = A_{ijklm}B_{jklm} \\
c &= \mathbf{A}:\mathbf{B} = A_{ij}B_{ij} & c_i &= \mathbf{c} = \mathbf{A}\vdots\!\vdots\mathbf{B} = A_{ijklmn}B_{jklmn} \\
c &= \mathbf{A}\vdots\mathbf{B} = A_{ijk}B_{ijk} & C_{ij} &= \mathbf{C} = \mathbf{A} \cdot \mathbf{b} = A_{ijk}b_k \\
c &= \mathbf{A}::\mathbf{B} = A_{ijkl}B_{ijkl} & C_{ij} &= \mathbf{C} = \mathbf{A}:\mathbf{B} = A_{ijkl}B_{kl} \\
c &= \mathbf{A}\vdots\!\vdots\mathbf{B} = A_{ijklm}B_{ijklm} & C_{ij} &= \mathbf{C} = \mathbf{A}\vdots\mathbf{B} = A_{ijklm}B_{klm} \quad \text{(A.2)} \\
c &= \mathbf{A}\vdots\!\vdots\mathbf{B} = A_{ijklmn}B_{ijklmn} & C_{ij} &= \mathbf{C} = \mathbf{A}::\mathbf{B} = A_{ijklmn}B_{klmn} \\
c_i = \mathbf{c} &= \mathbf{A} \cdot \mathbf{b} = A_{ij}b_j & C_{ijk} &= \mathbf{C} = \mathbf{A} \cdot \mathbf{b} = A_{ijkl}b_l \\
c_i = \mathbf{c} &= \mathbf{A}:\mathbf{B} = A_{ijk}b_{jk} & C_{ijk} &= \mathbf{C} = \mathbf{A}:\mathbf{B} = A_{ijklm}B_{lm} \\
c_i = \mathbf{c} &= \mathbf{A}\vdots\mathbf{B} = A_{ijkl}B_{jkl} & C_{ijkl} &= \mathbf{C} = \mathbf{A}:\mathbf{B} = A_{ijklmn}B_{lmn}
\end{aligned}
$$

Dyadic products

The dyadic product of two tensors is denoted by the symbol $\otimes$ and implies the dyadic combination of all basis vectors of the tensors. The tensorial order of a dyadic product of two tensors of order n and m is of order $n + m$, compare the following examples:

$$
\begin{aligned}
C_{ij} &= \mathbf{C} = \mathbf{a} \otimes \mathbf{b} = a_i b_j & C_{ijkl} &= \mathbf{C} = \mathbf{A} \otimes \mathbf{B} = A_{ij} B_{kl} \\
C_{ijk} &= \mathbf{C} = \mathbf{A} \otimes \mathbf{b} = A_{ij} b_k & C_{ijklm} &= \mathbf{C} = \mathbf{A} \otimes \mathbf{B} = A_{ijk} B_{lm} \quad \text{(A.3)} \\
C_{ijkl} &= \mathbf{C} = \mathbf{A} \otimes \mathbf{b} = A_{ijk} b_l & &\vdots
\end{aligned}
$$

Cross products

The cross product of vectors yields again a vector and may be geometrically interpreted in the context of a parallelepiped. One obtains

$$
c_k = \mathbf{c} = \mathbf{a} \times \mathbf{b} = -\mathbf{b} \times \mathbf{a} = \overset{3}{\mathbf{E}} : (\mathbf{a} \otimes \mathbf{b}) = e_{ijk} a_i b_j \,, \tag{A.4}
$$

with the Ricci permutation tensor of third order $\overset{3}{\mathbf{E}}$ according to

$$
e_{ijk} = \begin{cases} 1 &: \text{ even permutation} \\ -1 &: \text{ odd permutation} \\ 0 &: \text{ double indexing} \end{cases} \longrightarrow \begin{cases} e_{123} = e_{231} = e_{312} = 1 \\ e_{321} = e_{213} = e_{132} = -1 \\ \text{all remaining } e_{ijk} \text{ vanish} \end{cases}. \tag{A.5}
$$

Fundamental tensors

Fundamental tensors of second $\mathbf{I}$ and fourth order $\mathcal{I}$ are represented by products of the Kronecker Deltas δ_{ij}

$$
\mathbf{I} = \delta_{ij} \,, \qquad\qquad \mathcal{I} = \delta_{ik} \delta_{jl} \,, \tag{A.6}
$$

where $\delta_{ij} = 1$ for $i = j$ and $\delta_{ij} = 0$ for $i \neq j$. The Ricci permutation tensor introduced above denotes the fundamental tensor of third order.

Specific tensors and operations

The transposition of tensors is introduced in the following form in this thesis:

$$
\begin{aligned}
\mathbf{A} &= A_{ij} &\rightarrow \mathbf{A}^T &= A_{ji} & \mathbf{A} &= A_{ijklm} &\rightarrow \mathbf{A}^T &= A_{mlkji} \\
\mathbf{A} &= A_{ijk} &\rightarrow \mathbf{A}^T &= A_{kji} & \mathbf{A} &= A_{ijklmn} &\rightarrow \mathbf{A}^T &= A_{nmlkji} \quad \text{(A.7)} \\
\mathbf{A} &= A_{ijkl} &\rightarrow \mathbf{A}^T &= A_{lkji} & &\vdots
\end{aligned}
$$

In this context symmetric tensors $\mathbf{A} = \mathbf{A}^T$ and skew-symmetric (antimetric) tensors $\mathbf{A} = -\mathbf{A}^T$ can be distinguished. Thereby, the symmetric and skew-symmetric part of an arbitrary tensor is identified by

$$
\text{sym}\mathbf{A} = \frac{1}{2}(\mathbf{A} + \mathbf{A}^T) \,, \qquad\qquad \text{skw}\mathbf{A} = \frac{1}{2}(\mathbf{A} - \mathbf{A}^T) \,. \tag{A.8}
$$

If the inverse tensor $\mathbf{A}^{-1}$ of an arbitrary tensor exists, the fundamental tensors of second or fourth order are obtained. This depends on the order of $\mathbf{A}$, i. e. for the second order case $\mathbf{A} \cdot \mathbf{A}^{-1} = \mathbf{I}$ or the fourth order case $\mathbf{A} : \mathbf{A}^{-1} = \mathcal{I}$.

Axial vector

The axial vector $\overset{A}{\mathbf{a}}$, also denoted pseudo vector, can be used for the description of rotations in the form of a rotation vector. The axial vector is associated with the skew-symmetric part skw$\mathbf{A}$ of an arbitrary tensor $\mathbf{A}$ via

$$\overset{A}{\mathbf{a}} := \frac{1}{2}\overset{3}{\mathbf{E}}:\mathbf{A}^T = -\frac{1}{2}\overset{3}{\mathbf{E}}:(\text{skw}\mathbf{A}). \tag{A.9}$$

It is important to note that symmetric tensors do not posses an axial vector.

Norm of a tensor

In this thesis use is made of the scalar valued L_2 norm. The L_2 norm of an arbitrary tensorial quantity $\mathbf{a}$ or $\mathbf{A}$ is defined by the extraction of the square root of the scalar product of the respective tensor, i. e. for a tensor of first, second, third and fourth order one obtains

$$|\mathbf{a}| := \sqrt{\mathbf{a}\cdot\mathbf{a}}, \qquad |\mathbf{A}| := \sqrt{\mathbf{A}:\mathbf{A}}, \qquad |\mathbf{A}| := \sqrt{\mathbf{A}\vdots\mathbf{A}}, \qquad |\mathbf{A}| := \sqrt{\mathbf{A}::\mathbf{A}}. \tag{A.10}$$

Tensor analysis

The functions of the position vector are called field functions and derivatives with respect to the position vector are denoted as gradient of a function. One has to distinguish scalar- $a(\mathbf{x})$, vector- $\mathbf{a}(\mathbf{x})$ and tensor-valued $\mathbf{A}(\mathbf{x})$ functions

$$\begin{aligned}
\text{grad}\,a(\mathbf{x}) &:= \frac{\mathrm{d}a(\mathbf{x})}{\mathrm{d}\mathbf{x}} &= \mathbf{b}(\mathbf{x}) &\longrightarrow & \frac{\partial a(\mathbf{x})}{\partial x_i} &= a_{,i}, \\[2mm]
\text{grad}\,\mathbf{a}(\mathbf{x}) &:= \frac{\mathrm{d}\mathbf{a}(\mathbf{x})}{\mathrm{d}\mathbf{x}} &= \mathbf{B}(\mathbf{x}) &\longrightarrow & \frac{\partial a_i(\mathbf{x})}{\partial x_j} &= a_{i,j}, \\[2mm]
\text{grad}\,\mathbf{A}(\mathbf{x}) &:= \frac{\mathrm{d}\mathbf{A}(\mathbf{x})}{\mathrm{d}\mathbf{x}} &= \mathbf{B}(\mathbf{x}) &\longrightarrow & \frac{\partial A_{ij}(\mathbf{x})}{\partial x_k} &= A_{ij,k}.
\end{aligned} \tag{A.11}$$

Principally, the order of a quantity is increased by one via the gradient operator $\text{grad}\,(\cdot) = \nabla(\cdot)$, e. g. the gradient of a scalar is a tensor of first order and so on. Derivatives of functions with respect to arbitrary vectorial and tensorial variables are treated similarly, e. g. $\partial(\cdot)/\partial A_{ijk}$. These derivatives are built analogously to the preceding procedures. The notation $\text{Grad}\,(\cdot)$ refers to a derivative with respect to the initial configuration ($\rightarrow$ position vector $\mathbf{x}$) and $\text{grad}\,(\cdot)$ refers to a derivation with respect to the actual configuration ($\rightarrow$ position vector $\mathbf{X}$). In the context of balance laws an additional differential operator, namely the divergence operator $\text{div}\,(\cdot)$ is introduced. The divergence of a vector and tensor field are obtained as follows:

$$\text{div}\,\mathbf{a} := [\text{grad}\,\mathbf{a}(\mathbf{x})]\cdot\mathbf{I} =: a, \qquad \text{div}\,\mathbf{A} := [\text{grad}\,\mathbf{A}(\mathbf{x})]:\mathbf{I} =: \mathbf{a}. \tag{A.12}$$

In contrary to the gradient operator, the divergence operator $\text{div}\,(\cdot) = \nabla\cdot(\cdot)$ decreases the order of the respective function by one. In this thesis use is made of the following rules for $\text{grad}\,(\cdot)$ and $\text{div}\,(\cdot)$, whereby $\mathbf{a}$ and $\mathbf{b}$ represent vectors and $\mathbf{A}$ and $\mathbf{B}$ tensors of second order:

$$\begin{aligned}
\text{grad}\,\mathbf{x} &= \mathbf{I}, \\
\text{div}\,(\mathbf{a}\otimes\mathbf{b}) &= \mathbf{a}\,\text{div}\,\mathbf{b} + (\text{grad}\,\mathbf{a})\cdot\mathbf{b}, \\
\text{div}\,(\mathbf{A}\cdot\mathbf{b}) &= (\text{div}\,\mathbf{A}^T)\cdot\mathbf{b} + \mathbf{A}^T:\text{grad}\,\mathbf{b}, \\
\text{div}\,(\mathbf{a}\times\mathbf{B}) &= \mathbf{a}\times\text{div}\,\mathbf{B} + \text{grad}\,\mathbf{a}\times\mathbf{B}.
\end{aligned} \tag{A.13}$$

Integral theorems

Gaussian integral theorems provide for a transformation of surface to volume integrals. Thereby, $\mathbf{a} = \mathbf{a}(\mathbf{x})$ is a steady and sufficiently often steadily differentiable vector field.

$$
\begin{aligned}
\int_{\mathcal{B}} \operatorname{div} \mathbf{a} \, dv &= \int_{\mathcal{S}} \mathbf{a} \cdot \mathbf{n} \, da \,, \\
\int_{\mathcal{B}} \operatorname{div} \mathbf{A} \, dv &= \int_{\mathcal{S}} \mathbf{A} \cdot \mathbf{n} \, da \,.
\end{aligned}
\tag{A.14}
$$

Based on these theorems the extensively utilized theorem throughout this thesis is obtained

$$
\int_{\mathcal{S}} \mathbf{A} \, da = \int_{\mathcal{B}} \operatorname{div} \mathbf{A} \, dv \,.
\tag{A.15}
$$

Recall, that $\int_{\mathcal{B}}$ denotes a volume integration over the complete material body $\mathcal{B}$ and $\int_{\mathcal{S}}$ denotes a surface integration over the surface of the material body $\mathcal{S} = \partial\mathcal{B}$.

Appendix B

Numerical realization & program structure

Simplified representations of the program structures of the basic, beam enhanced and interface enhanced DEM models are given in figures B.1, B.2 and B.3. Note that the core of the numerical realizations is identical for all three versions. The shaded references at the right hand side of the charts link to the associated section of the text.

The numerical realization of a DEM code is a straightforward task. However, several stumbling blocks complicate its realization. It is not in the scope of this chapter to discuss general problems of DEM implementations. Useful information can be found in chapter 5 *'Tricks of the trade'* of *Allen & Tildesley's* [5] book or in several review articles on the DEM, compare among others those of *Cundall & Hart* [48] or *Dobry & Ng* [71]. In fact, the focus here is to point out difficulties in the context of the definition of the boundary conditions (b. c.) of relevant loading setups as well as problems that arise if an inappropriate time step is used.

Similar to the procedure in FEM simulations, the basic ingredient for the prescription of Neumann b. c. is the fixing of the degrees of freedom of particles. However, the application of the Dirichlet b. c. is accomplished by prescribing the particle velocities. Thus, most simulation results represent deformation controlled situations. A typical problem arises at the start of each simulation, if a constant velocity is prescribed at a specified boundary. The initial effect of elastic waves resulting from the movement of the boundaries may falsify the simulation result. Therefore, throughout the simulations in this thesis constant strain rate conditions are implemented in the following way: The loading is applied by constantly accelerating particles which define the boundary. When the particles reach a predefined velocity that is much smaller than the sound velocity of the material, the loading is skipped from a constant acceleration to a constant velocity. This procedure, proposed in *Potapov et al.* [202], ensures that this disturbing initial effect is reduced to a tolerable level, see the discussion by *Kun et al.* [139].

Another type of problem appears if the time step is too large. In order to encompass the known problems of explicit integration schemes special attention should be paid to the size of the time step. Usually, a critical time step size that is determined by the highest eigenvalue of the system may be introduced. For time increments larger than the critical value the calculation becomes unstable. The critical time step can be estimated via Courant's criterion $\Delta t_{crit} \leq \sqrt{m_i/k^*}$. Thereby, k^* represents the maximum stiffness within the system and denotes $k^* = E_p$ in the case of a basic (non-cohesive) model, $k^* = \max(E_p, E_b)$ in the case of a beam enhanced model and, finally, $k^* = \max(E_p, k_n, k_t)$ for the interface enhanced model. Normally, in DEM codes the time step is fixed at the beginning and never changed throughout the simulation. However, an adaptive time

step size adjustment is possible, as for example shown by *Bardet & Proubet* [10] or as implemented in *PFC* [120].

pre processing: particle generation $\mathbf{x}$	sect. 3.2
pre processing: initialization of neighborhoodlist	sect. 3.4.2
loop over all time steps	
prediction of geometric and kinematic variables $\mathbf{x}^{pr}, \dot{\mathbf{x}}^{pr}, \ddot{\mathbf{x}}^{pr}, ...$ with $\mathbf{x}$	
loop over all particles i	
loop over all neighboring particles j	
yes contact check no	
contact force by overlap area $\mathbf{f}^c = \mathbf{f}^c(\mathbf{x}^{pr}, \dot{\mathbf{x}}^{pr})$	sect. 3.4.1
updating force vector $\mathbf{f}_i = \mathbf{f}_i + \mathbf{f}_i^c$	
loop over all particles i	
solve equation of motion for particle i $\ddot{\mathbf{x}} = \mathbf{M}^{-1} \mathbf{f}_i(\mathbf{x}^{pr}, \dot{\mathbf{x}}^{pr})$ $\Delta \ddot{\mathbf{x}} = \ddot{\mathbf{x}} - \ddot{\mathbf{x}}^{pr}$	sect. 3.5
specification of boundary conditions	app. B
correction of geometric and kinematic variables $\mathbf{x}^{co} = \mathbf{x}^{co}(\Delta \ddot{\mathbf{x}}, \mathbf{f}_i), \; \dot{\mathbf{x}}^{co} = \dot{\mathbf{x}}^{co}(\Delta \ddot{\mathbf{x}}, \mathbf{f}_i), \; \ddot{\mathbf{x}}^{co} = \ddot{\mathbf{x}}^{co}(\Delta \ddot{\mathbf{x}}, \mathbf{f}_i) ...$	sect. 3.5
update of neighborhoodlist	sect. 3.4.2
post processing: e.g. homogenization $\langle \mathbf{T} \rangle, \langle \boldsymbol{\varepsilon} \rangle, etc.$	chap. 8/9

Figure B.1: Simplified simulation algorithm of basic DEM model according to chapter 3.

pre processing: particle generation $\mathbf{x}$	sect. 3.2
pre processing: initialization of neighborhoodlist	sect. 3.4.2

loop over all time steps

    prediction of geometric and kinematic variables
$\mathbf{x}^{pr}, \dot{\mathbf{x}}^{pr}, \ddot{\mathbf{x}}^{pr}, \dots$ with $\mathbf{x}$

    loop over all particles i

        loop over all neighboring particles j

	beam check	
yes		no

beam force by stiffness method $\mathbf{f}^b = \mathbf{f}^b(\mathbf{x}^{pr})$	sect. 4.3

	if no beam contact check	
yes		no

contact force by overlap area $\mathbf{f}^c = \mathbf{f}^c(\mathbf{x}^{pr}, \dot{\mathbf{x}}^{pr})$	sect. 3.4.1

updating force vector $\mathbf{f}_i = \mathbf{f}_i + \mathbf{f}_i^c + \mathbf{f}_i^b$

    loop over all particles i

solve equation of motion for particle i $\ddot{\mathbf{x}} = \mathbf{M}^{-1}\mathbf{f}_i(\mathbf{x}^{pr}, \dot{\mathbf{x}}^{pr})$ $\Delta\ddot{\mathbf{x}} = \ddot{\mathbf{x}} - \ddot{\mathbf{x}}^{pr}$	sect. 3.5

specification of boundary conditions	app. B

correction of geometric and kinematic variables $\mathbf{x}^{co} = \mathbf{x}^{co}(\Delta\ddot{\mathbf{x}}, \mathbf{f}_i), \dot{\mathbf{x}}^{co} = \dot{\mathbf{x}}^{co}(\Delta\ddot{\mathbf{x}}, \mathbf{f}_i), \ddot{\mathbf{x}}^{co} = \ddot{\mathbf{x}}^{co}(\Delta\ddot{\mathbf{x}}, \mathbf{f}_i)\dots$	sect. 3.5

loop over all neighboring particles i

    loop over all particles j

	beam connection check	
yes		no

no beam breaking $p_b \leq 1$	sect. 4.4

update of neighborhoodlist	sect. 3.4.2
post processing: e.g. homogenization $\langle\mathbf{T}\rangle, \langle\boldsymbol{\varepsilon}\rangle, etc.$	chap. 8/9

Figure B.2: Simplified simulation algorithm of beam enhanced DEM model.

| pre processing: particle generation $\mathbf{x}$ | sect. 3.2 |

| pre processing: initialization of neighborhoodlist | sect. 3.4.2 |

loop over all time steps

prediction of geometric and kinematic variables
$\mathbf{x}^{pr}, \dot{\mathbf{x}}^{pr}, \ddot{\mathbf{x}}^{pr}, ...$ with $\mathbf{x}$

loop over all particles i

loop over all neighboring particles j

| | bond check | |
| yes | | no |

| bond force by evaluation of interface law $\mathbf{f}^{bond} = \mathbf{f}^{bond}(\mathbf{x}^{pr})$ | sect. 5.3 |

| | if no bond contact check | |
| yes | | no |

| contact force by overlap area $\mathbf{f}^c = \mathbf{f}^c(\mathbf{x}^{pr}, \dot{\mathbf{x}}^{pr})$ | sect. 3.4.1 |

updating force vector $\mathbf{f}_i = \mathbf{f}_i + \mathbf{f}_i^c + \mathbf{f}_i^{bond}$

loop over all particles i

| solve equation of motion for particle i $\ddot{\mathbf{x}} = \mathbf{M}^{-1}\mathbf{f}_i(\mathbf{x}^{pr}, \dot{\mathbf{x}}^{pr})$ $\Delta\ddot{\mathbf{x}} = \ddot{\mathbf{x}} - \ddot{\mathbf{x}}^{pr}$ | sect. 3.5 |

| specification of boundary conditions | app. B |

| correction of geometric and kinematic variables $\mathbf{x}^{co} = \mathbf{x}^{co}(\Delta\ddot{\mathbf{x}}, \mathbf{f}_i), \dot{\mathbf{x}}^{co} = \dot{\mathbf{x}}^{co}(\Delta\ddot{\mathbf{x}}, \mathbf{f}_i), \ddot{\mathbf{x}}^{co} = \ddot{\mathbf{x}}^{co}(\Delta\ddot{\mathbf{x}}, \mathbf{f}_i) ...$ | sect. 3.5 |

loop over all particles i

loop over all neighboring particles j

| | bond connection check | |
| yes | | no |

| no bond elimination $\langle\kappa\rangle < 1$ | sect. 5.4 |

| update of neighborhoodlist | sect. 3.4.2 |

| post processing: e.g. homogenization $\langle\mathbf{T}\rangle, \langle\varepsilon\rangle, etc.$ | chap. 8/9 |

Figure B.3: Simplified simulation algorithm of interface enhanced DEM model.

Appendix C

Plasticity formulation

C.1 Return mapping scheme

The key ingredients of the return mapping scheme according to equation (5.6) are as follows:

term	f_1 active	f_2 active
$\dfrac{\partial f}{\partial \kappa}$	$\dfrac{\partial f_1}{\partial \kappa} = \sigma_n^{max}$	$\dfrac{\partial f_2}{\partial \kappa} = \sigma_t^{max}$
$\dfrac{\partial f}{\partial \boldsymbol{\sigma}}$	$\begin{bmatrix} \dfrac{\partial f_1}{\partial \sigma_n} \\ \dfrac{\partial f_1}{\partial \sigma_t} \end{bmatrix} = \begin{bmatrix} 1 \\ \tan\gamma \end{bmatrix}$	$\begin{bmatrix} \dfrac{\partial f_2}{\partial \sigma_n} \\ \dfrac{\partial f_2}{\partial \sigma_t} \end{bmatrix} = \begin{bmatrix} \tan\varphi \\ 1 \end{bmatrix}$
$\dfrac{\partial g}{\partial \boldsymbol{\sigma}}$	$\begin{bmatrix} \dfrac{\partial g_1}{\partial \sigma_n} \\ \dfrac{\partial g_1}{\partial \sigma_t} \end{bmatrix} = \begin{bmatrix} 1 \\ 0 \end{bmatrix}$	$\begin{bmatrix} \dfrac{\partial g_2}{\partial \sigma_n} \\ \dfrac{\partial g_2}{\partial \sigma_t} \end{bmatrix} = \begin{bmatrix} \tan\psi \\ 1 \end{bmatrix}$
$\dfrac{\partial \kappa}{\partial \mathbf{u}^p}$	$\begin{bmatrix} \dfrac{\partial \kappa_1}{\partial u_n^p} \\ \dfrac{\partial \kappa_1}{\partial u_t^p} \end{bmatrix} = \begin{bmatrix} \dfrac{1}{u_n^{max} - u_n^*} \\ 0 \end{bmatrix}$	$\begin{bmatrix} \dfrac{\partial \kappa_2}{\partial u_n^p} \\ \dfrac{\partial \kappa_2}{\partial u_t^p} \end{bmatrix} = \begin{bmatrix} 0 \\ \dfrac{1}{u_t^{max} - u_t^*} \end{bmatrix}$
$\Delta\mathbf{u}^p = \dot{\lambda}\dfrac{\partial g}{\partial \boldsymbol{\sigma}}$	$\dot{\lambda} \begin{bmatrix} \dfrac{\partial g_1}{\partial \sigma_n} \\ \dfrac{\partial g_1}{\partial \sigma_t} \end{bmatrix} = \dot{\lambda} \begin{bmatrix} 1 \\ 0 \end{bmatrix}$	$\dot{\lambda} \begin{bmatrix} \dfrac{\partial g_2}{\partial \sigma_n} \\ \dfrac{\partial g_2}{\partial \sigma_t} \end{bmatrix} = \dot{\lambda} \begin{bmatrix} \tan\psi \\ 1 \end{bmatrix}$

Table C.1: Ingredients of radial return mapping in equation (5.6).

If two active yield surfaces are present, as is the case in the singularity region of the failure surface (at the segue of different yield surface segments), the return mapping algorithm according to section 5.3 has to be adapted. Then, the functions that represent the yield surface are no longer continuously differentiable and, therefore, a unique flow direction

cannot be defined. In this corner or singularity regions two failure surfaces may become active. This complicates the computation of the new stress state along the lines of the return mapping algorithm. The solution of this problem is based on the work of *Koiter* [127] and follows the lines of *de Borst* [57, 58]. The case of two active yield surfaces occurs typically for Mohr-Coulomb (2D & 3D), Tresca (3D) or general multisurface plasticity formulations with combined yield surfaces. According to the article of *Koiter* [127] the plastic relative deformation can be defined as follows

$$\mathbf{u}^p = \dot{\lambda}_1 \frac{\partial g_1}{\partial \boldsymbol{\sigma}} + \dot{\lambda}_2 \frac{\partial g_2}{\partial \boldsymbol{\sigma}} \,. \tag{C.1}$$

At the end of the iteration step both the conditions $f_1(\boldsymbol{\sigma}, \kappa) = 0$ and $f_2(\boldsymbol{\sigma}, \kappa) = 0$ have to be fulfilled yielding

$$\boldsymbol{\sigma} = \boldsymbol{\sigma}^{tr} - \dot{\lambda}_1 \mathbf{K}^{bond} \cdot \frac{\partial g_1}{\partial \boldsymbol{\sigma}} - \dot{\lambda}_2 \mathbf{K}^{bond} \cdot \frac{\partial g_2}{\partial \boldsymbol{\sigma}} \,, \tag{C.2}$$

with

$$
\begin{aligned}
f_1\!\left(\boldsymbol{\sigma}^{tr} - \dot{\lambda}_1 \mathbf{K}^{bond} \cdot \frac{\partial g_1}{\partial \boldsymbol{\sigma}} - \dot{\lambda}_2 \mathbf{K}^{bond} \cdot \frac{\partial g_2}{\partial \boldsymbol{\sigma}}, \kappa\right) &= 0\,, \\
f_2\!\left(\boldsymbol{\sigma}^{tr} - \dot{\lambda}_1 \mathbf{K}^{bond} \cdot \frac{\partial g_1}{\partial \boldsymbol{\sigma}} - \dot{\lambda}_2 \mathbf{K}^{bond} \cdot \frac{\partial g_2}{\partial \boldsymbol{\sigma}}, \kappa\right) &= 0\,.
\end{aligned}
\tag{C.3}
$$

A Taylor expansion around $\boldsymbol{\sigma} = \boldsymbol{\sigma}^{tr}$ and $\kappa = \kappa^0$ results in

$$
\begin{aligned}
f_1(\boldsymbol{\sigma}, \kappa^0) &= \dot{\lambda}_1\left(h_1 + \left[\frac{\partial f_1}{\partial \boldsymbol{\sigma}}\right]\cdot \mathbf{K}^{bond} \cdot \left[\frac{\partial g_1}{\partial \boldsymbol{\sigma}}\right]\right) + \dot{\lambda}_2\left(h_2 + \left[\frac{\partial f_1}{\partial \boldsymbol{\sigma}}\right]\cdot \mathbf{K}^{bond} \cdot \left[\frac{\partial g_2}{\partial \boldsymbol{\sigma}}\right]\right), \\
f_2(\boldsymbol{\sigma}, \kappa^0) &= \dot{\lambda}_1\left(h_3 + \left[\frac{\partial f_2}{\partial \boldsymbol{\sigma}}\right]\cdot \mathbf{K}^{bond} \cdot \left[\frac{\partial g_1}{\partial \boldsymbol{\sigma}}\right]\right) + \dot{\lambda}_2\left(h_4 + \left[\frac{\partial f_2}{\partial \boldsymbol{\sigma}}\right]\cdot \mathbf{K}^{bond} \cdot \left[\frac{\partial g_2}{\partial \boldsymbol{\sigma}}\right]\right),
\end{aligned}
\tag{C.4}
$$

with

$$
\begin{aligned}
h_1 &= \left[\frac{\partial f_1}{\partial \kappa}\right]\left[\frac{\partial \kappa}{\partial \mathbf{u}^p}\right]\cdot \left[\frac{\partial g_1}{\partial \boldsymbol{\sigma}}\right], & h_2 &= \left[\frac{\partial f_1}{\partial \kappa}\right]\left[\frac{\partial \kappa}{\partial \mathbf{u}^p}\right]\cdot \left[\frac{\partial g_2}{\partial \boldsymbol{\sigma}}\right], \\
h_3 &= \left[\frac{\partial f_2}{\partial \kappa}\right]\left[\frac{\partial \kappa}{\partial \mathbf{u}^p}\right]\cdot \left[\frac{\partial g_1}{\partial \boldsymbol{\sigma}}\right], & h_4 &= \left[\frac{\partial f_2}{\partial \kappa}\right]\left[\frac{\partial \kappa}{\partial \mathbf{u}^p}\right]\cdot \left[\frac{\partial g_2}{\partial \boldsymbol{\sigma}}\right].
\end{aligned}
\tag{C.5}
$$

In the Taylor expansion only linear terms are kept and higher order terms are left out. Furthermore, it is assumed that $\dot{\kappa}$ is a linear function of the plastic relative deformations $\mathbf{u}^p$. Insofar, this procedure is only exact for linear softening or hardening material. With the aid of Cramer's rule and the following variables

$$
\begin{aligned}
\mu_1 &= \left(h_1 + \left[\frac{\partial f_1}{\boldsymbol{\sigma}}\right]\cdot \mathbf{K}^{bond} \cdot \left[\frac{\partial g_1}{\partial \boldsymbol{\sigma}}\right]\right), & \mu_2 &= \left(h_2 + \left[\frac{\partial f_1}{\partial \boldsymbol{\sigma}}\right]\cdot \mathbf{K}^{bond} \cdot \left[\frac{\partial g_2}{\partial \boldsymbol{\sigma}}\right]\right), \\
\mu_3 &= \left(h_3 + \left[\frac{\partial f_2}{\partial \boldsymbol{\sigma}}\right]\cdot \mathbf{K}^{bond} \cdot \left[\frac{\partial g_1}{\partial \boldsymbol{\sigma}}\right]\right), & \mu_4 &= \left(h_4 + \left[\frac{\partial f_2}{\partial \boldsymbol{\sigma}}\right]\cdot \mathbf{K}^{bond} \cdot \left[\frac{\partial g_2}{\partial \boldsymbol{\sigma}}\right]\right),
\end{aligned}
\tag{C.6}
$$

the plastic multipliers are obtained

$$\dot{\lambda}_1 = \frac{\mu_4 f_1(\boldsymbol{\sigma}^{tr}, \kappa) - \mu_2 f_2(\boldsymbol{\sigma}^{tr}, \kappa)}{\mu_1 \mu_4 - \mu_2 \mu_3} \,,$$

$$\dot{\lambda}_2 = \frac{\mu_1 f_2(\boldsymbol{\sigma}^{tr}, \kappa) - \mu_3 f_1(\boldsymbol{\sigma}^{tr}, \kappa)}{\mu_1 \mu_4 - \mu_2 \mu_3} \,. \tag{C.7}$$

Since a distinction between plastic normal relative deformations due to tensile softening and plastic normal deformations due to dilatant shear softening is made, two different evolution laws have been introduced, compare equations (5.10) and (5.11) and the graphical representation in figure 5.5. This means that the formalism originating from *de Borst* [57, 58] is slightly accommodated: κ_1 refers to the plastic relative deformations $\dot{\lambda}\frac{\partial g_1}{\partial \boldsymbol{\sigma}}$ and involves yield surface f_1. κ_2 refers to the plastic relative deformations $\dot{\lambda}\frac{\partial g_2}{\partial \boldsymbol{\sigma}}$ and involves yield surface f_2. Equations (C.5) are then rewritten

$$h_1 = \left(\left[\frac{\partial f_1}{\partial \kappa_1} \right] \left[\frac{\partial \kappa_1}{\partial \mathbf{u}^p} \right] \cdot \left[\frac{\partial g_1}{\partial \boldsymbol{\sigma}} \right] \right) , \qquad h_2 = \left(\left[\frac{\partial f_1}{\partial \kappa_2} \right] \left[\frac{\partial \kappa_2}{\partial \mathbf{u}^p} \right] \cdot \left[\frac{\partial g_2}{\partial \boldsymbol{\sigma}} \right] \right) ,$$

$$h_3 = \left(\left[\frac{\partial f_2}{\partial \kappa_1} \right] \left[\frac{\partial \kappa_1}{\partial \mathbf{u}^p} \right] \cdot \left[\frac{\partial g_1}{\partial \boldsymbol{\sigma}} \right] \right) , \qquad h_4 = \left(\left[\frac{\partial f_2}{\partial \kappa_2} \right] \left[\frac{\partial \kappa_2}{\partial \mathbf{u}^p} \right] \cdot \left[\frac{\partial g_2}{\partial \boldsymbol{\sigma}} \right] \right) . \tag{C.8}$$

C.2   Program structure at integration point level

A detailed description of the plasticity procedure at the integration point level is given in tabular format in figure C.1. The corresponding equations can be found in sections 5.2 to 5.4. $\mathbf{l}_{bond}(\xi_k)$ denotes the vector between the integration point and the particle center.

loop over all integration points k of interface

$\longrightarrow$ position vectors of bonded particles $\mathbf{x}_i$, $\mathbf{x}_j$ and, thus, geometry of interface known

incremental relative deformations

$$\Delta u_n(\xi_k) = u_n^{t+1}(\xi_k) - u_n^t(\xi_k) \qquad \Delta u_t(\xi_k) = u_t^{t+1}(\xi_k) - u_t^t(\xi_k)$$

trial spring forces

$$p_n^{tr}(\xi_k) = \frac{1}{n_{ip}}\left[p_n^{old}(\xi_k) + k_n\Delta u_n(\xi_k)\right] \qquad p_t^{tr}(\xi_k) = \frac{1}{n_{ip}}\left[p_t^{old}(\xi_k) + k_t\Delta u_t(\xi_k)\right]$$

trial stresses

$$\sigma_n^{tr}(\xi_k) = \frac{p_n^{tr}(\xi_k)}{h/n_{ip}} \qquad \sigma_t^{tr}(\xi_k) = \frac{p_t^{tr}(\xi_k)}{h/n_{ip}}$$

evaluation of yield condition and check which yield surface is active

$$f_1(\boldsymbol{\sigma}^{tr},\kappa^{old}),\ f_2(\boldsymbol{\sigma}^{tr},\kappa^{old}) \qquad \longrightarrow \qquad f_1 \text{ active, } f_2 \text{ active, } f_1 \ \& \ f_2 \text{ active}$$

bracket terms for return mapping $\rightarrow$ plastic multiplier

$$\left[\frac{\partial f}{\partial \kappa}\right],\ \left[\frac{\partial f}{\partial \boldsymbol{\sigma}}\right],\ \left[\frac{\partial g}{\partial \boldsymbol{\sigma}}\right],\ \left[\frac{\partial \kappa}{\partial \mathbf{u}^p}\right] \qquad \longrightarrow \qquad \dot{\lambda} \text{ via equation (5.6)}$$

corrected stress state

$$\boldsymbol{\sigma} = \boldsymbol{\sigma}^{tr} - \dot{\lambda}\mathbf{K}^{bond}\cdot\left[\frac{\partial g}{\partial \boldsymbol{\sigma}}\right] \quad \longrightarrow \quad \kappa \text{ via evaluation of conditions in equations (5.8)}$$

a–posteriori check if choice of active yield surface was correct

$$f_1(\boldsymbol{\sigma},\kappa),\ f_2(\boldsymbol{\sigma},\kappa) \quad \longrightarrow \quad \text{assumptions } (f_1 \text{ or } f_2 \text{ or } f_1 \ \& \ f_2 \text{ active}) \text{ correct?}$$

corrected spring forces

$$p_n(\xi_k) = \frac{h}{n_{ip}}\sigma_n(\xi_k) \qquad p_t(\xi_k) = \frac{h}{n_{ip}}\sigma_t(\xi_k)$$

save history variables

$$p_n(\xi_k),\ \ p_t(\xi_k),\ \ u_n^{t+1}(\xi_k),\ \ u_t^{t+1}(\xi_k) \ \ \text{and} \ \ \kappa(\xi_k)$$

summation of all k normal and tangential forces and softening parameters of interface

$$\langle\kappa\rangle = \frac{1}{n_{ip}}\sum_{k=1}^{n_{ip}}\kappa(\xi_k),\ \ \tilde{p}_n = \sum_{k=1}^{n_{ip}}p_n(\xi_k),\ \ \tilde{p}_t = \sum_{k=1}^{n_{ip}}p_t(\xi_k) \ \ \text{and} \ \ m_{coh} = \sum_{k=1}^{n_{ip}}\mathbf{f}(\xi_k)\times\mathbf{l}_{bond}(\xi_k)$$

transfer of forces to particle center (in global coordinates)

$$\mathbf{f}^{bond} = [f_x^{bond} \ \ f_y^{bond} \ \ m^{bond}]^T$$

Figure C.1: Interface plasticity law algorithm for one interface with k integration points.

Appendix D

Gyration & balance equations

D.1 Euler's gyration equation

The general form of the balance of angular momentum is represented by

$$\dot{\mathbf{h}}_0 := \frac{\mathrm{d}}{\mathrm{d}t}\mathbf{h}_0 = \mathbf{m}_0\,, \tag{D.1}$$

with the angular momentum $\mathbf{h}_0$ and the moments of the external forces $\mathbf{m}_0$.
$\mathbf{h}_0$ is defined by

$$
\begin{aligned}
\mathbf{h}_0 &= \int_{\mathcal{P}} \mathbf{x} \times \dot{\mathbf{x}}\,\mathrm{d}m = \int_{\mathcal{P}} (\mathbf{x}_M + \bar{\mathbf{x}}) \times (\dot{\mathbf{x}}_M + \dot{\bar{\mathbf{x}}})\,\mathrm{d}m \\
&= \underbrace{\int_{\mathcal{P}} \mathbf{x}_M \times \dot{\mathbf{x}}_M\,\mathrm{d}m}_{\mathbf{x}_M \,\times\, m\dot{\mathbf{x}}_M} + \underbrace{\int_{\mathcal{P}} \bar{\mathbf{x}} \times \dot{\bar{\mathbf{x}}}\,\mathrm{d}m}_{\mathbf{h}_M}\,,
\end{aligned}
\tag{D.2}
$$

where in the case of rigid body dynamics $\mathbf{x}$ is replaced by $\mathbf{x}_M + \bar{\mathbf{x}}$. The mixed terms that appear when evaluating the cross product in equation (D.2) vanish, as $\int_{\mathcal{P}} \rho\bar{\mathbf{x}}\,\mathrm{d}v = 0$ and, analogously, $\int_{\mathcal{P}} \rho\dot{\bar{\mathbf{x}}}\,\mathrm{d}v = 0$ hold. The first term in equation (D.2) denotes the angular momentum of the particle $\mathcal{P}$ with respect to the origin $\mathcal{O}$ and the second term refers to the angular momentum of $\mathcal{P}$ with respect to its center of mass M. Thus, the last term represents a fluctuation term.
The moments of the external forces $\mathbf{m}_0$ are defined by

$$
\begin{aligned}
\mathbf{m}_0 &= \int_{\partial\mathcal{P}} \mathbf{x} \times \mathbf{t}\,\mathrm{d}a + \int_{\mathcal{P}} \mathbf{x} \times \mathbf{b}\,\mathrm{d}m \\
&= \underbrace{\int_{\partial\mathcal{P}} \mathbf{x}_M \times \mathbf{t}\,\mathrm{d}a + \int_{\mathcal{P}} \mathbf{x}_M \times \mathbf{b}\,\mathrm{d}m}_{\mathbf{x}_M \,\times\, \mathbf{k}} + \underbrace{\int_{\partial\mathcal{P}} \bar{\mathbf{x}} \times \mathbf{t}\,\mathrm{d}a + \int_{\mathcal{P}} \bar{\mathbf{x}} \times \mathbf{b}\,\mathrm{d}m}_{\mathbf{m}_M}
\end{aligned}
\tag{D.3}
$$

where again the case of a rigid body with $\mathbf{x} = \mathbf{x}_M + \bar{\mathbf{x}}$ was considered. The first term $\mathbf{x}_M \times \mathbf{k}$ yields the moment of $\mathcal{P}$ with respect to the origin $\mathcal{O}$ and $\mathbf{m}_M$ denotes the moment of the particle $\mathcal{P}$ with respect to its center of mass. Note in passing that the second term of $\mathbf{m}_M$ in equation (D.3) generally vanishes since the center of gravitation and the center of mass coincide, while $\mathbf{b}$ is constant and, thus, independent of $\mathbf{x}$. If $\mathcal{P}$ is assumed as rigid body, i. e. the norms $|\bar{\mathbf{x}}|$ of the position vectors $\bar{\mathbf{x}}$ relative to M are constant, one obtains the corresponding velocities

$$\dot{\bar{\mathbf{x}}} = \boldsymbol{\omega} \times \bar{\mathbf{x}} =: \boldsymbol{\Omega} \cdot \bar{\mathbf{x}}\,. \tag{D.4}$$

$\boldsymbol{\omega}$ represents the rigid body rotation of $\mathcal{P}$ and $\boldsymbol{\Omega}$ denotes the skew-symmetric gyration tensor according to

$$\boldsymbol{\Omega} = - \overset{3}{\mathbf{E}} \cdot \boldsymbol{\omega} = \boldsymbol{\omega} \times \mathbf{I} \quad \longleftrightarrow \quad \boldsymbol{\omega} = \frac{1}{2} \overset{3}{\mathbf{E}} : \boldsymbol{\Omega}^T = -\frac{1}{2} \overset{3}{\mathbf{E}} : \boldsymbol{\Omega} . \tag{D.5}$$

Therein, $\boldsymbol{\omega}$ represents the axial vector of $\boldsymbol{\Omega}$. Insertion of equation (D.5) in equation (D.4), insertion of the corresponding result in $\mathbf{h}_M$ according to equation (D.2) and further reformulation yields

$$\begin{aligned} \mathbf{h}_M &= \int_{\mathcal{P}} \bar{\mathbf{x}} \times (\boldsymbol{\omega} \times \bar{\mathbf{x}}) \, \mathrm{d}m = \int_{\mathcal{P}} [(\bar{\mathbf{x}} \cdot \dot{\mathbf{x}}) \boldsymbol{\omega} - (\bar{\mathbf{x}} \cdot \boldsymbol{\omega}) \bar{\mathbf{x}}] \, \mathrm{d}m \\[2mm] &= \underbrace{\int_{\mathcal{P}} [(\bar{\mathbf{x}} \cdot \bar{\mathbf{x}}) \mathbf{I} - \bar{\mathbf{x}} \otimes \bar{\mathbf{x}}] \, \mathrm{d}m}_{\boldsymbol{\Theta}} \cdot \boldsymbol{\omega} \, , \end{aligned} \tag{D.6}$$

including the positive definite and symmetric mass tensor of inertia $\boldsymbol{\Theta} = \boldsymbol{\Theta}^T$. The scalar coefficients Θ_{ik} of this tensor in the form $\boldsymbol{\Theta} = \Theta_{ik}(\mathbf{e}_i \otimes \mathbf{e}_k)$ represent inertia terms. It is important to note that the basis vectors $\mathbf{e}_i$ and $\mathbf{e}_k$ are not constant with respect to a temporal change, while the coefficients Θ_{ik} are. In equation (D.6) the rigid body rotation $\boldsymbol{\omega}$ can be transferred behind the integral expression as it is constant with respect to $\bar{\mathbf{x}}$. The temporal differentiation with use of equation (D.4) leads to the Green-Naghdi rate

$$\overset{\diamond}{\boldsymbol{\Theta}} = \dot{\Theta}_{ik}(\mathbf{e}_i \otimes \mathbf{e}_k) + \Theta_{ik}(\underbrace{\boldsymbol{\Omega} \cdot \mathbf{e}_i}_{\dot{\mathbf{e}}_i} \otimes \mathbf{e}_k) + \Theta_{ik}(\mathbf{e}_i \otimes \underbrace{\boldsymbol{\Omega} \cdot \mathbf{e}_k}_{\dot{\mathbf{e}}_k}) \, , \tag{D.7}$$

which is taken with respect to a co-rotational frame fixed to the mass center M of $\mathcal{P}$. Since $\mathcal{P}$ was assumed as a rigid body with constant values $|\bar{\mathbf{x}}|$ the Green-Naghdi rate vanishes. Further reformulation provides the tensorial form

$$\overset{\diamond}{\boldsymbol{\Theta}} = \dot{\boldsymbol{\Theta}} - \boldsymbol{\Omega} \cdot \boldsymbol{\Theta} - \boldsymbol{\Theta} \cdot \boldsymbol{\Omega}^T = \mathbf{0} \, , \tag{D.8}$$

and, finally,

$$\dot{\boldsymbol{\Theta}} = \boldsymbol{\Omega} \cdot \boldsymbol{\Theta} + \boldsymbol{\Theta} \cdot \boldsymbol{\Omega}^T = 2\mathrm{sym}(\boldsymbol{\Omega} \cdot \boldsymbol{\Theta}) \, . \tag{D.9}$$

For example, if one considers spherical particles, the above consideration simplifies, as $\boldsymbol{\Theta} = \Theta_{ik}\mathbf{I}$, which yields

$$\dot{\boldsymbol{\Theta}} = 2\mathrm{sym}(\boldsymbol{\Omega} \cdot \Theta_{ik}\mathbf{I}) = 2\Theta_{ik}\mathrm{sym}(\boldsymbol{\Omega}) \, . \tag{D.10}$$

As the gyration tensor is skew-symmetric $\boldsymbol{\Omega} = -\boldsymbol{\Omega}^T$ the temporal derivative of the mass tensor of inertia vanishes, $\dot{\boldsymbol{\Theta}} = \mathbf{0}$.

Thus, the balance of angular momentum with respect to M takes the form

$$\dot{\mathbf{h}}_M = \mathbf{m}_M \quad \longleftrightarrow \quad (\boldsymbol{\Theta} \cdot \boldsymbol{\omega})\dot{} = \mathbf{m}_M \, , \tag{D.11}$$

where

$$(\boldsymbol{\Theta} \cdot \boldsymbol{\omega})\dot{} = \dot{\boldsymbol{\Theta}} \cdot \boldsymbol{\omega} + \boldsymbol{\Theta} \cdot \dot{\boldsymbol{\omega}} \, . \tag{D.12}$$

The combined insertion of equations (D.2) to (D.9) and (D.11) to (D.12) in equation (D.1) yields

$$\frac{\mathrm{d}}{\mathrm{d}t}\left(\int_{\mathcal{P}}[\mathbf{x}_M \times \dot{\mathbf{x}}_M + \boldsymbol{\Theta} \cdot \boldsymbol{\omega}]\,\mathrm{d}m\right) = \int_{\partial\mathcal{P}}[\mathbf{x}_M \times \mathbf{t} + \bar{\mathbf{m}}]\,\mathrm{d}a + \rho\int_{\mathcal{P}}[\mathbf{x}_M \times \mathbf{b} + \bar{\mathbf{x}} \times \mathbf{b}]\,\mathrm{d}v,$$

(D.13)

with $\bar{\mathbf{m}} = \bar{\mathbf{x}} \times \mathbf{t}$. Realization of the temporal differentiation, introduction of equations (D.9) and (D.12) on the left hand side and application of the Cauchy theorem on the right hand side leads to

$$\int_{\mathcal{P}}\mathbf{x}_M \times \rho\ddot{\mathbf{x}}_M + \boldsymbol{\Theta} \cdot \dot{\boldsymbol{\omega}} + 2\mathrm{sym}(\boldsymbol{\Omega} \cdot \boldsymbol{\Theta}) \cdot \boldsymbol{\omega}\,\mathrm{d}m = \int_{\mathcal{P}}\mathrm{div}\,(\mathbf{x}_M \times \mathbf{T}) + \mathrm{div}\,\bar{\mathbf{M}} + \rho(\mathbf{x}_M \times \mathbf{b} + \bar{\mathbf{x}} \times \mathbf{b})\,\mathrm{d}v.$$

(D.14)

Localization of equation (D.14) under consideration of the mass integration on the left hand side and using the identity $\mathrm{div}\,(\mathbf{x}_M \times \mathbf{T}) = \mathbf{x}_M \times \mathrm{div}\,\mathbf{T} + \mathbf{I} \times \mathbf{T}$ yields

$$\underbrace{\mathbf{x}_M \times \rho\ddot{\mathbf{x}}_M}_{\text{ⓑ}} + \underbrace{\rho\boldsymbol{\Theta} \cdot \dot{\boldsymbol{\omega}}}_{\text{ⓒ}} + \underbrace{2\rho\mathrm{sym}(\boldsymbol{\Omega} \cdot \boldsymbol{\Theta}) \cdot \boldsymbol{\omega}}_{\text{ⓒ}} = \underbrace{\mathbf{x}_M \times \mathrm{div}\,\mathbf{T}}_{\text{ⓑ}} + \underbrace{\mathbf{I} \times \mathbf{T}}_{\text{ⓐ}} + \underbrace{\mathrm{div}\,\bar{\mathbf{M}}}_{\text{ⓒ}} + \underbrace{\rho\mathbf{x}_M \times \mathbf{b}}_{\text{ⓑ}} + \underbrace{\rho\bar{\mathbf{x}} \times \mathbf{b}}_{\text{ⓒ}}.$$

(D.15)

Therein, ⓐ refers to terms contained in the standard Boltzmann theory and ⓑ refers to terms that vanish, if the local balance of momentum $\mathbf{x}_M \times (\mathrm{div}\,\mathbf{T} + \rho\mathbf{b} - \rho\ddot{\mathbf{x}}_M) = \mathbf{0}$ is valid. Finally, ⓒ refers to terms that are related to the micropolar theory. Note in passing that with decreasing $\bar{\mathbf{x}} \to 0$ the terms ⓒ in equation (D.15) would disappear and one ends up with the standard Boltzmann theory. Insertion of the local balance of momentum (see above) produces

$$\rho\boldsymbol{\Theta} \cdot \dot{\boldsymbol{\omega}} + 2\rho\mathrm{sym}(\boldsymbol{\Omega} \cdot \boldsymbol{\Theta}) \cdot \boldsymbol{\omega} = \mathbf{I} \times \mathbf{T} + \mathrm{div}\,\bar{\mathbf{M}} + \rho\bar{\mathbf{x}} \times \mathbf{b}, \tag{D.16}$$

which turns out to be the angular momentum balance of the Cosserat theory and Euler's gyration equation in the context of rigid body mechanics, respectively. Please keep in mind that the geometry of the particles (shape and dimension) is only contained in the mass moment of inertia $\boldsymbol{\Theta}$. The transition from a particle consideration to a material point implies a vanishing influence of the particle size, as $|\bar{\mathbf{x}}| \ll d$. With it, the mass tensor of inertia $\boldsymbol{\Theta}$ vanishes and the axiomatic character of equation (D.14) is lost.

D.2 Simplification of balance equations

As the volume of the particles decreases with order $\mathcal{O}(\varepsilon^3)$, while the corresponding surface decreases only with order $\mathcal{O}(\varepsilon^2)$, volume terms in the corresponding balance equations in sections 8.2.2 and 8.2.3 have been neglected. In order to show the effects of the scale separation line, area and volume elements can be defined by use of the order symbol ε as

$$\begin{aligned}\mathrm{d}x_i &= \varepsilon\,\mathrm{d}x_i = f(\varepsilon),\\ \mathrm{d}a_i &= \varepsilon\,\mathrm{d}x_j \times \varepsilon\,\mathrm{d}x_k = \varepsilon^2\mathrm{d}x_j \times \mathrm{d}x_k = \varepsilon^2\mathrm{d}a_i = f(\varepsilon^2),\\ \mathrm{d}v &= \varepsilon^2\,(\mathrm{d}x_1 \times \mathrm{d}x_2) \cdot \varepsilon\,\mathrm{d}x_3 = \varepsilon^3\mathrm{d}v = f(\varepsilon^3).\end{aligned} \tag{D.17}$$

Thereby the order symbol ε is introduced to display the scale difference in a formal manner. For example, upon insertion of the area and volume elements according to equations (D.17) in the balance of momentum on the RVE level $\mathcal{R}$ one obtains

$$
\begin{aligned}
\varepsilon^3 \int_{\mathcal{R}} \rho \mathbf{x} \, \mathrm{d}v &= \varepsilon^2 \int_{\partial \mathcal{R}} \mathbf{t} \, \mathrm{d}a + \varepsilon^3 \int_{\mathcal{R}} \rho \mathbf{b} \, \mathrm{d}v, \\
\varepsilon \int_{\mathcal{R}} \rho \mathbf{x} \, \mathrm{d}v &= \int_{\partial \mathcal{R}} \mathbf{t} \, \mathrm{d}a + \varepsilon \int_{\mathcal{R}} \rho \mathbf{b} \, \mathrm{d}v.
\end{aligned}
\tag{D.18}
$$

Application of the scale transition $\varepsilon \to 0$ along with $f(\varepsilon^n) \ll f(\varepsilon^n - 1)$ yields a simplified form of the balance of momentum

$$
\mathbf{0} = \int_{\partial \mathcal{R}} \mathbf{t} \, \mathrm{d}\mathbf{a}.
\tag{D.19}
$$

However, the above assumptions are valid only for the limiting case of small particles embedded in a large particle ensemble, where a scale separation $\varepsilon \to 0$ according to section 2.3.1 is obtained. Please bear in mind that the simplified forms of the balance equations are solely utilized for the post processing homogenization procedure. The validity of the scale separation assumptions is checked within the example in section 8.5.1.

Appendix E

Transition to "analytical" homogenization approaches

The inclusion of gradients in the context of particle mechanics and corresponding homogenization of particle composites is not new. Various authors introduced higher order gradients for a kind of "analytical" homogenization approach.

If a derivation of macroscopic moduli of a granular sample in terms of particle contact stiffnesses is asked for, a "analytical" homogenization along the lines of *Chang and co-workers* [34, 35, 36], compare also *Kuhl et al.* [138], is carried out. However, these procedures are only available for the case of very simple particle shapes. If the stress or strain state of a specific sample ought to be described based on arbitrary contact forces and particle shapes, a "numerical" homogenization over finite sized subassemblies or RVEs is considered. In both cases the starting point of the derivation, namely the general balance equations, are the same. In the context of a "analytical" homogenization constitutive equations on the macro scale, like a generalized Hooke's law, can be derived based on the kinematic and contact description of a particle sample. A parameter identification leads to clear definitions of the macroscopic moduli in terms of the particle contact stiffnesses, like the Lamé parameters, and in terms of the geometric ingredients, like the particle radius. Furthermore, material parameters (e. g. as the internal length scale) included in enhanced continuum theories like integral-, gradient- or micropolar-type approaches can be formally identified, compare among others the articles by *Chang* [34] and *Chang & Gao* [35, 36]. Therein, a stress and strain calculation is only done in an analytical format in order to obtain closed form solutions for the constitutive tensor. This is in contrast to the procedures applied in this thesis where the formulations are utilized rather for a numerical calculation of stresses and strains than for the stiffness of a sample. Thereby, the "numerical" homogenization as proposed herein is used to constitute higher order theories for example by detection of higher order stresses like the couple stresses in chapter 8.

Different restrictions and simplifications are inherent in the "analytical" homogenization approaches: First of all, explicit descriptions of the macroscopic moduli in terms of the microscopic (particle) ones are only available for equally sized circular or spherical particles. Furthermore, in order to identify higher order gradients or rotations and their energetically conjugate force measures a refined kinematic description through a Taylor series at the particle contact has to be introduced. Unfortunately, a thorough physical basis for this enhanced contact description (on the particle level) is missing. Basically, ideas used to extend continuum theories are adopted on a lower scale in a similar fashion. An example is the regularization in FEM models where the inclusion of displacement gradients in gradient models regularizes the solution, i. e. mesh-insensitive results are obtained. *Chang* transferred this idea straightforward to particle models, although one usually assumes that the inclusion of gradients within macroscopic models should reflect

effects on the microstructure, e. g. of a particle structure. Due to the author's general understanding gradients on a higher scale should be the outcome of a homogenization process applied on a higher scale rather than being the result of an implementation of such an enhancement directly on the smaller scale. Hence, this point constitutes the object of chapter 9 where a gradient formulation is motivated by means of an enhancement of the kinematic description of a RVE and a corresponding numerical evidence of the gradient terms.

In spite of the different matters of opinion the "analytical" and "numerical" approaches show interesting similarities that are examined for consistency reasons now. The articles by *Chang & Gao* [35, 36] include a similar Taylor series approach, as presented in section 9.2.1. Indeed, instead of enhancing the kinematic description of a RVE (as done in the present thesis), they enhance the kinematics of each single particle contact. Equation (9.2) displays the actual position vector of a particle $\mathcal{N}$ within a RVE dependent on the position vector of the base particle $\mathcal{M}$ by use of the initial distance vector $\mathbf{\Delta x}_0$. The definition of the displacement vector is constituted as follows

$$\mathbf{u}^{\mathcal{N}} = \mathbf{x}_t^{\mathcal{N}} - \mathbf{x}_0^{\mathcal{N}} = \left(\mathbf{x}_t^{\mathcal{M}} + \mathbf{\Delta x}_t\right) - \left(\mathbf{x}_0^{\mathcal{M}} + \mathbf{\Delta x}_0\right) = \underbrace{\mathbf{x}_t^{\mathcal{M}} - \mathbf{x}_0^{\mathcal{M}}}_{\mathbf{u}^{\mathcal{M}}} + \underbrace{\mathbf{\Delta x}_t - \mathbf{\Delta x}_0}_{\mathbf{\Delta u}} . \qquad \text{(E.1)}$$

In contrast to that, *Chang* in various of his articles starting from the one by *Chang & Ma* [37] used a Taylor series for the displacement of two neighboring particles instead of a Taylor expansion with respect to the position vectors:

$$\begin{aligned}
\mathbf{u}^{\mathcal{N}} &= \frac{1}{0!}\mathbf{u}^{\mathcal{M}} + \frac{1}{1!}\frac{\partial \mathbf{u}_t^{\mathcal{M}}}{\partial \left(\mathbf{x}_0^{\mathcal{M}}\right)} \cdot \mathbf{\Delta x}_0 + \frac{1}{2!}\frac{\partial^2 \mathbf{u}_t^{\mathcal{M}}}{\partial \left(\mathbf{x}_0^{\mathcal{M}}\right)^2}:\mathbf{\Delta x}_0 \otimes \mathbf{\Delta x}_0 + \\
&\quad \frac{1}{3!}\frac{\partial^3 \mathbf{u}_t^{\mathcal{M}}}{\partial \left(\mathbf{x}_0^{\mathcal{M}}\right)^3}\vdots\mathbf{\Delta x}_0 \otimes \mathbf{\Delta x}_0 \otimes \mathbf{\Delta x}_0 + \tilde{\mathbf{w}} , \\
&= \mathbf{u}^{\mathcal{M}} + \mathbf{\Delta u}. \qquad\qquad\qquad\qquad\qquad\qquad\qquad\qquad \text{(E.2)}
\end{aligned}$$

Generally, the following transformations

$$\frac{\partial \mathbf{u}}{\partial \mathbf{X}} = \frac{\partial \mathbf{x} - \partial \mathbf{X}}{\partial \mathbf{X}} = \frac{\partial \mathbf{x}}{\partial \mathbf{X}} - \mathbf{I} \qquad \rightarrow \qquad \frac{\partial^2 \mathbf{u}}{\partial \mathbf{X}^2} = \frac{\partial^2 \mathbf{x}}{\partial \mathbf{X}^2} - \frac{\partial \mathbf{I}}{\partial \mathbf{X}} = \frac{\partial^2 \mathbf{x}}{\partial \mathbf{X}^2} \qquad \text{(E.3)}$$

and an analogous transformation for the corresponding third order term in equation (E.2) are valid. With the aid of these transformations and the identities $\mathbf{X} = \mathbf{x}_0^{\mathcal{M}}$ and $\mathbf{x} = \mathbf{x}_t^{\mathcal{M}}$, the quadratic and cubic terms in equation (E.2) are identified as the average displacement gradients $\mathbf{G}$ and $\mathbf{K}$, introduced in equation (9.2). A subtraction of equation (E.1) (with use of $\mathbf{\Delta x}_t$ from equation (9.2)) from equation (E.2) (with use of the transformations according to equations (E.3)) yields

$$\left[\mathbf{F} \cdot \mathbf{\Delta x}_0 - \mathbf{I} \cdot \mathbf{\Delta x}_0\right] = \left[\frac{\partial \mathbf{u}_t^{\mathcal{M}}}{\partial \left(\mathbf{x}_0^{\mathcal{M}}\right)} \cdot \mathbf{\Delta x}_0\right] \qquad \rightarrow \qquad [\mathbf{F} - \mathbf{I}] = \underbrace{\left[\frac{\partial \mathbf{u}_t^{\mathcal{M}}}{\partial \left(\mathbf{x}_0^{\mathcal{M}}\right)}\right]}_{\mathbf{H}} . \qquad \text{(E.4)}$$

According to the definition of the material deformation gradient in equation (2.1) the left hand side of equation (E.4) defines exactly the material displacement gradient. Hence, equations (E.1) and (E.2) are identical. This constitutes the identity of the different derivations: one based on the material deformation gradient and the other one based on the material displacement gradient.

References

[1] **Aifantis, E. C.** (**1978**): 'A proposal for continuum with microstructure', *Mech. Res. Comm.*, Vol. 5, pp. 139–145.

[2] **Aifantis, E. C.** (**1984**): 'On the microstructural origin of certain inelastic modes', *J. Engng. Mat. Tech.*, Vol. 106, pp. 326–330.

[3] **Aifantis, E. C.** (**2003**): 'Update on a class of gradient theories', *Mech. Mat.*, Vol. 35, pp. 259–280.

[4] **Alder, B. J., Wainwright, T. E.** (**1959**): 'Studies in molecular dynamics. I: General method', *J. Chem. Phys.*, Vol. 31, pp. 459–466.

[5] **Allen, M. P., Tildesley, D. J.** (**1987**): *Computer Simulation of Liquids*, Oxford University Press, Oxford, England, UK.

[6] **Anderson, E., Bai, Z., Bischof, C., Blackford, S., Demmel, J., Dongarra, J., Du Croz, J., Greenbaum, A., Hammarling, S., McKenney, A., Sorensen, D.** (**1999**): *LAPACK Users' Guide, Third Edition*, Society for Industrial and Applied Mathematics, Philadelphia, PA, USA.

[7] **Aström, J. A., Herrmann, H. J., Timonen, J.** (**2000**): 'Granular packings and fault zones', *Phys. Rev. Lett.*, Vol. 84, pp. 638–641.

[8] **Bagi, K.** (**1996**): 'Stress and strain in granular assemblies', *Mech. Mat.*, Vol. 22, pp. 165–177.

[9] **Bagi, K., Bojtar, I.** (**2001**): 'Different microstructural strain tensors for granular assemblies', in: **Bicanic, N.** (ed.), *Proc. of ICADD-4 - 4th Int. Conf. on Analysis of Discontinuous Deformation, Glasgow, Scotland, UK*, University of Glasgow Press, pp. 261–270.

[10] **Bardet, J. P., Proubet, J.** (**1991**): 'Adaptive dynamic relaxation for statics of granular materials', *Comp. & Struct.*, Vol. 39, pp. 221–229.

[11] **Bardet, J. P., Vardoulakis, I.** (**2001**): 'The asymmetry of stress in granular media', *Int. J. Solids & Structures*, Vol. 38, pp. 353–367.

[12] **Barr** (**1981**): 'Superquadrics and angle-preserving transformations', *IEEE Comp. Graph. Appl.*, Vol. 1, pp. 11–23.

[13] **Bathe, K. J.** (**1996**): *Finite Element Procedures*, Prentice-Hall, Inc., Englewood Cliffs, NJ, USA.

[14] **Bažant, Z. P., Christensen, M.** (**1972**): 'Analogy between micropolar continuum and grid frameworks under initial stress', *Int. J. Solids & Structures*, Vol. 8, pp. 327–346.

[15] **Bažant, Z. P., Jirásek, M.** (**2002**): 'Nonlocal integral formulations of plasticity and damage: Survey of progress', *J. Engng. Mech.*, Vol. 128, pp. 1119–1149.

[16] **Bažant, Z. P., Oh, B. H.** (**1985**): 'Microplane model for progressive fracture of concrete and rock', *J. Engng. Mech.*, Vol. 111, pp. 559–582.

[17] **Bažant, Z. P., Planas, J.** (**1997**): *Fracture and Size Effect in Concrete and Other Quasibrittle Materials*, CRC Press, Boca Raton, FL, USA.

[18] **Bažant, Z. P., Tabbara, M., Kazemi, M. T., Pijaudier-Cabot, G.** (**1990**): 'Random particle model for fracture of aggregate or fibre composites', *J. Engng. Mech.*, Vol. 116, pp. 1686–1705.

[19] **Bear, J., Bachmat, Y.** (**1991**): *Introduction to Modeling of Transport Phenomena in Porous Media*, Kluwer Academic Publishers, Dordrecht, The Netherlands.

[20] **Belytschko, T., Krongauz, Y., Organ, D., Fleming, M., Krysl, P.** (**1996**): 'Meshless methods: An overview and recent developments', *Comp. Meth. Appl. Mech. Engng.*, Vol. 139, pp. 3–47.

[21] **Beranek, W. J., Hobbelmann, G. J.** (**1994**): 'Constitutive modelling of structural concrete as an assemblage of spheres', in: **de Borst, R., Bicanic, N., Mang, H.** (eds.), *Computational Modelling of Concrete Structures - Proc. of EURO-C, Innsbruck, Austria*, Pinedrige Press, Swansea, pp. 37–51.

[22] **Bicanic, N.** (ed.) (**2001**): *Proc. of ICADD-4 - 4th Int. Conf. on Analysis of Discontinuous Deformation, Glasgow, Scotland, UK*, University of Glasgow Press.

[23] **Bogdanova-Bontcheva, N., Lippmann, H.** (**1975**): 'Rotationssymmetrisches ebenes Flie"sen eines granularen Modellmaterials', *Acta Mechanica*, Vol. 21, pp. 93–113.

[24] **Brara, A., Camborde, F., Klepaczko, J. R., Mariotti, C.** (**1999**): 'Experimental and numerical study of concrete at high strain rates in tension', *Mech. Mat.*, Vol. 33, pp. 33–45.

[25] **Brendel, L., Dippel, S.** (**1998**): 'Lasting contacts in molecular dynamics simulations', in: **Herrmann, H. J., Hovi, J.-P., Luding, S.** (eds.), *Physics of Dry Granular Materials*, NATO-ASI Series E: Applied Science - Vol. 350, Kluwer Academic Publishers, Dordrecht, The Netherlands, pp. 313–318.

[26] **Brzoska, S.** (**2002**): *Numerik und Simulation von Mauerwerk mit einem diskreten Modellierungsansatz - Anwendung auf praxisbezogene Beispiele*. Diplomarbeit, Institut für Baustatik, Universität Stuttgart, Germany.

[27] **Burt, N. J., Dougill, W.** (**1977**): 'Progressive failure in a model heterogeneous medium', *J. Engng. Mech.*, Vol. 103, pp. 365–376.

[28] **Camacho, G. T., Ortiz, M.** (**1996**): 'Computational modelling of impact damage in brittle materials', *Int. J. Solids & Structures*, Vol. 33, pp. 2899–2938.

[29] **Cambou, B., Dubujet, F., Emeriault, F., Sidoroff, F.** (**1995**): 'Homogenization for granular materials', *Eur. J. Mech. A/Solids*, Vol. 14, pp. 255–276.

[30] **Carol, I., Lopez, C. M., Roa, O.** (**2001**): 'Micromechanical analysis of quasi-brittle materials using fracture-based interface elements', *Int. J. Num. Meth. Engng.*, Vol. 52, pp. 193–215.

[31] **Carol, I., Prat, P. C., Lopez, C. M.** (**1997**): 'Normal/shear cracking model: Application to discrete crack analysis', *J. Engng. Mech.*, Vol. 123, pp. 765–773.

[32] **Castro-Montero, A., Jia, Z., Shah, S. P.** (**1995**): 'Evaluation of damage in Brazilian test using holographic interferometry', *ACI Mat. J.*, Vol. 92, pp. 268–275.

[33] **Chambon, R., Caillerie, D., Matsushima, T.** (**2001**): 'Plastic continuum with microstructure, local second gradient theories for geomaterials: Localization studies', *Int. J. Solids & Structures*, Vol. 38, pp. 8503–8527.

[34] **Chang, C. S.** (**1998**): 'Modeling of granular materials with intrinsic length', *J. Phys. IV France*, pp. Pr8–71–Pr8–78.

[35] **Chang, C. S., Gao, J.** (**1995**): 'Second-gradient constitutive theory for granular material with random packing structure', *Int. J. Solids & Structures*, Vol. 32, pp. 2279–2293.

[36] **Chang, C. S., Gao, J.** (**1996**): 'Kinematic and static hypotheses for constitutive modelling of granulates considering particle rotation', *Acta Mechanica*, Vol. 115, pp. 213–229.

[37] **Chang, C. S., Ma, L.** (**1991**): 'A micromechanical-based micropolar theory for deformation of granular solids', *Int. J. Solids & Structures*, Vol. 28, pp. 67–86.

[38] **Chang, C. S., Misra, A.** (**1990**): 'Application of uniform strain theory to heterogeneous granular solids', *J. Engng. Mech.*, Vol. 116, pp. 2310–2328.

[39] **Christoffersen, J., Mehrabadi, M. M., Nemat-Nasser, S.** (**1981**): 'A micromechanical description of granular material behaviour', *J. Appl. Mech.*, Vol. 48, pp. 339–344.

[40] **Ciarlet, P. G.** (**1988**): *Mathematical Elasticity - Volume I: Three-dimensional Elasticity*, North Holland, Amsterdam, The Netherlands.

[41] **Cleary, P.** (**2000**): 'DEM simulation of industrial particle flows: Case studies of dragline excavators, mixing in tumblers and centrifugal mills', *Powd. Tech.*, Vol. 109, pp. 83–104.

[42] **Cleary, P.** (**2001**): 'Modelling comminution devices using DEM', *Int. J. Num. Anal. Meth. Geomech.*, Vol. 25, pp. 83–105.

[43] **Cosserat, E., Cosserat, F.** (**1909**): *Théorie des corps déformable*, A. Hermann et Fils, Paris, France.

[44] **Cowin, S. C.** (**1985**): 'The relationship between the elasticity tensor and the fabric tensor', *Mech. Mat.*, Vol. 4, pp. 137–147.

[45] **Cundall, P. A.** (**1971**): 'A computer model for simulating progressive, large-scale movements in blocky rock systems', in: *Proc. of the Int. Symp. of Rock Fracture, Nancy, France*, paper no. II.8.

[46] **Cundall, P. A.** (**2001**): 'A discontinuous future for numerical modelling in geomechanics', *Geotech. Engng.*, Vol. 149, pp. 41–47.

[47] **Cundall, P. A., Drescher, A., Strack, O. D. L.** (**1982**): 'Numerical experiments on granular assemblies; Measurements and observations', in: **Vermeer, P. A., Luger, H. J.** (eds.), *Deformation and Failure of Granular Materials - Proc. of IUTAM Conf. on Deformation and Failure of Granular Materials*, A. A. Balkema, Rotterdam, The Netherlands, pp. 355–370.

[48] **Cundall, P. A., Hart, R. D.** (**1992**): 'Numerical modelling of discontinua', *Engng. Comp.*, Vol. 9, pp. 101–113.

[49] **Cundall, P. A., Strack, O. D. L.** (**1979**): 'A discrete numerical model for granular assemblages', *Géotechnique*, Vol. 29, pp. 47–65.

[50] **D'Addetta, G. A., Kuhl, E., Kun, F., Ramm, E.** (**1999**): 'Micromechanical modelling of "concrete" cracking', in: **Wunderlich, W.** (ed.), *Solids, Structures and coupled Problems - Proc. of the Eur. Conf. on Computational Mechanics, Munich, Germany*, cd-rom.

[51] **D'Addetta, G. A., Kun, F., Herrmann, H. J., Ramm, E.** (**2001**): 'From solids to granulates - discrete element simulations of fracture and fragmentation processes in geomaterials', in: **Vermeer, P. A., Diebels, S., Ehlers, W., Herrmann, H. J., Luding, S., Ramm, E.** (eds.), *Continuous and Discontinuous Modelling of Cohesive Frictional Materials, Lecture Notes in Physics 586*, Springer-Verlag, Berlin, Germany, pp. 231–258.

[52] **D'Addetta, G. A., Kun, F., Ramm, E.** (**2002**): 'On the application of a discrete model to the fracture process of cohesive granular materials', *Granular Matter*, Vol. 4, pp. 77–90.

[53] **D'Addetta, G. A., Ramm, E., Diebels, S., Ehlers, W.** (**2002**): 'Homogenization for particle assemblies.', in: **Cook, B. K., Jensen, R. P.** (eds.), *Discrete Element Methods - Numerical Modeling of Discontinua - Proc. 3rd Int. Conf. on DEM, Santa Fe, NM, USA, Geotechnical Special Publication No. 117*, ASCE, Reston, VI, USA, pp. 259–264.

[54] **D'Addetta, G. A., Ramm, E., Diebels, S., Ehlers, W.** (**2004**): 'A particle center based homogenization strategy for particle assemblies', *Engng. Comp.*, Vol. 21, pp. 360–383.

[55] **D'Addetta, G. A., Ramm, E., Kun, F.** (**2001**): 'Fracture simulation of cohesive frictional materials by discrete element models', in: **Bicanic, N.** (ed.), *Proc. of ICADD-4 - 4th Int. Conf. on Analysis of Discontinuous Deformation, Glasgow, Scotland, UK*, University of Glasgow Press, pp. 135–157.

[56] **Dantu, P.** (**1957**): 'Contribution à l'étude mécanique et géometrique des milieux pulvérulents', in: **Glanville, W. H.** (ed.), *Proc. of the 4th Int. Conf. on Soil Mechanics and Foundation Engineering*, London, England, UK, pp. 144–148.

[57] **de Borst, R.** (**1986**): *Nonlinear analysis of frictional materials*, Ph.D. Thesis, Technische Universiteit Delft, The Netherlands.

[58] **de Borst, R.** (**1987**): 'Integration of plasticity equations for singular yield functions', *Comp. & Struct.*, Vol. 26, pp. 823–829.

[59] **de Borst, R., Mühlhaus, H.-B.** (**1992**): 'Gradient-dependent plasticity: Formulation and algorithmic aspects', *Int. J. Num. Meth. Engng.*, Vol. 35, pp. 521–539.

[60] **de Borst, R., Pankay, Bicanic, N.** (**1991**): 'A note on singularity indicators for Mohr-Coulomb type yield criteria', *Comp. & Struct.*, Vol. 39, pp. 219–220.

[61] **Delaplace, A., Pijaudier-Cabot, G., Roux, S.** (**1996**): 'Progressive damage in discrete models and consequences on continuum modelling', *J. Mech. Phys. Solids*, Vol. 44, pp. 99–136.

[62] **Desrues, J., Chambon, R., Mokni, M., Mazerolle, F.** (**1996**): 'Void ratio evolution inside shear bands in triaxial sand specimens studied by computed tomography', *Géotechnique*, Vol. 46, pp. 529–546.

[63] **Diebels, S.** (**2000**): *Mikropolare Zweiphasenmodelle: Formulierung auf der Basis der Theorie Poröser Medien*, Habilitationsschrift, Bericht Nr. II-4, Instut für Mechanik, LS II, Universität Stuttgart, Germany.

[64] **Diebels, S.** (**2002**): *Partikelmethoden & Mikromechanik*, Vorlesungsmanuskript, Institut für Mechanik, LS II, Universität Stuttgart, Germany.

[65] **Diebels, S., Ehlers, W.** (**2001**): 'Homogenization method for granular assemblies', in: **Wall, W. A., Bletzinger, K.-U., Schweizerhof, K.** (eds.), *Trends in Computational Mechanics, Lochau, Austria*, CIMNE, Barcelona, Spain, pp. 79–88.

[66] **Diebels, S., Steeb, H.** (**2002**): 'The size effect in foams and its theoretical and numerical investigation', *Proc. Roy. Soc. Lond. A*, Vol. 458, pp. 2869–2883.

[67] **Diebels, S., Steeb, H.** (**2003**): 'Stress and couple stress in foams', *Comp. Mat. Sci.*, Vol. 28, pp. 714–722.

[68] **Diekkämper, R.** (**1985**): 'Structural analysis of degenerating framework models for the numerical simulation of material behaviour', in: **Pande, G. N.** (ed.), *Proc. of Int. Conf. on Numerical Methods in Engineering, Theory and Application - NUMETA*, Swansea, Wales, UK, pp. 417–427.

[69] **Dietsche, A.** (**1993**): *Lokale Effekte in linear-elastischen und elasto-plastischen Cosserat-Kontinua*, Ph.D. Thesis, Instut für Mechanik, Universität Karlsruhe, Germany.

[70] **Dippel, S.** (**1998**): *Microscopic dynamics of granular materials*, Ph.D. Thesis, Bericht Nr. 3510, Forschungszentrum Jülich, Höchstleistungszentrum Jülich, Germany.

[71] **Dobry, R., Ng, T. T.** (**1992**): 'Discrete modelling of stress-strain behaviour of granular media at small and large strains', *Engng. Comp.*, Vol. 9, pp. 129–143.

[72] **Donzé, F. V., Magnier, S.-A.** (**1995**): 'Formulation of a 3-D numerical model of brittle behaviour', *Geophys. J. Int.*, Vol. 122, pp. 790–802.

[73] **Donzé, F. V., Magnier, S.-A., Daudeville, L., Mariotti, C., Davenne, L.** (**1999**): 'Numerical study of compressive behavior of concrete at high strain rates', *J. Engng. Mech.*, Vol. 125, pp. 1154–1163.

[74] **Drescher, A., De Josseling De Jong, G.** (**1972**): 'Photoelastic verification of a mechanical model for the flow of a granular material', *J. Mech. Phys. Solids*, Vol. 20, pp. 337–351.

[75] **Drugan, W. J., Willis, J. R.** (**1996**): 'A micromechanics-based nonlocal constitutive equation and estimates of representative volume element size for elastic composites', *J. Mech. Phys. Solids*, Vol. 44, pp. 497–524.

[76] **Ehlers, W., Diebels, S., Michelitsch, T.** (**2001**): 'Microscopic modelling of granular materials taking into account particle rotations', in: **Vermeer, P. A., Diebels, S., Ehlers, W., Herrmann, H. J., Luding, S., Ramm, E.** (eds.), *Continuous and Discontinuous Modelling of Cohesive Frictional Materials, Lecture Notes in Physics 586*, Springer-Verlag, Berlin, Germany, pp. 259–274.

[77] **Ehlers, W., Ramm, E., Diebels, S., D'Addetta, G. A.** (**2003**): 'From particle ensembles to Cosserat continua: Homogenization of contact forces towards stresses and couple stresses', *Int. J. Solids & Structures*, Vol. 40, pp. 6681–6702.

[78] **Ehlers, W., Volk, W.** (**1998**): 'On theoretical and numerical methods in the theory of porous media based on polar and non-polar elasto-plastic solid materials', *Int. J. Solids & Structures*, Vol. 35, pp. 4597–4616.

[79] **Eringen, A. C.** (**1968**): 'Mechanics of micromorphic continua', in: **Kröner, E.** (ed.), *Mechanics of Generalized Continua, Proc. of the IUTAM Symp., Freudenstadt/Stuttgart, Germany, 1967*, Springer-Verlag, Berlin, Germany, pp. 18–35.

[80] **Eringen, A. C.** (**1981**): 'On nonlocal plasticity', *Int. J. Engng. Sci.*, Vol. 19, pp. 1461–1474.

[81] **Eringen, A. C., Edelen, D. G. B.** (**1972**): 'On nonlocal elasticity', *Int. J. Engng. Sci.*, Vol. 10, pp. 233–248.

[82] **Evans, R. H., Marathe, H. S.** (**1968**): 'Microcracking and stress-strain curves for concrete in tension', *Materiaux et constructions*, Vol. 1, pp. 61–65.

[83] **Feng, Y. T., Han, K., Owen, D. R. J.** (**2002**): 'An advancing front packing of polygons, ellipses and spheres', in: **Cook, B. K., Jensen, R. P.** (eds.), *Discrete Element Methods - Numerical Modeling of Discontinua - Proc. 3rd Int. Conf. on DEM, Santa Fe, NM, USA, Geotechnical Special Publication No. 117*, ASCE, Reston, VI, USA, pp. 93–98.

[84] **Feng, Y. T., Owen, D. R. J.** (**2002**): 'An energy based corner to contact algorithm', in: **Cook, B. K., Jensen, R. P.** (eds.), *Discrete Element Methods - Numerical Modeling of Discontinua - Proc. 3rd Int. Conf. on DEM, Santa Fe, NM, USA, Geotechnical Special Publication No. 117*, ASCE, Reston, VI, USA, pp. 32–37.

[85] **Feng, Y. T., Owen, D. R. J.** (**2003**): 'Filling domain with disks: An advancing front approach', *Int. J. Num. Meth. Engng.*, Vol. 56, pp. 699–714.

[86] **Feng, Y. T., Owen, D. R. J.** (**2004**): 'A 2D polygon/polygon contact model: algorithmic aspects', *Engng. Comp.*, Vol. 21, pp. 265–277.

[87] **Fleck, N. A., Hutchinson, J. W.** (**1997**): 'On first strain-gradient theories in linear elasticity', *Adv. Appl. Mech.*, Vol. 33, pp. 295–361.

[88] **Gallagher, J. J., Friedman, N., Handin, J., Sowers, G. M.** (**1974**): 'Experimental studies relating to microfracture in sandstone', *Tectonophys.*, Vol. 21, pp. 203–247.

[89] **Geers, M. G. D.** (**1997**): *Experimental analysis and computational modelling of damage and fracture*, Ph.D. Thesis, Technische Universiteit Eindhoven, The Netherlands.

[90] **Geers, M. G. D.** (**2003**), 'Experimental determination of the deformation tensor **F** and strain fields', Personal communication.

[91] **Geers, M. G. D., de Borst, R., Brekelmans, W. A. M.** (**1996**): 'Computing strain fields from discrete displacements in 2D-solids', *Int. J. Solids & Structures*, Vol. 33, pp. 4293–4307.

[92] **Germain, P.** (**1973**): 'The method of virtual power in continuum mechanics. Part 2: Microstructure', *SIAM J. Appl. Math.*, Vol. 25, pp. 556–575.

[93] **Goodman, R. E., Taylor, R. L., Brekke, T. L.** (**1968**): 'A model for the mechanics of jointed rock', *ASCE J. Soil Mech. Found. Div.*, Vol. 94, pp. 637–659.

[94] **Green, A. E., Rivlin, R. S.** (**1964**): 'Multipolar continuum mechanics', *Arch. Rat. Mech. Anal.*, Vol. 17, pp. 113–147.

[95] **Grujicic, M., Cao, G., Joseph, P. F.** (**2003**): 'Multiscale modelling of deformation and fracture of polycrystalline lamellar γ-TiAl+α_2-Ti$_3$Al alloys', *Int. J. Multiscale Comp. Engng.*, Vol. 1, pp. 1–21.

[96] **Günther, W.** (**1958**): 'Zur Statik und Kinematik des Cosseratschen Kontinuums', *Abhandlungen der Braunschweigischen Wissenschaftlichen Gesellschaft*, Vol. 10, pp. 195–213.

[97] **Gussmann, P.** (**1986**): *Die Methode der kinematischen Elemente*, Mitteilung Nr. 25, Institut für Geotechnik, Universität Stuttgart, Germany.

[98] **Hairer, E., Norsett, S. P., Wanner, G.** (**1993**): *Solving Ordinary Differential Equations I - Nonstiff Problems*, Springer-Verlag, Berlin, Germany.

[99] **Hairer, E., Wanner, G.** (**1996**): *Solving Ordinary Differential Equations II - Stiff and Differential-Agebraic Problems*, Springer-Verlag, Berlin, Germany.

[100] **Hallbauer, D.-K., Wagner, H., Cook, N. G. W.** (**1973**): 'Some observations concerning the microscopic and mechanical behaviour of quartzite specimens in stiff, triaxial compression tests', *Int. J. Rock Mech. Min. Sci. & Geomech. Abstr.*, Vol. 10, pp. 713–726.

[101] **Hansen, A., Roux, S., Herrmann, H. J.** (**1989**): 'Rupture of central force lattices', *J. Phys. France*, Vol. 50, pp. 733–744.

[102] **Hashin, Z.** (**1983**): 'Analysis of composite materials - a survey', *J. Appl. Mech.*, Vol. 50, pp. 481–505.

[103] **Herrmann, H. J.** (**2001**): 'Structures in deformed packings', *Granular Matter*, Vol. 3, pp. 15–18.

[104] **Herrmann, H. J., Hansen, A., Roux, S.** (**1989**): 'Fracture of disordered, elastic lattices in two dimensions', *Phys. Rev. B*, Vol. 39, pp. 1637–1648.

[105] **Herrmann, H. J., Roux, S.** (eds.) (**1990**): *Statistical Models for the Fracture of Disordered Media*, North Holland, Amsterdam, The Netherlands.

[106] **Hertz, H.** (**1881**): 'Über die Berührung fester elastischer Körper', *Zeitschrift für die reine und angewandte Mathematik*, Vol. 39, pp. 156–171.

[107] **Hill, R.** (**1952**): 'The elastic behaviour of a crystalline aggregate', *Proc. Phys. Soc. Lond. A*, Vol. 65, pp. 349–354.

[108] **Hill, R.** (**1963**): 'Elastic properties of reinforced solids; some theoretical principles', *J. Mech. Phys. Solids*, Vol. 11, pp. 357–372.

[109] **Hill, R.** (**1965**): 'Continuum micro-mechanics of elastoplastic polycrystals', *J. Mech. Phys. Solids*, Vol. 13, pp. 89–101.

[110] **Hill, R.** (**1967**): 'The essential structure of constitutive laws for material composites and polycrystals', *J. Mech. Phys. Solids*, Vol. 15, pp. 79–95.

[111] **Hillerborg, A., Modéer, M., Petersson, P. E.** (**1976**): 'Analysis of crack formation and crack growth in concrete by means of fracture mechanics and finite elements', *Cem. Concr. Res.*, Vol. 6, pp. 773–782.

[112] **Hocking, G.** (**1992**): 'The discrete element method for analysis of fragmentation of discontinua', *Engng. Comp.*, Vol. 9, pp. 145–155.

[113] **Hrennikoff, A.** (**1941**): 'Solution of problems of elasticity by the framework method', *J. Appl. Mech. Trans. ASME*, Vol. 8, pp. A169–A175.

[114] **Huang, H.** (**1999**): *Discrete element modeling of tool-rock interaction*, Ph.D. Thesis, University of Minnesota, MN, USA.

[115] **Huet, C.** (**1997**): 'An integrated micromechanics and statistical continuum thermodynamics approach for studying the fracture behaviour of microcracked heterogeneous materials with delayed response', *Engng. Fract. Mech.*, Vol. 58, pp. 459–556.

[116] **Hughes, T. J. R.** (**2000**): *The Finite Element Method - Vol 1*, Dover Publications, Inc., Mineaola, NY, USA.

[117] **Ibrahimbegovic, A., Delaplace, A.** (**2003**): 'Discrete modelling of cracking of brittle materials in large relative motion and localization problems.', in: **Miehe, C.** (ed.), *Proc. of IUTAM Symp. on Computational Mechanics of Solid Materials at Large Strains, Stuttgart, Germany - Solid Mechanics and its Applications: Volume 108*, Kluwer Academic Publishers, Dordrecht, The Netherlands.

[118] **Ibrahimbegovic, A., Delaplace, A.** (**2003**): 'Microscale and mesoscale discrete models for dynamic fracture of structures built of brittle material', *Comp. & Struct.*, Vol. 81, pp. 1255–1265.

[119] **Issa, J. A., Nelson, R. B.** (**1992**): 'Numerical analysis of micromechanical behaviour of granular materials', *Engng. Comp.*, Vol. 9, pp. 211–223.

[120] **Itasca Consulting Group** (**2002**): *PFC Manual*, Itasca Consulting Group, Minneapolis, MN, USA.

[121] **Iwashita, K., Oda, M.** (**1998**): 'Rolling resistance at contacts in simulation of shear band development by DEM', *J. Engng. Mech.*, Vol. 124, pp. 285–292.

[122] **Iwashita, K., Oda, M.** (**2000**): 'Micro-deformation mechanism of shear banding process based on modified distinct element method', *Powd. Tech.*, Vol. 109, pp. 192–205.

[123] **Jean, M.** (**1999**): 'The non smooth contact dynamics method', *Comp. Meth. Appl. Mech. Engng.*, Vol. 177, pp. 235–257.

[124] **Jirásek, M., Bažant, Z. P.** (**2001**): *Inelastic Analysis of Structures*, John Wiley & Sons, Chichester, England, UK.

[125] **Kanatani, K.-I.** (**1984**): 'Distribution of directional data and fabric tensors', *Int. J. Engng. Sci.*, Vol. 22, pp. 149–164.

[126] **Kohring, G. A., Melin, S., Puhl, H., Tillemans, H. J., Vermoehlen, W.** (**1995**): 'Computer simulations of critical, non-stationary granular flow through a hopper', *Comp. Meth. Appl. Mech. Engng.*, Vol. 14, pp. 273–281.

[127] **Koiter, W. T.** (**1953**): 'Stress-strain relations, uniqueness and variational theorems for elastic-plastic materials with a singular yield surface', *Quart. Appl. Math.*, Vol. 11, pp. 350–354.

[128] **Kouznetsova, V. G.** (**2002**): *Computational homogenization for the multi-scale analysis of multi-phase materials*, Ph.D. Thesis, Technische Universiteit Eindhoven, The Netherlands.

[129] **Kouznetsova, V. G., Geers, M. G. D., Brekelmans, W. A. M.** (**2002**): 'Multi-scale constitutive modelling of heterogeneous materials with a gradient-enhanced computational homogenization scheme', *Int. J. Num. Meth. Engng.*, Vol. 54, pp. 1235–1260.

[130] **Krajcinovic, D.** (**1996**): *Damage Mechanics*, North Holland, Amsterdam, The Netherlands.

[131] **Krajcinovic, D., Basista, M.** (**1991**): 'Rupture of central-force lattices revisited', *J. Phys. I France*, Vol. 1, pp. 241–245.

[132] **Krajcinovic, D., Mastilovic, S.** (**1999**): 'High-velocity expansion of a cavity within a brittle material', *J. Mech. Phys. Solids*, Vol. 47, pp. 577–610.

[133] **Kröner, E.** (**1967**): 'Elasticity theory of materials with long range cohesive forces', *Int. J. Solids & Structures*, Vol. 3, pp. 731–742.

[134] **Kruyt, N. P.** (**1994**): *Aspects of constitutive relations for cohesionless granular materials*, Ph.D. Thesis, University of Twente, The Netherlands.

[135] **Kruyt, N. P., Rothenburg, L.** (**1996**): 'Micromechanical definition of the strain tensor for granular materials', *J. Appl. Mech.*, Vol. 118, pp. 706–711.

[136] **Kuhl, D., Müller, S., Meschke, G.** (**2001**): 'An extension of the microplane model for the modeling of anisotropic elasticity and damage of particle based recycling materials', in: **Wall, W. A., Bletzinger, K.-U., Schweizerhof, K.** (eds.), *Trends in Computational Mechanics, Lochau, Austria*, CIMNE, Barcelona, Spain, pp. 145–154.

[137] **Kuhl, E.** (**2000**): *Numerische Modelle für kohäsive Reibungsmaterialien*, Ph.D. Thesis, Bericht Nr. 32, Institut für Baustatik, Universität Stuttgart, Germany.

[138] **Kuhl, E., D'Addetta, G. A., Herrmann, H. J., Ramm, E.** (**2000**): 'A comparison of discrete granular material models with continuous microplane formulations', *Granular Matter*, Vol. 2, pp. 113–121.

[139] **Kun, F., D'Addetta, G. A., Ramm, E., Herrmann, H. J.** (**1999**): 'Two-dimensional dynamic simulation of fracture and fragmentation of solids', *Comp. Ass. Mech. Engng.*, Vol. 6, pp. 385–402.

[140] **Kun, F., Herrmann, H. J.** (**1996**): 'Fragmentation of colliding discs', *Int. J. Mod. Phys. C*, Vol. 7, pp. 837–855.

[141] **Kun, F., Herrmann, H. J.** (**1996**): 'A study of fragmentation processes using a discrete element method', *Comp. Meth. Appl. Mech. Engng.*, Vol. 138, pp. 3–18.

[142] **Kun, F., Herrmann, H. J.** (**1999**): 'Transition from damage to fragmentation in collision of solids', *Phys. Rev. E*, Vol. 59, pp. 2623–2632.

[143] **Kuntsche, K.** (**1982**): *Materialverhalten von wassergesätigtem Ton bei ebenene und zylindrischen Verformungen*, Ph.D. Thesis, Bericht Nr. 91, Institut für Bodenmechanik und Felsmechanik, Universität Karlsruhe, Germany.

[144] **Lätzel, M.** (**2003**): *From microscopic simulations towards a macroscopic description of granular media*, Ph.D. Thesis, Institut für Computeranwendungen 1, Universität Stuttgart, Germany.

[145] **Lätzel, M., Luding, S., Herrmann, H. J.** (**2000**): 'Macroscopic material properties from quasi-static, microscopic simulations of a two-dimensional shear-cell', *Granular Matter*, Vol. 2, pp. 123–135.

[146] **Lätzel, M., Luding, S., Herrmann, H. J., Howell, D. W., Behringer, R. P.** (**2003**): 'Comparing simulation and experiment of a 2D granular couette shear device', *Eur. Phys. J. E*, Vol. 11, pp. 325–333.

[147] **Lemaitre, J., Chaboche, J.-L.** (**1990**): *Mechanics of Solid Materials*, University Press, Cambridge, England, UK.

[148] **Li, S., Liu, W. K.** (**2002**): 'Meshfree and particle methods and their applications', *Appl. Mech. Rev.*, Vol. 55, pp. 1–34.

[149] **Liao, C.-L., Chang, T.-P., Young, D.-H., Chang, C. S.** (**1997**): 'Stress-strain relationship for granular materials based on the hypothesis of best fit', *Int. J. Solids & Structures*, Vol. 34, pp. 4087–4100.

[150] **Lockner, D. A., Byerlee, J. D., Kuksenko, V., Ponomarev, A., Sidorin, A.** (**1992**): 'Observation of quasistatic fault growth from acoustic emissions', in: **Evans, B., Wong, T.-F.** (eds.), *Fault Mechanics and Transport Properties of Rocks*, Academic Press, London, England, UK, pp. 3–31.

[151] **Love, A. E. H.** (**1927**): *A Treatise on the Mathematical Theory of Elasticity*, University Press, Cambridge, England, UK.

[152] **Lubarda, V. A., Krajcinovic, D.** (**1993**): 'Damage tensors and the crack density distribution', *Int. J. Solids & Structures*, Vol. 30, pp. 2859–2877.

[153] **Luding, S.** (**1998**): 'Collisions and contacts between two particles', in: **Herrmann, H. J., Hovi, J.-P., Luding, S.** (eds.), *Physics of Dry Granular Materials*, NATO-ASI Series E: Applied Science - Vol. 350, Kluwer Academic Publishers, Dordrecht, The Netherlands, pp. 285–304.

[154] **Luding, S.** (**2003**): 'Micro-macro transition for an-isotropic, frictional granular packings', *Int. J. Solids & Structures*, submitted.

[155] **Luding, S.** (**2004**): *Molecular dynamics simulations of granular materials*, John Wiley & Sons, Chichester, England, UK.

[156] **Luding, S., Herrmann, H. J.** (**2001**): 'Micro-macro transition for cohesive granular media', in: **Diebels, S.** (ed.), *Zur Beschreibung komplexen Materialverhaltens: Beiträge anlä"slich des 50. Geburtstags von Herrn Prof. Dr.-Ing. Wolfgang Ehlers*, Institut für Mechanik, LS II, Universität Stuttgart, Germany, pp. 121–133.

[157] **Luding, S., Lätzel, M., Volk, W., Diebels, S., Herrmann, H. J.** (**2001**): 'From discrete element simulations to a continuum model', *Comp. Meth. Appl. Mech. Engng.*, Vol. 191, pp. 21–28.

[158] **Lusche, M.** (**1972**): *Beitrag zum Bruchmechanismus von auf Druck beanspruchtem Normal- und Leichtbeton mit geschlossenem Gefüge*, Verein Deutscher Zementwerke (VDZ), Schriftenreihe der Zementindustrie, Heft 39/1972.

[159] **Magnier, S.-A., Donzé, F. V.** (**1998**): 'Numerical simulations of impacts using a discrete element method', *Mech. Coh. Frict. Mat.*, Vol. 3, pp. 257–276.

[160] **Mahnken, R., Kuhl, E.** (**1999**): 'Parameter identification of gradient enhanced damage models with the finite element method', *Eur. J. Mech. A Solids*, Vol. 18, pp. 819–835.

[161] **Malvern, L. E.** (**1969**): *Introduction to the Mechanics of a Continuous Medium*, Prentice-Hall, Inc., Englewood Cliffs, NJ, USA.

[162] **Marcher, T.** (**2002**): *Resultate eines Versuchsprogramms an Beaucaire Mergel*, Bericht Nr. 49, Institut für Geotechnik, Universität Stuttgart, Germany.

[163] **Marcher, T.** (**2003**): *Nichtlokale Modellierung der Entfestigung dichter Sande und steifer Tone*, Ph.D. Thesis, Bericht Nr. 50, Institut für Geotechnik, Universität Stuttgart, Germany.

[164] **Marsden, J. E., Hughes, T. J. R.** (**1983**): *Mathematical Foundations of Elasticity*, Prentice-Hall, Inc., Englewood Cliffs, NJ, USA.

[165] **Matuttis, H.-G.** (**1998**): 'Simulation of the pressure distribution under a two-dimensional heap of polygonal particles', *Granular Matter*, Vol. 1, pp. 83–91.

[166] **Matuttis, H.-G., Luding, S., Herrmann, H. J.** (**2000**): 'Discrete element simulations of dense packings and heaps made of spherical and non-spherical particles', *Powd. Tech.*, Vol. 109, pp. 278–292.

[167] **Menrath, H.** (**1999**): *Numerische Simulation des nichtlinearen Tragverhaltens von Stahlverbundträgern*, Ph.D. Thesis, Bericht Nr. 29, Institut für Baustatik, Universität Stuttgart, Germany.

[168] **Metropolis, N., Rosenbluth, A. W., Rosenbluth, M. N., Teller, A. H., Teller, E.** (**1953**): 'Equations of state calculations by fast computing machines', *J. Chem. Phys.*, Vol. 21, pp. 1087–1092.

[169] **Miehe, C., Koch, A.** (**2002**): 'Computational micro-to-macro transitions for discretized microstructures undergoing small strains', *Arch. Appl. Mech.*, Vol. 72, pp. 300–317.

[170] **Miehe, C., Schröder, J., Bayreuther, C.** (**2002**): 'Homogenization analysis of linear composite materials on discretized fluctuations on the micro-structure', *Acta Mechanica*, Vol. 155, pp. 1–16.

[171] **Miehe, C., Schröder, J., Schotte, J.** (**1999**): 'Computational homogenization analysis in finite plasticity - simulation of texture development in polycrystalline materials', *Comp. Meth. Appl. Mech. Engng.*, Vol. 171, pp. 387–418.

[172] **Mindlin, R. D.** (**1964**): 'Micro-structure in linear elasticity', *Arch. Rat. Mech. Anal.*, Vol. 16, pp. 51–78.

[173] **Mindlin, R. D.** (**1965**): 'Second gradient of strain and surface-tension in linear elasticity', *Int. J. Solids & Structures*, Vol. 1, pp. 417–438.

[174] **Mindlin, R. D., Deresiewicz, H.** (**1953**): 'Elastic spheres in contact under varying oblique forces', *J. Appl. Mech. Trans. ASME*, Vol. 20, pp. 327–344.

[175] **Mohr, O.** (**1882**): 'Über die Darstellung des Spannungszustandes und des Deformationszustandes eines Körperelementes und über die Anwendung derselben in der Festigkeitslehre', *Civilingenieur*, Vol. 28, pp. 113–156.

[176] **Moreau, J. J.** (**1994**): 'Some numerical methods in multibody dynamics: Application to granular materials', *Eur. J. Mech. A/Solids*, Vol. 13, pp. 93–114.

[177] **Moukarzel, C., Herrmann, H. J.** (**1992**): 'A vectorizable random lattice', *J. Stat. Phys.*, Vol. 68, pp. 911–923.

[178] **Mühlhaus, H.-B.** (ed.) (**1995**): *Continuum Models for Materials with Microstructure*, John Wiley & Sons, Chichester, England, UK.

[179] **Mühlhaus, H.-B., Aifantis, E. C.** (**1991**): 'A variational principle for gradient plasticity', *Int. J. Solids & Structures*, Vol. 28, pp. 845–857.

[180] **Mühlhaus, H.-B., Sakaguchi, H., Wei, Y.** (**1997**): 'Particle based modelling of dynamic fracture in jointed rock', in: **Yuan** (ed.), *Proc. of the 9th Int. Conf. of the International Association of Computer Methods and Advances in Geomechanics - IACMAG 97, Wuhan, China*, A. A. Balkema, Rotterdam, The Netherlands, pp. 207–216.

[181] **Mühlhaus, H.-B., Vardoulakis, I.** (**1987**): 'The thickness of shear bands in granular materials', *Géotechnique*, Vol. 37, pp. 271–283.

[182] **Munjiza, A., Owen, D. R. J., Bicanic, N.** (**1995**): 'A combined finite/discrete element method in transient dynamics of fracturing solids.', *Engng. Comp.*, Vol. 12, pp. 145–174.

[183] **Mura, T.** (**1987**): *Micromechanics of Defects in Solids*, Kluwer Academic Publishers, Dordrecht, The Netherlands.

[184] **Nante, M.-C.** (**2003**): *Quantification of a discrete particle approach for cohesive-frictional materials*. Research internship report, Institut für Baustatik, Universität Stuttgart, Germany.

[185] **Nemat-Nasser, S., Hori, M.** (**1999**): *Micromechanics: Overall Properties of Heterogeneous Materials*, Elsevier Science Publisher, Amsterdam, The Netherlands.

[186] **Ngo, D., Scordelis, A. C.** (**1967**): 'Finite element analysis of reinforced concrete beams', *ACI Mat. J.*, Vol. 64, pp. 152–163.

[187] **Nowacki, W.** (**1986**): *Theory of Asymmetric Elasticity*, Pergamon Press, Oxford, England, UK.

[188] **Nübel, K.** (**2002**): *Experimental and numerical investigation of shear localization in granular material*, Ph.D. Thesis, Bericht Nr. 159, Institut für Bodenmechanik und Felsmechanik, Universität Karlsruhe, Germany.

[189] **Nübel, K., Gudehus, G.** (**2000**): 'Numerical evolution of localized dilated shear zones', in: **Mühlhaus, H. B.** (ed.), *Proc. of the Int. Conf. on Bifurcation and Localization, Perth, Australia*, A. A. Balkema, Rotterdam, The Netherlands, pp. 1–7.

[190] **Oda, M., Iwashita, K.** (**1999**): *Mechanics of Granular Materials*, A. A. Balkema, Rotterdam, The Netherlands.

[191] **Oda, M., Iwashita, K.** (**2000**): 'Study on couple stress and shear band development in granular media based on numerical simulation analyses', *Int. J. Engng. Sci.*, Vol. 38, pp. 1713–1740.

[192] **Oda, M., Kazama, H.** (**1998**): 'Microstructure of shear bands and its relation to the mechanisms of dilatancy and failure of dense granular soils', *Géotechnique*, Vol. 48, pp. 465–481.

[193] **Oda, M., Konishi, J., Nemat-Nasser, S.** (**1980**): 'Some experimentally based fundamental results on the mechanical behaviour of granular materials', *Géotechnique*, Vol. 30, pp. 479–495.

[194] **Ostoja-Starzewski, M.** (**2002**): 'Microstructural randomness versus representative volume element in thermomechanics', *J. Appl. Mech.*, Vol. 69, pp. 25–35.

[195] **Pamin, J.** (**1994**): *Gradient-dependent plasticity in numerical simulation of localization phenomena*, Ph.D. Thesis, Technische Universiteit Delft, The Netherlands.

[196] **Peters, G. W. M.** (**1987**): *Tools for the measurement of stress and strain fields in soft tissue*, Ph.D. Thesis, Technische Universiteit Eindhoven, The Netherlands.

[197] **Pijaudier-Cabot, G., Bažant, Z. P.** (**1987**): 'Nonlocal damage theory', *J. Engng. Mech.*, Vol. 113, pp. 1512–1533.

[198] **Plieninger, M.** (**2001**): *Numerische Simulation von Mauerwerk mit einem diskreten Modellierungsansatz*. Diplomarbeit, Institut für Baustatik, Universität Stuttgart, Germany.

[199] **Poliakov, A. N., Herrmann, H. J.** (**1994**): 'Self-organized criticality of plastic shear bands in rocks', *Geophys. Res. Lett.*, Vol. 21, pp. 2143–2146.

[200] **Potapov, A. V., Campbell, C. S.** (**1996**): 'A three-dimensional dynamic simulation of brittle solid fracture', *Int. J. Mod. Phy. C*, Vol. 7, pp. 717–729.

[201] **Potapov, A. V., Hopkins, M. A., Campbell, C. S.** (**1995**): 'A two-dimensional dynamic simulation of solid fracture - part I: Description of the model', *Int. J. Mod. Phy. C*, Vol. 6, pp. 371–398.

[202] **Potapov, A. V., Hopkins, M. A., Campbell, C. S.** (**1995**): 'A two-dimensional dynamic simulation of solid fracture - part II: Examples', *Int. J. Mod. Phy. C*, Vol. 6, pp. 399–425.

[203] **Preparata, F., Shamos, M.** (**1985**): *Computational Geometry - An Introduction*, Springer, New York, NY, USA.

[204] **Přikryl, R., Lokajíček, T., Li, C., Rudajev, V.** (**2003**): 'Acoustic emission characteristics and failure of uniaxially stressed granitic rocks: The effect of rock fabric', *Rock Mech. Rock Engng.*, Vol. 36, pp. 255–270.

[205] **Ramm, E., D'Addetta, G. A., Kuhl, E.** (**2000**): 'Geomaterials: Continuum or discontinuum, that is the question', in: **Oñate, E., Owen, D. R. J.** (eds.), *Proc. of the 6th Conf. on Computational Plasticity, Barcelona, Spain*, cd-rom.

[206] **Ramm, E., D'Addetta, G. A., Leukart, M.** (**2003**): 'Interrelations between continuum and discontinuum models for geomaterials', in: **Oñate, E., Bugeda, G., Suarez, B.** (eds.), *Proc. of the 7th Conf. on Computational Plasticity, Barcelona, Spain*, cd-rom.

[207] **Renka, R. J.** (**1996**): 'Algorithm 751: TRIPACK: A constrained two-dimensional delaunay triangulation package', *ACM Trans. Math. Software*, Vol. 22, pp. 1–8.

[208] **Rocco, C., Guinea, G. V., Planas, J., Elices, M.** (**1999**): 'Mechanism of rupture in splitting test', *ACI Mat. J.*, Vol. 96, pp. 52–60.

[209] **Rothenburg, L., Selvadurai, A. P. S.** (**1981**): 'A micromechanical definition of the Cauchy stress tensor for particulate media', in: **Selvadurai, A. P. S.** (ed.), *Proc. of the Int. Symp. on the Mechanical Behaviour of Structured Media, Ottawa, Canada - Studies in Applied Mechanics 5 Part B*, Elsevier Science Publishers, Amsterdam, The Netherlands, pp. 469–486.

[210] **Rots, J. G.** (**1988**): *Computational modelling of concrete fracture*, Ph.D. Thesis, Technische Universiteit Delft, The Netherlands.

[211] **Roux, S., Guyon, E.** (**1985**): 'Mechanical percolation: A small beam lattice study', *J. Phys. Lett.*, Vol. 46, pp. L999–L1004.

[212] **Sakaguchi, H., Murakami, A.** (**2002**): 'Initial packing in discrete element modelling.', in: **Cook, B. K., Jensen, R. P.** (eds.), *Discrete Element Methods - Numerical Modeling of Discontinua - Proc. 3rd Int. Conf. on DEM, Santa Fe, NM, USA, Geotechnical Special Publication No. 117*, ASCE, Reston, VI, USA, pp. 104–106.

[213] **Schaefer, H.** (**1958**): 'Das Cosserat-Kontinuum', *ZAMM*, Vol. 47, pp. 485–498.

[214] **Schellekens, J. C. J.** (**1992**): *Computational strategies for composite structures*, Ph.D. Thesis, Technische Universiteit Delft, The Netherlands.

[215] **Schlangen, E., Garboczi, E. J.** (**1996**): 'New method for simulating fracture using an elastically uniform random geometry lattice', *Int. J. Engng. Sci.*, Vol. 34, pp. 1131–1144.

[216] **Schlangen, E., Garboczi, E. J.** (**1997**): 'Fracture simulations of concrete using lattice models: Computational aspects', *Engng. Fract. Mech.*, Vol. 57, pp. 319–332.

[217] **Schlangen, E., van Mier, J. G. M.** (**1992**): 'Experimental and numerical analysis of micromechanisms of fracture of cement-based composites', *Cem. Concr. Res.*, Vol. 14, pp. 105–118.

[218] **Schneebeli, G.** (**1957**): 'Une analogie mécanique pour l'étude de la stabilité des ouvrages en terre à deux dimensions', in: **Glanville, W. H.** (ed.), *Proc. of the 4th Int. Conf. on Soil Mechanics and Foundation Engineering*, London, England, UK, pp. 228–232.

[219] **Schorn, H.** (**1982**): 'Zur Einführung numerischer Berechnungsverfahren in die Ermittlung strukturorientierter Stoffgesetze', in: **Diekkämper, R., Arnold, P., Schrader, K.-H.** (eds.), *Strukturmechanik und numerische Verfahren: K.-H. Schrader zum 60. Geburtstag*, Bochum, Germany, pp. 319–341.

[220] **Schorn, H.** (**1986**): 'Numerical simulation of composite materials as concrete', in: **Wittmann, F.** (ed.), *Fracture Toughness and Fracture Energy of Concrete - Proc. Int. Conference on Fracture Mechanics of Concrete*, Elsevier Science Publishers, Amsterdam, The Netherlands, pp. 177–188.

[221] **Selvadurai, A., Sepehr, K.** (**1999**): 'Two-dimensional discrete element simulations of ice-structure interaction', *Int. J. Solids & Structures*, Vol. 36, pp. 4919–4940.

[222] **Shi, G.-H.** (**1985**): 'Generalization of two-dimensional discontinuous deformation analysis for forward modelling', *Int. J. Num. Anal. Meth. Geomech.*, Vol. 9, pp. 541–556.

[223] **Shi, G.-H.** (**1992**): 'Discontinuous deformation analysis: A new numerical model for the static and dynamics of deformable block structures', *Engng. Comp.*, Vol. 9, pp. 157–168.

[224] **Simo, J. C., Hughes, T. J. R.** (**1998**): *Computational Inelasticity*, Springer, New York, NY, USA.

[225] **Smit, R. J. M., Brekelmans, W. A. M., Meijer, H. E. H.** (**1998**): 'Prediction of the mechanical behavior of nonlinear heterogeneous systems by multi-level finite element modeling', *Comp. Meth. Appl. Mech. Engng.*, Vol. 155, pp. 181–192.

[226] **Smith, W. O., Foot, P. D., Busang, P. F.** (**1929**): 'Packing of homogeneous spheres', *Phys. Rev.*, Vol. 34, pp. 1271–1274.

[227] **Stankowski, T.** (**1990**): *Numerical simulation of progressive failure in particle composites*, Ph.D. Thesis, University of Colorado, Boulder, CO, USA.

[228] **Stein, E., Barthold, F.-J.** (**1996**): 'Elastizitätstheorie', in: **Mehlhorn, G.** (ed.), *Der Ingenieurbau: Grundwissen - Bd. 4: Werkstoffe, Elastizitätstheorie*, Ernst & Sohn, Berlin, Germany, pp. 165–428.

[229] **Steinmann, P., Stein, E.** (**1997**): 'A unifying treatise of variational principles for two types of micropolar continua', *Acta Mechanica*, Vol. 121, pp. 215–232.

[230] **Steinmann, P., Willam, K.** (**1991**): 'Localization within the framework of micropolar elastoplasticity', in: **Brüller, O., Mannl, V., Najar, J.** (eds.), *Advances in Continuum Mechanics*, Springer-Verlag, Berlin, Germany, pp. 296–313.

[231] **Stroeven, P.** (**1974**): *Some aspects of the micromechanics of concrete*, Ph.D. Thesis, Technische Universiteit Delft, The Netherlands.

[232] **Sulem, J., Vardoulakis, I., Papamichos, E.** (**1995**): 'Microstructure and scale effect in granular rocks', in: **Mühlhaus, H.-B.** (ed.), *Continuum Models for Materials with Microstructure*, John Wiley & Sons, Chichester, England, UK, pp. 201–237.

[233] **Szillard, R.** (**1974**): *Theory and Analysis of Plates - Classical and Numerical Methods*, Prentice-Hall, Inc., Englewood Cliffs, NJ, USA.

[234] **Tavarez, T. A., Plesha, M. A., Bank, L. B.** (**2002**): 'Discrete element method (DEM) for modelling solid and particulate media.', in: **Cook, B. K., Jensen, R. P.** (eds.), *Discrete Element Methods - Numerical Modeling of Discontinua - Proc. 3rd Int. Conf. on DEM, Santa Fe, NM, USA, Geotechnical Special Publication No. 117*, ASCE, Reston, VI, USA, pp. 155–160.

[235] **Taylor, G. I.** (**1938**): 'Plastic strain in metals', *J. Inst. Met.*, Vol. 62, pp. 307–324.

[236] **Tejchman, J., Gudehus, G.** (**2001**): 'Shearing of a narrow granular layer with polar quantities', *Int. J. Num. Anal. Meth. Geomech.*, Vol. 25, pp. 1–28.

[237] **Tillemans, H.-J., Herrmann, H. J.** (**1995**): 'Simulating deformations of granular solids under shear', *Physica A*, Vol. 217, pp. 261–288.

[238] **Topolnicki, M.** (**1987**): *Observed stress-strain behaviour of remoulded saturated clay and examination of two constitutive models*, Ph.D. Thesis, Bericht Nr. 107, Institut für Bodenmechanik und Felsmechanik, Universität Karlsruhe, Germany.

[239] **Truesdell, C., Noll, W.** (**1965**): 'The non-linear field theories of mechanics', in: **Flügge, S.** (ed.), *Handbuch der Physik III/3*, Springer-Verlag, Berlin, Germany.

[240] **Truesdell, C., Toupin, R. A.** (**1960**): 'The classical field theories', in: **Flügge, S.** (ed.), *Handbuch der Physik III/1*, Springer-Verlag, Berlin, Germany.

[241] **Unger, T., Brendel, L., Wolf, D. E., Kertész, J.** (**2002**): 'Elastic behavior in contact dynamics of rigid particles', *Phys. Rev. E*, Vol. 65.

[242] **van der Sluis, O.** (**2001**): *Homogenisation of structured elastoviscoplastic solids*, Ph.D. Thesis, Technische Universiteit Eindhoven, The Netherlands.

[243] **van Mier, J. G. M.** (**1997**): *Fracture Processes of Concrete*, CRC Press, Boca Raton, FL, USA.

[244] **van Mier, J. G. M., Schlangen, E., Vervuurt, A.** (**1995**): 'Lattice type fracture models for concrete', in: **Mühlhaus, H.-B.** (ed.), *Continuum Models for Materials with Microstructure*, John Wiley & Sons, Chichester, England, UK, pp. 341–377.

[245] **van Mier, J. G. M., Schlangen, E., Vervuurt, A., van Vliet, M. R. A.** (**1995**): 'Damage analysis of brittle disordered materials: Concrete and rock', in: **Bakker, A.** (ed.), *Mechanical Behaviour of Materials - Proc. of the ICM 7*, Delft University Press, Delft, The Netherlands, pp. 101–126.

[246] **Vardoulakis, I., Aifantis, E. C.** (**1989**): 'Gradient dependent dilatancy and its implications in shear banding and liquefaction', *Ingenieur-Archiv*, Vol. 59, pp. 197–208.

[247] **Vardoulakis, I., Aifantis, E. C.** (**1991**): 'A gradient flow theory of plasticity for granular materials', *Acta Mechanica*, Vol. 87, pp. 197–217.

[248] **Vardoulakis, I., Graf, B.** (**1985**): 'Calibration of constitutive models for granular materials using data from biaxial experiments', *Géotechnique*, Vol. 35, pp. 299–317.

[249] **Vermeer, P. A., Diebels, S., Ehlers, W., Herrmann, H. J., Luding, S., Ramm, E.** (eds.) (**2001**): *Continuous and Discontinuous Modelling of Cohesive Frictional Materials, Lecture Notes in Physics 586*, Springer-Verlag, Berlin, Germany.

[250] **Viggiani, G., Küntz, M., Desrues, J.** (**2001**): 'An experimental investigation of the relationships between grain size distribution and shear banding in sand', in: **Vermeer, P. A., Diebels, S., Ehlers, W., Herrmann, H. J., Luding, S., Ramm, E.** (eds.), *Continuous and Discontinuous Modelling of Cohesive Frictional Materials, Lecture Notes in Physics 586*, Springer-Verlag, Berlin, Germany, pp. 111–127.

[251] **Volk, W.** (**1999**): *Untersuchung des Lokalisierungsverhaltens mikropolarer poröser Medien mit Hilfe der Cosserat-Theorie*, Ph.D. Thesis, Bericht Nr. II-2, Instut für Mechanik, LS II, Universität Stuttgart, Germany.

[252] **Volk, W., Diebels, S., Lätzel, M., Luding, S.** (**2001**): 'Analogiebetrachtungen für mikropolare Kontinua mit Anwendung auf den Biaxialversuch', in: **Diebels, S.** (ed.), *Zur Beschreibung komplexen Materialverhaltens: Beiträge anlä"slich des 50. Geburtstags von Herrn Prof. Dr.-Ing. Wolfgang Ehlers*, Institut für Mechanik, LS II, Universität Stuttgart, Germany, pp. 189–206.

[253] **Vonk, R.** (**1989**): *Influence of boundary conditions on softening of concrete loaded in compression*, Report TUE/BKO 89.14, Faculteit Bouwkunde, Technische Universiteit Eindhoven, The Netherlands.

[254] **Vonk, R.** (**1990**): *Constitutive model describing interface behaviour with tensile and shear softening*, Report TUE/BKO 90.12, Faculteit Bouwkunde, Technische Universiteit Eindhoven, The Netherlands.

[255] **Vonk, R.** (**1992**): *Softening of concrete loaded in compression*, Ph.D. Thesis, Technische Universiteit Eindhoven, The Netherlands.

[256] **Vujosevic, M., Krajcinovic, D.** (**1998**): 'Strain localization - short to long correlation length transition', *Int. J. Solids & Structures*, Vol. 35, pp. 4147–4166.

[257] **Walton, O.** (**1983**): 'Particle-dynamics calculation of shear flow', in: **Jenkins, J. T., Satake, M.** (eds.), *Mechanics of Granular Materials: New Models and Constitutive Relations*, Elsevier Science Publishers, Amsterdam, The Netherlands, pp. 327–338.

[258] **Williams, J. R., O'Connor, R.** (**1995**): 'A linear complexity intersection algorithm for discrete element simulation of arbitrary geometries', *Engng. Comp.*, Vol. 12, pp. 185–201.

[259] **Williams, J. R., O'Connor, R.** (**1999**): 'Discrete element simulation and the contact problem', *Arch. Comp. Meth. Engng.*, Vol. 6, pp. 279–304.

[260] **Williams, J. R., Pentland, A.** (**1992**): 'Superquadratics and modal dynamics for discrete element in interactive design', *Engng. Comp.*, Vol. 9, pp. 115–127.

[261] **Winkler, B. J.** (**2001**): *Traglastuntersuchungen von unbewehrten und bewehrten Betonstrukturen auf der Grundlage eines objektiven Werkstoffgesetzes für Beton*, Ph.D. Thesis, Institut für Baustatik, Festigkeitslehre und Tragwerkslehre, Leopold-Franzens-Universität Innsbruck, Austria.

[262] **Wittmann, F. H., Roelfstra, P. E., Sadouki, H.** (**1985**): 'Simulation and analysis of composite structures', *Mat. Sci. Engng.*, Vol. 68, pp. 239–248.

[263] **Xu, X.-P., Needleman, A.** (**1994**): 'Numerical simulations of fast crack growth in brittle solids', *J. Mech. Phys. Solids*, Vol. 42, pp. 1397–1434.

[264] **Zervos, A., Papanastasiou, P., Vardoulakis, I.** (**2001**): 'A finite element displacement formulation for gradient elastoplasticity', *Int. J. Num. Meth. Engng.*, Vol. 50, pp. 1369–1388.

[265] **Zhong, X., Chang, C. S.** (**1999**): 'Micromechanical modeling for behavior of cementitious granular materials', *J. Engng. Mech.*, Vol. 125, pp. 1280–1285.

[266] **Zienkiewicz, O. C., Taylor, R. L.** (**2000**): *The Finite Element Method: The Basis*, Butterworth-Heinemann, London, England, UK.

[267] **Zubelewicz, A., Bažant, Z. P.** (**1987**): 'Interface element modeling of fracture in aggregate composites', *J. Engng. Mech.*, Vol. 113, pp. 1619–1630.

Lebenslauf

Name:		Gian Antonio D'Addetta
Geburtstag:		15.11.1971
Geburtsort:		Karlsruhe
Staatsangehörigkeit:		italienisch
Eltern:		Pietro und Luciana D'Addetta, geb. Tonon

Familienstand: ledig

1978	–	1982	Nebeniusgrundschule Karlsruhe
1982	–	1991	Goethe-Gymnasium Karlsruhe Abschluß: Abitur
10/1991	–	09/1997	Studium Bauingenieurwesen an der Universität Karlsruhe
		09/1997	Abschluß: Dipl.-Ing. (mit Auszeichnung)
		06/1998	Tulla Ehrenmedaille für den besten Abschluss im Jahrgang 1997/1998 der Fakultät für Bauingenieur- und Vermessungswesen der Universität Karlsruhe und Bilfinger-und-Berger Preis für besondere Studienleistungen
05/1998	–	04/2004	Wissenschaftlicher Mitarbeiter am Institut für Baustatik der Universität Stuttgart

Berichte des Instituts für Baustatik der Universität Stuttgart

74-1   **M. Becker, J. Bühler, G. Lang-Lendorff, K. Papailiou, J. M. Sättele:**
Kontaktkurs EDV im konstruktiven Ingenieurbau.

74-2   **G. Werner:**
Experimentelle und theoretische Untersuchungen zur Ermittlung des Tragverhaltens biege- und verdrehbeanspruchter Stäbe mit I-Querschnitt.

74-3   **K. Tompert:**
Berechnung kreiszylindrischer Silos auf elastischer Unterlage.

74-4   **W. Riehle:**
Studie über verallgemeinerte Variationsfunktionale und ihre Anwendung bei der Methode der finiten Plattenelemente.

75-1   **G. Müller, R. M. Rembold, J. M. Sättele, K. H. Schweizerhof, W. Wissmann:**
Platten-Theorie, Berechnung, Bemessung. Teil I.

75-2   **G. Müller:**
Numerische Behandlung der Kirchhoffschen und Reissnerschen Plattentheorie nach einer diskretisierten und erweiterten Trefftz-Methode.

75-3   **E. A. Castrillón O.:**
Beitrag zur Berechnung langer dünnwandiger dreizelliger Träger unter Berücksichtigung der Profilverformung.

76-1   **W. Block, G. Eisenbiegler, R. D. Kugler, H. Lieb, G. Müller, J. Müller, K.-H. Reineck, J. Schlaich, K. H. Schweizerhof, F. Seible:**
Platten-Theorie, Berechnung, Bemessung. Teil II.

76-2   **E. Ramm:**
Geometrisch nichtlineare Elastostatik und finite Elemente.

77-1   **B.-M. Sulke:**
Berechnung dünnwandiger prismatischer Faltwerke mit verformbarem mehrzelligen Querschnitt.

78-1   **F. Fujii:**
Anwendung der Methode der finiten Elemente auf die Berechnung von Stahlbetonplatten.

79-1   **B. Brendel:**
Geometrisch nichtlineare Elastostabilität.

79-2   **H. G. Berg:**
Tragverhalten und Formfindung versteifter Kuppelschalen über quadratischem Grundriß auf Einzelstützen.

79-3   **F. W. Bornscheuer, B. Brendel, L. Häfner, E. Ramm, J. M. Sättele:**
Fallstudien zu Schalentragwerken (in englischer Sprache).

80-1   **R. I. Del Gaizo:**
Liegende zylindrische Behälter und Rohre auf Sattellagern endlicher Breite.

80-2   **R. W. Rembold:**
Beitrag zum Tragverhalten ausgewählter Plattentragwerke unter Berücksichtigung der Reissnerschen Theorie und der Methode der gemischten finiten Elemente.

80-3   **J. M. Sättele:**
Ein finites Elementkonzept zur Berechnung von Platten und Schalen bei stofflicher und geometrischer Nichtlinearität.

82-1   **L. Häfner:**
Einfluß einer Rundschweißnaht auf die Stabilität und Traglast des axialbelasteten Kreiszylinders.

82-2   **K. Schweizerhof:**
Nichtlineare Berechnung von Tragwerken unter verformungsabhängiger Belastung mit finiten Elementen.

82-3   **H.-P. Andrä:**
Zum Tragverhalten des Auflagerbereichs von Flachdecken.

1 (1983)   **P. Osterrieder:**
Traglastberechnung von räumlichen Stabwerken bei großen Verformungen mit finiten Elementen.

2 (1983)   **T. A. Kompfner:**
Ein finites Elementmodell für die geometrisch und physikalisch nichtlineare Berechnung von Stahlbetonschalen.

3 (1983)   **A. Diack:**
Beitrag zur Stabilität längsversteifter Kreiszylinderschalen unter Axialdruck.

4 (1984)   **A. Burmeister, F. W. Bornscheuer, E. Ramm:**
Traglasten von Kugelbehältern mit Stutzen und Formabweichungen unter Innendruck und Stützenlängskraft.

5 (1985)   **H. Stegmüller:**
Grenzlastberechnungen flüssigkeitsgefüllter Schalen mit „degenerierten" Schalenelementen.

6 (1987)   **A. Burmeister:**
Dynamische Stabilität nach der Methode der finiten Elemente mit Anwendung auf Kugelschalen.

7 (1987)   G. Kammler:
Ein finites Elementmodell zur Berechnung von Trägern und Stützen mit offenem, dünnwandigem Querschnitt unter Berücksichtigung der Interaktion zwischen globalem und lokalem Versagen.

8 (1988)   A. Matzenmiller:
Ein rationales Lösungskonzept für geometrisch und physikalisch nichtlineare Strukturberechnungen.

9 (1989)   D. Tao:
Die Technik der reduzierten Basis bei nichtlinearen finiten Element-Berechnungen.

10 (1989)   K. Weimar:
Ein nichtlineares Balkenelement mit Anwendung als Längssteifen axialbelasteter Kreiszylinder.

11 (1990)   K.-U. Bletzinger:
Formoptimierung von Flächentragwerken.

12 (1990)   S. Kimmich:
Strukturoptimierung und Sensibilitätsanalyse mit finiten Elementen.

13 (1991)   U. Andelfinger:
Untersuchungen zur Zuverlässigkeit hybrid-gemischter finiter Elemente für Flächentragwerke.

14 (1992)   N. Büchter:
Zusammenführung von Degenerationskonzept und Schalentheorie bei endlichen Rotationen.

15 (1992)   T. J. Hofmann:
Beitrag zur verfeinerten Balkentheorie.

16 (1994)   D. Roehl:
Zur Berechnung von großen elastoplastischen Deformationen bei Flächentragwerken und Kontinua.

17 (1994)   R. Reitinger:
Stabilität und Optimierung imperfektionsempfindlicher Tragwerke.

18 (1995)   R. Suanno:
Ein dreidimensionales Simulationsmodell für Stahlbeton mit Plastizität und Schädigung.

19 (1995)   M. Braun:
Nichtlineare Analysen von geschichteten, elastischen Flächentragwerken.

20 (1996)   N. Rehle:
Adaptive Finite Element Verfahren bei der Analyse von Flächentragwerken.

21 (1996)   C. Haußer:
Effiziente Dreieckselemente für Flächentragwerke.

22 (1996)   D. Kuhl:
Stabile Zeitintegrationsalgorithmen in der nichtlinearen Elastodynamik dünnwandiger Tragwerke.

23 (1998)   H. Schmidts:
Zur effizienten Modellierung und Analyse von Hochhaustragwerken.

24 (1998)   H. Wang:
Interaktion des lokalen und globalen Stabilitätsverhaltens dünnwandiger Stäbe.

25 (1998)   K. Maute:
Topologie- und Formoptimierung von dünnwandigen Flächentragwerken.

26 (1998)   B. Maurer:
Karl Culmann und die graphische Statik.

27 (1998)   F. Cirak:
Adaptive Finite-Element-Methoden bei der nichtlinearen Analyse von Flächentragwerken.

28 (1998)   M. Trautz:
Zur Entwicklung von Form und Struktur historischer Gewölbe aus der Sicht der Statik.

29 (1999)   H. Menrath:
Numerische Simulation des nichtlinearen Tragverhaltens von Stahlverbundträgern.

30 (1999)   M. Bischoff:
Theorie und Numerik einer dreidimensionalen Schalenformulierung.

31 (1999)   W. A. Wall:
Fluid-Struktur-Interaktion mit stabilisierten Finiten Elementen.

32 (2000)   E. Kuhl:
Numerische Modelle für kohäsive Reibungsmaterialien.

33 (2001)   A. Maute:
Adaptive Finite-Element-Methoden in der Strukturdynamik.

34 (2001)   S. Schwarz:
Sensitivitätsanalyse und Optimierung bei nichtlinearem Strukturverhalten.

35 (2001)   A. Haufe:
Dreidimensionale Simulation bewehrter Flächentragwerke aus Beton mit der Plastizitätstheorie.

36 (2001)   D. P. Mok:
Partitionierte Lösungsverfahren in der Strukturdynamik und der Fluid-Struktur-Interaktion.

37 (2002)   H. Steeb:
Fehlerschätzer für FE-Berechnungen bei entfestigenden Materialien.

38 (2002)   K. Krausz:
Tragverhalten gemauerter Tonnengewölbe mit Stichkappen.

39 (2002)   M. Hörmann:
Nichtlineare Versagensanalyse von Faserverbundstrukturen.

40 (2003)   V. Gravemeier:
The Variational Multiscale Method for Laminar and Turbulent Incompressible Flow.

41 (2004)   R. Kemmler:
Stabilität und große Verschiebungen in der Topologie- und Formoptimierung.